

SEMICONDUCTOR | CATALYST INTERFACES IN PHOTOELECTROCHEMICAL  
DEVICES: CHARGE TRANSPORT THEORY, EXPERIMENTAL TECHNIQUE  
DEVELOPMENT, AND NANOSCALE APPLICATIONS

by

FORREST ALFRED LLOYD LASKOWSKI

A DISSERTATION

Presented to the Department of Chemistry  
and the Graduate School of the University of Oregon  
in partial fulfillment of the requirements  
for the degree of  
Doctor of Philosophy

September 2019

## DISSERTATION APPROVAL PAGE

Student: Forrest Alfred Lloyd Laskowski

Title: Semiconductor | Catalyst Interfaces in Photoelectrochemical Devices: Charge Transport Theory, Experimental Technique Development, and Nanoscale Applications

This dissertation has been accepted and approved in partial fulfillment of the requirements for the Doctor of Philosophy degree in the Department of Chemistry by:

Mark C. Lonergan	Chairperson
Shannon W. Boettcher	Advisor
George V. Nazin	Core Member
Benjamín J. Alemán	Institutional Representative

and

Janet Woodruff-Borden      Vice Provost and Dean of the Graduate School

Original approval signatures are on file with the University of Oregon Graduate School.

Degree awarded September 2019

© 2019 Forrest Alfred Lloyd Laskowski

## DISSERTATION ABSTRACT

Forrest Alfred Lloyd Laskowski

Doctor of Philosophy

Department of Chemistry

September 2019

Title: Semiconductor | Catalyst Interfaces in Photoelectrochemical Devices: Charge Transport Theory, Experimental Technique Development, and Nanoscale Applications

Photoelectrochemical energy conversion is a promising method to harvest incident sunlight and convert/store the energy in stable hydrogen gas bonds. The process is reliant on coupling between a light-absorbing semiconductor and an electrocatalyst responsible for enhancing the oxygen/hydrogen evolution reaction. However, photoelectrochemical energy storage remains inefficient, in part because the semiconductor|catalyst interface is not well understood. Attaining a clearer understanding of the interface is critically important because it is responsible for separation and collection of photogenerated charge.

In the following dissertation the behavior of the semiconductor|catalyst interface is experimentally and theoretically analyzed. Chapter 1 introduces the reader to two experimental techniques which facilitate interfacial understanding: dual-working-electrode photoelectrochemistry and potential sensing electrochemical atomic force microscopy. These techniques enable direct observation of potential and current transport across the semiconductor|catalyst interface during device operation. Chapter 2 applies these techniques to examine two common electrochemical experimental methods. The results suggest that analyzing the semiconductor|catalyst interface with the two methods is more challenging than previously appreciated. Chapter 3 presents an analytical model describing

charge transport across the semiconductor|catalyst interface. In Chapter 4 the experimental techniques from Chapter 1 are applied to analyze the semiconductor|catalyst behavior of two model systems with interfacial heterogeneity. The anomalously good performance of some devices is attributed to an increase in interfacial selectivity caused by the “pinch-off” effect.

This work builds upon and improves understanding of the semiconductor|catalyst interface in photoelectrochemical devices. The dissertation contains previously published and un-published co-authored materials.

## CURRICULUM VITAE

NAME OF AUTHOR: Forrest Alfred Lloyd Laskowski

### GRADUATE AND UNDERGRADUATE SCHOOLS ATTENDED:

University of Oregon, Eugene  
Carroll College, Helena

### DEGREES AWARDED:

Doctor of Philosophy, Chemistry, 2019, University of Oregon  
Bachelor of Arts, Chemistry, 2012, Carroll College  
Bachelor of Arts, Computer Science, 2012, Carroll College

### AREAS OF SPECIAL INTEREST:

Materials Science: Solar Cells and Renewable Energies  
Materials Science: Energy Storage

### PROFESSIONAL EXPERIENCE:

Post Bachelor Researcher, Pacific Northwest National Labs, 2012-2014

### GRANTS, AWARDS, AND HONORS:

Roy F. Simperman Scholarship, Carroll College, 2010-2012  
NSF Graduate Research Fellowship, University of Oregon, 2014  
RESF Renewable Energy Scholarship, University of Oregon, 2017  
CAS Dissertation Research Fellowship, University of Oregon, 2018

### PUBLICATIONS:

F. A. L. Laskowski, M. R. Nellist, R. Venkatkarthick, S. W. Boettcher. Junction Behavior of n-Si Protected by Thin Ni from Dual Working Electrode Photoelectrochemistry, *Energy & Environmental Science*, 2017, 10(2), 570-579.

M. R. Nellist, F. A. L. Laskowski, J. Qiu, H. Hajibabaei, K. Sivula, T. W. Hamann, S. W. Boettcher. Potential-Sensing Electrochemical Atomic Force Microscopy for In Operando Analysis of Water-Splitting Catalysts and Interfaces, *Nature Energy*, 2018, 1, 46-52.

Published: F. A. L. Laskowski\*, M. R. Nellist\*, J. Qiu, S. W. Boettcher. Metal Oxide/(oxy)hydroxide Overlayers as Hole Collectors and Oxygen-Evolution Catalysts on Water-Splitting Photoanodes, *Journal of the American Chemical Society*, 2019, 141(4), 1394-1405. \*co-first author

M. R. Nellist\*, F. A. L. Laskowski\*, F. Lin, T. J. Mills, S. W. Boettcher. Semiconductor–Electrocatalyst Interfaces: Theory, Experiment, and Applications in Photoelectrochemical Water Splitting, *Accounts of Chemical Research*, 2016, 49, 733-740. \*co-first author

F. A. L. Laskowski, J. Qiu, M. R. Nellist, S. Z. Oener, A. M. Gordon, S. W. Boettcher. Transient Photocurrents on Catalyst-Modified n-Si Photoelectrodes: Insight from Dual-Working Electrode Photoelectrochemistry, *Sustainable Energy & Fuels*, 2018, 2, 1995-2005.

Published: J. Qiu, H. Hajibabaei, M. R. Nellist, F. A. L. Laskowski, T. W. Hamann, S. W. Boettcher. Direct In Situ Measurement of Charge Transfer Processes During Photoelectrochemical Water Oxidation on Catalyzed Hematite, *ACS Central Science*, 2017, 3(9), 1015-1025.

T. J. Mills, F. A. L. Laskowski, C. Dette, M. R. Nellist, S. W. Boettcher. The Role of Surface States in Electrocatalyst-Modified Semiconductor Photoelectrodes: Theory and Simulations, *arXiv*, 2017, 1707.03112.

A. S. Batchellor, G. Kwon, F. A. L. Laskowski, D. M. Tiede, S. W. Boettcher. Domain Structures of Ni and NiFe (Oxy) Hydroxide Oxygen-Evolution Catalysts from X-ray Pair Distribution Function Analysis, *The Journal of Physical Chemistry C*, 2017, 121(45), 25421-25429.

M. R. Nellist, J. Qiu, F. A. L. Laskowski, F. M. Toma, S. W. Boettcher. Potential-Sensing Electrochemical AFM Shows CoPi as a Hole Collector and Oxygen Evolution Catalyst on BiVO<sub>4</sub> Water-Splitting Photoanodes, *ACS Energy Letters*, 2018, 3(9), 2286-2291.

J. Qiu, H. Hajibabaei, M. R. Nellist, F. A. L. Laskowski, S. Z. Oener, T. W. Hamann, S. W. Boettcher. Catalyst Deposition on Photoanodes: The Roles of Intrinsic Catalytic Activity, Catalyst Electrical Conductivity, and Semiconductor Morphology, *ACS Energy Letters*, 2018, 3(4), 961-969.

F. A. L. Laskowski, S. Z. Oener, M. R. Nellist, A. M. Gordon, D. C. Bain, J. L. Fehrs, S. W. Boettcher. Nanoscale Semiconductor/Catalyst Interfaces in Photoelectrochemistry, Accepted at Nature Materials.

F. A. L. Laskowski, M. R. Nellist, C. Dette, S. W. Boettcher. Unified Theory and Simulation for Surface State Influence on Photoelectrodes, In Preparation.

F. A. L. Laskowski, M. R. Nellist, J. Qiu, A. M. Gordon, S. W. Boettcher. Interpretation of Hole Scavenged Photoanode Behavior from Dual Working Electrode Photoelectrochemistry, In Preparation.



## ACKNOWLEDGMENTS

This work was funded in part by the Department of Energy, Basic Energy Sciences, award number DE-SC0014279. The atomic force microscope was purchased using funds provided by the NSF Major Research Instrumentation Program, grant DMR-1532225. This work made use of shared instrumentation in the CAMCOR and Rapid Materials Prototyping facilities, which are supported by grants from the M. J. Murdock Charitable Trust, the W. M. Keck Foundation, ONAMI, and the NSF. Additional support was provided from the Sloan and Dreyfus foundations. I was supported by a NSF graduate research fellowship, number 1309047, and the University of Oregon CAS Dissertation Fellowship.

The work was significantly facilitated by the expertise of CAMCOR staff. I am particularly grateful to Dr. Stephen Golledge, Dr. Fuding Lin, and Robert Fischer for their expert guidance when conducting XPS, ALD, SEM, and a myriad of eccentric tasks in CAMCOR. I would like to thank the University of Oregon machine shop, and especially John Boosinger, for creating various electrochemical accessories. I am also very appreciative of the administrative staff working in the University of Oregon Chemistry Department. I appreciate Christi Mabinuori, Leah O'Brien, Jim Rasmussen, Diane Lachenmeier, Kathy Noakes, Janet Macha, and Gerri Ravjaa who answered countless questions over these five years, facilitated chemical acquisitions, and helped organize conference travel.

The work would not have been possible without the aid and guidance of Shannon Boettcher, my advisor. I want to thank Shannon for forcing me to defend most of my worst ideas, for giving me the freedom to approach graduate school at my own pace, and for pushing me to improve my scientific writing. Most of all I want to thank Shannon for his wealth of scientific insight and guidance at every stage of my PhD. I applied to the University of Oregon for the opportunity to work with Shannon. It was the right decision.

Thank you to Mark Lonergan, Benjamín Alemán, and George Nazin (my committee members) for facilitating my scientific development. I'd also like to thank Mark Lonergan for his Semiconductor Device Physics class. I was woefully lacking in prerequisites for that class, but Mark's teaching ability is such that many of the concepts stuck and became foundational.

To my undergraduate professors, Dr. Kyle Strode, Dr. Colin Thomas, and Dr. Ron Wilde, thank you for humoring endless chemical questions, writing letters of recommendation, and encouraging me to attend graduate school.

To the Boettcher Group, I want to thank all of you for fostering a lab environment that made me look forward to coming into work (most days). From the very beginning I felt encouraged and supported by all of you. I want to thank Dr. Annie Greenaway, Dr. Michaela (Burke) Stevens, Dr. Lisa Enman, Dr. Matt Kast, Dr. Adam Smith, Dr. Fuding Lin, Dr. Jason Boucher and Dr. Adam Batchellor for building the amazing lab culture that existed when I first arrived. It takes work and I appreciate that you all put the time in. I'd like to thank Dr. Matt Kast, Dr. Mike Nellist, Dr. Adam Smith, and Lizzie Cochran for the particularly enjoyable late night conversations. I will always miss those evenings. Thank you Christopher Funch for being a constant source of joy at lab outings and doing more than anyone else to ensure the group runs smoothly. Also, thank you Chris and Lizzie for your collective empathy throughout this "graduating" experience. I'd like to thank the

researchers who allowed me to mentor them: Adrian Gordon, Radhakrishnan Venkatkarthick, David Bain, and Aaron Kaufman. It was great having each of you in the group and thank you for your scientific enthusiasm. Thank you to Sebastian Oener and Jingjing Qiu for your routine guidance and solid scientific contributions to this work. I hope I can be as great of as post doc as you each were. I would be remiss not to mention the newest Boettcher Lab members: Grace Lindquist, Jessica Fehrs, and Raina Krivina. You've each made our lab outings more enjoyable and I'm glad knowing that the lab is being left in capable hands. Finally, to Dr. Michael Nellist and Dr. Matt Kast thank you for the great memories outside of work – I appreciate your friendships.

Thank you to Dr. Adam Jansons and Dr. Luke Wheeler, my roommates & friends during the first two years of graduate school, for all the great hikes you dragged me on. I will always remember the wonderful costume parties we threw together. And Adam, thanks for dragging me to Cuba – it was a great experience. To my best friends back home, Evin Ozer and Ryan Lorenz, thanks for being a constant source of support. I have always appreciated your undying interest in my science, especially during the times when I didn't believe in it myself. Thank you for taking the time to maintain our relationship even though I moved far far away. To my sisters, Sierra & Autumn, thank you for tolerating my desire to move away for graduate school and for thinking that what I'm doing is "cool". To my mom, Donna Sebastian, thank you always believing in my academic abilities and for pushing me to be better. I didn't give you the appreciation you deserved for all the extra after-school tutoring during grade school. To my dad, Randy Laskowski, there is nobody more interested in my science than you are – thank you so much for always staying involved. And thank you for financially backing me during tough times, I would never have made it to graduate school without you. To Aurora Ginzburg, my significant other, thank you for the years of mutual support, for all the wonderful trips we took together (but you mostly planned), and for a home life that I look forward to at the end of every day. I could never adequately describe how much you have improved my graduate school experience. Thank you for being there for me. To Tonks and Lupin, \*appreciation meow\*.

## TABLE OF CONTENTS

Chapter	Page
I. INTRODUCTION .....	1
Paper A: Metal Oxide/(oxy)hydroxide Overlayers as Hole Collectors and Oxygen-Evolution Catalysts on Water-Splitting Photoanodes.....	2
Introduction.....	2
Dual-working-electrode photoelectrochemistry – from macroscopic to nanoscopic measurements.....	7
Using DWE to Understand the Role(s) of Catalytic Layers in Oxygen-Evolving Photoanodes .....	9
Ni-Protected Si Photoanodes .....	11
Catalyst-Coated Fe <sub>2</sub> O <sub>3</sub> Photoelectrodes.....	12
Catalyst-coated BiVO <sub>4</sub> Photoelectrodes .....	16
Relating Shunt Recombination in Catalyst-Coated Photoelectrodes to Catalyst Carrier Collection.....	18
Outlook .....	20
Limitations .....	20
Further technique development/implementation .....	21
Improving photoelectrodes .....	23
Paper B: Semiconductor - Electrocatalyst Interfaces: Theory, Experiment, and Applications in Photoelectrochemical Water Splitting.....	23
Introduction.....	24
Materials: Semiconductors and Electrocatalysts .....	26
Semiconductors.....	27
Electrocatalysts .....	27
Classification of Interface Types .....	28
Semiconductor-Catalyst Interfacial Charge Transfer .....	30

Chapter	Page
In Situ Electrical Measurements of sem cat Interfaces .....	33
Catalyst Activity and Electrolyte Permeability.....	34
The Role of Surface States.....	36
Outlook: Designing Improved Interfaces.....	38
II. UNDERSTANDING AND IMPROVING UPON PHOTOELECTROCHEMICAL EXPERIMENTAL METHODS USING DUAL WORKING ELECTRODE STRATEGIES.....	40
Paper C: Transient Photocurrents on Catalyst-Modified n-Si Photoelectrodes: Insight from Dual-Working Electrode Photoelectrochemistry .....	41
Introduction.....	41
Methods.....	44
Photoanode fabrication and electrochemical characterization.....	44
Effects of catalyst loading on transient photocurrent response .....	46
Dual-working-electrode measurements of catalyst potential during photocurrent transients .....	48
Dual-working-electrode measurements of the protection-layer potential during photocurrent transients.....	52
Conclusions.....	55
Paper D: Behavior of Catalyst-Modified n-Si Photoelectrodes in the Presence of a Sacrificial Hole Scavenger: Insight from Dual-Working Electrode Photoelectrochemistry.....	57
Introduction.....	57
Experimental.....	59
Results & Discussion .....	60
Conclusions.....	64
III. ANALYTICAL AND NUMERICAL APPROACHES FOR MODELING CHARGE TRANSPORT IN PHOTOELECTROCHEMICAL DEVICES.....	66

Chapter	Page
Paper E: Theory and Simulation for the Effects of Surface States on Charge Transport in Photoelectrochemical Devices.....	67
Introduction.....	67
Model.....	68
Terminology: catalyst sites and surface states.....	68
Notation, variables, and parameters.....	69
Treatment of semiconductor hole transport.....	69
The Generalized Gärtner Model.....	70
Interfacial electron transfer: surface states, catalyst, and solution.....	72
Electron transfer model.....	72
Interfacial currents.....	73
Solution to the model equations.....	74
Results and Discussion.....	75
Non-ideal photodiodes.....	75
Basic transfer models.....	76
Adaptive catalysts — no surface states.....	76
Unscreened metallic surface states – no catalyst.....	79
Full transfer models.....	81
Series behavior — surface-state mediated transfer.....	82
Parallel effect — compensating for $V_H$ .....	84
Conclusion.....	86
IV. IDENTIFYING NANOSCALE PHENOMENA AT PHOTOELECTROCHEMICAL INTERFACES: THE PINCH-OFF EFFECT.....	88
Paper F: Junction Behavior of n-Si Photoanodes Protected by Thin Ni Elucidated from Dual Working Electrode Photoelectrochemistry.....	89

Chapter	Page
Broader Context.....	89
Introduction.....	90
Methods.....	93
Photoanode Fabrication and Electrochemical Characterization .....	93
Material Characterization.....	95
Results and Discussion .....	95
Photoelectrode and Junction Behavior as a Function of Ni Thickness.....	95
Effect of electrochemical activation .....	97
Elucidation of junction behavior through dual working electrode photoelectrochemistry.....	100
In-situ Tuning of Catalyst Activity to Assess Interface Properties.....	102
Physical picture of junction behavior .....	103
Conclusions.....	107
Paper G: Nanoscale Semiconductor/Catalyst Interfaces in Photoelectrochemistry.....	108
Introduction.....	108
Photoelectrochemistry of n-Si decorated with Ni nanoislands .....	110
Analytical Model of Size-Dependent Photovoltages – The Pinch-off Effect.....	114
Chemical Identity of the High-Barrier Region .....	117
Pinch-off in Photoelectrode Devices .....	121
Conclusions.....	122
V. CONCLUSIONS.....	124
APPENDICES .....	125
A. SUPPORTING INFORMATION FOR PAPER C .....	125

Chapter	Page
B. SUPPORTING INFORMATION FOR PAPER D .....	130
C. SUPPORTING INFORMATION FOR PAPER E.....	132
D. SUPPORTING INFORMATION FOR PAPER F.....	177
E. SUPPORTING INFORMATION FOR PAPER G .....	193
REFERENCES CITED.....	232
A. References for Paper A .....	232
B. References for Paper B.....	239
C. References for Paper C.....	244
D. References for Paper D .....	251
E. References for Paper E .....	265
F. References for Paper F.....	267
G. References for Paper G .....	271
H. References for Paper E Supporting Information.....	276
I. References for Paper F Supporting Information.....	277
J. References for Paper G Supporting Information.....	278

## LIST OF FIGURES

Figure	Page
A.1. Comparison of different roles of catalytic overlayers on semiconductor-coated photoanodes.....	4
A.2. Comparison of dual-working-electrode photoelectrochemistry techniques .....	6
A.3. Using nanoelectrodes to measure surface potential .....	8
A.4. Conceptual model showing how a catalyst-coated photoanode might operate under various conditions .....	10
A.5. Evolution of the photoelectrochemical response over many electrochemical cycles for a Ni-coated n-Si photoanode .....	11
A.6. Photogenerated hole transfer at the $\alpha\text{-Fe}_2\text{O}_3 \text{Ni}_{0.8}\text{Fe}_{0.2}\text{O}_x\text{H}_y$ interface.....	13
A.7. In-situ measurements of catalyst potential for $\text{Ni}_{0.8}\text{Fe}_{0.2}\text{O}_x\text{H}_y$ and CoPi on hematite and ITO .....	15
A.8. Nanoelectrode potential measurements for CoPi on $\text{BiVO}_4$ and FTO.....	17
A.9. Shunt recombination in catalyst-coated porous semiconductors .....	18
B.1. Band diagram depiction of charge transport through semiconductor/catalyst/solution interfaces .....	25
B.2. Comparison of electrolyte-permeable and non-permeable catalyst layers.....	28
B.3. Band diagrams for sem cat interfaces in dark and illuminated conditions.....	29
B.4. Simulated J-V behavior and energy diagrams for sem cat junctions .....	32
B.5. Depiction of Dual-working-electrode photoelectrochemistry.....	33
B.6. Experimental sem cat open-circuit photovoltages.....	34
B.7. Experimental J-V curves for dense and electrolyte-permeable catalysts .....	36
B.8. Effect of surface states on permeable catalysts .....	38
B.9. Effect of catalyst on interface carrier selectivity.....	39
C.1. Illuminated voltammetry collected after each transient experiment as a function of photodeposited catalyst loading .....	46



Figure	Page
C.2. Transient response as a function of catalyst loading.....	48
C.3. Measurement of catalyst potential during transient experiments.....	49
C.4. Schematic band diagrams of transition of system between dark and light states.....	51
C.5. Sensing the protection layer electrochemical potential.....	53
C.6. Transients vs. catalyst loading on the same sample shown in Figure 2A.2 .....	55
D.1. Comparison of electrochemical behavior for a n-Si   Ni photoanode with and without a 0.5 M H <sub>2</sub> O <sub>2</sub> hole scavenger.....	61
D.2. Comparison of electrochemical behavior for a n-Si   Ni photoanode with and without a 0.5 M H <sub>2</sub> O <sub>2</sub> hole scavenger while sensing the catalyst's electrochemical potential.....	62
D.3. Comparison of electrochemical behavior for a n-Si   Ir photoanode with and without a 0.5 M H <sub>2</sub> O <sub>2</sub> hole scavenger.....	64
E.1. Response for a .....	76
E.2. Adaptive catalyst model .....	77
E.3. Metallic surface state behavior.....	80
E.4 Full model – series behavior.....	83
E.5. Full model – parallel behavior.....	85
F.1. Schematic depicting a n-type photoanode protected with a catalyst material and a second working electrode for DWE measurements .....	92
F.2. Comparison of WE1 and WE2 for devices with varied Ni thickness.....	96
F.3. Illuminated cycling of n-Si protected with 5 nm Ni in pH 9.8 K-borate buffer.....	98
F.4. Catalyst electrochemical potential sensing via WE2.....	101
F.5. Dark J-V characteristics for the 5 nm n-Si photoanodes .....	102
F.6. Illuminated PEC response due to Fe incorporation .....	103
F.7. Schematic of ultrathin Ni protection on n-Si.....	105

Figure	Page
G.1. Characteristics of photoanodes fabricated by electrodepositing Ni nanoislands onto n-Si.....	111
G.2. Characterization of n-Si/Ni photoelectrodes obtained from the 5-s deposition.....	113
G.3. Simulations showing how the pinch-off model explains performance enhancements with catalyst nanocontacts.....	116
G.4. Dual-working-electrode (DWE) device measurements show that high-barrier contacts are formed from the oxidized NiOOH during operation.....	118
G.5. n-Si/Ni nanocontacts produce a pinched-off junction after activation .....	120
C.S1. Two dual-working-electrode (DWE) deposition strategies .....	125
C.S2. Transient integration comparison between the different extents of catalyst loading.....	126
C.S3. Comparison of electrode activity before and after the first transient experiment.....	126
C.S4. Cyclic voltammogram through the WE2 contact after transient experiments showing position of the oxidation and reduction waves for the catalyst .....	127
C.S5. Full transient behavior for the electrode used to sense the protection layer electrochemical potential (from Figure C.5).....	127
C.S6. Cyclic voltammogram through the WE2 contact after transient experiments .....	128
C.S7. Integration of the photocurrent transients from Figure C.5 of the main text....	129
D.S1. Comparison of electrochemical behavior for a n-Si   Ir photoanode with and without a 0.5 M H <sub>2</sub> O <sub>2</sub> hole scavenger.....	130
D.S2. Comparison of H <sub>2</sub> O <sub>2</sub> and H <sub>2</sub> O oxidation responses before and after Co-Pi deposition on a Fe <sub>2</sub> O <sub>3</sub> photoanode.....	131
E.S1. Model schematic .....	133
E.S2. Equation S2.13 solved for equilibrium Helmholtz potential at various values of Esso .....	142
E.S3. Hole concentration profile and the currents generated by the generalized Gärtner model .....	149

Figure	Page
E.S4. Simulation results for the system without surface states.....	167
E.S5. Simulation results for the system without surface states.....	168
E.S6. Simulation results for model exhibiting parallel behavior .....	169
E.S7. Additional simulation results for model exhibiting parallel behavior.....	170
E.S8. Simulation results for model exhibiting parallel behavior .....	171
E.S9. Additional simulation results for model exhibiting parallel behavior.....	172
E.S10. Model code section 1.....	173
E.S11. Model code section 2.....	174
E.S12. Model code section 3.....	175
E.S13. Model code section 4.....	176
F.S1. Shorting test for photoelectrodes.....	178
F.S2. Comparison of WE1 and WE2 with extended ageing.....	179
F.S3. Dual-working-electrode technique applied to Au control.....	180
F.S4. Illuminated degradation of an n-Si photoanode protected with 2 nm metallic Ni.....	181
F.S5. Illuminated degradation of an n-Si photoanode protected with electrochemically deposited Ni.....	181
F.S6. Dark in-situ LSV characteristics for an intentionally buried n-Si   Au junction .....	182
F.S7. Dark in-situ LSV characteristics for n-Si photoanodes protected with 3 and 5 nm of Ni .....	184
F.S8. Illuminated $10 \text{ mV s}^{-1}$ LSVs collected through WE1 before and after Fe incorporation.....	185
F.S9. XPS spectra of n-Si protected with 3 nm of Ni after electrochemical cycling.....	186
F.S10. Select sputter times selected from Figure F.S9a to identify key peak positions .....	187

Figure	Page
F.S11. XPS spectra at select sputter times for control samples of n-Si protected with 3 nm of Ni without electrochemical cycling.....	188
F.S12. XPS spectra of Ni(OH) <sub>2</sub> electrodeposited (-2 mA for 60 s in a 0.1 Ni(NO <sub>3</sub> ) <sub>2</sub> solution) onto Au, after electrochemical cycling.....	189
F.S13. Comparison of illuminated CVs for n-Si protected with 3 nm Ni after activation protocol .....	191
F.S14. AFM images of n-Si protected with 3 nm of Ni.....	192
F.S15. SEM image of n-Si protected with 3 nm of Ni after electrochemical cycling.....	192
G.S1. Typical chronoamperometry data for electrodepositions used to produce photoanodes with n-Si/Ni nanocontacts.....	195
G.S2. SEM, cross-sectional TEM, and high-angle annular dark field (HAADF) TEM images for Ni nanoislands electrodeposited for 5 s on n-Si .....	197
G.S3. EDX composition maps collected using ChemiSTEM mode on a FEI TITAN 80-200 TEM/STEM for islands before and after activation in 1 M KOH.....	198
G.S4. Ideality factors extracted from the dark J-V curves measured through single nanoislands via AFM.....	199
G.S5. Raw operando photovoltage data corresponding to Figure G.2d in main manuscript.....	200
G.S6. Built-in laser alignment for the Bruker AFM .....	201
G.S7. Comparison of AFM island dimensions to those measured by SEM.....	202
G.S8. The photoelectrochemical behavior of Ni islands electrodeposited onto a Pt substrate and Butler-Volmer fit .....	205
G.S9. Mott-Schottky analysis results for bare Si as a function of activation cycles.....	206
G.S10. Example impedance behavior of a dual-working-electrode device with the catalyst held in either an oxidized or reduced state .....	208
G.S11. Mott-Schottky data representation and fits for the dual-working-electrode devices.....	209

Figure	Page
G.S12. Photovoltage measurements from the dual-working-electrode (DWE) devices.....	209
G.S13. The effect of continued activation on n-Si photoanodes with 5 s Ni electrodeposition.....	211
G.S14. COMSOL Multiphysics numerical model for pinched-off contacts .....	213
G.S15. COMSOL Multiphysics numerical J-V data for pinched-off contacts and SEM/AFM images depicting catalyst redeposition after activation in 1 M K-borate .....	215
G.S16. Comparison between photoanodes with continuous 60 s Ni electrodeposition and those with sequential electrodeposition where an activation procedure is performed at 5 and 10 s .....	216
G.S17. A possible strategy for creating selective contacts using pinch-off.....	217
G.S18 Python 3 code for modeling pinch-off: #1.....	218
G.S19 Python 3 code for modeling pinch-off: #2.....	218
G.S20 Python 3 code for modeling pinch-off: #3.....	219
G.S21 Python 3 code for modeling pinch-off: #4.....	219
G.S22 Python 3 code for modeling pinch-off: #5.....	220
G.S23 Python 3 code for modeling pinch-off: #6.....	220
G.S24 Python 3 code for modeling pinch-off: #7.....	221
G.S25 Python 3 code for modeling pinch-off: #8.....	221
G.S26 Python 3 code for modeling pinch-off: #9.....	222
G.S27 Python 3 code for modeling pinch-off: #10.....	222
G.S28 Python 3 code for modeling pinch-off: #11.....	223
G.S29 Python 3 code for modeling pinch-off: #12.....	223
G.S30 Python 3 code for modeling pinch-off: #13.....	224
G.S31 Python 3 code for modeling pinch-off: #14.....	224
G.S32 Python 3 code for modeling pinch-off: #15.....	225

Figure	Page
G.S33 Python 3 code for modeling pinch-off: #16.....	226
G.S34 Python 3 code for modeling pinch-off: #17.....	227
G.S35 Python 3 code for modeling pinch-off: #18.....	228
G.S36 Python 3 code for modeling pinch-off: #19.....	229
G.S37 Python 3 code for modeling pinch-off: #20.....	230
G.S38 Python 3 code for modeling pinch-off: #21.....	230
G.S39 Python 3 code for modeling pinch-off: #22.....	231

## LIST OF TABLES

Table	Page
E.S1 Definition for all terms found in the charge transport modeling.....	138
G.S1 List of all variables, dependent expressions, coordinates and constants for pinch-off model.....	194

## CHAPTER I: INTRODUCTION

This chapter is divided into two sub-sections encompassing two completed bodies of work: a review published in the *Journal of the American Chemical Society* and a perspective published in *Accounts of Chemical Research*. These publications provide the reader an introduction to catalyzed oxygen evolution on photoanodes and the various techniques discussed throughout this thesis. Experiments reliant of dual-working-electrode (DWE) photoelectrochemistry are featured extensively in later chapters and are well introduced by the subsequent two publications. The DWE techniques are employed in Chapter 2 to better interpret data resulting from transient photocurrent and hole scavenger experimental methods. In Chapter 4, the semiconductor|catalyst junction behavior of n-Si photoanodes is initially elucidated using DWE experiments. The DWE concept is then adapted onto an atomic force microscope to probe the junction behavior of nanoscale features. The atomic force microscope adaption is referred to as potential-sensing electrochemical atomic-force microscopy (PS-EC-AFM) and this is also covered throughout the subsequent two publications.

Section A, Metal Oxide/(oxy) hydroxide Overlayers as Hole Collectors and Oxygen-Evolution Catalysts on Water-Splitting Photoanodes, contains co-authored material previously published as: Laskowski, F. A. L.‡; Nellist, M. R.‡; Qiu, J.; & Boettcher, S. W. Metal Oxide/(oxy) hydroxide Overlayers as Hole Collectors and Oxygen-Evolution Catalysts on Water-Splitting Photoanodes. *Journal of the American Chemical Society*, 141(4), 13941405 (2018). ‡joint authorship

Section B, Semiconductor–Electrocatalyst Interfaces: Theory, Experiment, and Applications in Photoelectrochemical Water Splitting, contains co-authored material previously published as: Nellist, M. R.‡; Laskowski, F. A. L.‡; Lin, F.; Mills, T. J.; & Boettcher, S. W. Semiconductor–Electrocatalyst Interfaces: Theory, Experiment, and Applications in Photoelectrochemical Water Splitting. *Accounts of Chemical Research*, 49(4), 733-740 (2016). ‡joint authorship

Prof. Boettcher, M. Nellist, and I conceived of the review/perspective directions. I coauthored all drafts of these publications and produced most figures. M. Nellist and I shared equal writing burden and intellectual contribution in each case. Prof. Boettcher extensively edited each draft of the manuscript with editorial assistance from J. Qiu. Author ordering between M. Nellist and I on these two publications was determined by an impartial coin flip, courtesy of M. G. Kast.



## Paper A

# Metal Oxide/(oxy)hydroxide Overlayers as Hole Collectors and Oxygen-Evolution Catalysts on Water-Splitting Photoanodes

Forrest A. L. Laskowski,<sup>†</sup> Michael R. Nellist,<sup>†</sup> Jingjing Qiu, Shannon W. Boettcher\*

<sup>†</sup> These authors contributed equally to the work.

### 1. Introduction

Solar-water-splitting provides a mechanism to convert and store solar energy in the form of stable chemical bonds. Water-splitting systems often include semiconductor photoanodes, such as n-Fe<sub>2</sub>O<sub>3</sub> and n-BiVO<sub>4</sub>, which use photogenerated holes to oxidize water. These photoanodes often exhibit improved performance when coated with metal-oxide/(oxy)hydroxide overlayers that are catalytic for the water oxidation reaction. The mechanism for this improvement, however, remains a controversial topic. This is, in part, due to a lack of experimental techniques that are able to directly track the flow of photogenerated holes in such multicomponent systems. In this *Perspective* we illustrate how this issue can be addressed by using a second working electrode to make direct current/voltage measurements on the catalytic overlayer during operation in a photoelectrochemical cell. We discuss examples where the second working electrode is a thin metallic film deposited on the catalyst layer, as well as where it is the tip of a conducting atomic-force-microscopy probe. In applying these techniques to multiple semiconductors (Fe<sub>2</sub>O<sub>3</sub>, BiVO<sub>4</sub>, Si) paired with various metal-(oxy)hydroxide overlayers (e.g. Ni(Fe)O<sub>x</sub>H<sub>y</sub> and CoO<sub>x</sub>H<sub>y</sub>), we found in all cases investigated that the overlayers collect photogenerated holes from the semiconductor, charging to potentials sufficient to drive water oxidation. The overlayers studied thus form charge-separating heterojunctions with the semiconductor as well as serve as water-oxidation catalysts.

Semiconductors coated with electrocatalysts are key components of photoelectrochemical water-splitting systems that generate hydrogen and oxygen gas from sunlight and water.<sup>1</sup> Oxide semiconductors, such as Fe<sub>2</sub>O<sub>3</sub> and BiVO<sub>4</sub>, have been studied extensively for driving the oxygen-evolution half reaction because they are in principle inexpensive and chemically stable under oxidizing conditions.<sup>2-5</sup> To increase performance such photoanodes are typically coated by electrocatalyst layers.<sup>6-9</sup> However, the mechanisms of charge transfer and the fate of photogenerated carriers in these combined systems are not well understood.<sup>10-11</sup> The semiconductors are generally polycrystalline with various facets and grain boundaries which affect

electronic transport.<sup>4, 12-13</sup> The surfaces are often defective, populated by surface states with varying densities and energies.<sup>14-15</sup> Water-oxidation catalysts are typically (photo)electrodeposited metal (oxy)hydroxides such as nickel-iron oxyhydroxide ( $\text{Ni(Fe)O}_x\text{H}_y$ ) or cobalt oxyhydroxide phosphate (CoPi), and the resulting catalyst films are disordered, porous and often permeable to electrolyte.<sup>16-20</sup>

The precise role of the catalytic layers remains a central question and is the focus of this *Perspective*. The layers are generally referred to as “catalysts” because when applied to conductive electrodes (in the dark) they evolve oxygen at low overpotentials.<sup>16-19</sup> When applied to semiconductor (sem) photoanode surfaces they typically enhance the photocurrent onset potential and/or the total photocurrent for water oxidation.<sup>1, 21</sup> The origin of this enhancement, however, is the subject of significant discussion. Many have assumed a simple model where the catalyst (cat) collects holes from the semiconductor and then uses those holes to drive water oxidation at more cathodic potential than is possible in the absence of the catalyst (Figure A.1a).<sup>6, 22</sup> Recent work using impedance analysis by the Hamann and Gamelin groups have supported this, indicating that CoPi on  $\text{Fe}_2\text{O}_3$  serves to collect photogenerated holes.<sup>22-23</sup> Others have argued that catalysts play an indirect role in enhancing photoelectrode performance by, for example, chemically passivating defects on the semiconductor surface responsible for electron-hole pair recombination.<sup>14-15, 24-25</sup> In this view, the semiconductor’s ability to oxidize water improves because a larger steady-state concentration of surface holes is available to drive water oxidation (Figure A.1b). A related hypothesis suggests that the catalyst passivates semiconductor surface states responsible for Fermi-level pinning.<sup>22, 26</sup> Once passivated, the semiconductor band bending increases for a given applied potential and the near-surface concentration of conduction-band electrons is decreased, thus decreasing the forward recombination electron current. Finally, the catalyst could create a solid-state heterojunction with more-favorable band bending (Figure A.1c) than the semiconductor/liquid junction.<sup>9, 27-29</sup> Examples of the possible behaviors for catalyst layers on semiconductor photoanodes are given in Figure A.1.

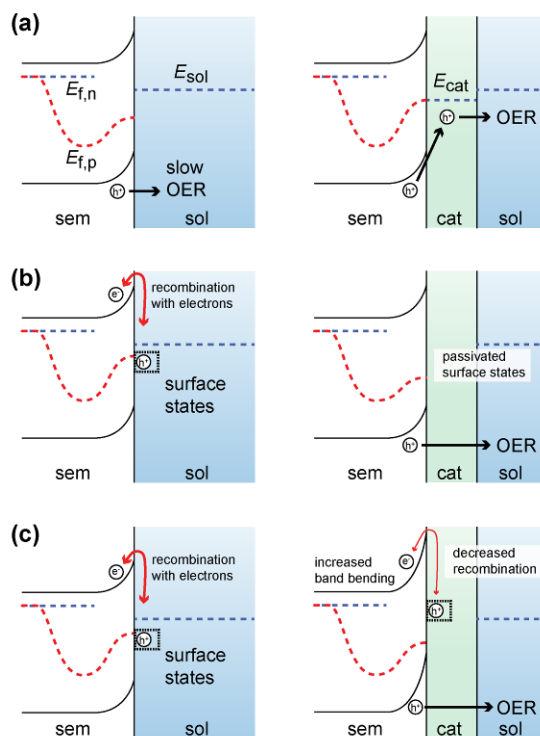


**Figure A.1. Comparison of different roles of catalytic overlayers on semiconductor-coated photoanodes.** The photoanodes depicted in the left column show the illuminated band diagram before catalyst deposition. The right column illustrates how the behavior changes once a catalyst is deposited for each case. All depictions are shown with the same arbitrary applied potential such that oxygen evolution occurs.  $E_{f,n}$  is the quasi-Fermi level of the electrons,  $E_{f,p}$  is the quasi-Fermi level of the holes,  $E_{sol}$  is solution Fermi level (taken to be equal to  $q\epsilon_{O_2/OH^-}$  where  $\epsilon_{O_2/OH^-}$  is the thermodynamic potential for water oxidation), and  $E_{cat}$  is Fermi level of the catalyst overlayer. (a) Slow OER kinetics on the semiconductor surface inhibits facile oxygen evolution. The catalyst enhances oxygen evolution by collecting photo-generated holes from the semiconductor and using them to oxidize water. (b) The presence of surface states results in significant recombination current. The “catalyst” effectively passivates these states and enables greater water oxidation on the semiconductor surface as the surface hole concentration is increased at steady state. (c) A large electron concentration at the conduction-band edge promotes forward recombination electron current. This diminishes the semiconductor’s ability to drive OER because holes are lost to recombination. Deposition of a catalyst results in greater band-bending which decreases the forward electronic dark current. The increased hole population allows the semiconductor to more effectively oxidize water. Note: for the schemes in (b) and (c) water oxidation may occur directly on the semiconductor surface (through the electrolyte-permeable catalyst overlayer).

Several experimental techniques have been developed/applied to differentiate between the various hypotheses describing how catalytic layers improve performance. Durrant and coworkers, among others, have employed transient absorption spectroscopy (TAS) and photoinduced-absorption (PIA) optical techniques to investigate the fate of photogenerated holes on CoPi-coated hematite ( $\text{Fe}_2\text{O}_3$ ) and bismuth vanadate ( $\text{BiVO}_4$ ).<sup>9, 27-43</sup> The TAS technique is a pump-probe technique in which “fingerprints” of the holes in the transient optical-absorption spectra, following an excitation pulse, are identified and their decay monitored as a function of time. PIA is similar but the optical signature of accumulated holes is monitored at quasi-steady state. These techniques are powerful in that the authors show changes in the optical absorption spectra, with applied potential, which correlate to changes in the measured OER current. However, various assumptions are required when using the absorption signal to follow the fate of photogenerated holes. For example, one must be able to assign a given optical signal to a hole trapped in the semiconductor itself, on the semiconductor surface, or in the catalyst. One must also carefully calibrate for the quantity of catalyst present and its optical extinction coefficient. Using these optical techniques Durrant and coworkers concluded that although isolated CoPi is a water oxidation catalyst, it does not drive water oxidation either on  $\text{Fe}_2\text{O}_3$  or  $\text{BiVO}_4$  and instead primarily serves to passivate surface states (Figure A.1b).<sup>9, 27, 29</sup>

Intensity-modulated photocurrent spectroscopy (IMPS), has also been used to examine the role of CoPi and  $\text{Ni}(\text{Fe})\text{O}_x\text{H}_y$  catalysts on  $\text{Fe}_2\text{O}_3$  and  $\text{BiVO}_4$ .<sup>24-26, 44-48</sup> In the IMPS technique, the semiconductor is illuminated with a periodically modulated light source at a constant applied potential and the photocurrent response is measured as a function of the modulation frequency. The resulting data can be analyzed by applying a first-order kinetic model which accounts for minority carrier generation and collection (modeled via the Gärtner hole current), the hole concentration in surface states, recombination with conduction-band electrons at surface states, and charge transfer to solution.<sup>47</sup> Apparent recombination and transfer rate constants can then be extracted from the data. Interestingly, for both CoPi on  $\text{BiVO}_4$ , and  $\text{Ni}(\text{Fe})\text{O}_x\text{H}_y$  on  $\text{Fe}_2\text{O}_3$ , the “catalyst” was found to significantly decrease the apparent recombination rate constant while not significantly affecting the apparent rate constant for transfer to solution (i.e. catalysis).<sup>25-26, 47</sup> It was thus concluded that these catalysts serve to passivate surface states, not increase water oxidation kinetics. We note that this interpretation relies on the validity of the model used to analyze the IMPS data. The original model was developed for a simple system in the absence of a catalyst and contains only two kinetic processes.<sup>45, 47</sup> The catalyst-coated semiconductor system is more complex because forward and

reverse hole and electron transfer between semiconductor, surface state, catalyst, and solution subsystems may all occur.

In this perspective we focus on “dual-working-electrode” methods developed in our research group to directly probe the flow of charge carriers in catalyst-coated photoanodes.<sup>49-57</sup> The techniques all rely upon electrical contact to the catalyst layer to directly measure the catalyst’s operating potential in-situ during photoelectrochemical experiments. The work builds on previous efforts to measure quasi-Fermi levels using secondary electrodes in dye-sensitized<sup>58</sup> and bulk-semiconductor photoelectrochemical cells,<sup>59</sup> as well as work on semiconductor|conducting-polymer<sup>60</sup> and semiconductor|nanoparticle interfaces.<sup>61</sup> In one example, this contact is a thin electrolyte-permeable OER-inert metal film deposited on top of the catalyst layer (Figure A.2a).<sup>49-50, 53-54</sup> In another example, the second contact is the metallized tip of a conducting atomic-force-microscope (AFM) probe (Figure A.2b).<sup>51, 55</sup> These techniques are straightforward in that simplifying assumptions are not required to draw conclusions from the obtained data. For example, the accumulation of holes in the catalyst layer during photoelectrochemistry can be directly sensed by the potential of the second working electrode. We find, contrary to the results of the TAS/PIA and IMPS studies, that typical catalysts such as CoPi and Ni(Fe)O<sub>x</sub>H<sub>y</sub> collect holes and drive water oxidation across the studied semiconductor systems. Others have used these techniques to examine TiO<sub>2</sub>-protected cathodes,<sup>62</sup> properties of semiconductor-liquid junctions,<sup>63</sup> and buried junctions in water-splitting dye-sensitized photoelectrochemical cells.<sup>64</sup>

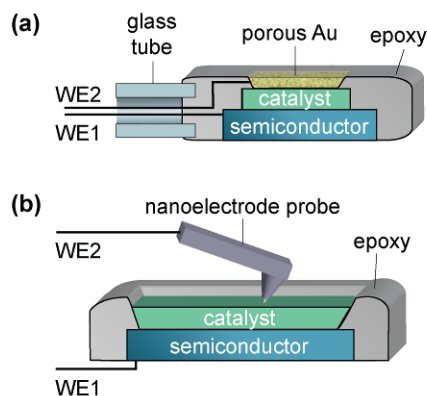


**Figure A.2. Comparison of dual-working-electrode photoelectrochemistry techniques.** In both cases, the first working electrode (WE1) is attached to the semiconductor backside via an ohmic contact. (a) For the macroscopic technique, a porous Au thin film is deposited onto the surface of the catalyst and electrically connected to the second working electrode (WE2). (b) For the nanoscale approach, a conductive nano-electrode AFM probe is used instead of the Au film.

## 2. Dual-working-electrode photoelectrochemistry – from macroscopic to nanoscopic measurements

The basic concepts underlying the fundamental and practical aspects of dual-working-electrode photoelectrochemistry (DWE PEC) have been previously reviewed.<sup>50, 56</sup> As in traditional PEC measurements, the DWE PEC setup features a semiconductor whose potential can be manipulated by a potentiostat through an ohmic back contact. We refer to this connection as the primary working electrode (WE1) and it can be used to measure current response while sweeping the semiconductor potential  $V_{\text{sem}}$ . As discussed above, photoanodes are often studied with catalyst surface layers which reduce the potential required to drive water oxidation at a given current density. For DWE PEC experiments, a second contact is applied to the catalyst layer by thermally evaporating an Au film onto the catalyst surface to serve as the second working electrode (WE2). Au is selected due to its low intrinsic OER activity, high conductivity, and electrolyte permeability (at sufficiently thin deposition thicknesses). The second working electrode enables the current/potential to be measured or controlled at the catalyst film independent of the semiconductor and WE1.

The DWE technique has been applied to study a variety of well-defined sem|cat systems, such as  $\text{TiO}_2$ , Si and planar  $\text{Fe}_2\text{O}_3$  with uniform catalyst layers, and will be discussed below. However, many of the most commonly studied photoelectrodes for water oxidation consist of three-dimensionally structured semiconductors coupled to catalysts which may not uniformly cover the photoelectrode surface.<sup>52</sup> Application of a thin Au top contact is challenging on these types of systems because the Au may short to the underlying semiconductor surface (creating a Schottky-type junction). For especially rough surfaces the Au may not interconnect well when deposited at thicknesses sufficiently thin for electrolyte permeability.<sup>56</sup>

To overcome these challenges, we translated the technique to the nanoscale using recently developed nanoelectrode AFM probes.<sup>51</sup> These nanoelectrode AFM probes are conductive, with a thin insulating layer coating the entire probe except for the exposed tip (Figure A.3a). By scanning the electrode surface, the probes can be used to image the morphology and catalyst coverage. For photoanodes with incomplete catalyst coverage, this initial image allows the semiconductor surface to be distinguished from locations with catalyst coating. Once a topological map is acquired, the AFM can land the probe at a selected location and collect surface-potential data for the duration of a (photo)electrochemical experiment. This setup is depicted in Figure A.2b. For *operando* AFM experiments a custom electrochemical cell and AFM stage were built to enable back illumination and the use of an Ag/AgCl reference electrode.

To demonstrate the ability of the probe to measure surface potential, we imaged an electrode consisting of Au/Ti-coated glass in the electrochemical AFM cell. With the nanoelectrode probe contacting the submerged Au surface (in a potassium phosphate buffer), the potential of the Au was stepped using WE1 and measured using the probe (WE2). As expected, the measured potential at WE2 traced the applied potential at WE1 (Figure A.3b). This result demonstrated that the nanoscale AFM probe can accurately measure the surface potential of a biased electrode in solution.

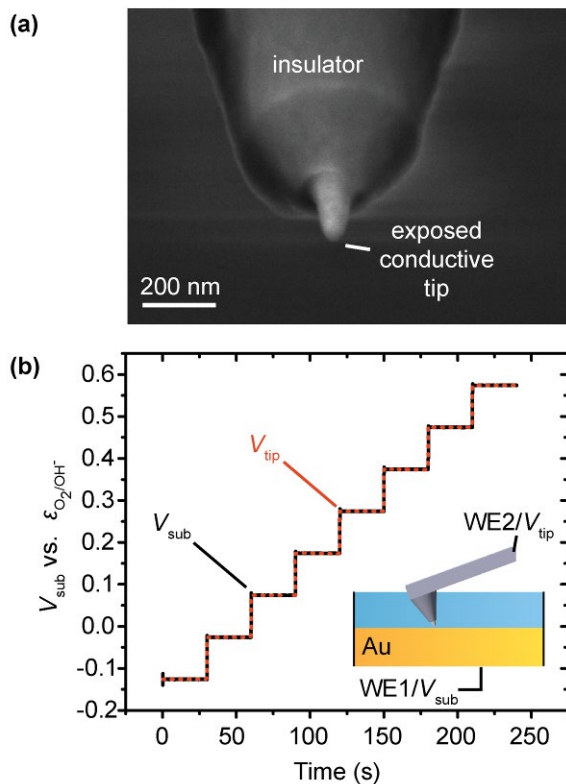


**Figure A.3. Using nanoelectrodes to measure surface potential.** (a) Scanning electron microscopy (SEM) image of nanoelectrode AFM probes used for nanoscale potential sensing. The Si probes coated with a conductive material (e.g. Pt) that is fully insulated except at the exposed tip. (b) Stepping the potential of an Au electrode anodically in 100 mV increments, while measuring the potential of the Au electrode using a nanoelectrode probe resting on the Au surface. This data shows the nanoscale electrode probe can be used to measure the surface potential of a biased electrode in an electrochemical cell. Adapted from Ref 55.

The importance of the nanoscale DWE technique, which we refer to as potential-sensing electrochemical atomic-force microscopy (PS-EC-AFM), is that the surface electrochemical

potential – i.e. the free energy of the reactive electrons – on a catalyst can be measured in situ without evaporation of a macroscopic second-working-electrode contact. This allows for a large diversity of samples to be studied. Additionally, because the technique is AFM-based it, in principle, enables simultaneous topographic and potential mapping of the electrode surface. This might help guide design of improved photoanodes by relating spatial heterogeneity of the photoelectrode interface to desirable electrochemical properties.<sup>65</sup>

### **3. Using DWE to Understand the Role(s) of Catalytic Layers in Oxygen-Evolving Photoanodes**

The experimental approaches described above provide an opportunity to study the fundamental role of overlayers in enhancing oxygen evolution on photoanodes. Here we provide an overview of the range of behaviors we have observed via DWE measurements. These behaviors are consistent with the model depicted in Figure A.4. In the model, the catalyst sits on the surface of the semiconductor and remains inactive in its reduced resting state while in the dark. Upon illumination, a hole-quasi-Fermi level is established in the semiconductor and holes accumulate at the semiconductor surface. Transfer of the surface holes into the catalyst, which is often an extended electronic system, is thermodynamically favorable and occurs efficiently compared to direct transfer to solution which requires driving the oxygen-evolution reaction. Holes injected into the catalyst layer increase the electrochemical potential of the catalyst until steady state is achieved. Because the catalysts studied are typically permeable to electrolyte and redox active (e.g. they contain Ni or Co cations that have multiple oxidation states accessible<sup>19-20, 49, 66</sup>), holes can accumulate throughout the “bulk” of the catalyst layer. The system reaches steady state when the net flux of holes into the catalyst is equal to the net flux out of the catalyst. This occurs when either (1) the rate of holes recombining with conduction band electrons equals the rate of hole injection into the catalyst or (2) the catalyst electrochemical potential becomes sufficient to directly drive OER at the rate of injected holes minus the rate of recombination (Figure A.4c). The catalyst’s ability to perform OER can be thought of in terms of Butler-Volmer or Tafel kinetics where the catalytic current depends exponentially on potential,<sup>67</sup> as can be measured directly by supplying potential via WE2 in the dark and measuring the resulting current at WE2 (demonstrated in the subsequent section). This direct measurement allows us to unambiguously relate the rate of oxygen evolution for a catalyst sitting on a semiconductor surface to the catalyst’s electrochemical potential. As the applied semiconductor bias or light intensity increases (causing an increase in photocurrent), the catalyst charges to a more-positive electrochemical potential to maintain current



continuity. Below we provide data across several catalyst/semiconductor systems that support this model.

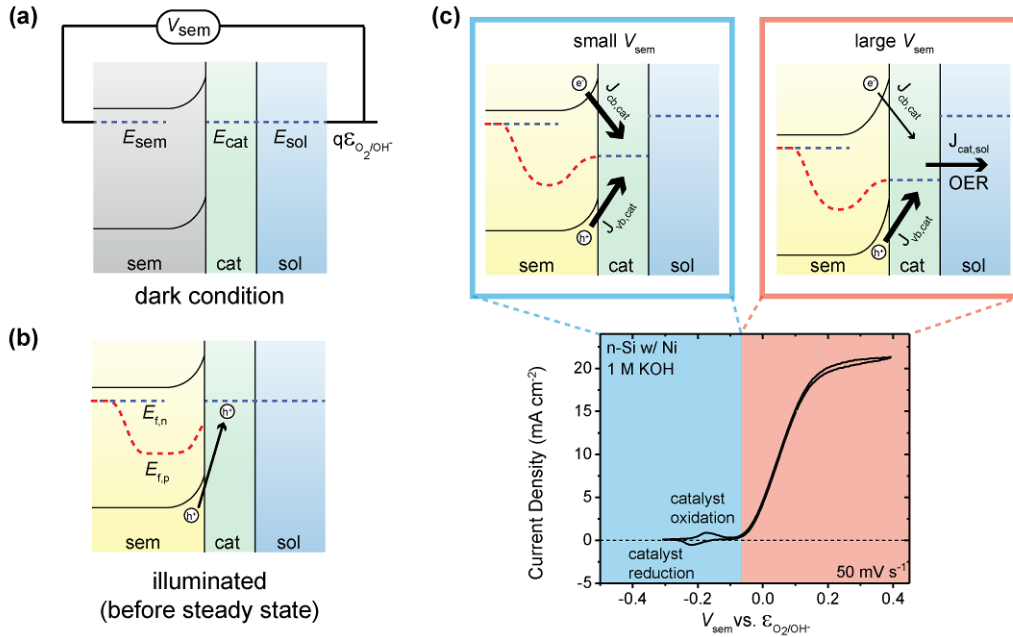


**Figure A.4. Conceptual model showing how a catalyst-coated photoanode might operate under various conditions.** (a) In the dark the Fermi levels equilibrate and the catalyst rests in an inactive state. Here  $E_{sem}$ ,  $E_{cat}$ , and  $E_{sol}$  represent the electrochemical potential of the semiconductor, catalyst, and solution.  $V_{sem}$  is the applied potential between the semiconductor back contact and the thermodynamic reference point for reversible oxygen evolution ( $\epsilon_{O_2/OH^-}$ ). (b) Upon illumination, a hole quasi-Fermi level ( $E_{f,p}$ ) is generated. Holes at the sem|cat interface transfer to the catalyst if easily-oxidized catalyst species are present (e.g. driving the  $Ni^{2+/3+}$  or  $Co^{2+/3+}$  redox couple in (oxy)hydroxide catalysts). (c) At steady state two broad regimes can be identified depending on the applied potential. At sufficiently low applied potentials the hole current from the valence band to catalyst ( $J_{vb,cat}$ ) is balanced by the recombination current from electrons in the conduction band to catalyst ( $J_{cb,cat}$ ). In this regime the catalyst might become oxidized but does not reach a sufficient potential to drive oxygen evolution (it cannot be sufficiently charged because  $J_{vb,cat} = -J_{cb,cat}$  at steady state). At sufficiently larger (positive) applied potentials the recombination current diminishes (as the electron concentration at the conduction band edge is decreased) and the catalyst is charged to an oxidizing potential where it can match the net junction current. In this case  $J_{vb,cat} + J_{cb,cat} = J_{cat,sol}$  at steady state.

### 3.1 Ni-Protected Si Photoanodes

The macroscopic DWE technique was applied to Si photoanodes to better understand efficiency increases reported when applying sufficiently thin catalyst/protection layers. Because Si is oxidized under OER conditions, the catalyst must play a protective role in addition to a catalytic role.<sup>68-69</sup> We studied devices where 3, 5, and 20 nm of Ni were thermally evaporated onto the Si surface. During operating conditions (illuminated and at anodic applied potentials) some of the Ni converts to  $\text{Ni}(\text{Fe})\text{O}_x\text{H}_y$  and serves as the catalyst. For these devices the junction is considered “buried”, meaning the charge-separating junction is not exposed to electrolyte. This condition precludes the OER from occurring on the semiconductor surface, therefore the photocurrent must pass through the catalyst layer (note: any exposed Si is unable to perform OER as it is preferentially oxidized). Aside from the increased understanding of Si photoanodes, the results are important because they illustrate how DWE measurements behave on a system where photogenerated charge clearly transfers to the catalyst layer.

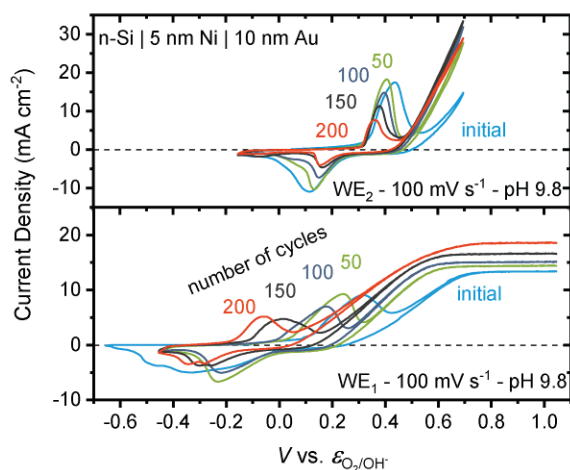


**Figure A.5. Evolution of the photoelectrochemical response over many electrochemical cycles for a Ni-coated n-Si photoanode.** Bottom panel: Using WE1 the illuminated photoanode is cycled through the potential range shown. After every 50<sup>th</sup> cycle, the experiment is paused while voltammetry data is collected via WE2. Top panel: The data collected via WE2 every 50 cycles shows the catalyst’s intrinsic activity. The results demonstrate the DWE’s ability to separate catalytic effects from junction effects. Although the onset of photocurrent shifts cathodic with continued cycling as shown in the bottom panel, this shift is not accounted for by changes in the intrinsic catalytic activity shown in the top panel. After an initial 50-cycle activation period, the catalyst activity remains largely constant while the photoelectrode performance continues to improve with additional cycling. Adapted from Ref 54.

The DWE technique was used to determine that thin Ni catalyst/protection layers enhance Si photoanodes via changes to the rectifying junction compared to thick Ni layers. With sufficiently thin layers, the solution permeates regions of the protection layer and passivates the underlying Si. The increase in activity was attributed to the development of pinched-off Ni|Si point contacts.<sup>54</sup> The DWE technique was useful in achieving this understanding because it allowed for separation of catalytic-enhancement from junction-enhancement effects. As the photoanodes were electrochemically cycled the onset of water oxidation improved (Figure A.5 – bottom panel). By using WE2 the catalyst layer was independently cycled (Figure A.5 – top panel) and it was shown that the catalytic activity remained constant (after an initial activation period) and therefore changes in catalytic activity could not be causing the overall enhanced photoanode performance with cycling. The electrochemical potential of the catalyst layer was measured as a function of potential applied to the semiconductor back contact and revealed a ~440 mV photovoltage for the best devices, after activation. This represents a 300 mV increase in the photovoltage compared to devices with thicker (~20 nm) Ni protection layers. Further DWE tests indicated that even the best devices retained their buried-junction behavior indicative of direct contact between remaining metallic Ni nanoparticles and the Si surface. Through these measurements, the DWE technique enabled us to identify that the enhanced photoelectrode efficiency originated specifically from changes to the rectifying junction and that the junction remained buried despite these changes.

The presence of junction inhomogeneity presents an opportunity to more-rigorously understand photoanodes by employing spatially resolved DWE measurements. These opportunities are discussed alongside the nanoscale DWE technique in a later section.

### 3.2 Catalyst-Coated Fe<sub>2</sub>O<sub>3</sub> Photoelectrodes

We have studied the behavior of several catalysts on hematite ( $\alpha$ -Fe<sub>2</sub>O<sub>3</sub>); a system which significantly differs from Si. Hematite is stable under oxidative conditions and thus the catalyst need not chemically protect the semiconductor surface. In fact, the systems that exhibit the highest efficiency use (photo)electrodeposited electrolyte-permeable catalysts such as CoPi and Ni(Fe)O<sub>x</sub>H<sub>y</sub>.<sup>17-19, 21</sup> Water oxidation can in principle happen on either the semiconductor surface or within the catalyst – the fate of photogenerated holes is not known *a priori*. Hematite also exhibits significant surface-state density which may serve to trap photogenerated carriers and mediate the water oxidation activity on the semiconductor surface. By employing DWE experiments we show that electrolyte-permeable catalysts quantitatively collect photogenerated holes and directly drive the OER when placed on hematite.

To apply the DWE methods, we obtained smooth, pinhole-free hematite films that were fabricated using atomic layer deposition (ALD) by Hamann and coworkers<sup>70-71</sup> and coated them with smooth films of  $\text{Ni}_{0.8}\text{Fe}_{0.2}\text{O}_x\text{H}_y$  catalyst using photochemical metal-organic deposition.<sup>52-53</sup> The surface uniformity allowed for deposition of a continuous, electrolyte-permeable Au film (to serve as WE2) that only contacts the catalyst layer without shunting to the underlying hematite film.

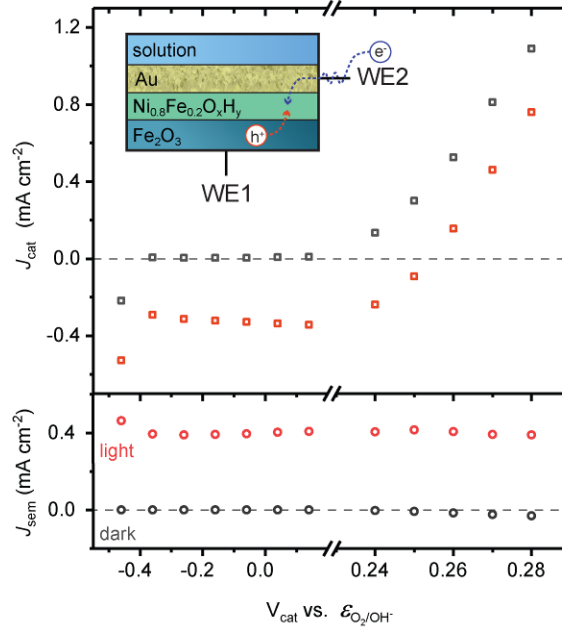


**Figure A.6. Photogenerated hole transfer at the  $\alpha\text{-Fe}_2\text{O}_3|\text{Ni}_{0.8}\text{Fe}_{0.2}\text{O}_x\text{H}_y$  interface.** With  $V_{\text{sem}}$  held at 0 V vs.  $\epsilon_{\text{O}_2/\text{OH}^-}$ ,  $J_{\text{sem}}$  and  $J_{\text{cat}}$  are measured as a function of  $V_{\text{cat}}$  and the illumination condition (light/dark). Under illumination  $J_{\text{sem}}$  measures  $\sim 0.4 \text{ mA cm}^{-2}$  and  $J_{\text{cat}}$  exhibits a  $\sim 0.4 \text{ mA cm}^{-2}$  decrease in current density relative to  $J_{\text{cat}}$  in the dark. To hold  $V_{\text{cat}}$  at a constant potential, WE2 must inject electrons to neutralize any holes collected from the semiconductor. Since the difference between  $J_{\text{cat,light}}$  and  $J_{\text{cat,dark}}$  is comparable to  $J_{\text{sem,light}}$ , the result indicates that the photogenerated holes responsible for the photocurrent are collected by the catalyst. Adapted from Ref 53.

Two key measurements were made to understand the fate of the photogenerated holes in the hematite. In the first (Figure A.6), we independently measure the photocurrent at WE1 ( $J_{\text{sem}}$ ) and the catalyst current at WE2 ( $J_{\text{cat}}$ ) while holding the catalyst potential ( $V_{\text{cat}}$  vs.  $\epsilon_{\text{O}_2/\text{OH}^-}$ ) at a series of fixed potentials. Upon illumination, the current measured at WE1 increases while the current measured at WE2 decreases by the same amount (Figure A.6). For the WE2 contact to hold the catalyst at a fixed potential, it must compensate for any injected holes by injecting electrons

into the catalyst (or, equivalently, removing the injected holes). The DWE PEC measurement can thus be used to directly track the flow of photogenerated holes and demonstrates that the majority of those holes transfer into the catalyst film over a wide range of conditions.

In a second experiment, we assessed whether the potential reached by the catalyst film on hematite was sufficient to drive water oxidation. First, we deposited a catalyst film on conducting indium-tin oxide (ITO), followed by a thin Au layer on top of the catalyst. The oxygen-evolution current was then measured at a series of applied potentials to the ITO and plotted versus the potential measured on the top Au contact (Figure A.7a). Next, a catalyst layer with identical composition and thickness was deposited on a hematite film, followed by a thin Au layer on top of the catalyst. Under illumination, the potential of the catalyst was measured (at the top Au contact) as a function of the photocurrent measured at the semiconductor back contact. We found that the catalyst layer is charged to similar potentials driving OER for a given current density independent of whether the holes originate from ITO or are photogenerated in hematite (Figure A.7a). This shows  $\text{Ni}_{0.8}\text{Fe}_{0.2}\text{O}_x\text{H}_y$  is oxidized by the photogenerated holes to an operating potential sufficient to drive water oxidation at rates commensurate with the measured photocurrent (on WE1). Thus, the  $\text{Ni}_{0.8}\text{Fe}_{0.2}\text{O}_x\text{H}_y$  catalyst layer acts as both a hole collector and OER catalyst on hematite thin films.

The macroscopic DWE measurements are limited to systems with smooth electrocatalyst layers that are stable to vacuum deposition of the secondary contact. This limits the range of systems that can be explored, most notably precluding examination of the electrodeposited CoPi catalyst on  $\text{Fe}_2\text{O}_3$ .<sup>55</sup> To address this issue, we used the potential-sensing electrochemical AFM (PS-EC-AFM) technique. This enables surface/catalyst potential measurements on systems that were not previously possible, including photo-electrodeposited catalyst on metal-oxide semiconductors.

We used the PS-EC-AFM to monitor, during (photo)electrochemical oxygen evolution, the operating electrochemical potential of a CoPi catalyst layer when paired with an illuminated  $\text{Fe}_2\text{O}_3$  semiconductor or a non-illuminated ITO conductive substrate (Figure A.7b). This allows us to directly sense when holes accumulate in the catalyst and whether enough holes accumulate to drive water oxidation. The experiment is straightforward to execute (although we note the specialized tips are fragile, currently expensive, and require practice/care to use) and the data easy to directly interpret. For this system we demonstrated that the CoPi accepts sufficient holes to undergo oxidation and then reaches an electrochemical potential where it drives water oxidation at a rate commensurate with the measured photocurrent. This was consistent to what we found for  $\text{Ni}(\text{Fe})\text{O}_x\text{H}_y$  coated  $\text{Fe}_2\text{O}_3$  using the macroscopic DWE technique.

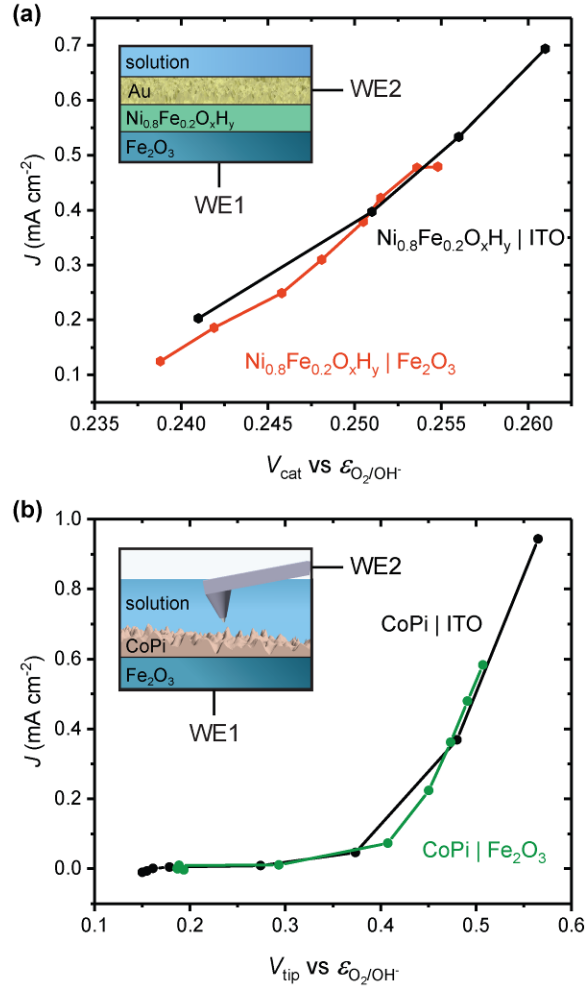


**Figure A.7. In-situ measurements of catalyst potential for Ni<sub>0.8</sub>Fe<sub>0.2</sub>O<sub>x</sub>H<sub>y</sub> and CoPi on hematite and ITO.** (a) The potential of the catalyst ( $V_{\text{cat}}$ ), as measured by a macroscopic second electrode, related to the current passing through the Ni<sub>0.2</sub>Fe<sub>0.2</sub>O<sub>x</sub>H<sub>y</sub>-coated hematite photoanode under illumination (orange curve). The result was compared to the analogous system of Ni<sub>0.8</sub>Fe<sub>0.2</sub>O<sub>x</sub>H<sub>y</sub>-coated ITO electrode where current is driven solely by the potential applied to the ITO (black points). (b) The potential of the catalyst ( $V_{\text{tip}}$ ), as measured by the nanoelectrode probe, related to the current passing through the CoPi-coated hematite photoanode under illumination (green points). The result was compared to the behavior of CoPi-coated ITO (black points). Because ITO is a poor OER catalyst, we know, in the case of Ni<sub>0.8</sub>Fe<sub>0.2</sub>O<sub>x</sub>H<sub>y</sub> and CoPi on ITO, all the OER current flows through the catalyst. We thus also know precisely what catalyst potential is required to pass a given OER current. If the catalyst did not act as an OER catalyst on hematite, then its potential would be lower at a given (photo)current when on hematite than when on ITO. The fact that the potential of the catalysts, for a given current density, was the same, regardless of

the type of substrate and source of holes, indicates  $\text{Ni}_{0.2}\text{Fe}_{0.8}\text{O}_x\text{H}_y$  and CoPi drive the OER in both cases. Adapted from Ref. 53 and 55.

### 3.3 Catalyst-coated $\text{BiVO}_4$ Photoelectrodes

The most-efficient oxide-based photoanodes for oxygen evolution are comprised of catalyst-coated  $\text{BiVO}_4$  nanostructures.<sup>72-73</sup> Recent efforts have aimed to understand the degree to which catalyst overlayers on  $\text{BiVO}_4$  are responsible for driving water oxidation relative to water oxidation occurring on the  $\text{BiVO}_4$  surface itself.<sup>29, 36</sup> Some studies have applied photo-induced absorption measurements in which changes in the optical absorbance of CoPi catalyst on  $\text{BiVO}_4$  are related to the extent of catalyst oxidation. The results show that the density of photoinduced  $\text{Co}^{3+}$  species is threefold lower on CoPi |  $\text{BiVO}_4$  devices than on a control CoPi | FTO sample, when both are driving the same current. This suggests CoPi never reaches sufficiently anodic potentials to drive water oxidation because holes on the  $\text{BiVO}_4$  surface oxidize water directly. Related recent work by van de Krol and others using intensity-modulated photocurrent spectroscopy came to a similar conclusion for  $\text{BiVO}_4|\text{CoPi}$  under low applied potentials ( $V_{\text{sem}} < 1$  V vs. RHE).<sup>74</sup> At higher potentials, they hypothesize that water oxidation partially occurs via the CoPi as  $\text{BiVO}_4$  kinetics for water oxidation are too slow.

To complement these studies, we investigated CoPi |  $\text{BiVO}_4$  using the PS-EC-AFM. In Figure A.8a, the measured catalyst potential is plotted as a function of the potential applied to the semiconductor back ohmic contact (WE1) and overlaid on a conventional  $J$ - $V$  curve for the same device collected through WE1. A large step in the catalyst potential (Figure A.8a) is measured as the catalyst transitions from nominally  $\text{Co}^{2+}$  to  $\text{Co}^{3+}$  near the onset of water oxidation. This is a result of the conversion of electrically-insulating  $\text{Co}(\text{OH})_2$  to the conductive and OER-active  $\text{CoOOH}$  within the CoPi. As the photocurrent increases at higher applied potentials to WE1, so does the catalyst potential measured at WE2. This is direct evidence that the catalyst is charged by holes from the semiconductor.

As with the  $\text{Fe}_2\text{O}_3$  experiments, we assess whether the catalyst is sufficiently charged by  $\text{BiVO}_4$  to drive water oxidation at the photocurrent density. To do this we again compare the surface potentials of CoPi on  $\text{BiVO}_4$  to CoPi on fluorine-doped tin oxide (FTO) conductive glass over a range of current densities (in the former case the current originates from photoinjected holes, whereas in the latter case holes are directly injected from the conducting glass in the dark). For all-examined current densities, the surface potential of CoPi is nearly identical irrespective of the substrate (Figure A.8b). This result shows that on  $\text{BiVO}_4$ , the CoPi reaches an electrochemical potential where CoPi-mediated water oxidation accounts for and equals the observed photocurrent.

The holes that are consumed for water oxidation first transfer to the catalyst – they do not appear to drive water oxidation on the  $\text{BiVO}_4$  surface. A useful next experiment would be to perform the optical photo-induced absorption measurements<sup>29, 36</sup> on the exact-same set of samples with which the potential-sensing measurements are made so that the discrepancy between the two measurements can be resolved.

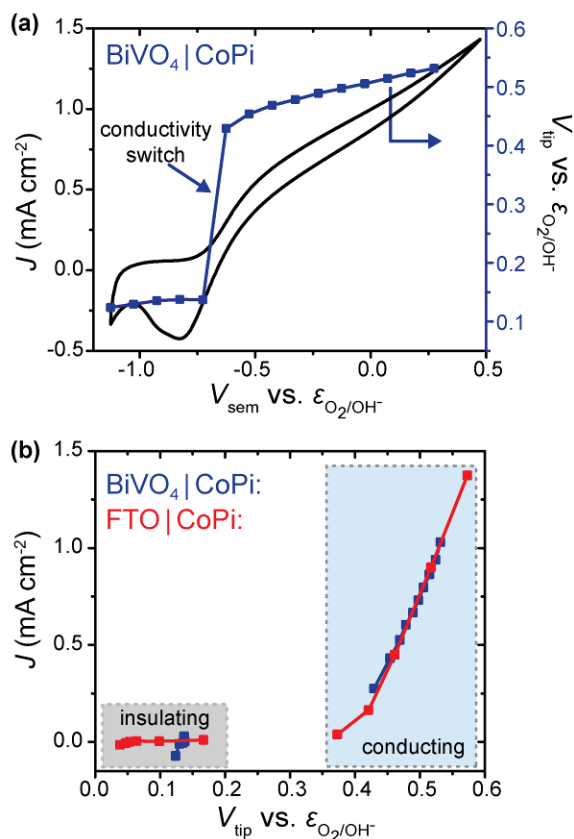


**Figure A.8. Nanoelectrode potential measurements for CoPi on  $\text{BiVO}_4$  and FTO.** (a) The measured  $V_{\text{tip}}$  reports on the catalyst potential as a function of the potential applied to the  $\text{BiVO}_4$  back contact ( $V_{\text{sem}}$ ). The large step in the  $V_{\text{tip}}$  corresponds to the transfer of photogenerated holes from  $\text{BiVO}_4$  to CoPi, causing it to oxidize to  $\text{CoOOH}$  which is electrically conductive and whose potential can be sensed accurately. (b) The data relates the potential of CoPi ( $V_{\text{tip}}$ ) to the current density measured at WE1. The results compare CoPi on  $\text{BiVO}_4$  to CoPi on FTO and show that the CoPi reaches the same electrochemical potential in both cases. This indicates CoPi is driving water oxidation on  $\text{BiVO}_4$ . Adapted from Ref 69.



### 3.4 Relating Shunt Recombination in Catalyst-Coated Photoelectrodes to Catalyst Carrier Collection

In much of our previous work we have focused on single-crystal or polycrystalline thin-film model systems. However, the highest-performing photoelectrodes typically feature high-surface-area and porous semiconductors.<sup>72-73, 75</sup> We discovered a simple but critically important mechanism of recombination that is unique to catalyst-coated semiconductors of this type. For these systems, pinholes in the porous semiconductor can fill with catalyst during deposition and act as shunt pathways to the back contact (Figure A.9a). Under illumination, photogenerated holes transfer to the catalyst but then recombine with electrons at the catalyst|conductor interface.

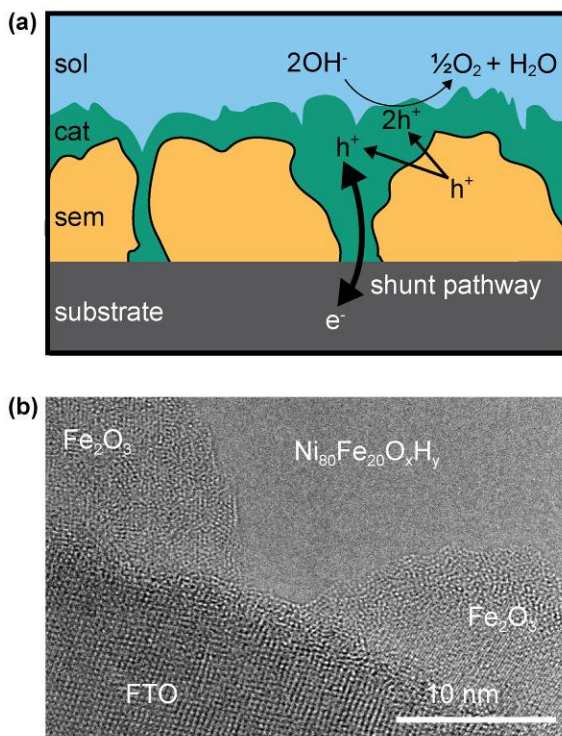


**Figure A.9. Shunt recombination in catalyst-coated porous semiconductors.** (a) The presence of pinholes throughout the semiconductor film could lead to the conductive substrate being exposed. With sufficient catalyst deposited on the surface, a shunting pathway is generated which results in high rates of recombination. (b) High-resolution TEM cross-section showing a pinhole in an electrodeposited  $Fe_2O_3$  film which allows the  $Ni_{80}Fe_{20}O_xH_y$  catalyst to directly contact the conductive FTO substrate. Adapted from Ref. 52.

To explore this shunting-recombination mechanism we examined hematite thin films as a model system. One film was deposited by ALD and was free of pinholes, the other film was

deposited by electrodeposition and small holes in the film were apparent by cross-sectional TEM (Figure A.9b). The incomplete coverage of the semiconductor on the conducting-oxide film for the electrodeposited hematite film could also be ascertained from the voltammetry behavior of the electrode in the presence of a reversible redox couple like ferro/ferricyanide.

The shunting mechanism manifested itself in a number of different ways. (1) We found that use of an electrically conductive catalyst, such as  $\text{Ni}_{0.8}\text{Fe}_{0.2}\text{O}_x\text{H}_y$ , dramatically reduced the photoanode performance of electrodeposited hematite but enhanced the performance of pinhole-free ALD hematite. Electrically insulating  $\text{Ni}_{0.2}\text{Fe}_{0.8}\text{O}_x\text{H}_y$ , however, did not show shunt recombination on either sample. (2) Very thin coatings of photoelectrodeposited conductive catalysts worked for both samples because the catalyst layers weren't thick enough to significantly contact both semiconductor and conductive oxide substrate. (3) Two sets of catalyst oxidation/reduction peaks were observed in illuminated cyclic voltammograms when the catalyst was shunting to the conducting electrode. The more-anodic set represents catalyst domains near/touching the conductive substrate. The more-cathodic peak set represents catalyst domains further from the conductive substrate that are in contact with the semiconductor and are shifted cathodic by the photovoltage. At applied potentials between the two sets of peaks, photogenerated holes from the  $\text{Fe}_2\text{O}_3$  can oxidize the catalyst, but electrons from the conducting substrate work to reduce it. Thus, only a portion of the catalyst, further from the conductor, is oxidized. (4) Current flowing through the shunts was directly measured using the dual-working-electrode configuration. Similar results were found for spincoated  $\text{BiVO}_4$  thin films, indicating that the shunting recombination mechanism is general across materials and catalyst systems as well as deposition techniques.<sup>76</sup> These features described above can therefore be used to generally identify whether or not shunt recombination is affecting the performance of any given photoanode system.

Eliminating the shunt pathways through the catalyst is critical to achieving high-performance catalyst-coated photoanodes. There are several ways to do this. If one is building a three-dimensional nanostructured/porous semiconductor one could completely coat the conducting electrode support with a thin layer of the semiconductor prior to depositing the nanostructured semiconductor. Selective photo-assisted electrodeposition of thin catalyst layers on the semiconductor surface or using electrically insulating catalyst layers also prevent shunting. A final option is to passivate the pinholes selectively with an insulator to block direct contact. This might be possible with electrodeposition of an insulator.<sup>77</sup>

Finally, we note that these observations of shunt recombination support the mechanistic picture where the catalyst collects photogenerated holes from the semiconductor and drives the

OER (Figure A.4). If holes did not transfer to the catalyst to drive OER, then one would not observe the shunting behavior seen here.

#### 4. Outlook

The results discussed here demonstrate that for a variety of semiconductor ( $\text{BiVO}_4$ ,  $\text{Fe}_2\text{O}_3$ , Si) and catalyst ( $\text{CoPi}$ ,  $\text{Ni}(\text{Fe})\text{O}_x\text{H}_y$ ) systems, the catalyst overlayer functions both as a hole collector and the site for water oxidation. In all examined sem|cat systems, macroscopic or nanoscopic DWE measurements revealed that the catalyst reaches an electrochemical potential sufficient to drive OER at the same rate as the measured photocurrent. We note that these findings are straightforward and unambiguous; the DWE technique features a direct electrical probe of the catalyst surface and requires no modeling or assumptions to measure the catalyst electrochemical potential.

**Limitations.** The techniques described here, however, cannot measure surface-state density nor the possible effects of catalyst materials in passivating surface states, as has been suggested by others.<sup>9, 25, 29</sup> The measurements can only identify the surface potential and extent of photogenerated charge which reaches the catalyst. It is indeed likely that the catalyst plays multiples roles in many cases. That is, catalyst application could enhance photoelectrochemical performance by simultaneously passivating surface-recombination centers, by improving the sem|cat heterojunction's built-in electric field, and/or by improving the kinetics for the OER. The details, however, of how (oxy)hydroxide catalyst layers might chemically passivate semiconductor surfaces remain to be discovered. Nonetheless, these may all be important considerations for the improved design of photoanodes.

The results discussed here may not universally apply to all sem|cat systems. Different materials preparation routes may give rise to larger semiconductor surface-recombination velocities and/or native catalytic activity as well as different magnitudes of equilibrium band banding due to the presence of varying types of surface terminations and defects. Upon application of the catalytic surface layer, enhanced photoelectrode performance could, in some cases, thus be more-attributable to changes in junction behavior than to a decrease in catalytic overpotential. Nonetheless, we generally suspect that in all cases the metal oxide/(oxy)hydroxide catalysts accept photogenerated holes from the illuminated semiconductor – the kinetics of driving redox chemistry in a transition metal oxide/(oxy)hydroxide catalyst layer should be significantly faster than driving oxygen redox chemistry directly on the semiconductor surface. The hole quasi-Fermi level in the semiconductor is thus expected to be in quasi-equilibrium with the catalyst Fermi level under steady-state conditions. Researchers investigating sem|cat photoanodes who find evidence of water oxidation

occurring directly on the semiconductor surface could use the macroscopic or nanoscopic DWE techniques to directly verify these findings. Finally, although we examine redox-active Ni/Co/Fe-based catalysts here, we note that the measurement techniques discussed will work equally well on any catalytic material that is electronically conductive and therefore amenable to potential sensing.

**Further technique development/implementation.** Additional information might be learned from combining several techniques on the same samples. For example, a challenge in the TAS and PIA techniques is knowing precisely what population of holes the optical-absorption spectrum represents. Does it represent all holes that are OER intermediates, only a subset of those holes, or is it a different population of holes that is in quasi-equilibrium with the OER intermediate population? By using DWE to monitor the catalyst electrochemical potential during TAS/PIA experiments, one could directly correlate changes in the optical signal to charging/discharge of the catalyst as well as the rate at which the catalyst is performing OER. This might allow one to differentiate between holes trapped in the catalyst layer from those trapped in, for example, shallow defect states.<sup>9, 33</sup> The combination of DWE photoelectrochemistry and IMPS analysis may also be useful. For example, the second working electrode can be used to affect the catalyst's electrochemical potential during IMPS experiments. Doing this might allow one to systematically map how the catalyst electrochemical potential affects the apparent recombination and charge-transfer rate constants.

Further development of the techniques reported here is also possible. For example, using the PS-EC-AFM to spatially map catalyst potential across a surface may enhance understanding of how semiconductor morphology affects the operational catalyst potential – the locations of the highest catalyst potentials should correlate to locations of the largest photocurrent driven by the semiconductor. Such a measurement would only work, however, if the catalyst did not form a continuous conductive film that would all sit at the same potential. In another example, the technique might better illustrate the function of the *n*-Si|Ni electrodes discussed above where the development of barrier-height inhomogeneity led to increased PEC performance. It may be possible to locally monitor this development in-situ. If key contributors to efficiency can be identified, one might intentionally engineer an improved junction. Another possible use of PS-EC-AFM is in examining how grain boundaries and crystalline facets influence the local photovoltage of a sem|cat junction. In these types of experiments the semiconductor surface might be topographically and electrically characterized (for example using (photo)conducting AFM)<sup>65</sup> in air using the nanoelectrode AFM tip, before catalyst deposition. Without moving the cell, a catalyst deposition solution could then be introduced to photodeposit a catalyst of interest. After flushing the deposition

solution, the local catalyst deposits would be characterized for photovoltage, with the result mapped back onto the bare semiconductor surface characterization.

There are practical challenges that must be overcome, however, to enable PS-EC-AFM spatial mapping of catalyst surface potentials. The measurement time is set by how quickly the tip electronically equilibrates with the catalyst. While this is fast ( $< 1$  s) when the tip is in direct contact with a highly conductive metallic surface (e.g. Au), it can be quite slow (i.e.  $\sim 30$  s) when contacting the much-less-conductive Ni/Co/Fe oxyhydroxide layers.<sup>55</sup> The measurement time constant might be improved with better-designed potential-measurement electronics (which we have not yet attempted) or by increasing the interaction force between the tip and substrate (which risks the tip integrity). A second challenge is that imaging the surface topography with the tip in contact (for potential measurement) rapidly degrades the conductive point of the tip. Practically, we have found that the simplest approach to gain spatially relevant surface-potential information is to first image the sample in tapping mode, without collecting electrical data, and then land the tip on key areas of interest for surface-potential measurements. The *operando* cell and sample stage must be engineered such that drift is minimized and features remain in place for a sufficient time after taking the initial topographic image.

For the macroscopic DWE devices, there may be opportunities to employ impedance-type analyses which are not possible with traditional electrodes. In a typical three-electrode PEC experiment, potential applied to the semiconductor back contact can result in electrostatic potential drops across the semiconductor depletion region and the Helmholtz double layer. Interpretation of impedance results then requires the use of more-complicated equivalent circuits, especially in the presence of surface states and catalyst layers.<sup>23, 78</sup> Introduction of the second working electrode allows one to hold the catalyst, and possibly surface states, at a fixed potential and thereby measure directly the capacitance of the sem|cat junction. These types of measurements may further elucidate the role that surface states play in catalyzed photoanodes. For example, one could measure the flat-band potential of the semiconductor as a function of the potential of the catalyst (controlled by WE2). For an electrolyte-permeable catalyst this might provide information on the surface-state density if these are in quasi-equilibrium with the catalyst electronic states.

Although we have discussed primarily potential-sensing measurements in this *Perspective*, the dual-working-electrode techniques can also be used to measure the current-voltage behavior across the sem|cat junction directly. We have previously demonstrated this on model  $n$ -TiO<sub>2</sub>|cat systems with a macroscopic second working electrode.<sup>49</sup> The experiment is performed by holding the catalyst at a fixed potential (where it is electrically conductive such that resistance through the catalyst layer does not dominate the response) with WE2, while sweeping the potential of the

semiconductor back contact and recording the current as a function of  $V_{WE1}-V_{WE2}$ . Similar measurements could in principle be made on a single catalytic nanoparticle using the conducting nanoelectrode AFM tip as WE2, although background currents may be significant and will likely need to be corrected for.

**Improving photoelectrodes.** The ability to measure and understand the role of catalyst layers is important in developing improved designs for photoelectrodes. Identifying the catalyst's primary influence(s) on photoanode performance informs researchers on what could be further optimized and to what extent. The DWE analysis discussed here is straightforward, involving few assumptions, and indicates that the electrocatalytic layers on the photoanodes tested here harvest the photogenerated holes from the semiconductor and use them for oxygen evolution. Because the catalyst serves as a hole collector, future research could focus on using interfacial layers to improve the sem|cat junction by reducing forward electronic current while still allowing for sufficiently facile hole collection, as is often done for solid-state solar cells<sup>79-82</sup> (this can be thought of increasing the interface carrier selectivity<sup>83</sup>). Mechanisms by which such an interfacial layer could reduce the forward electron current at the sem|cat junction include increasing the electrostatic barrier height (thereby reducing the density of surface majority electrons), passivating surface states<sup>84</sup> (which reduces the number of acceptor states for surface electrons to transfer into), or adding a tunneling barrier (that decreases the transmission coefficient for electrons).<sup>85</sup> The results also indicate that the electrical conductivity of the catalyst, its stability/transformation under electrochemical conditions, and its kinetics for the OER are all important considerations when designing photoanodes.

## Paper B

### Semiconductor - Electrocatalyst Interfaces: Theory, Experiment, and Applications in Photoelectrochemical Water Splitting

Michael R. Nellist<sup>†</sup>, Forrest A. L. Laskowski<sup>†</sup>, Fuding Lin, Thomas J. Mills, Shannon W. Boettcher\*

<sup>†</sup> These authors contributed equally to the work.

## 1. Introduction

Light-absorbing semiconductor electrodes coated with electrocatalysts are key components of photoelectrochemical energy conversion and storage systems. Efforts to optimize these systems have been slowed by an inadequate understanding of the semiconductor-electrocatalyst (sem|cat) interface. The sem|cat interface is important because it separates and collects photoexcited charge carriers from the semiconductor. The photovoltage generated by the interface drives “uphill” photochemical reactions, such as water splitting to form hydrogen fuel. Here we describe efforts to understand the microscopic processes and materials parameters governing interfacial electron transfer between light-absorbing semiconductors, electrocatalysts, and solution.

We highlight the properties of transition-metal oxyhydroxide electrocatalysts, such as Ni(Fe)OOH, because they are the fastest oxygen-evolution catalysts known in alkaline media and are (typically) permeable to electrolyte. We describe the physics that govern the charge-transfer kinetics for different interface types, and show how numerical simulations can explain the response of composite systems. Emphasis is placed on “limiting” behavior. Electrocatalysts that are permeable to electrolyte form “adaptive” junctions where the interface energetics change during operation as charge accumulates in the catalyst, but is screened locally by electrolyte ions. Electrocatalysts that are dense, and thus impermeable to electrolyte, form buried junctions where the interface physics are unchanged during operation.

Experiments to directly measure the interface behavior and test the theory/simulations are challenging because conventional photoelectrochemical techniques do not measure the electrocatalyst potential during operation. We developed dual-working-electrode (DWE) photoelectrochemistry to address this limitation. A second electrode is attached to the catalyst layer to sense or control current/voltage independent from that of the semiconductor back ohmic contact. Consistent with simulations, electrolyte-permeable, redox-active catalysts such as Ni(Fe)OOH form “adaptive” junctions where the effective barrier height for electron exchange depends on the potential of the catalyst. This is in contrast to sem|cat interfaces with dense electrolyte-impermeable catalysts, such as nanocrystalline IrO<sub>x</sub>, that behave like solid-state buried (Schottky-like) junctions.

These results elucidate a design principle for catalyzed photoelectrodes. The buried heterojunctions formed by dense catalysts are often limited by Fermi-level pinning and low photovoltages. Catalysts deposited by “soft” methods, such as electrodeposition, form adaptive junctions that tend to provide larger photovoltages and efficiencies. We also preview efforts to improve theory/simulations to account for the presence of surface states and discuss the prospect of carrier-selective catalyst contacts.

High-efficiency photoelectrochemical water-splitting systems require integrating electrocatalysts (cat) onto light-absorbing semiconductors (sem). Despite the central role that the sem|cat interface plays in collecting one carrier over the other and generating photovoltage, the energetics and charge transfer processes at catalyzed semiconductor interfaces are poorly understood. A simple picture is that the semiconductor absorbs light and separates charge while the catalyst increases the rate of the hydrogen- or oxygen-evolution reaction (HER or OER, respectively). Experiments by different groups, however, show that after deposition of OER catalysts onto *n*-type semiconductors, the photoelectrode characteristics (e.g. the photovoltage, photocurrent, and fill-factor) change in a way often inconsistent with this view.<sup>1,2</sup> Parallel hypotheses have attributed this behavior to changes in surface recombination,<sup>3,4</sup> band bending,<sup>5</sup> interface-charge trapping,<sup>6</sup> optical effects,<sup>7</sup> or kinetics.<sup>8-11</sup> Several factors make unravelling these different effects difficult. First, electrocatalysts are not well-defined electronic materials (e.g. a metal or semiconductor), but are often porous, hydrated, and redox-active solids. How does one describe such non-traditional electronic interfaces? Second, most of the semiconductor systems that have been studied are polycrystalline and/or nanostructured, which makes interpreting elementary processes difficult. Third, there is a lack of experimental tools to directly measure the interfacial processes.

In this *Account* we discuss our use of simulation and new photoelectrochemical experiments to clarify the microscopic details of electron transfer in catalyzed water-oxidizing photoelectrodes. We connect the microscopic processes to the observable current-voltage responses, and discuss possible design principles for high-performance systems.

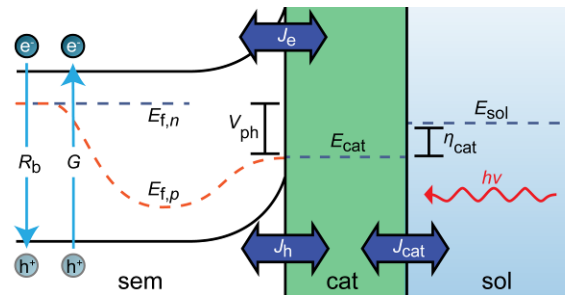


**Figure B.1. Band diagram depiction of charge transport through semiconductor/catalyst/solution interfaces.** Steady-state currents and Fermi levels are depicted for an illuminated electrocatalyst-modified *n*-type semiconductor in solution. The symbols are defined in the text.



Figure B.1 shows basic processes in a catalyzed photoelectrode. The semiconductor, catalyst, and solution are all characterized by electrochemical potentials (Fermi levels) which equilibrate in the dark ( $E_{f,n}$ ,  $E_{cat}$ , and  $E_{sol}$ , respectively). Under illumination the concentration of minority holes increases and thus the hole quasi-Fermi level  $E_{f,p}$  drops down from the electron level  $E_{f,n}$  to create a photovoltage  $V_{ph}$  at the sem|cat interface. During steady-state photodriven oxygen evolution,  $E_{cat}$  is driven lower on the electron energy scale (more positive on the electrochemical scale) than  $E_{sol}$  (the thermodynamic oxygen potential), such that there is a net positive current from catalyst to solution. The degree to which  $E_{f,p}$  separates from  $E_{f,n}$  at the semiconductor surface is governed by the relative forward and reverse rates of electron and hole transport at the sem|cat interface in addition to the rates of bulk recombination ( $R_b$ ) and generation ( $G$ ). The hole current density is given by  $J_p = \mu_p p \nabla E_{f,p}$  where  $\mu_p$  is the hole mobility and  $\nabla E_{f,p}$  is the hole quasi-Fermi-level gradient.

Traditional photoelectrochemical measurements use an ohmic contact to the back of the semiconductor (i.e. the left side of the diagram in Figure B.1) to sweep the semiconductor potential  $E_{sem}$  (which is also the majority-carrier Fermi level  $E_{f,n}$  in the bulk), and measure the resulting current in both the light and dark. It is difficult from such measurements to determine how the individual charge-transfer, catalysis, and recombination steps affect the  $J$ - $V$  response. First, it is not possible to determine which portion of the total applied potential (i.e.  $qV_{app} = E_{sem} - E_{sol}$ ) drops at the sem|cat interface versus at the cat|sol interface because one cannot determine  $E_{cat}$ . Further, the current measured is the sum of the net electron and hole currents and it is not possible to distinguish whether the holes or electrons flow into the catalyst or directly into the solution.

A number of techniques have been used to augment traditional photoelectrochemical measurement. Transient absorption spectroscopies<sup>12</sup> provide insight into the various recombination processes,<sup>5,6</sup> though data interpretation is complicated by the pulsed-laser excitation – photoelectrodes operate at steady state under low light intensity. Methods based on impedance are powerful,<sup>13</sup> but rely on fitting equivalent circuits, which are complicated for multicomponent systems. Here we describe alternative methods that provide direct information about the interface, as well as theory and simulation to corroborate the measurements.

## 2. Materials: Semiconductors and Electrocatalysts

Among device geometries proposed for a solar-water-splitting system, one compelling option employs two semiconductors in series, with different bandgaps, to absorb different portions of the solar spectrum.<sup>14</sup> One semiconductor, operating as a photoanode, drives water oxidation to

form  $O_2(g)$ , while the other, operating as a photocathode, drives water reduction to form  $H_2(g)$ . Electrocatalysts decorate both semiconductors to increase the kinetics of the fuel-forming reactions. While the sem|cat interface is important in both, we focus here on the photoanode.

**Semiconductors.** Oxides, such as  $Fe_2O_3$ ,  $BiVO_4$ , and  $WO_3$ , have been studied extensively as water-oxidizing photoanodes, in part because they can be simply made and, being already oxidized, are reasonably stable under the appropriate-pH OER conditions.<sup>15</sup> The oxides are typically polycrystalline and the sem|cat interface thus likely non-uniform. Recently, there has been a revived interest in using thin oxide films to stabilize *n*-Si and *n*-GaAs photoanodes which have superior electronic properties (mobility, carrier lifetime) but corrode under anodic conditions.<sup>16</sup> Fabrication of high-quality *pn* junctions, that provide for large photovoltages, is straightforward on Si/GaAs. For oxide photoelectrodes there are limited methods to fabricate solid-state *pn* junctions; tuning the properties of the sem|cat interface is therefore particularly important.

**Electrocatalysts.** To understand the interface, it is critical to understand the electrocatalyst's electronic and electrochemical properties. In the simplest case the catalyst is a dense solid with high electrical conductivity (e.g. a metal or degenerate semiconductor). The sem|cat interface is thus expected to form a Schottky-type heterojunction. For example, nanocrystalline  $IrO_2$  films exhibit metallic conductivity while nanocrystalline  $Co_3O_4$  films are *p*-type semiconductors.<sup>17</sup>

Many catalysts, however, are not dense crystalline solids.<sup>18</sup> Under alkaline conditions the fastest known water oxidation catalysts are Ni-Fe oxyhydroxides ( $Ni_{1-x}Fe_xO_yH_z$  with  $x \sim 0.25$ ).<sup>19,20</sup> These oxyhydroxide catalysts appear thermodynamically stable; Ni-oxide-based catalysts reconfigure to the oxyhydroxide structure under OER conditions.<sup>19</sup> They are highly disordered but locally consist of Ni(Fe)OOH nanosheets.<sup>21,22</sup> Each Ni in the film is electrochemically active and can be cycled between the  $2^+$  and  $3^+/4^+$  oxidation states.<sup>23</sup> This requires both electrical and ionic conductivity throughout the “solid” catalyst. We term this catalyst type “electrolyte-permeable” (Figure B.2a). Electrolyte-permeable catalysts display interesting electronic properties. Ni(Fe)(OH)<sub>2</sub> in the resting state is an electronic insulator. Once oxidized to Ni(Fe)OOH it becomes conductive. Other common catalysts also show “bulk” redox behavior and “volume activity” consistent with electrolyte-permeability. These include Co(Fe)OOH (which also shows conductivity-switching),<sup>24,25</sup> “CoPi” and “NiBi” in near-neutral solutions,<sup>26,27</sup> and electrodeposited hydrous oxides of  $IrO_xH_y$  and  $RuO_xH_y$ .<sup>28,29</sup> Thermally prepared  $IrO_2$  oxides don't display volume electrochemistry; they are dense and electrolyte-impermeable.

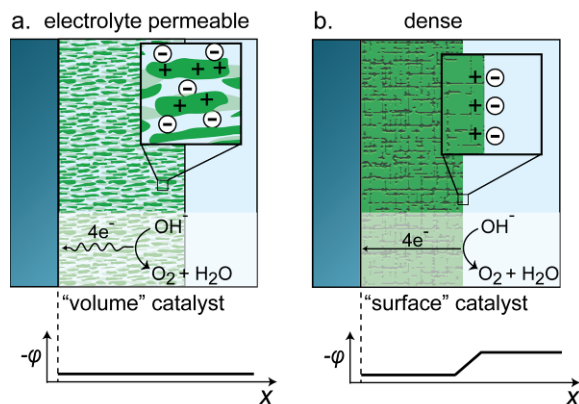


**Figure B.2. Comparison of electrolyte-permeable and non-permeable catalyst layers.** (a) Electrolyte-permeable catalysts screen electronic charge on the catalyst with mobile solution ions (inset), resulting in no electrostatic potential drop across the catalyst. (b) Dense films are impermeable to electrolyte; any charge on the catalyst is balanced by a classical double layer.

## 2. Classification of Interface Types

The physical structure of the catalyst (dense solid or electrolyte permeable) dramatically affects the nature of the sem|cat interface and how it behaves in the dark and under illumination. The qualitative basis for this hypothesis is simple. Dense catalysts, such as Pt, crystalline NiO, or crystalline IrO<sub>2</sub>, must accommodate injected charge near the electrolyte/catalyst boundary to achieve charge neutrality (Figure B.2b). This results in change in the electrostatic potential drop across a classical Helmholtz layer ( $\Delta V_H$ ). As catalytic activity decreases,  $\Delta V_{H,cat}$  across the cat|sol interface required to drive the reaction at a given photocurrent density increases. We refer to sem|cat interfaces with electrolyte-impermeable and electronically conductive catalysts as “buried” junctions, consistent with photoelectrochemical terminology.<sup>30,31</sup>

If the catalyst is electrolyte-permeable and redox active, holes that accumulate in the catalyst drive oxidative redox chemistry (one example is  $\text{Ni}(\text{OH})_2 + \text{OH}^- \rightarrow \text{NiOOH} + \text{H}_2\text{O} + e^-$ ). Because the electronic charge is compensated by the coupled ion motion within the electrolyte-permeated catalyst, *no electrostatic potential drop is expected within the catalyst layer or across the cat|sol interface* (Figure B.2a). This also assumes good catalyst electronic conductivity, as we demonstrated experimentally for NiOOH/CoOOH based systems.<sup>18</sup> Instead the “work function” of the catalyst changes in situ (Figure B.3b). This type of interface is practically important because, as discussed above, the most-active Ni(Fe)OOH and Co(Fe)OOH OER catalysts in neutral-to-basic media are electrolyte permeable. Such catalysts have been used in the best-performing oxide photoanodes for water oxidation, e.g. hydrous IrO<sub>x</sub> catalyzed Fe<sub>2</sub>O<sub>3</sub> and FeOOH/NiOOH catalyzed

$\text{BiVO}_4$ .<sup>11,32</sup> We have termed these sem|cat interfaces “adaptive”, following work on photoactive mixed ionic/electronic conducting polymer interfaces.<sup>33</sup>

Whether a sem|cat interface is expected to be of the “buried” or adaptive type is determined by whether or not electrolyte can physically permeate between the catalyst and semiconductor layers and thus completely screen catalyst charge. A physically realizable adaptive junction interface could thus also be one where crystalline OER catalysts with an electrolyte-permeable shell are deposited on a semiconductor surface. Dispersed nanoparticle catalysts that form *mixed* buried and electrolyte junctions and that are spatially inhomogeneous are another interface class that will not be discussed here.<sup>14</sup>

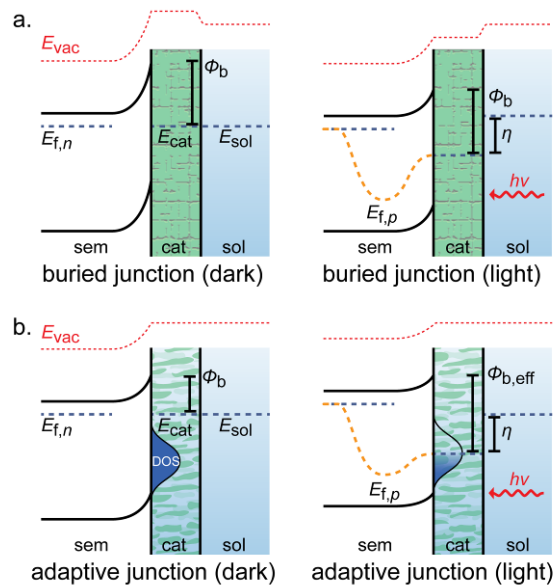


**Figure B.3. Band diagrams for sem|cat interfaces in dark and illuminated conditions.** (a) Dense and (b) electrolyte-permeable catalysts at (left) dark equilibrium and (right) under illumination at a fixed current density.  $E_{vac}$  is the vacuum energy level; other symbols are defined in the text. The barrier height  $\phi_b$  is the separation between the semiconductor conduction band edge and the catalyst Fermi level. For the buried junction,  $\phi_b$  remains constant between dark and light conditions. For the adaptive junction, the effective barrier height,  $\phi_{b,eff}$  increases under illumination at a fixed current density as a result of catalyst oxidation. The hole quasi-Fermi level is shown to decay back to the bulk Fermi level at the back contact over a shortened distance for clarity.

### 3. Semiconductor-Catalyst Interfacial Charge Transfer

Theory and simulation help in predicting the behavior of catalyzed photoelectrodes and determining whether experimental data are consistent with proposed microscopic mechanisms. Although the theory of sem|sol interfaces is well developed,<sup>34</sup> there has been limited work to account for surface-attached electrocatalysts. Previously, equivalent electrical circuits were used to model sem|cat|sol systems.<sup>35-37</sup> This approach implicitly assumes that the electrocatalytic process at the cat|sol interface is independent of the photovoltage generation and charge separation process at the sem|cat interface. This assumption is valid when the catalyst layer is dense and electrically conductive (i.e. a buried junction, Figure B.3a), or when the catalyst is coated on a solid-state photovoltaic cell.<sup>38</sup> Equivalent-circuit models cannot model photoelectrodes with electrolyte-permeable catalysts where, as the catalyst drives OER, the catalyst and the interface both change (Figure B.3b).

We developed a model for sem|cat|sol systems that accounts for the kinetics of charge transfer between the semiconductor, catalyst, and solution for both buried and adaptive junctions.<sup>39</sup> We numerically simulate generation, recombination, drift, and diffusion in the semiconductor. We derive the boundary conditions for the semiconductor/catalyst current ( $J_{\text{jxn}}$ ) based on the simulated equilibrium ( $\bar{n}_s, \bar{p}_s$ ), and non-equilibrium ( $n_s, p_s$ ) surface electron and hole concentrations.

We tested the model with buried junctions where the results from simpler equivalent circuits are expected to be valid. We use

$$J_{\text{jxn,buried}} = k_p(p_s - \bar{p}_s) - k_n(n_s - \bar{n}_s) \quad (1)$$

where  $k_p$  and  $k_n$  are the forward rate constants for hole and electron transfer, respectively, between the semiconductor and the dense catalyst. The first term,  $k_p(p_s - \bar{p}_s)$ , represents forward and backward hole currents, respectively, and the second term, forward and backward electron currents. Here,  $J_{\text{jxn,buried}}$  does not depend on the catalyst potential because charge accumulates and causes a potential drop at the cat|sol interface, without affecting the buried interface. This expression simplifies to the ideal photodiode equation if a constant photogenerated hole flux  $J_{\text{ph}} = k_p(p_s - \bar{p}_s)$  is assumed (thereby ignoring backwards hole current) and the electrons are in quasi-equilibrium such that  $k_n(n_s - \bar{n}_s) = J_0(e^{-qV/kT} - 1)$ . Notice that, for an  $n$ -type semiconductor, the majority-carrier reverse current (electrons moving from catalyst to

semiconductor) is the equilibrium exchange current,  $J_{0,n} = k_n \bar{n}_s$ , which is set by the equilibrium barrier height at the sem|cat interface.

For electrolyte-permeable catalysts (adaptive junctions) the situation is different, since the redox state of the electrocatalyst film is variable. This effectively changes the “work-function” of the catalyst during operation. The sem|cat interface current  $J_{jxn,adapt}$  now depends on the electrochemical potential of the catalyst layer  $V_{cat}$  as

$$J_{jxn,adapt} = k_p(p_s - \bar{p}_s e^{qV_{cat}/kT}) - k_n(n_s - \bar{n}_s e^{-qV_{cat}/kT}) \quad (2)$$

Note that the forward currents ( $k_n n_s$  and  $k_p p_s$ ) are the same as the buried junction case. This relies on the assumption that changing the charge state of the electrocatalyst film does not substantially alter the electronic states in the catalyst that are at energies near the semiconductor valence and conduction band edges. It also ignores the role of surface states in mediating charge transfer, which we discuss below.<sup>40</sup> The reverse currents, however, are influenced by the change in the catalyst potential ( $V_{cat}$ ), through the addition of the  $e^{-qV_{cat}/kT}$  term. This term accounts for the fact that the Fermi level in the catalyst layer moves independent of the semiconductor band positions, thus modeling the “effective” barrier height(s) for charge transfer into the semiconductor from the catalyst.

The catalyst further reacts with the solution, which we model using a Butler-Volmer expression that represents the typical experimental response,<sup>19</sup>

$$J_{cat} = J_{o,cat}(e^{qV_{cat}/2kT} - e^{-qV_{cat}/2kT}) \quad (3)$$

where  $J_{o,cat}$  is the exchange current density for the OER reaction on the catalyst. Equations (1) - (3) thus govern the carrier fluxes between the semiconductor, catalyst, and solution in the two cases discussed. We also simulated molecular catalyst systems.<sup>39</sup>

The most significant simulation result is the observation that for the electrolyte-permeable catalyst, the  $J$ - $V$  curves are nearly insensitive to the catalyst activity  $J_{o,cat}$  (when  $E_v$  is much more positive than  $E_{sol}$ ), in contrast to the buried junction case (Figure B.4). This behavior is explained by the steady-state band diagrams shown in Figure B.4b. For the electrolyte-permeable case, the catalyst Fermi level moves down (more anodic) under operation to compensate for slow OER kinetics. This leads to a larger “effective” barrier height  $\phi_{b,eff}$  and thus a larger sem|cat photovoltage.

In the case of the dense catalyst, increased activity requires the accumulation of charge at the cat|sol interface “consuming” a portion of the photovoltage in the semiconductor. These simulation results provide a platform from which to interpret experimental data discussed below. For mesoscopic or highly nanostructured semiconductor photoelectrodes, the form of the expressions governing the surface carrier concentrations would be different, but the fundamental differences between electrolyte screening in dense and permeated catalysts systems is the same.

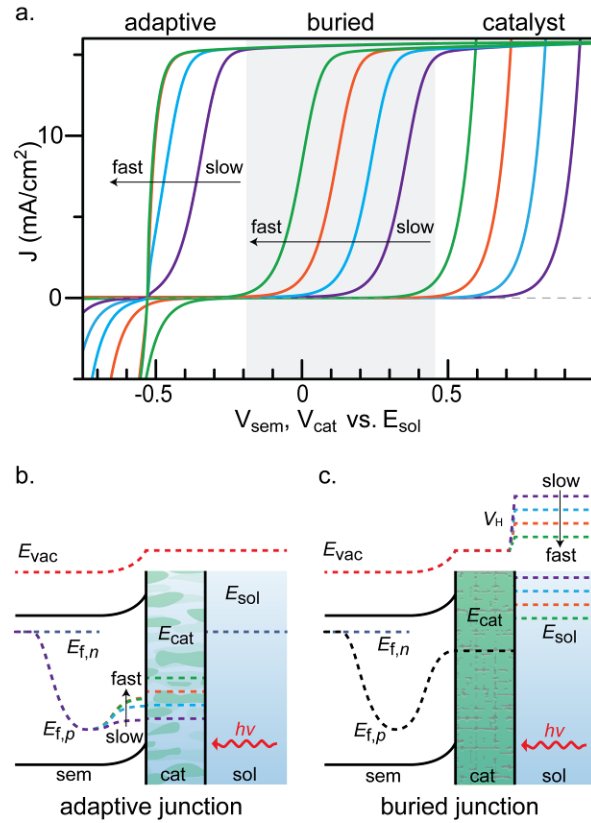


**Figure B.4. Simulated  $J$ - $V$  behavior and energy diagrams for sem|cat junctions.** (a) Comparison of simulated illuminated  $J$ - $V$  curves for a range of  $J_{0,\text{cat}}$  (i.e. catalyst activities) for the buried and adaptive models.<sup>39</sup> Catalyst-only dark curves are shown also. Qualitative band diagrams under illumination for the (b) “adaptive” sem|cat interface at short circuit ( $V_{\text{sem}} = 0$  vs.  $V_{\text{sol}}$ ) and (c) the “buried” sem|cat interface at the applied potentials of 0.2 V (green, fast catalyst) to 0.5 V (purple, slow catalyst) needed to maintain a the same current in each case.  $E_{\text{cat}}$ ,  $E_{f,p}$ , and  $E_{\text{sol}}$  are sketched as colored curves that correspond to those in (a) for the catalyst layers with different exchange currents (i.e. slow versus fast), but the same resting state Fermi level ( $E_{\text{cat}} = E_{\text{sol}}$ ). Quantitative simulations can be found in reference 40.

#### 4. In Situ Electrical Measurements of sem|cat Interfaces

To address the experimental limitations of conventional photoelectrochemistry and to collect data that can be directly compared to theory, we developed a “dual-working-electrode” photoelectrochemical (DWE PEC) measurement platform (Figure B.5).<sup>41</sup>

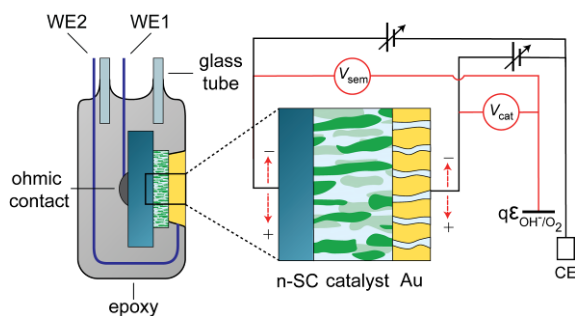


**Figure B.5. Depiction of Dual-working-electrode photoelectrochemistry.** Semiconductor and electrocatalyst potentials are independently measured/ varied relative to the reversible oxygen potential,  $\epsilon_{\text{O}_2/\text{OH}^-}$  (which is equivalent to  $E_{\text{sol}}$  in the model). WE1 makes an ohmic contact to the semiconductor and WE2 is attached to a thin, electrolyte-porous gold layer deposited onto the catalyst.

We tested the platform by characterizing catalyst-coated single-crystal  $n\text{-TiO}_2$ , which is useful for fundamental studies.  $\text{TiO}_2$  is commercially available as single crystals with well-defined surfaces, has reproducible photoelectrochemical response and is essentially insoluble at all pH.

We spin-cast or electrodeposit catalyst films on the  $\text{TiO}_2$  surface and make ohmic contact to the back. The catalyst is coated with a thin Au ( $\sim 10$  nm) layer using vacuum evaporation. We ensure no shorting between Au and  $\text{TiO}_2$  using electrical measurements. The Au forms a porous conductive film on the catalyst surface that is electrolyte permeable and optically transmissive. We confirm the layer is permeable by measuring the reversible electrochemistry and OER activity of the catalyst layer using the top Au film as the working electrode.

The Au makes electrical contact to the catalyst film and thus can be used to measure or control the catalyst potential *in situ* and monitor the current passed through the catalyst. The DWE PEC experiment is implemented using a bipotentiostat, which allows simultaneous control of the two working electrode (WE) potentials. We define WE1 as the back contact to the  $\text{TiO}_2$  and WE2 as the Au-catalyst surface contact. Despite direct solution contact, the Au is assumed to be in quasi-equilibrium with the catalyst layer because the kinetics for oxygen evolution and reduction on Au are slow.



We focused our initial study on two catalyst materials – nanocrystalline  $\text{IrO}_x$  and  $\text{Ni}(\text{Fe})\text{O}_x\text{H}_y$  films that were predicted to form buried and adaptive junctions, respectively.<sup>41</sup> We first monitored the flow of holes and electrons in the light and dark, respectively, by collecting the carriers that flow into the catalyst with WE2. The data shows that the holes generated in  $\text{TiO}_2$  flow first into the catalyst, prior to driving OER. This result was important because for the related  $\text{Co-Pi}/\text{Fe}_2\text{O}_3$  system, it was suggested that the holes bypass the catalyst and directly react with the electrolyte.<sup>42</sup>

We measured the sem|cat junction  $V_{oc}$  by varying  $E_{cat}$  and measuring  $E_{sem}$  at steady state under illumination. The difference between  $E_{cat}$  and  $E_{sem}$  is the sem|cat  $V_{oc}$ , which cannot be measured using conventional photoelectrochemistry. The data (Figure B.6) show that the junction  $V_{oc}$  is independent of  $E_{cat}$  for  $\text{TiO}_2|\text{IrO}_x$  and a linear function of  $E_{cat}$  for  $\text{TiO}_2|\text{Ni}(\text{OH})_2$ , as predicted from simulations for a buried and adaptive junction, respectively. Other DWE measurements were also consistent with the adaptive and buried junction concepts.<sup>41</sup>

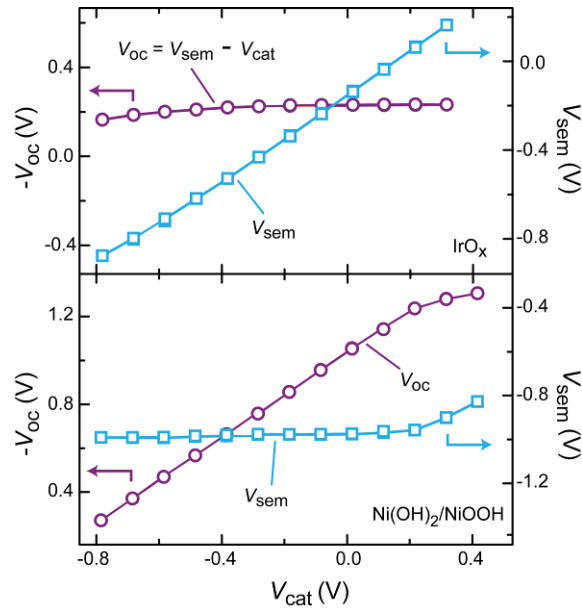


**Figure B.6. Experimental sem|cat open-circuit photovoltages.** (top)  $\text{IrO}_x$ -coated and (bottom)  $\text{Ni}(\text{OH})_2/\text{NiOOH}$ -coated  $\text{TiO}_2$ . For buried junctions, the sem|cat  $V_{oc}$  is independent of the catalyst potential  $V_{cat}$ .

## 5. Catalyst Activity and Electrolyte Permeability

The DWE technique is limited by the need for devices with an integrated second working electrode. Fabricating such structures and ensuring that the Au layer does not short to the

underlying semiconductor layer can be technically challenging. To test a wide range of electrocatalysts on single-crystal  $\text{TiO}_2$ , and further test the predictions of theory, we also used conventional current-voltage and impedance analysis.<sup>17</sup>

We found that for electrolyte-permeable catalysts electrodeposited on  $\text{TiO}_2$  (hydrous  $\text{IrO}_x$ ,  $\text{CoO}_x\text{H}_y$ ,  $\text{FeO}_x\text{H}_y$ , and  $\text{NiO}_x\text{H}_y$ ) the photovoltage output and fill factor for the combined system was *independent* of the catalyst identity (Figure B.7, top). When the catalysts were spun cast in a dense, nanocrystalline form, the junction performance varied dramatically for the different catalysts and was worse than with the electrolyte-permeable catalysts. Electrochemical impedance-spectroscopy analysis of the electrodes showed that the electrolyte-permeable catalysts did not effect the semiconductor band positions, while the dense catalyst layers caused large changes to the impedance data. These observations are consistent with our simulations<sup>39</sup> that predict for semiconductors with deep valence bands, like  $\text{TiO}_2$ , the device performance should be independent of the electrocatalyst activity if it is electrolyte permeable.

For photoelectrodes with smaller bandgaps, and thus less-positive valence-band positions, the activity of the electrocatalyst is important. This is because  $E_{\text{cat}}$ , even in the adaptive-junction limit, cannot move more positive than the valence-band edge. Analyzing the interface properties as a function of catalyst activity for small band gap semiconductors such as  $\text{BiVO}_4$  or  $n\text{-Si}$ , will thus be important for future work.

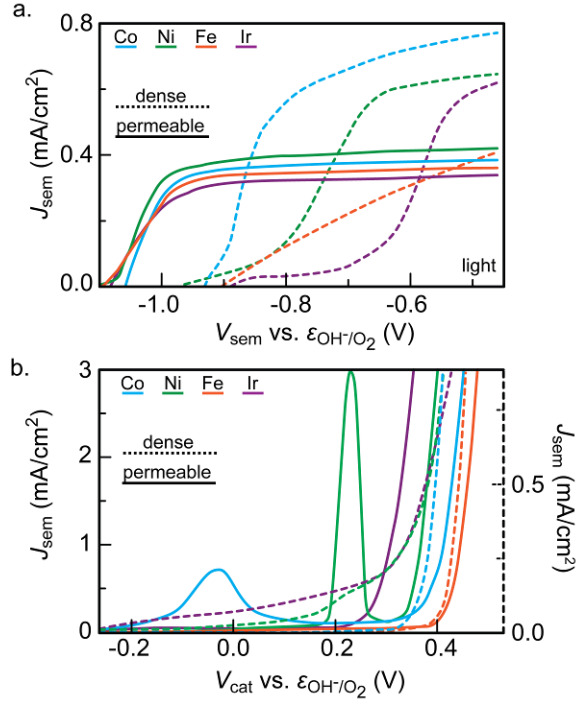


**Figure B.7. Experimental  $J$ - $V$  curves for dense and electrolyte-permeable catalysts.** (a) Dense oxide catalysts (dashed) on  $TiO_2$  show varied response due to different junction properties, while permeable electrodeposited catalysts on  $TiO_2$  (solid) show similar responses. (b) The response of the same series of catalysts deposited on conductive electrodes.

## 6. The Role of Surface States

Surface states cause a variety of photoelectrode behavior including increasing surface recombination,<sup>6</sup> storing charge,<sup>43</sup> and pinning the Fermi-level.<sup>8,44</sup> While the basic effects of surface states on the steady-state and dynamical response of photoelectrodes have been derived,<sup>45-48</sup> there is no predictive model to describe the effect of surface states in the presence of a catalyst overlayer. The concept of a “surface state” (ss) itself is poorly defined in the case of a boundary between two phases where an interphase region may exist, as pointed out by Peter.<sup>48</sup> The surface interphase may trap electronic charge, but also may or may not allow for partial permeation of electrolyte (consider the possibility of an  $\alpha$ - $Fe_2O_3$  crystal with a hydrated  $FeOOH$  surface layer). Existing models do not account for the possible effects of electrolyte screening on ss charge. They also make various simplifying assumptions (e.g. the Gärtner approximation, neglecting backwards transfer from surface states to semiconductor, or assuming surfaces states only communicate with either the semiconductor or the solution).<sup>49</sup>

We developed a model describing the semiconductor physics (generation, recombination, drift, diffusion) combined with the kinetics of carrier exchange between coupled surface-state, catalyst, and solution subsystems. We account for cases where charge in the surface states is screened by electrolyte and where it is not. While the simulations will be published elsewhere, we highlight key insight in this *Account*.

The effects of surface states are most pronounced when the catalyst layer is electrolyte permeable and the charge in the surface state cannot be screened by the electrolyte (e.g. because the state is directly on the dense semiconductor, solution ions cannot permeate around it). We assume that the surface states are in quasi-equilibrium with the catalyst (i.e. that they have the same Fermi level) because the electron-exchange rates between the metal cations of the catalyst and surface states are faster than those of water oxidation. As the filling of the surface state changes there is thus a change in the Helmholtz potential ( $\Delta V_{H,ss}$ ) at the semiconductor surface.

Simulations show that adding catalyst to a semiconductor surface can change the surface-state charge by reducing the potential needed to drive holes into solution. This can lead to an *apparent* “passivation” of the states. The effect, however, is not chemical passivation. Figure B.8a and 8c show how, for a poor catalyst,  $E_{cat}$  must move far positive of  $E_{sol}$  in order to drive the catalytic reaction at the light-limited photocurrent rate. Because the surface state and catalyst are in quasi-equilibrium, they “charge” together. The surface states thus charge more for a slow catalyst than for a fast one. These results may help explain the photoelectrochemical response of Co oxyhydroxide/phosphate (CoPi) catalysts on  $n$ -Fe<sub>2</sub>O<sub>3</sub>, which is known to have a high surface-state density.<sup>5,6,10,12,13,42,50</sup> We suggest CoPi increases the rate of water oxidation, moving the steady-state surface potential more negative, reducing the surface-state charging (and hence  $\Delta V_{H,ss}$ ), and thus shifting the photocurrent onset potential cathodic. Some evidence for such an effect of CoPi on  $n$ -Fe<sub>2</sub>O<sub>3</sub> has been observed.<sup>50</sup>

In the limit of low surface-state density, the surface states do not hold enough charge to significantly change  $\Delta V_{H,ss}$  and the interface behaves as an adaptive junction where catalyst activity doesn’t substantially affect photoelectrode response (Figure B.8c and d).

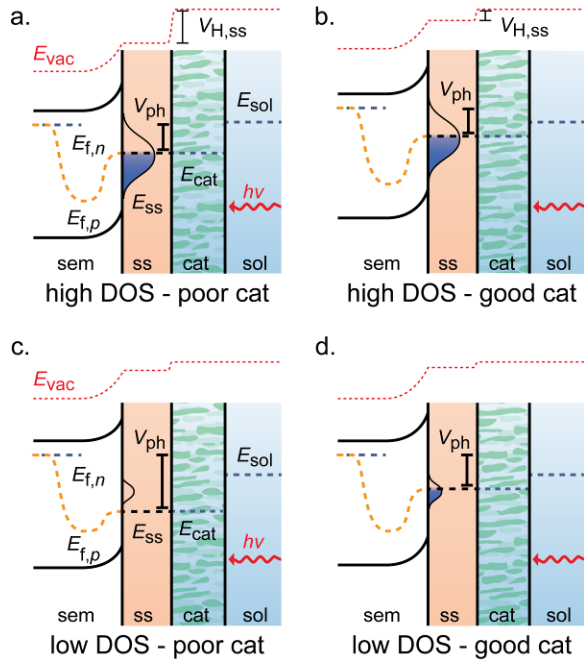


**Figure B.8. Effect of surface states on permeable catalysts.** In the limit of a large surface-state density (a and b), permeable catalysts behave like buried junctions and changes in catalyst activity cause changes in  $V_{H,ss}$ . In the low-surface-state-density limit (c and d), changes in surface-state filling don't affect  $V_{H,ss}$  and the system behaves like the adaptive junction.

## 7. Outlook: Designing Improved Interfaces

The PEC and simulation results discussed here demonstrate the role of electrolyte-permeability and catalyst charging on interface properties and photoelectrode response. The “adaptive-junction” concept explains why the best-performing oxide photoanodes use catalysts deposited using “soft” conditions (e.g. electrodeposition) where the catalyst remains disordered and electrolyte-permeated.<sup>32</sup> These findings are expected to apply to photoelectrodes with smaller band-gaps (e.g.  $\text{Fe}_2\text{O}_3$ ,  $\text{BiVO}_4$ , or Si) although the adaptive interface may not be able to entirely compensate catalyst overpotential as on  $\text{TiO}_2$ .

There are additional strategies/principles for the design of improved sem|cat|sol interfaces. One approach is to create optimized buried junctions with conductive and chemically stable surfaces onto which the highest-activity catalysts, such as  $\text{Ni(Fe)OOH}$ , can be deposited. This approach works well for Si and GaAs, because processes are established to fabricate solid-state junctions that generate photovoltages approaching the theoretical bulk-recombination limits.<sup>51</sup> For

many materials, such as oxides, methods to manufacture solid-state junctions are not well developed.

Fundamentally, the rate of forward electron transfer (i.e. recombination current) must be minimized to maximize photoanode performance (see Eqn. 2). One way to reduce electron transfer is to move the band-edge positions to maximize band bending and minimize the surface concentration of electrons  $n_s$ .<sup>52</sup> The second is to selectively reduce the rate constant for electron transfer into the catalyst over that for holes, i.e. make the catalyst a *carrier-selective* contact.<sup>53</sup> By tuning composition one might create a catalyst with few electronic states available at the appropriate energy to accept electrons from the conduction band, and many states available to accept holes (Figure B.9).

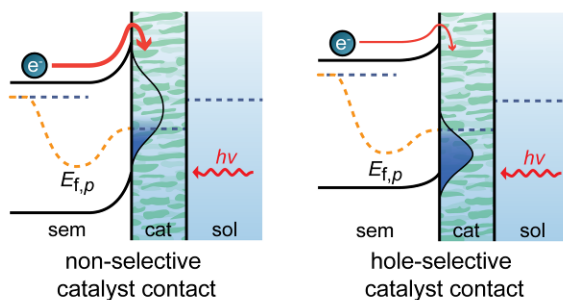


**Figure B.9. Effect of catalyst on interface carrier selectivity.**

## CHAPTER II: UNDERSTANDING AND IMPROVING UPON PHOTOELECTROCHEMICAL EXPERIMENTAL METHODS USING DUAL WORKING ELECTRODE STRATEGIES

Having established the utility of the dual-working-electrode technique in the previous chapter, here they are applied to better understand existing photoelectrochemical experimental methods. This chapter is divided into two sub-sections encompassing a previously published body of work and a yet-to-be published manuscript. The first is an investigation of a commonly employed photocurrent transient method and is published in *Sustainable Energy & Fuels*. The work finds that behavior of photocurrent transients, produced when the illumination incident on a photoanode is switched on or off, is atypical if a redox active catalyst is present on a photoanode surface. This finding is important because the effect on photocurrent transient behavior, which is often analyzed to determine the lifetime of photogenerated carriers, is significant and would lead to incorrect interpretations if not accounted for. The findings would not have been possible without the DWE technique, which allowed the electrochemical potential of the catalyst to be monitored during transient decays.

The second paper features an investigation of hole scavenger methods which we anticipate submitting to *ACS Energy Letters*. The work questions a common assumption in hole scavenger based experiments: that the hole scavenger (an easily oxidized compound added to the solution) will quantitatively harvest any photogenerated holes arriving at the photoanode/solution interface. Photocurrents measured in the presence of hole scavengers are often compared to those measured without, under the assumption that the photoanode behaves similarly in each case. However, results show that behavior of redox active catalysts on the photoanode surface can be affected by hole scavenger presence. Whereas a Ni-based catalyst was oxidized to nominally NiOOH during water oxidation, it remained in a reduced Ni(OH)<sub>2</sub> state when a H<sub>2</sub>O<sub>2</sub> hole scavenger was present. This difference changes the conductivity of the catalyst layer and can impede the arrival of holes at the photoanode/solution interface. The findings suggest that care should be taken when assessing hole scavenged photocurrents, often used to calculate water oxidation kinetics, in the presence of a redox active catalyst. These findings were enabled by the DWE technique, which was used to monitor the oxidation state of the catalyst and examine its intrinsic activity in the presence of a hole scavenger.

Section A, Transient Photocurrents on Catalyst-Modified n-Si Photoelectrodes: Insight from Dual-Working Electrode Photoelectrochemistry, contains co-authored material previously published as: Laskowski, F. A. L.; Qiu, J.; Nellist, M. R.; Oener, S. Z.; Gordon, A. M.; Boettcher,

S. W. (2018). Transient Photocurrents on Catalyst-Modified n-Si Photoelectrodes: Insight from Dual-Working Electrode Photoelectrochemistry. *Sustainable Energy & Fuels*, 2(9), 1995-2005 (2018).

Section B, Investigation of Hole Scavenger Experiments for Catalyzed Photoanodes, contains co-authored material yet to be published as: Laskowski, F. A. L.; Nellist, M. R.; Qiu, J.; Gordon, A. M.; Boettcher, S. W. Interpretation of Hole Scavenged Photoanode Behavior from Dual Working Electrode Photoelectrochemistry, In Preparation. (style of ACS Energy Letters).

Prof. Boettcher and I conceived of these projects. I performed and directed experiments, collected data with help from A. Gordon, and analyzed data with help from M. Nellist, J. Qiu, S. Oener, and A. Gordon. I wrote the paper with help from Prof. Boettcher and editorial assistance from all authors.

## Paper C

### **Transient Photocurrents on Catalyst-Modified n-Si Photoelectrodes: Insight from Dual-Working Electrode Photoelectrochemistry**

Forrest A. L. Laskowski, Jingjing Qiu, Michael R. Nellist, Sebastian Z. Oener, Adrian M. Gordon, Shannon W. Boettcher\*

#### **1. Introduction**

Semiconductor photoelectrodes coated with electrocatalysts are an important component of water-splitting cells that convert and store solar energy. Surface states on light-absorbing semiconductors can function as recombination centers and lower the performance of water-splitting systems. To characterize the presence and impact of surface states on catalyst-coated semiconductors, transient photoelectrochemical behavior is often studied. These experiments typically assume that the filling/emptying of surface states at the semiconductor interface causes transients to occur whenever the incident illumination intensity is perturbed. Analyzing transients may then reveal the density of surface states and their effect on carrier recombination. However, the transient technique does not directly measure the origin of the transient behavior, and utility of the experiment requires assuming the underlying process. Here, we use a dual-working-electrode technique applied to Ni-protected n-Si photoanodes coated with Ni (oxy)hydroxide catalyst to examine transient behavior of catalyst-coated photoelectrodes. We find that the most pronounced transients are due to catalyst redox activity. By directly measuring the catalyst redox state, we



confirm that transients are related to either catalyst oxidation to NiOOH or reduction to Ni(OH)<sub>2</sub>. We also find that the redox-active catalyst moderates how quickly the depletion region and Helmholtz electrostatic potentials relax after each illumination perturbation. The results indicate that a redox-active catalyst can serve as a “parallel capacitor” which influences both the decay time and shape of transients. This data shows that photocurrent transients on catalyzed photoanodes are influenced by the catalyst’s redox-activity and are not solely based on surface state loading/emptying.

Photoelectrochemical water splitting, achieved by integrating a photocathode and photoanode, converts and stores solar energy in the form of hydrogen fuel.<sup>1</sup> Integrated systems absorb sunlight and use the photo-generated carriers to drive the oxygen evolution (OER) and hydrogen evolution (HER) reactions, simultaneously. However, various processes limit efficiency, especially for the photoanode. The presence of surface states on semiconductors has been shown to increase carrier recombination, thereby decreasing conversion efficiencies.<sup>2-13</sup> To enhance performance, photoanodes are often functionalized with a catalyst which is thought to suppress surface recombination,<sup>14-16</sup> improve OER kinetics,<sup>17,18</sup> and/or improve the carrier-selectivity of the interface (e.g. increased band bending).<sup>19,20</sup> Some have attributed catalyst enhancement more specifically to the passivation of surface states.<sup>21,22</sup> To quantify the impacts of surface states, transient photocurrent analysis has been often applied to understand catalyst-coated photoanodes.<sup>9,23</sup>

Transient photocurrent analysis interprets the dynamic response of a photoelectrode as the incident light intensity is modulated.<sup>24-26</sup> In a typical experiment, current response is collected as an incident light source is periodically switched on and off. Current spikes which rapidly decay to a steady-state value, termed transients, oftentimes occur directly after each switch. Transients are thought to be the sum of short-term non-faradaic processes and the steady-state faradaic current (e.g. OER, HER).<sup>27-32</sup> The exact nature of the non-faradaic processes is system dependent and, for some systems, subject to on-going debate. However, the non-faradaic responses are typically attributed to charge accumulation in the semiconductor depletion region, in the Helmholtz double-layer, or at surface states.<sup>9,13,23,29,33-44</sup> For systems where the precise mechanism is deduced, integration of the current-time transient trace is used to characterize the magnitude of charge accumulation.<sup>9,45-48</sup> Fitting transient decays, and extracting time constants, has been used to characterize the apparent lifetime of the photogenerated “carriers” (presumably at surface sites) and decay times (from peak to steady-state) have been used to differentiate between plausible decay mechanisms.<sup>30,38,47,49-51</sup>

Application of transient photocurrent analysis to catalyzed photoanodes has produced diverse results. For  $\text{Fe}_2\text{O}_3$  photoanodes decorated with cobalt oxyhydroxide phosphate (Co-Pi) catalyst, numerous studies have concluded that the presence of the catalyst increases both the integrated charge in the transient and its amplitude relative to bare photoanodes.<sup>20,23,52-55</sup> Others have found that Co-Pi catalysts suppress the integrated charge in the transient when applied to  $\text{Fe}_2\text{O}_3$ .<sup>9,56</sup> One study found that Co-Pi application yields smaller but broader transients.<sup>57</sup> Application of Ni- and Ir-based catalysts has been reported to increase the integrated charge in the transient while a report on a Fe-based catalyst found that transients were suppressed.<sup>32,50,58-60</sup> Reports on a “carbon-dot” catalyst and a sub-monolayer Co oxyhydroxide catalyst both found no impact on  $\text{Fe}_2\text{O}_3$  transients.<sup>61,62</sup> For  $\text{BiVO}_4$  photoanodes, Co-Pi and Ru-based catalysts have been shown to result in more pronounced transients with increased integration.<sup>21,63</sup> But others have found that Co-Pi catalysts and  $\text{In}_2\text{O}_3$  coatings suppress transients on  $\text{BiVO}_4$ .<sup>64-68</sup> Meanwhile, reports on  $\text{Ta}_3\text{N}_5$  photoanodes suggest that  $\text{IrO}_2$  catalysts suppress transients while Ni- and Fe-based catalysts significantly increase them.<sup>69-71</sup>

The extent of diverse results has led to a variety of fundamental explanations. In explaining increased amplitude and charge integral of transients, some studies have found that the integrated charge in the transient increases as a function of catalyst loading.<sup>23,50,52,55</sup> They suggest that on-transients represent catalyst oxidation and off-transients represent reduction. More general hypotheses suggest that recombination pathways are introduced by catalyst deposition.<sup>54,72</sup> This has been attributed to the catalyst creating more surface states which increases recombination or by simply increasing the surface capacitance.<sup>53,58</sup> A related explanation suggests that catalysts can function as hole storage layers which increases charge integration of transients by promoting recombination with conduction-band electrons.<sup>32,71</sup> One group has suggested that slower transient decay times represent longer lifetimes for photogenerated charges.<sup>21</sup> Explanations for transient suppression generally suggest that the catalyst suppresses recombination. It has been concluded that catalysts may reduce recombination within the depletion region, although the mechanism by which this would occur is unclear.<sup>65</sup> Others report that transients represent surface-state recombination and that catalysts act to “deload” the surface states before recombination can occur.<sup>48,59,68</sup> Decreased transients have also been attributed to general suppression of recombination at the semiconductor/liquid interface.<sup>73</sup> Still others have suggested that transients represent charge build up at the semiconductor/liquid interface or in surface states; the catalyst acts to consume this charge instead of allowing build-up.<sup>69,74</sup> We note that many of these explanations could occur simultaneously; for instance, application of a catalyst could increase surface capacitance while simultaneously passivating surface states.

To better understand photocurrent transients on catalyst-coated semiconductor photoelectrodes we employ a well-defined Si-based model system.<sup>75</sup> Since Si self-passivates under OER conditions when making solution contact, we use a Ni protection layer which doubles as the catalyst. An advantage in examining this system is that the surface state density on Si is thought to be significantly smaller than either Fe<sub>2</sub>O<sub>3</sub> or BiVO<sub>4</sub>.<sup>22,76-81</sup> Since the Si surface must be buried under the protection layer, it is unlikely that Si|Ni interface states are affected during experiments where additional catalyst is electrodeposited. Thus, we assume that defect-state related charging effects are minor by comparison to other systems. The Si photoanodes protected by a conformal protection layer, are also amenable to the dual-working-electrode (DWE) photoelectrochemical technique.<sup>82,83</sup> In this technique an electrolyte permeable Au contact, deposited on the catalyst surface, is used to sense the catalyst activity. We employ the DWE technique to directly measure the electrochemical potential of a Ni-based catalyst, during transient experiments. We find that transients are most pronounced in the potential region where illumination changes lead to catalyst redox transitions (as measured by the secondary electrode). The integrated charge of the transients in this potential region is larger than that at other potentials. We also find that the transient shape is influenced by the extent of catalyst loading. Since the rectifying junction is buried under a protection layer (and thereby unaffected by additional catalyst loading), this finding suggests that the redox-active catalyst acts as a capacitor which slows the photoanodes transition to steady-state after each illumination change. Based on these results we discuss the impacts of redox-active catalysts on interpretation of photocurrent transients.

## 2. Methods

### 2.1 Photoanode fabrication and electrochemical characterization

The fabrication of photoanodes closely followed the preparation described in our previous work.<sup>75</sup> P-doped [100] n-Si wafers (resistivity 0.65-0.95 ohm·cm) were diced into 1 × 1 cm squares and sonicated for 10 min in acetone (99.8%, Fisher Chemical), iso-propyl alcohol (99.9%, Fisher Chemical) and nanopure water (18.2 MΩ). Diced squares were then cleaned for 30 min in boiling Piranha (3:1 by volume H<sub>2</sub>SO<sub>4</sub>: H<sub>2</sub>O<sub>2</sub>, 100 °C, both procured from Fisher Chemical), rinsed twice and dried under filtered N<sub>2</sub> (0.01 micron – McMaster-Carr). The Ni protection layer and catalyst were deposited without removing the native oxide via electron beam evaporation (Amod evaporation system) at ~0.1 Å s<sup>-1</sup> from a Fabmate crucible (Kurt Lesker) packed with Ni pellets (Kurt Lesker, 1/4" diameter & 1/2" length, 99.995%). In a typical deposition, 5 nm of Ni metal was deposited; this produces lower performing photoanodes (decreased photovoltage) relative to our previous work but ensures photoanode longevity

and protects against shorting during DWE deposition.<sup>75</sup> An ohmic back contact was achieved by scratching through the native oxide on the backside of the n-Si, wetting with Ga-In eutectic ( $\geq 99.99\%$ , Sigma Aldrich), and then affixing a Sn-Cu wire (30 AWG) within the eutectic. The Sn-Cu wire was affixed via hot glue and threaded through a 3.5 mm-diameter glass tube which serves as the electrode stem. The backside of the Si and the Sn-Cu wire were then sealed off, to prevent solution contact, with epoxy (Loctite Hysol 1C).

Before additional fabrication steps, the electrodes were activated by cycling 50 times at 100 mV s<sup>-1</sup> in pH 9.5 1 M potassium borate buffer (K-borate). Cycles were performed under  $\sim 1$  sun AM1.5G illumination (Abet Technologies, model 10500) in a potential window with endpoints 200 mV cathodic of the Ni reduction peak and 200 mV anodic of the Ni oxidation peak. This process converts a portion of the Ni protection layer to an active Ni(Fe)(OH)<sub>2</sub>/Ni(Fe)OOH catalyst. To examine the impacts of catalyst loading, additional Ni(Fe)OOH was electrochemically photodeposited by saturating the buffer with NiCl<sub>2</sub> (calculated to 0.1 M NiCl<sub>2</sub>) and then continuing the illuminated cycling (15-30 additional cycles). We note that unintentional trace Fe cations incorporate into the catalyst, but since this is not the focus of the present work we will hereafter refer to the catalyst as Ni(OH)<sub>2</sub>/NiOOH.<sup>84-86</sup>

The secondary working electrode was deposited in one of two ways, depending on the intended experimental purpose. To sense the catalyst electrochemical potential, 10 nm of Au was thermally deposited directly after the electrochemical NiOOH deposition. This ensures that the Au does not short to the metallic protection layer and only senses the redox-active catalyst. To sense the protection layer electrochemical potential, the 10 nm of Au were thermally deposited directly prior to electrochemical NiOOH deposition. The difference between these two configurations is reflected in the data obtained from the second working electrode (WE<sub>2</sub>). The data is either characteristic of conductivity transitions when sensing the catalyst electrochemical potential (Ni (oxy)hydroxide is only conductive when oxidized) or depicts conductive behavior irrespective of applied potential when sensing the metallic Ni protection layer electrochemical potential.<sup>86</sup> In both cases, the Au was thermally deposited at  $\sim 2 \text{ \AA s}^{-1}$  from an alumina-coated boat (Kurt Lesker). A schematic depiction of the two different DWE deposition strategies can be found in Figure C.S1.

Electrodes were electrochemically characterized in 50 mL of aq. 1 M K-borate buffer (pH  $\sim 9.5$ ) using a BioLogic SP200 bipotentiostat. All experiments were performed with a Pt counter electrode and either a Ag/AgCl or Hg/HgO reference electrode. Cyclic voltammograms were not corrected for uncompensated series resistance. For transient experiments the photoanode was poised at various applied potentials while the light was manually switched off/on each minute. Three off-transients and three on-transients were collected at each applied potential. All experiments were performed with mild stirring.

At least three electrodes were examined for each experiment described below; a single representative electrode is selected for explanation of results. All the potentials are referenced to  $\varepsilon_{\text{O}_2/\text{OH}^-}$  according to the following equation:

$$V (\text{vs. } \varepsilon_{\text{O}_2/\text{OH}^-}) = V_{\text{experimental}} (\text{vs. } \varepsilon_{\text{reference}}) + \varepsilon_{\text{reference}} (\text{vs. SHE}) + 0.059 * pH - 1.23 \text{ V}$$

### 3. Effects of catalyst loading on transient photocurrent response

To understand if redox-active catalysts influence photocurrent transients, we first examined Ni-protected n-Si photoanodes with varied catalyst loadings. For these devices we iterated between collecting illuminated cyclic voltammograms (CVs), collecting photocurrent transient data, and photo-depositing additional redox active NiOOH. Photodeposition was performed by saturating the solution with NiCl<sub>2</sub> and performing 15 CVs, under illumination, as described in the experimental section. To quantify the extent of redox-active NiOOH present, the cathodic redox peak from each CV (corresponding to NiOOH reduction) was integrated (Figure C.1).

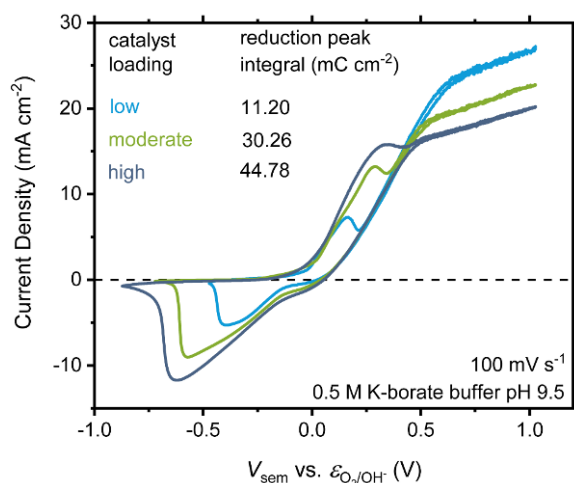


**Figure C.1. Illuminated voltammetry collected after each transient experiment as a function of photodeposited catalyst loading.** All experiments were performed on the same electrode where catalyst loading (low, moderate, high) was increased after each transient experiment (immediately after the CVs shown here). The inset shows the results of the integration of the cathodic redox peak, which is proportional to the number of redox-active Ni sites in the catalyst layer. The data shows the extent of redox-active catalyst present during each transient experiment.

Transients are first collected with the photoelectrode poised at an applied potential ( $V_{\text{sem}}$ ) within the reduction wave of the catalyst ( $\sim -0.2$  V vs. the thermodynamic potential for water oxidation,  $\epsilon_{\text{O}_2/\text{OH}^-}$ ) and then at each 25 mV increment as the photoelectrode is stepped 600 mV anodic of the starting potential (Figure C.2). The photoanode is held at each potential step for 7 min, during which time the light is switched off at the beginning of each odd numbered minute and on at the beginning of each even numbered minute. Anodic and cathodic transients exist over the entire applied potential range. However, integration of the current transients reveals a potential region ( $>250$  mV), for each experiment, where transient integrated charge is increased. As additional catalyst is photodeposited the region of increased integrated charge shifts cathodic and the integrated charge increases.

The region of increased integrated charge can be attributed to oxidation/reduction of the Ni catalyst. This conclusion is supported by comparing the integrated charge for each photodeposition step (Figure C.S2). As more catalyst is photodeposited, the integrated charge in the voltammetry (Figure C.1) and the transient (Figure C.2) increase together. The cathodic shift of the region of increased integrated charge is attributed to an increase in the photovoltage as the photoelectrode ages (Figure C.2 and Figure C.S3). The ageing phenomenon, explained in our previous work, relates to the protection layer becoming increasingly electrolyte permeable.<sup>75</sup> This explanation is consistent with the anodic shift in OER onset seen when comparing voltammograms immediately before and after the first transient experiment (Figure C.S3). The data in this section thus shows that (1) the catalyst layer affects the transient response, (2) the effect is most pronounced in the region of increased integrated transient charge, and (3) that higher loading of catalyst yields larger integrated charge in the transients.

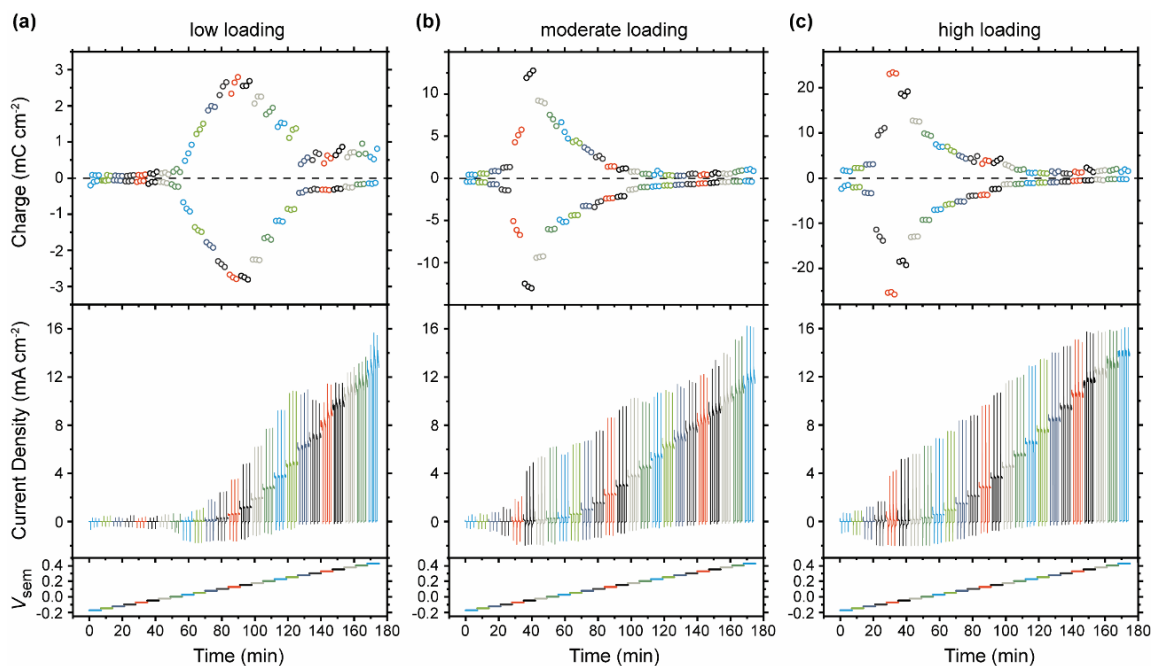


**Figure C.2. Transient response as a function of catalyst loading.** The bottom pane shows  $V_{\text{sem}}$  vs.  $\varepsilon_{\text{O}_2/\text{OH}^-}$  as a function of time. The middle pane depicts the transient photocurrent response collected every 1 ms. The top pane depicts the integration of the transients which reveals a  $>250$  mV range where integrated charge is most prominent. Comparison between the different extents of catalyst loading: **(a)** low, **(b)** moderate, and **(c)** high, shows that increased loading produces larger integrated charge in the transients.

#### 4. Dual-working-electrode measurements of catalyst potential during photocurrent transients

To directly measure the catalyst behavior during transient experiments, the dual-working-electrode (DWE) photoelectrochemistry technique was used. In these experiments, the first working electrode ( $\text{WE}_1$ ) was attached to an ohmic contact on the backside of the n-Si semiconductor and the second working electrode ( $\text{WE}_2$ ) was attached to a thin electrolyte-permeable Au top-contact (see Figure C.S1 for additional details). The Au layer was evaporated onto the photoanode after both activation and additional NiOOH had been photodeposited. Due to the fragile nature of this secondary contact (it tends to be exfoliated by prolonged oxygen evolution),  $\text{WE}_1$  is stepped in 100 mV increments instead of 25 mV increments. Data is collected every 100 ms to accentuate the region of increased integrated transient charge. Illumination chopping periodicity and all other experimental parameters remain the same as in Section 3.1.

During each experiment the current density at WE<sub>1</sub> ( $J_{\text{sem}}$ ) and the voltage at WE<sub>2</sub> ( $V_{\text{cat}}$ ) are simultaneously recorded (Figure C.3).

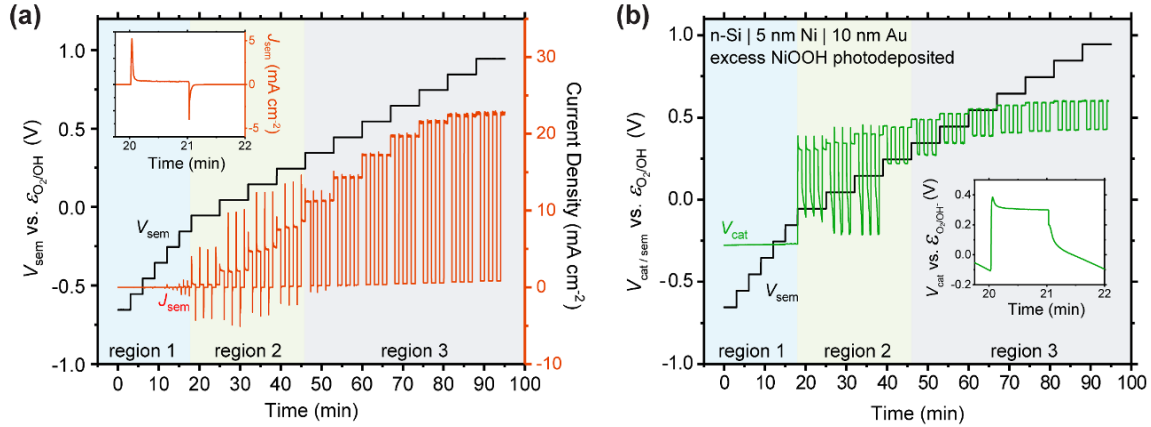


**Figure C.3. Measurement of catalyst potential during transient experiments.** Three light-on/light-off transient sets were recorded for each potential ( $V_{\text{sem}}$ ) step. Three regions of activity are denoted (discussed in the main text) on each panel. **(a)** Transient  $J_{\text{sem}}$  response (red) as a function of time and hence WE<sub>1</sub> applied potential ( $V_{\text{sem}}$ ). Transients are only apparent in region 2. **(b)**  $V_{\text{cat}}$  (WE<sub>2</sub>) response (green) for the same transients. When the light is turned off, two regions of  $V_{\text{cat}}$  decay (panel b) are exhibited in region 2: a quick decay followed by a slower decay which fails to reach a steady-state value before the light is turned back on. Insets in both panels show one set of transients in region 2. The data shows that the catalyst potential  $V_{\text{cat}}$ , for regions 2 and 3, varies in tandem with the transient photocurrent response – i.e. during on-transients the catalyst is oxidized and during off-transients the catalyst is reduced.

The chopped illumination data exhibits three regions of distinct transient behavior (Figure C.3). In the first region, corresponding to the first six  $V_{\text{sem}}$  voltage steps (-0.65 to -0.15 V vs.  $\epsilon_{\text{O}_2/\text{OH}^-}$ ), transients are absent or very small. The catalyst potential,  $V_{\text{cat}}$ , measured via WE<sub>2</sub> and the semiconductor current density,  $J_{\text{sem}}$ , remain constant in this region (Figures C.3a and 3b); i.e.  $J_{\text{sem}}$  and  $V_{\text{cat}}$  are nonresponsive to both the applied  $V_{\text{sem}}$  and to changes in the illumination condition. Catalyst voltammograms (collected via WE<sub>2</sub> directly after transient experiments, see Figure C.S4) show that the onset of catalyst oxidation occurs at  $\sim 0.3$  V vs.  $\epsilon_{\text{O}_2/\text{OH}^-}$ . Because  $V_{\text{cat}}$  remains near -0.3 V vs.  $\epsilon_{\text{O}_2/\text{OH}^-}$  throughout region 1 of the transient experiment, the catalyst remains in its non-conductive Ni(OH)<sub>2</sub> state.



In region 2, on- and off-transients are observed for  $V_{\text{sem}}$  potentials between -0.05 and 0.25 V vs.  $\epsilon_{\text{O}_2/\text{OH}^-}$ . As the light is turned on both  $J_{\text{sem}}$  and  $V_{\text{cat}}$  quickly increase before decaying to a steady-state value (Figure C.3a). Integration of the largest  $J_{\text{sem}}$  on-transient ( $6.5 \text{ mC cm}^{-2}$ ) compares favorably to integration of the redox wave in the catalyst voltammograms shown in Figure C.S4 ( $8 \text{ mC cm}^{-2}$ ). The on-transients thus represent catalyst oxidation in this region. When the light is switched off both  $J_{\text{sem}}$  and  $V_{\text{cat}}$  simultaneously decrease.  $J_{\text{sem}}$  exhibits a negative current transient before decaying back to  $\sim 0 \text{ mA cm}^{-2}$ .

For many of these electrodes, the magnitudes of the integrated  $J_{\text{sem}}$  off-transients are  $\sim 30\%$  smaller than the integrated on-transients. Additionally, for these electrodes,  $V_{\text{cat}}$  exhibits a quick initial decay (through the first  $\sim 200 \text{ mV}$ ) followed by a much slower decay thereafter (Figure C.3b - inset). These two findings are explained as follows. When the light turns off the hole population collapses and hole quasi-Fermi level returns to the majority electron Fermi level. Electrons are then transferred from the conduction band to the catalyst directly in contact with the semiconductor, reducing NiOOH to Ni(OH)<sub>2</sub>. Because Ni(OH)<sub>2</sub> is an electronic insulator, reduction of the near-surface NiOOH may electronically isolate regions of the catalyst further from the semiconductor|catalyst interface. For these isolated catalyst areas, the catalyst cannot be re-reduced from the semiconductor and thus the oxidized state must relax via a slower equilibrium with the solution (i.e. to discharge and generate oxygen gas). Hence the light-off  $V_{\text{cat}}$  response is characterized by a quick decay followed by a slow decay (Figure C.3b - inset). This picture is supported by the fact that the slow  $V_{\text{cat}}$  decay occurs after  $J_{\text{sem}}$  has reached its dark steady-state value ( $\sim 0 \text{ mA cm}^{-2}$ ).

In Region 3 ( $V_{\text{sem}} = 0.35 - 0.95 \text{ V vs. } \epsilon_{\text{O}_2/\text{OH}^-}$ ), no transients are observed. However, unlike region 1, both  $J_{\text{sem}}$  and  $V_{\text{cat}}$  are responsive to the light condition. As the light is turned on,  $J_{\text{sem}}$  and  $V_{\text{cat}}$  simultaneously increase and achieve a steady-state. When the light is turned off they each relax to respective lower values and achieve a new steady-state. The fact that  $V_{\text{cat}}$  reaches steady-state in the dark demonstrates that the catalyst remains oxidized and that WE<sub>2</sub> is in electronic contact with the semiconductor. This is further evidenced by the lack of a second slower  $V_{\text{cat}}$  decay, and the lack of the  $J_{\text{sem}}$  on/off-transients. We also note that, in Region 3,  $V_{\text{cat}}$  remains positive of  $\sim 0.3 \text{ V vs } \epsilon_{\text{O}_2/\text{OH}^-}$  (the oxidation onset potential measured for the catalyst alone, see Figure C.S4). This data indicates that the surface majority carrier Fermi-level is no longer capable of reducing the catalyst in the dark. Instead, the small leakage current from the semiconductor is sufficient to keep the catalyst oxidized. During light-on,  $V_{\text{cat}}$  increases but no redox transition occurs.

The data presented above for regions 1, 2 and 3 indicate that a significant transient response only occurs when the dark-to-light range of  $V_{\text{cat}}$  ( $\Delta V_{\text{cat}}$ ) overlaps the catalyst's redox-active potential range. The catalyst's redox activity range can be measured directly using WE<sub>2</sub> for the same device on which transients are measured. For the device in Figure C.3 catalyst reduction occurs at  $\sim 0.25$  V vs.  $\epsilon_{\text{O}_2/\text{OH}^-}$  and oxidation occurs at  $\sim 0.3$  V vs.  $\epsilon_{\text{O}_2/\text{OH}^-}$  (Figure C.S4). For regions 1 and 3, the measured  $V_{\text{cat}}$  remains below or above this redox activity range, respectively (Figure C.3b). However, for region 2 where transients are most pronounced,  $V_{\text{cat}}$  transitions through the redox range immediately following each light switch. This directly shows that the most pronounced transient behavior is associated with the oxidation and reduction of the catalyst. The appearance of transients is an indication that  $\Delta V_{\text{cat}}$  is partially or fully eclipsing the range of catalyst redox activity.

To help explain this finding, band diagrams for the processes occurring in region 2 are depicted in Figure C.4. In the dark, the applied potential is such that the majority carrier Fermi level ( $E_{f,n}$ ) rests slightly cathodic of the catalyst's redox-activity region. Once illuminated, the generated minority-carrier profile results in a photovoltage which drives the oxidation of the catalyst. Charge accumulation at the solution interface pushes the protection-layer Fermi level ( $E_{\text{Ni}}$ ) through the region of catalyst redox activity. The catalyst Fermi level ( $E_{\text{cat}}$ ) remains in quasi-equilibrium with the protection layer and this results in the catalyst oxidation. Removal of the light source leads to re-reduction of the catalyst as the hole quasi-Fermi-level ( $E_{f,p}$ ) equalizes with  $E_{f,n}$ . Thus, the transient behavior depicted in region 2 occurs as a function of the applied potential and the photovoltage. Significant transients occur whenever the applied  $V_{\text{sem}}$  places  $E_{f,n}$  cathodic of the redox activity region in the dark and the photovoltage is sufficiently large such that the photogenerated holes can drive water oxidation in the light.

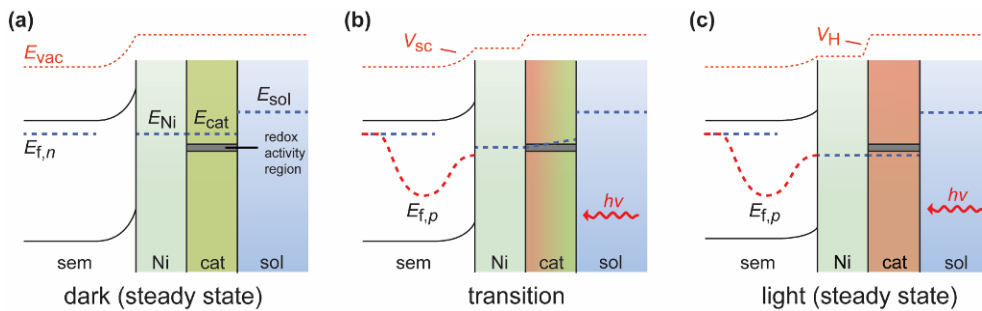


**Figure C.4. Schematic band diagrams of transition of system between dark and light states.**

The green catalyst represents  $\text{Ni}(\text{OH})_2$  while the red catalyst represents  $\text{NiOOH}$ . The transition behavior (panel b) depicts a gradient in redox states that may occur as the catalyst transitions from

Ni(OH)<sub>2</sub> to NiOOH. The semiconductor, metallic Ni protection layer, redox active catalyst and solution are represented by sem, Ni, cat, and sol, respectively.  $E_{\text{Ni}}$ ,  $E_{\text{cat}}$ , and  $E_{\text{sol}}$  represent the electrochemical potential for the protection layer, catalyst, and solution, respectively. The quasi-Fermi levels are depicted by  $E_{\text{f,n}}$  and  $E_{\text{f,p}}$ . A redox activity region (gray box) represents a catalyst “redox density of states (DOS)” which are filled/emptied during redox transitions. The vacuum level, represented by  $E_{\text{vac}}$ , is shown as modified by the electrostatic potential.  $V_{\text{sc}}$  and  $V_{\text{H}}$  represent the depletion region electrostatic potential and Helmholtz electrostatic potential, respectively. Note here that during transient experiments  $\Delta V_{\text{sc}}$  must equal  $-\Delta V_{\text{H}}$  to maintain  $E_{\text{sem}}$  fixed versus  $E_{\text{sol}}$ , as is controlled by the potentiostat. For region 2, the dark majority carrier level is sufficiently cathodic to reduce the catalyst (panel a). Once illuminated, holes arriving at the solution interface force an increase in  $V_{\text{H}}$  which eventually moves  $E_{\text{Ni}}$  to the redox activity region (panel b).  $E_{\text{cat}}$  maintains quasi-equilibrium with  $E_{\text{Ni}}$  and this causes oxidation of the catalyst (panel c). The temporal transition to the illuminated steady-state is slowed by the catalyst layer because holes that would be contributing to increasing  $V_{\text{H}}$  are now partially being consumed for catalyst redox chemistry. Since  $\Delta V_{\text{sc}} = -\Delta V_{\text{H}}$ , the band unbending is also slowed, and the transient photocurrent response is characterized by larger currents over a longer duration.

## 5. Dual-working-electrode measurements of the protection-layer potential during photocurrent transients

We next consider the shape of the transient responses and explain it in terms of a band picture. We make measurements on electrodes where the thin electrolyte-permeable Au layer is deposited after photoanode activation, but before additional NiOOH catalyst is photodeposited onto the surface. This results in contact between the Au WE<sub>2</sub> and the Ni metallic protection layer, as can be seen by the fact that  $V_{\text{cat}}$  is now responsive to light on/off cycles at all potentials (Figure C.S5); i.e. the measurement is not limited by the insulating nature of the reduced Ni(OH)<sub>2</sub> form of the catalyst. Measuring the surface potential does not require that the catalyst is in an electrically conductive state. Instead of sensing the redox-active catalyst electrochemical potential, the contact now equilibrates with the protection layer electrochemical potential. Since the protection layer consists of dense metallic Ni, during transients its electrochemical potential can only be modified by charge built-up at the metal|solution interface (the catalyst layer is permeable to electrolyte). Thus, by observing the protection layer electrochemical potential we sense changes to the Helmholtz electrostatic potential (shown in Figure C.4c).

Figure C.5 shows cathodic  $J_{\text{sem}}$  transients and the associated  $V_{\text{Ni}}$  response for a device with the second working electrode attached directly to the metallic Ni protection layer. Transient

integrated charge and the complete  $J_{\text{sem}}$  and  $V_{\text{Ni}}$  dataset can be found in Figure C.S5. We select five of the cathodic transients to examine in more detail. Figure C.5a depicts a cathodic transient from region 1, i.e. at  $V_{\text{sem}}$  cathodic of the catalyst redox activity. Transients shown in Figure C.5b, C.5c, and C.5d are from region 2, in order of increasing anodic applied potentials. The transient shown in Figure C.5e is from region 3, at  $V_{\text{sem}}$  anodic of the catalyst redox potential region. When the catalyst redox activity is not present (regions 1 and 3), the current transient completely decays to steady-state within 1 s (Figure C.5a and C.5e). The  $V_{\text{Ni}}$  response mirrors the decay time and the decay shape. For the transients in Figure C.5b and 5c, the photocurrent decays over a much longer timeframe ( $>5$  s) and deviates from the visibly exponential shape of those in Figure C.5a and 5e. The exponential current decay to steady-state is interrupted by a region of more moderate decay (diminished slope).  $V_{\text{Ni}}$  decays over the same timeframe and visibly mirrors the shape of the current decay. Finally, the transient in Figure C.5d lacks the complex shape of the previous two, but decays over a longer timeframe than either transient in Figure C.5a or 5e. All three transients selected from region 2 show significantly slower decay times and exhibit  $V_{\text{Ni}}$  responses which mirror the  $J_{\text{sem}}$  decay shape.

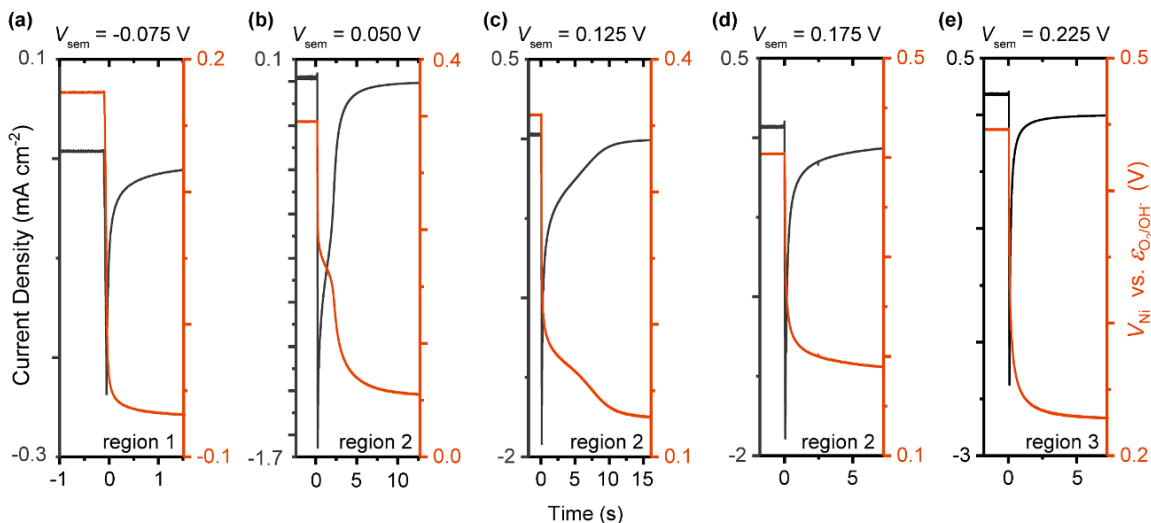


**Figure C.5. Sensing the protection layer electrochemical potential.** Results depict  $J_{\text{sem}}$  and  $V_{\text{Ni}}$  from five representative transients as sensed via  $\text{WE}_1$  and  $\text{WE}_2$ , respectively. Panel (a) shows a transient from region 1. Panels (b), (c) and (d) show transients from region 2 in order of increasingly anodic applied potential. Panel (e) shows a transient in region 3. This data shows that when the off-transient causes  $V_{\text{Ni}}$  to traverse the onset of catalyst reduction (at  $\sim 0.20$  vs.  $\epsilon_{\text{O}_2/\text{OH}^-}$ ) the decay in the protection layer electrochemical potential is slowed (Figure C.S6). The decay shape for  $J_{\text{sem}}$  becomes visibly more complex and this shape is mirrored by the  $V_{\text{Ni}}$  decay.

The above results indicate that the redox-active Ni (oxy)hydroxide catalyst acts as a “capacitor” which moderates how quickly the semiconductor depletion region and Helmholtz electrostatic potentials relax when moving from light to dark. For the transients in Figure C.5b and 5c,  $V_{Ni}$  collapses quickly in each case until it reaches  $\sim 0.2$  V vs.  $\epsilon_{O_2/OH^-}$ . This potential is consistent with where the redox-active catalyst is converted from NiOOH to Ni(OH)<sub>2</sub>, and so it represents the edge of the catalyst’s “redox density of states (DoS)” (Figure C.S6a). Once the Helmholtz potential has decayed to place  $E_{Ni}$  near the catalyst reduction onset, electrons injected from the conduction band can reduce the catalyst, in addition to accumulating at the Ni|solution interface. If charge is not injected into the catalyst, for example due to slow charge transfer kinetics between Ni and catalyst, the fast exponential decay would continue without any region of slowed transient decay.<sup>9,47,87,88</sup> However, the data above shows that the decay is slowed, indicating that charges are injected into the catalyst once  $V_H$  has sufficiently relaxed.

The potential range for the more moderate slope in region 2 of the transient decays is associated with the catalyst’s redox DoS. In the Figure C.5b transient, the “diminished”  $V_{Ni}$  decay occurs through a  $\sim 40$  mV range, while for the Figure C.5c transient the “diminished” decay occurs through a  $\sim 38$  mV range. This data suggests that the catalyst contains a redox DoS spanning 38-40 mV, which is consistent the redox peak widths for WE<sub>2</sub> voltammetry collected at 1 mV s<sup>-1</sup> (Figure C.S6b). Once the Helmholtz electrostatic potential aligns  $E_{Ni}$  with the edge of this 38-40 mV region, the redox states begin to compete for consumption of injected electrons; any change in the Helmholtz electrostatic potential must correlate with the same potential change in the catalyst redox DoS. Upon filling the catalyst DoS the catalyst “parallel capacitance” vanishes, and current/voltage decay can once again continue exponentially. This final point is experimentally supported by the resumed rapid  $V_{Ni}$  decay after the 38-40 mV have transpired (Figures C.5b and C.5c).

For further evidence that the catalyst redox DoS moderates the transient photocurrent/photovoltage decay we return to the loading dependence data from Section 3.1. In Figure C.6a all three transient loadings are compared at a constant applied potential near the OER onset. To account for shifts in the transient integration region due to different photovoltages provided by the rectifying junction, in Figure C.6b the transients which exhibit maximum charge integration at each loading are also compared. In both cases, increased loading produces not only an increase in the integration of the anodic transient but also a broadened transient decay shape. The cathodic transients exhibit more-exponential behavior but their decay to zero current is also broadened as loading increases. The cathodic transients at moderate and high catalyst loading fail

to reach zero current before the light is switched on again. By contrast, the low loading cathodic transient returns to zero in both examples. These results demonstrate that larger absolute transient currents are sustained for longer when more catalyst is coated onto the photoanode.

The catalyst loading results can be related to the band-bending model in Figure C.4. For the anodic light-on transients, where photocurrent decay is governed by the rate of electrons injected from the conduction band, increased catalyst loading causes the semiconductor bands to unbend more slowly. For the cathodic transients, where decay is related to how quickly the bands regain their dark equilibrium state, increased catalyst loading causes the bands to re-bend over a longer duration. These findings are consistent with the above understanding, where interaction with the catalyst redox states slows how quickly the Helmholtz electrostatic potential responds to changes in the illumination. As the number of catalyst redox states increases the electrostatic potential transition further slows and so the transient relaxation time increases.

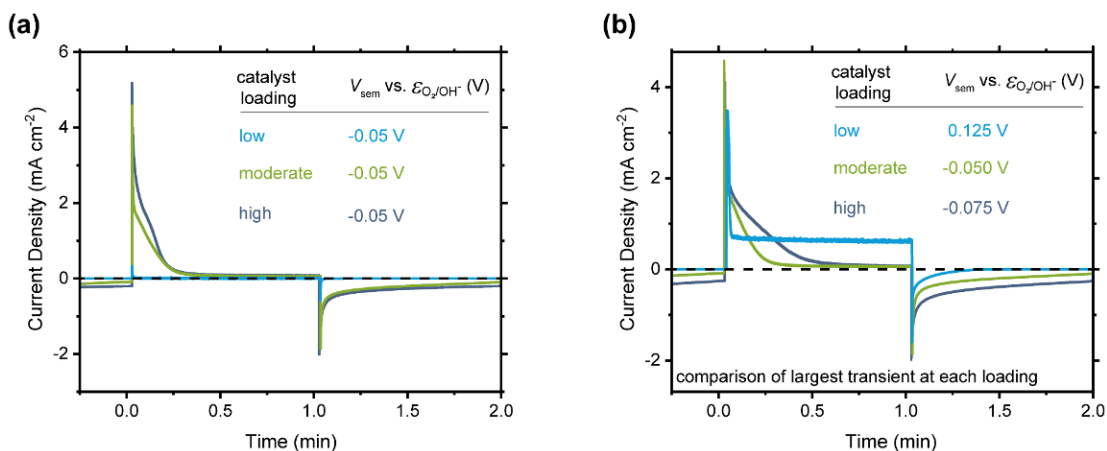


**Figure C.6. Transients vs. catalyst loading on the same sample shown in Figure C.2.** One set of on/off transients selected from the overall data. **(a)** All three loadings compared at -50 mV vs. E<sub>O<sub>2</sub>/OH<sup>-</sup></sub>. **(b)** Comparison of the transient with largest charge integration at each catalyst loading extent. The applied potential for each loading is shown in the inset. Increased loading in each case results in broader transient features. Anodic transients exhibit non-exponential decay as loading increases. The results show that increased catalyst loading causes broader transients oftentimes with complex decay shapes.

## 6. Conclusions

Experiments on Ni-protected n-Si illustrate how photocurrent transients are affected by the presence of a redox-active catalyst. The application of the catalyst produces three distinct regions of transient activity. At sufficiently low and high applied potentials, only very quick transients

appear with relatively small charge integration. Between these two regions of activity exists a region with large charge integration and relatively slow decay times. Here, we find that the integrated charge is related to the quantity of redox-active catalyst on the semiconductor surface. DWE experiments reveal that this behavior takes place when the applied potential is such that: (a) the majority carrier Fermi level can reduce the catalyst in the dark and (b) the minority carrier Fermi level can oxidize the catalyst once illuminated. Since the photovoltage is given by the difference between the two quasi-Fermi levels, photoanodes with greater photovoltages are expected to exhibit this behavior over a greater applied potential range.

The presence of a redox-active catalyst slows the electrostatic relaxation events during transient experiments. This occurs whenever an illumination switch causes the surface electrochemical potential at the protection layer to pass through the catalyst's redox density of states. With little or no catalyst, relaxation is characterized by carriers injected from the semiconductor interacting to increase/decrease the Helmholtz electrostatic potential at the Ni protection layer surface. In the presence of the Ni (oxy)hydroxide catalyst this relaxation process is slowed because some of the carriers are now consumed for catalyst redox activity. A larger catalyst redox density of states promotes this effect, by essentially acting as a larger parallel capacitor, and gives rise to more complex and extended transient decay shapes. This explains, in part, the more complex and/or extended decay shapes that arise after catalyst application in many recent reports on a variety of oxide photoanodes.<sup>23,32,52,55,57,63,66,70-73,89-91</sup> We note that this behavior is dependent on the catalyst being in quasi-equilibrium with the surface electrochemical potential. For systems without quasi-equilibrium (slow transfer between semiconductor and catalyst), the electrostatic profile may relax before redox activity takes place. One situation where such behavior occurs is in the re-reduction of the oxidized Ni (oxy)hydroxide catalyst during the off-transient; initial discharge can result in an electrically insulating near-semiconductor layer which prevents complete reduction of the catalyst from the semiconductor. Similarly, in systems employing the Co-Pi catalyst, lack of cathodic off-transients may be related to slow reduction kinetics.<sup>16,23,64,74,90</sup>

The utility of transient photocurrent experiments relies on assigning transients to a specific process. For example, using transient integration to quantify surface states requires attributing the transient response to surface state filling/emptying. However, we show that redox-active catalysts can influence transients, causing increased integrated charge in the transient, extended decay times, and complex decay shapes. These findings have general implications for analyzing photoelectrochemical transients – those on catalyzed systems may represent more processes than the filling/emptying of surface states. If the catalyst's redox DoS overlaps a surface-state DoS then transients are expected to be influenced by both. For these transients, decay time characterization

and transient integration describe the conflated relaxation processes and may not accurately depict either isolated process. Additionally, for systems with larger photovoltages (e.g.  $\text{BiVO}_4$ ,  $\text{Fe}_2\text{O}_3$ ), we anticipate that this conflated relaxation response occurs over a greater applied potential range. Comparison of photocurrent transients as a function of catalyst mass loading can be employed to indicate if and where the catalyst is influencing transients. When catalyst influence is present, multi-exponential decay fits may be useful in isolating processes that occur before/after interaction with the catalyst redox DoS. Several groups have reported that single exponential fits are insufficient for fitting decay time constants for catalyzed systems and have relied on multi-exponential fits.<sup>49,50,55</sup> However, for processes occurring at similar time scales, the DWE technique is useful as it provides a direct measure of the catalyst charging. The DWE measurement could be used to separate out the extent of transient behavior due to catalyst charging, relative to that due to surface-state charging.

## **Paper D**

### **Behavior of Catalyst-Modified n-Si Photoelectrodes in the Presence of a Sacrificial Hole Scavenger: Insight from Dual-Working Electrode Photoelectrochemistry**

Forrest A. L. Laskowski, Michael R. Nellist, Jingjing Qiu, Adrian M. Gordon, and Shannon W. Boettcher

#### **1. Introduction**

Hole scavengers – easily oxidized soluble solution species – are routinely used to quantitatively characterize photoelectrochemical devices. For solar water splitting devices, hole scavengers can be used to capture photogenerated minority carriers that arrive at the semiconductor|liquid junction which might otherwise recombine or be consumed in water oxidation. Hole scavenger-based analysis assumes that hole scavenger presence results in efficient collection of all photogenerated holes arriving at the semiconductor|liquid or catalyst|liquid junction. By taking the ratio of the steady state photocurrents with and without hole scavenger presence, at a given applied potential, an overall charge injection efficiency for water oxidation is calculated. This charge injection efficiency represents the deviation from the “ideal” case where the hole scavenger is present. Using a dual-working-electrode approach, we demonstrate that presence of a hole scavenger does not always result in ideal charge injection especially when common redox-active catalysts (e.g. Ni-, Co-, and Fe-based (oxy)hydroxides) are present on the



photoanode surface. We show that hole scavenger presence can force the catalyst to remain in a lower oxidation state than would be present for water oxidation, sans hole scavenger. If the reduced catalyst state is electrically insulating, then charge collection will decrease and thereby artificially inflate the hole-scavenger-based calculation of charge injection efficiency. The results demonstrate a common misconception in the application of hole scavenger analysis and should facilitate more target application of the technique.

Poor photoanode performance limits the viability of many solar-water-splitting systems.<sup>1</sup> One challenge is slow oxygen-evolution reaction kinetics on the photoanode surface.<sup>1-5</sup> Photogenerated holes arriving at the semiconductor/solution surface cannot efficiently inject into oxygen-evolution acceptor states. Slow injection results in a large surface hole concentration which promotes electron-hole recombination and thereby lowers device efficiency. The addition of catalytic layers onto the surface of the photoanode is one way to address sluggish charge injection. However, the charge injection efficiency of many catalyzed photoanodes remains sub-optimal.<sup>6-9</sup> To characterize the charge injection efficiency of promising photoanodes, researchers have turned to hole scavengers, easily oxidized hole species, which facilitate charge collection.<sup>10-12</sup> Comparison of a photoanode current-potential response with and without hole scavenger presence is used to calculate a promising photoanode's charge injection efficiency. Thus, the hole scavenger technique is one way to measure the impact of oxygen evolution reaction kinetics on the photoanode. The charge injection efficiency can be used to identify promising photoanodes (e.g. by showing that many holes arrive the active surface) or to guide the improvement of existing photoanodes (e.g. by quantifying the deficiency in surface catalytic rate).

The utility of the hole scavenger technique has led to widespread adoption since Dotan et al. popularized the H<sub>2</sub>O<sub>2</sub> hole scavenger in 2011.<sup>10, 11</sup> Since then, the hole scavenger technique has been most commonly used to quantify charge injection efficiency on photoanodes without catalyst layers, especially when investigating Fe<sub>2</sub>O<sub>3</sub> photoanodes.<sup>10, 13-63</sup> The technique has also been commonly applied to BiVO<sub>4</sub>,<sup>64-85</sup> CuWO<sub>4</sub>,<sup>86-91</sup> and WO<sub>3</sub><sup>92-100</sup> photoanodes using either H<sub>2</sub>O<sub>2</sub> or Na<sub>2</sub>SO<sub>3</sub> as the hole scavenger species. A few groups have also used hole scavengers to characterize the charge injection efficiency of TiO<sub>2</sub> photoanodes<sup>101-104</sup> and a variety of more unique photoanode systems.<sup>105-121</sup> More recently, hole scavenger analysis has been increasingly applied to catalyzed systems, most commonly to calculate the charge injection efficiency of BiVO<sub>4</sub> and Fe<sub>2</sub>O<sub>3</sub> photoanodes coated with Co-, Fe-, or Ni-based electrocatalysts.<sup>6, 7, 122-147</sup>

Here we use a dual-working-electrode (DWE) technique to explore the interaction between catalyzed photoanodes and hole scavengers.<sup>148-150</sup> The technique makes use of a second working electrode deposited on top of the catalyst layer that is able to sense the catalyst's electrochemical

potential during device operation. The findings reveal that the photoresponse of the catalyst-coated photoanode, with and without hole scavenger presence, originates from two physically different systems. In electrolyte without hole scavenger, water oxidation generally occurs with the catalyst in an oxidized form (e.g. Ni(Fe) oxyhydroxide). Whereas, in the presence of a hole scavenger, oxidation of the hole scavenger occurs with the catalyst in a reduced form (e.g. Ni(Fe) hydroxide). If the reduced form of the catalyst is electrically insulating (as is true for Ni- and Co-based (oxy)hydroxide catalysts), retention of the reduced form can inhibit charge injection during hole scavenger characterization. We explore these findings on a model n-Si photoanode and then briefly discuss additional findings on a Fe<sub>2</sub>O<sub>3</sub> photoanode.

## 2. Experimental

Photoanode fabrication resembles that previously reported.<sup>149</sup> Briefly, P-doped [100] n-Si (resistivity 0.65-0.95 ohm·cm), diced into 1 × 1 cm squares, were used as substrates. For cleaning, the Si squares were sequentially sonicated, for 10 min, in acetone (99.8%, Fisher Chemical), isopropyl alcohol (99.9%, Fisher Chemical), and nanopure water (18.2 MΩ). The squares were then submerged in boiling Piranha (3:1 by volume H<sub>2</sub>SO<sub>4</sub>: H<sub>2</sub>O<sub>2</sub>, 100 °C, Fisher Chemical) for 30 min, rinsed twice with nanopure water, and dried under N<sub>2</sub>. Since n-Si lacks stability when contacting the electrolyte solution, a 5-nm-thick Ni protection layer was deposited via E-beam evaporation at ~0.1 Å s<sup>-1</sup>.<sup>151,152</sup> In-Ga eutectic (≥99.99%, Sigma Aldrich) was applied to the backside of the Si to form an ohmic contact. A Sn-Cu wire, serving as the back-contact, was placed within the eutectic. The other end of the Sn-Cu wire was threaded through a 3.5 mm-diameter glass tube which serves as an electrode stem. The Si backside, eutectic, Sn-Cu wire, and glass tube were sealed with epoxy (Loctite Hysol 1C) to preclude solution contact.

Before deposition of the second contact, the electrodes were cycled 50 times in 1 M aq. potassium borate buffered to pH ~9.5, under illumination, through a potential range with endpoints defined 200 mV cathodic of NiOOH reduction and 200 mV anodic of Ni(OH)<sub>2</sub> oxidation, using a BioLogic SP200 bipotentiostat. This activation procedure generates a layer of redox active Ni(OH)<sub>2</sub>/NiOOH on the Ni protection layer surface. We note that Fe incorporates into the catalyst during the activation step as the electrolytes were not rigorously Fe-free.<sup>153-155</sup> After activation, the surface was rinsed with nanopure water and dried under flowing N<sub>2</sub>. The second working electrode contact, Au, was thermally deposited at ~2 Å s<sup>-1</sup> to a thickness of X nm on top of the catalyst layer and onto the surrounding epoxy in which the electrode was embedded. A Sn-Cu wire was affixed to this layer via silver paint. Electrodes were electrochemically characterized in aq. 1 M potassium borate buffer (pH ~9.5) while

using a Pt counter electrode and an Ag/AgCl reference electrode. For hole-scavenged experiments, H<sub>2</sub>O<sub>2</sub> was introduced into the electrolyte such that 0.5 M H<sub>2</sub>O<sub>2</sub> concentration was achieved. An Abet Technologies solar simulator was used to generate ~1 sun of AM1.5G illumination. Experiments were performed with mild stirring and in triplicate. A representative sample is used to explain each set of results.

### 3. Results & Discussion

To understand how hole scavengers affect catalyzed photoanodes, we use a dual-working-electrode (DWE) technique to independently monitor/control the catalyst potential. The n-Si photoanodes were coated with a 5-nm-thick Ni protection layer which was partially converted into a redox-active Ni(Fe)OOH/Ni(Fe)(OH)<sub>2</sub> catalyst by electrochemical cycling. After cycling, a thin Au layer, serving as the secondary working electrode (WE<sub>2</sub>), was thermally evaporated onto the catalyst surface. Since the Au layer only contacts the catalyst, it can either be used to monitor the catalyst electrochemical potential during electrochemical experiments or it can be used to directly control the catalyst potential.<sup>149</sup> Direct control of the catalyst potential through WE<sub>2</sub> allows for one to measure the catalyst's intrinsic oxygen evolution reaction (OER) activity. Comparing the intrinsic catalyst *J-E* response collected by controlling the potential of WE<sub>2</sub> to the illuminated photoanode curve, collected by controlling the potential of the primary electrode (WE<sub>1</sub>), reveals a difference in OER onset (Figure D.1). This onset difference is caused by the Fermi-level splitting during illumination and can be thought of as the photovoltage. Repeating the same DWE experiments in the presence of the H<sub>2</sub>O<sub>2</sub> hole scavenger allows us to independently monitor the changes in catalysis and photovoltage.

The Ni-based catalyst exhibits OER onset (measured versus WE<sub>2</sub>) when the potential applied to the catalyst ( $V_{\text{cat}}$ ) = ~ 0.4 V vs. the thermodynamic potential for water oxidation ( $\epsilon_{\text{O}_2/\text{OH}^-}$ ), in the absence of the hole scavenger (Figure D.1 – *cat*<sub>H<sub>2</sub>O</sub> curve). The same experiment, in the presence of H<sub>2</sub>O<sub>2</sub>, reveals the onset of H<sub>2</sub>O<sub>2</sub> oxidation at ~ -0.3 V vs.  $\epsilon_{\text{O}_2/\text{OH}^-}$  (Figure D.1 – *cat*<sub>H<sub>2</sub>O<sub>2</sub></sub> curve). The difference in onset is expected as  $\epsilon_{\text{O}_2/\text{H}_2\text{O}_2}$  lies 550 mV cathodic of  $\epsilon_{\text{O}_2/\text{OH}^-}$  and the rate constant for H<sub>2</sub>O<sub>2</sub> oxidation is 10-100 larger than for H<sub>2</sub>O oxidation.<sup>10, 11</sup> Data collected through the semiconductor contact (WE<sub>1</sub>), under illumination but in the absence of the hole scavenger, exhibits OER onset when the potential applied to the semiconductor ( $V_{\text{sem}}$ ) = ~ 0.3 V vs.  $\epsilon_{\text{O}_2/\text{OH}^-}$  (Figure D.1 – *sem*<sub>H<sub>2</sub>O</sub> curve). Thus, for water oxidation, the photoanode exhibits a photovoltage of only ~ 100 mV (i.e. this is the difference in OER onset potentials measured at WE<sub>1</sub> and WE<sub>2</sub>). This low photovoltage is due to the thick Ni layer used in this particular experiment.

Once  $\text{H}_2\text{O}_2$  is introduced, the onset of  $\text{H}_2\text{O}_2$  oxidation on the illuminated photoanode occurs at  $\sim 0$  V vs.  $\epsilon_{\text{O}_2/\text{OH}^-}$  (Figure D.1 –  $\text{sem}_{\text{H}_2\text{O}_2}$  curve). This result is surprising, because the illuminated photoanode performs  $\text{H}_2\text{O}_2$  oxidation at potentials *less cathodic* than the Ni-based catalyst in isolation – it is harder to perform  $\text{H}_2\text{O}_2$  oxidation on the catalyst-coated photoanode than the catalyst alone. The photovoltage of the n-Si/Ni system for  $\text{H}_2\text{O}_2$  oxidation is apparently a negative number ( $\sim -300$  mV), which is not physically meaningful. Because the hole scavenger is serving to enhance charge injection into solution, it is surprising that the photovoltage would change when moving from  $\text{H}_2\text{O}$  to  $\text{H}_2\text{O}_2$  oxidation.

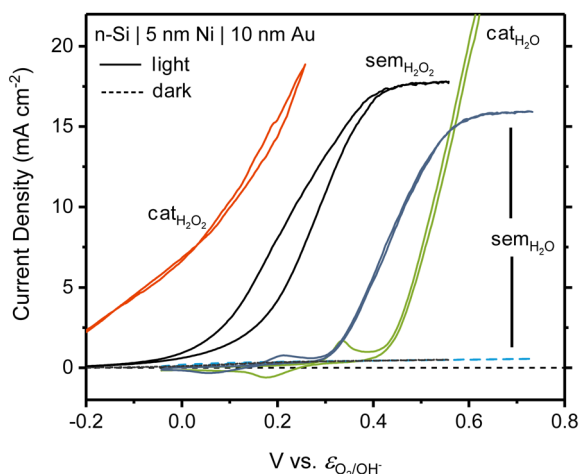


**Figure D.1. Comparison of electrochemical behavior for a n-Si | Ni photoanode with and without a 0.5 M  $\text{H}_2\text{O}_2$  hole scavenger.** All experiments were performed on the same electrode without altering its position relative to the 1 sun solar simulator source. The curves labeled with the  $\text{H}_2\text{O}$  subscript indicate experiments without hole scavenger, whereas the  $\text{H}_2\text{O}_2$  subscript indicates 0.5 M  $\text{H}_2\text{O}_2$  hole scavenger was added to the electrolyte. Curves labeled “sem” indicate that cyclic voltammetry data was collected with the potentiostat controlling potential at the semiconductor back-contact. Curves labeled “cat” indicate that the data was collected by controlling the potential to the secondary Au contact. The two dashed curves represent the *sem* behavior in the dark and show that leakage current is minimal both cases. The difference in OER onset for the  $\text{sem}_{\text{H}_2\text{O}}$  and  $\text{cat}_{\text{H}_2\text{O}}$  is the photoanode’s photovoltage. Unexpectedly, the photovoltage is not retained once  $\text{H}_2\text{O}_2$  is introduced, instead  $\text{cat}_{\text{H}_2\text{O}_2}$  shows a more cathodic current onset for  $\text{H}_2\text{O}_2$  oxidation than  $\text{sem}_{\text{H}_2\text{O}_2}$ .

To deduce why the *apparent photovoltage* changes, we monitor the catalyst electrochemical potential through WE2 while controlling the semiconductor back-contact potential

through WE1 (Figure D.2). From the redox wave in Figure D.1 for  $cat_{H_2O}$ , catalyst oxidation occurs at  $\sim 0.3$  V vs.  $\epsilon_{O_2/OH^-}$  (i.e. where the anodic wave is observed). For  $H_2O$  oxidation through the semiconductor back-contact, the catalyst surface potential passes this oxidation threshold when  $V_{sem} = \sim 0.2$  V vs.  $\epsilon_{O_2/OH^-}$ . This value is consistent with the appearance of the oxidative redox peak and with the 100 mV photovoltage previously discussed. Thus at  $V_{sem} = \sim 0.2$  V vs.  $\epsilon_{O_2/OH^-}$  the catalyst converts to its oxidized NiOOH form. However, for  $H_2O_2$  oxidation through the semiconductor back-contact, the measured catalyst surface potential never passes this oxidation threshold. When the light-limiting photocurrent is reached for  $H_2O_2$  oxidation, the surface potential saturates at  $\sim 0.2$  V vs.  $\epsilon_{O_2/OH^-}$ , 100 mV short of the oxidation threshold. This finding indicates that the catalyst remains in its reduced, electrically insulating  $Ni(OH)_2$  form during  $H_2O_2$  oxidation. Because the hole scavenger readily accepts surface holes, it prevents the catalyst from charging to the electrochemical potential required for catalyst oxidation.

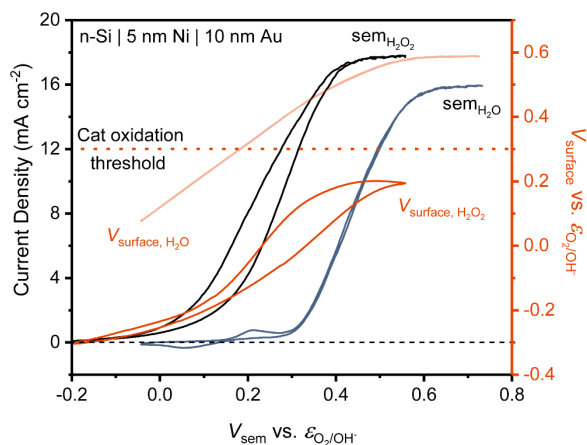


**Figure D.2. Comparison of electrochemical behavior for a n-Si | Ni photoanode with and without a 0.5 M  $H_2O_2$  hole scavenger while sensing the catalyst's electrochemical potential.** The data was collected on the same electrode as in Figure D.1. The curves labeled with the  $H_2O$  subscript indicate experiments without hole scavenger, whereas the  $H_2O_2$  subscript indicates the presence of hole scavenger. Curves labeled “sem” indicate that cyclic voltammetry data was collected with the potentiostat controlling the semiconductor back-contact potential (WE1). Curves labeled  $V_{surface}$ , represent the potential being sensed by the WE<sub>2</sub> gold contact during the experiment. “Catalyst oxidation threshold” is the  $V_{cat}$  value from Figure D.1 where the  $cat_{H_2O}$  oxidative redox peak occurs. The results show that the catalyst is oxidized when the photoanode is used for water oxidation but remains reduced during  $H_2O_2$  oxidation.

The finding that the catalyst remains reduced during  $\text{H}_2\text{O}_2$  oxidation is corroborated by three additional results. First, in Figure D.1 both  $\text{H}_2\text{O}$  oxidation curves exhibit distinct redox peaks associated with the redox chemical conversions of the Ni-based catalyst. For the  $\text{H}_2\text{O}_2$  oxidation curves the redox peaks are absent, suggesting that the catalyst never changes oxidation state in the presence of the hole scavenger. Second,  $\text{NiOOH}$  is known to be less optically transmissive than  $\text{Ni(OH)}_2$ .<sup>156, 157</sup> This fact is reflected in the light-limited photocurrent when controlling the semiconductor back-contact potential. For  $\text{H}_2\text{O}$  oxidation the light-limited photocurrent reaches  $\sim 16 \text{ mA cm}^{-2}$ , whereas it reaches  $\sim 18 \text{ mA cm}^{-2}$  for  $\text{H}_2\text{O}_2$  oxidation (Figure D.2). The difference in the light-limited photocurrent indicates that more light is absorbed in the case of  $\text{H}_2\text{O}_2$  oxidation, which is consistent with retention of the more optically transmissive  $\text{Ni(OH)}_2$  species. Finally, the  $cat_{\text{H}_2\text{O}_2}$  curve in Figure D.1 demonstrates that the catalyst only needs to reach  $\sim 0.2 \text{ V vs. } \epsilon_{\text{O}_2/\text{OH}^-}$  to match the light-limited photocurrent of  $18 \text{ mA cm}^{-2}$  for  $\text{H}_2\text{O}_2$  oxidation and thus satisfy current continuity across the semiconductor/catalyst interface. Because catalyst oxidation does not occur until  $\sim 0.3 \text{ V vs. } \epsilon_{\text{O}_2/\text{OH}^-}$ , the catalyst need not be oxidized during  $\text{H}_2\text{O}_2$  oxidation.

The apparent photovoltage change for the catalyst-coated n-Si discussed above when moving from  $\text{H}_2\text{O}$  to  $\text{H}_2\text{O}_2$  oxidation is attributed to retention of the reduced, insulating catalyst during  $\text{H}_2\text{O}_2$  oxidation. Since  $\text{Ni(OH)}_2$  is much more electrically resistive than  $\text{NiOOH}$ , we hypothesize that the retained  $\text{Ni(OH)}_2$  acts as a charge injection barrier. Photogenerated holes arriving at the  $\text{Ni(OH)}_2$  either experience an  $iR$  loss when passing to the solution interface or must tunnel through the  $\text{Ni(OH)}_2$  prior to  $\text{H}_2\text{O}_2$  oxidation. To support this hypothesis, we repeated the DWE experiments while using a 5-nm-thick Ir metal catalyst deposited by thermal vacuum evaporation. The Ir OER catalyst is selected because its oxidized surface ( $\text{IrO}_x$ ) remains electrically conductive over a wide potential range. As expected, the  $\sim 250 \text{ mV}$  photovoltage exhibited during  $\text{H}_2\text{O}$  oxidation on the Ir-catalyzed system is largely retained during  $\text{H}_2\text{O}_2$  oxidation (Figure D.3). The intrinsic  $\text{H}_2\text{O}_2$  oxidation activity ( $cat_{\text{H}_2\text{O}_2}$ ) measured via the Au WE2 on the n-Si|Ir|Au sample (Figure D.3) is comparable to that measured for the n-Si|Ni|Au same (Figure D.1). Thus, the photovoltage is retained not because of a change in  $\text{H}_2\text{O}_2$  oxidation kinetics when introducing the Ir catalyst. The photovoltage is retained because the Ir-catalyzed  $sem_{\text{H}_2\text{O}_2}$  curve has shifted cathodic of the  $cat_{\text{H}_2\text{O}_2}$  curve. This result shows that without  $\text{Ni(OH)}_2$  present the apparent photovoltage is the same for both  $\text{H}_2\text{O}$  and  $\text{H}_2\text{O}_2$  oxidation. Because the  $\text{H}_2\text{O}_2$  catalyst activities are similar, we conclude that the Ir-catalyst eliminated the charge injection barrier which existed for the Ni-catalyst.

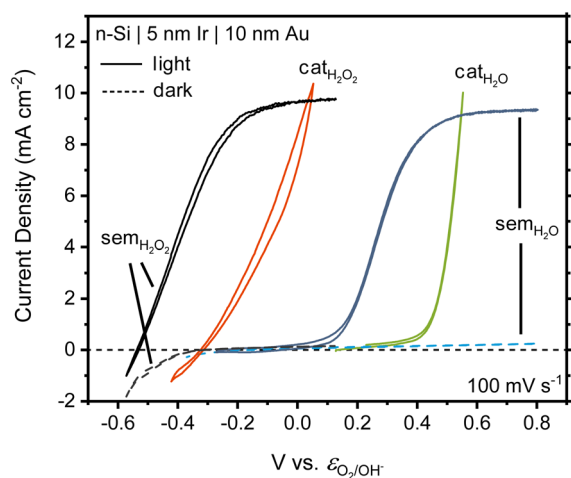


**Figure D.3. Comparison of electrochemical behavior for a n-Si | Ir photoanode with and without a 0.5 M H<sub>2</sub>O<sub>2</sub> hole scavenger.** All experiments were performed on the same electrode without altering its position relative to the 1 sun solar simulator source. The curves labeled with the H<sub>2</sub>O subscript indicate experiments without hole scavenger present, whereas the H<sub>2</sub>O<sub>2</sub> subscript indicates hole scavenger was present. Curves labeled “*sem*” indicate that cyclic voltammetry data was collected by applying the potential to the semiconductor back-contact. Curves labeled “*cat*” indicate that the data was collected by applying the potential to the secondary Au contact. The two dashed curves represent the *sem* behavior in the dark and show that leakage current is minimal. The difference in OER onset for the *sem*<sub>H<sub>2</sub>O</sub> and *cat*<sub>H<sub>2</sub>O</sub> is the photoanode’s photovoltage. The results show that the photovoltage is retained once H<sub>2</sub>O<sub>2</sub> is introduced. In this case, the H<sub>2</sub>O<sub>2</sub> acts to enhance charge injection in to solution at more cathodic potentials without holding the catalyst in a reduced, insulating state.

#### 4. Conclusions

The findings in this work indicate that redox-active catalysts may behave as a charge injection barrier during hole scavenger experiments. This behavior is expected to occur for catalysts where the reduced form is an electronic insulator – a characteristic shared by many common Fe-, Co-, and Ni- based oxy(hydroxide) catalysts.<sup>158-162</sup> For systems where this behavior occurs, calculation of the charge injection efficiency will be inflated because the denominator (hole scavenged activity), assumed to represent quantitative charge injection, may not actually represent quantitative charge injection. Instead, the denominator is the photoanodes behavior in the presence of a charge injection barrier which would not exist under non-scavenger operating conditions. We anticipate that highly engineered systems, with multi-layer catalysts, bay also be affected by the

charge injection barrier described here.<sup>132, 145, 152</sup> This is because the outer levels of the catalyst are at risk of being electronically segregated from the semiconductor's surface during hole scavenger experiments. For these systems, calculation of charge injection efficiency may become a comparison of the highly engineered structure in H<sub>2</sub>O to a much less engineered structure in hole scavenger.

An important generality consideration for the results presented is the lack of a semiconductor | solution interface on the n-Si model system. Because many common photoanode semiconductors (BiVO<sub>4</sub>, Fe<sub>2</sub>O<sub>3</sub>, CuWO<sub>3</sub>) are tolerant of solution contact, solution-permeable catalysts are often electrodeposited.<sup>163</sup> For these systems, it may be that the reduced catalyst simply acts as a spectator while hole scavenger oxidation occurs at the semiconductor | solution interface. Although we do not conclusively answer this question, we did briefly examine Fe<sub>2</sub>O<sub>3</sub> catalyzed by Co-Pi (results in Figure D.S2). The H<sub>2</sub>O<sub>2</sub> oxidation results showed that bare Fe<sub>2</sub>O<sub>3</sub> outperforms Co-Pi catalyzed Fe<sub>2</sub>O<sub>3</sub> at sufficiently cathodic potentials but performs worse at more anodic potentials. If the catalyst were only acting as spectator, we might expect both curves to be identical. A possible explanation for the behavior seen here is that the deposition of the catalyst passivated some surface states, leading to increased activity at sufficiently anodic potentials. However, the reduced catalyst may also act to block a portion of the surface catalytic area (relative to bare Fe<sub>2</sub>O<sub>3</sub>), resulting in lower activity at sufficiently cathodic potentials.

Due to the inability to control for surface state passivation we cannot definitively say how ion permeable catalysts impact hole scavenger results. However, investigators should remain cognizant when interpreting hole scavenger results on catalyzed photoanodes. The results herein show that the presence of a hole scavenger can cause the catalyst to retain a state which differs from its state during comparable H<sub>2</sub>O oxidation experiments. The difference in catalyst state may impact the catalyst's ability to accept photogenerated holes, result in a charge injection barrier and cause a decrease in the photoanode's catalytic active area. For these systems, the charge injection efficiency calculated from the hole scavenger technique will be artificially inflated – with results suggesting that the photoanode is performing closer to perfect charge injection than it is.



### **CHAPTER III: ANALYTICAL AND NUMERICAL APPROACHES FOR MODELING CHARGE TRANSPORT IN PHOTOELECTROCHEMICAL DEVICES**

In the previous chapter the dual-working-electrode technique was used to monitor a catalyst's electrochemical state during photoanode operation. The work investigated two common photoelectrochemical experimental methods and identified how those methods are affected by redox active catalysts. The results suggest that analyzing photocurrent transients (to determine minority carrier lifetimes) and hole-scavenged photocurrents (to determine charge injection efficiency) is not straightforward when redox active catalysts are present. Since many of the best performing photoanodes feature redox active catalysts (e.g. oxides of Ni, Co, and Fe), it is often challenging to understand the role electrocatalysts play in enhancing the oxygen evolution reaction. This is unfortunate because the catalyst's role is heavily contested in the photoanode literature base. Many publications suggest that it collects charge from the semiconductor and then provides a more kinetically facile oxygen evolution route. Others have suggested that its primary role is to passivate defects on the semiconductor surface which would otherwise enhance recombination. Still others have said that it serves to improve band bending within the semiconductor depletion region which improves charge separation. A better understanding of the electrocatalysts role is desirable and would lead to more targeted design principles for improving photoanodes.

The electrocatalysts role in enhancing oxygen evolution has been previously analyzed by the Boettcher lab through numerically modeling current continuity. However, numerical approaches are not ideal because they require significant computational resources (based on iteratively solving coupled differential equations) and may be challenging for researchers without computer science training to implement. This chapter focuses on deriving analytical expressions to describe how electrocatalysts fundamentally enhance photoelectrochemical water oxidation. Particular attention is paid to how the electrocatalyst behaves with and without the presence of semiconductor surface states. Solving the expressions requires limited computational resources and should be significantly more accessible than the previous numerical approach. We anticipate submitting this yet-to-be published manuscript to Physical Review Letters.

Section A, Theory and Simulation for the Effects of Surface States on Charge Transport in Photoelectrochemical Devices, contains co-authored material yet to be published as: Laskowski, F, A, L.; Nellist, M. R.; Dette, C.; Boettcher, S. W. Unified Theory and Simulation for Surface State Influence on Photoelectrodes, In Preparation. (style of Physical Review Letters)

Prof. Boettcher and I conceived of the project. I performed the simulation work and analyzed data with help from M. Nellist and C. Dette. I wrote the paper with help from Prof. Boettcher, initial mathematical direction from T.J. Mills, and editorial assistance from M. Nellist.

## Paper E

### Theory and Simulation for the Effects of Surface States on Charge Transport in Photoelectrochemical Devices

Forrest A. L. Laskowski, Michael R. Nellist, Christian Dette, Thomas J. Mills and Shannon W. Boettcher

#### 1 Introduction

Understanding how electrocatalysts modify the oxygen evolution reaction (OER) on semiconducting photoelectrodes is broadly important in improving photoelectrochemical (PEC) based energy storage solutions. Recent studies have identified similar trends on several semiconductor materials (i.e.  $\text{Fe}_2\text{O}_3$ ,  $\text{TiO}_2$ ,  $\text{BiVO}_4$ , and  $\text{WO}_3$ ) when coated with oxide based electrocatalysts of Co, Ni, Fe, Ga, and Al.<sup>1-14</sup> Addition of this thin oxide overlayer tends to cathodically shift the potential of photocurrent onset and/or increases the maximum photocurrent, leading to greater collection efficiencies. To achieve highly efficient devices, it is important to understand the origin of this behavior and the factors that can lead to its optimization.

Numerous mechanisms have been proposed to explain the oxide's role, each supported by data from a range of analysis methods. It is generally agreed that carrier recombination is the main loss pathway and that the overlayers function to suppress surface recombination, but there are several ways in which this might occur. Transient absorption spectroscopy (TAS) has demonstrated that water oxidation requires the existence of long-lived photogenerated holes in bare  $\text{Fe}_2\text{O}_3$ ,  $\text{TiO}_2$ , and  $\text{WO}_3$ .<sup>15-19</sup> At sufficiently positive biases carrier recombination is reduced because the space charge region is depleted of electrons; consequently, increased photo-generated hole lifetimes promote water oxidation. Experiments involving Co and Ga oxide overlayers, where OER onset is cathodically shifted, suggest that these oxides enhance hole lifetimes.<sup>14, 16, 20</sup> Such a phenomenon could be explained by the semiconductor-oxide interface forming an n-p heterojunction, by the oxide depleting electron density from the semiconductor space charge region, or by the oxide increasing the band bending in the semiconductor; these explanations are not all entirely distinct from one another, but they all imply that the oxide plays a non-catalytic role in facilitating the OER.

It only enhances the oxidation rate indirectly, by modifying the nature of the semiconductor-electrolyte interface.

Other evidence, particularly on Co oxide layers, points towards a catalytic role.<sup>5, 10-11, 21</sup> It has been suggested that Co oxide layers function to increase the kinetics of the OER, by removing the bottleneck of charge transfer to solution. In this view, the overlayer does not modify the energetics of the interface, but functions like a traditional catalyst by speeding up the interfacial charge transfer. By moving positive charge out of the semiconductor this mechanism also has the ultimate effect of decreasing surface recombination. Another view suggests that oxide overlayers chemically passivate semiconductor surface states, thus suppressing surface recombination directly rather than through modifying either the nature of the space charge region or the surface hole concentration.<sup>8-9</sup>

To better understand these mechanisms, we build upon our previous numerical models. Here, we show how semiconductor charge transport can be analytically approximated - removing the need for numerical differential equation solvers. We derive expressions accounting for the presence of surface states which are used to calculate the surface state filling and the potential drop caused by surface charge. We obtain a simple analytical approximation that is easily solved to yield the relevant system energetics and the steady-state  $J(V)$  response. The proposed mechanisms are evaluated in the context of this model to explain the enhancement conferred by the oxide overlayers.

## **2. Model**

### **2.1 Terminology: catalyst sites and surface states**

From a modeling perspective, surface states and catalyst sites are very similar; both can react with electrons and holes in the semiconductor, functioning as recombination centers, and both can transfer charge to the solution, acting as OER sites.<sup>2-3</sup> However, in this work we investigate only catalytic overlayers, so we will use the term “catalyst” to refer to these overlayers, bearing in mind that surface states can also act catalytically. Hence, the main distinguishing feature of surface states and catalyst sites is that surface states are an intrinsic part of the semiconductor material, whereas catalysts form a separate phase attached to the surface, and are often thin, porous overlayers.<sup>5, 13</sup>

We will assume in this work that the catalysts are ion-permeable. Because of this ion permeability, ions from the solution can intercalate into the catalyst and screen the electric field there.<sup>22-23</sup> Thus, the Helmholtz layer and its potential drop occur at the semiconductor surface rather than the catalyst-solution interface. Additionally, we assume that catalyst sites can be screened by

solution ions, but surface states cannot. Surface states often occur in high enough concentration that charging them can affect the Helmholtz potential, thus also altering the potential drop across the semiconductor depletion region and in turn the surface electron and hole concentrations.<sup>24-26</sup>

Further, we exclude transfer directly from semiconductor to solution as this is unlikely to be a significant current source.<sup>5</sup> For simplicity we will assume that the surface states are all at a single energy ( $E_{ss}^o$ ), as is done in the traditional Shockley-Read-Hall surface recombination model.<sup>27-28</sup> We will also treat a one-electron redox reaction instead of the actual four-electron OER to avoid the complications of multi-step reactions. We neglect changes in the flat-band potential by the addition of an overlayer. This is consistent with the use of very thin overlayers where Mott-Schottky analysis has shown that the flat-band potential is not appreciably modified by the addition.<sup>29</sup>

## 2.2 Notation, variables, and parameters

Notations and formalisms for our model are exhaustively described in supporting information E.S1. Electron and hole densities in the semiconductor are labeled  $n$  and  $p$ , respectively, with the subscript  $s$  indicating the value at the semiconductor surface. We generally use overbars (e.g.  $\bar{n}$ ) to indicate equilibrium quantities, but in the case of current densities overbars indicate exchange currents (i.e. the unidirectional equilibrium currents rather than the total equilibrium current, which is zero). Current densities are labeled  $J_{y,z}$ , where current flows from subsystem  $y$  to  $z$ . The subscripts *sem*, *vb*, *cb*, *ss*, *cat*, and *sol* are used as respective abbreviations for the semiconductor, valence band, conduction band, surface states, catalyst, and the solution. Energies and potentials are treated as unitless quantities, reduced by the thermal energy ( $kT$ ) and the thermal voltage ( $kT/q$ ), respectively. The semiconductor interface is at  $x = 0$  and the edge of the depletion region is at  $x = -w$ , where  $w$  is the depletion region width.

## 2.3 Treatment of semiconductor hole transport

It is commonly assumed<sup>2,30</sup> that the surface electrons are at quasi-equilibrium with the bulk ( $E_n \approx 0$ ), and that the hole current ( $J_p$ ) is equal to the Gärtner current ( $J_G$ ).<sup>31</sup> The Gärtner current is an analytical expression which neglects the behavior of the holes in the depletion region, assuming perfect hole conductivity with no limitation. It has been recognized that the Gärtner model is insufficient when the reaction kinetics are slow due to buildup of minority carriers in the depletion region.<sup>32-34</sup>

Our previous work numerically solved the semiconductor transport and continuity equations to obtain the surface hole and electron densities  $p_s$  and  $n_s$ .<sup>23</sup> We found that setting  $J_p = J_G$  is not always a good approximation, particularly for ion-permeable catalysts. This is because, as the catalyst becomes oxidized, there are fewer available neutral sites to oxidize. To sustain the current more holes are required to further oxidize the catalyst, and so a larger  $p_s$  is needed. The semiconductor may not be able to provide enough holes for the current to reach  $J_G$ , in which case the forward current is limited by transport of holes to the interface. This effect is more pronounced in systems with ion-permeable catalysts, because the catalyst can become highly oxidized at much lower biases than in systems with impermeable catalysts.<sup>23</sup>

To account for the hole transport limitation, we require a generalization of the Gärtner model that treats the depletion region. There are two main effects of the buildup of minority carriers in the depletion region: a large diffusional back-current due to the high concentration gradient, and increased recombination in the depletion region. The latter effect has been treated before<sup>33, 35-36</sup> but the analysis is rather involved; here we use a simple approximation of the hole concentration profile to treat depletion region recombination. We discuss the approximation error in supporting information E.S6.

### 2.3.1 The Generalized Gärtner Model

This derivation closely follows the original one by Gärtner.<sup>31</sup> We make two generalizations: (1) the hole concentration at the edge of the depletion region can be non-zero (thereby relaxing Gärtner's fast surface kinetics assumption), and (2) recombination occurs in the depletion region. The full derivation is shown in supporting information E.S5 to illustrate how the generalizations fit naturally into the original treatment.

The hole distribution in the bulk is explicitly computed in supporting information E.S5. In the depletion region, the transport equations can be solved (also see E.S5) to write the hole concentration profile  $p(x)$  in terms of the hole concentration at the edge of the depletion region  $p_w$ ,

$$p(x) \approx p_w e^{-\phi} \quad (1)$$

where  $\phi$  is the electrostatic potential. The error in this approximation is on the order  $\lambda/\delta$ ; thus, this holds when the Debye length is much smaller than the diffusion length. In supporting information E.S6 we show that, even when this assumption is relaxed, the current takes the same form as the original Gärtner current in that it is linear in  $J_G$  and  $p_w$ .

The hole continuity equation is

$$\frac{1}{q} \frac{dJ_p}{dx} = G(x) - R(x) \quad (2)$$

where  $q$  is the elementary charge,  $J_p$  is the hole current,  $G(x)$  is generation, and  $R(x)$  is recombination. Integrating across the depletion region gives,

$$J_p = J_{bulk} + J_{\phi,dep} - J_{R,dep} \quad (3)$$

Where  $J_p = J(0)$  is the total hole current passing through the surface,  $J_{bulk} = J(-w)$  is the hole current from the bulk to the depletion region,  $J_{\phi,dep}$  is the current generated by illumination in the depletion region, and  $J_{R,dep}$  is the depletion recombination current. Assuming quasiequilibrium for holes ( $p_s = p_w e^{V_{sc}}$ ) and solving the differential equations with the boundary conditions  $p(-\infty) = \bar{p}$  and  $p(-w) = p_w$  yields the expression

$$J_p = J_G - \bar{J}_R e^{\bar{V}_{sc} - V_{sc}} \frac{p_s}{\bar{p}_s} \quad (4)$$

where  $V_{sc}$  is the total electrostatic drop across the semiconductor depletion region.  $\bar{J}_R$  is the depletion back-current and recombination current at equilibrium:

$$\bar{J}_R = q \left( \frac{D_p}{\delta} + k_R w \bar{n} \right) \bar{p}_s e^{-\bar{V}_{sc}} \quad (5)$$

where  $D_p$  is the hole diffusion coefficient,  $\delta$  is the hole diffusion length, and  $k_R$  is the second-order recombination constant. (Note that due to the appearance of  $w$ , this quantity is not exactly constant, but can be treated as such for practical purposes.)

The result is the original Gärtner equation modified by two terms that arise from the relaxed assumptions. The first term,  $q D_p \bar{p}_s e^{-\bar{V}_{sc}} / \delta$ , describes the diffusive current of holes back into the bulk and the second term,  $q k_R w \bar{n} \bar{p}_s e^{-\bar{V}_{sc}}$ , describes direct depletion recombination. Since the end outcome of both terms is a recombination event, we refer to them collectively as “depletion

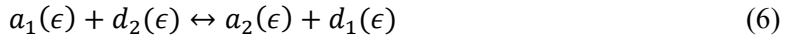
recombination". This generalization of the Gärtner current enables analytical description of the semiconductor transport, generation, and recombination processes.

## 2.4 Interfacial electron transfer: surface states, catalyst, and solution

For simplicity, we use a single-energy surface state model (as in the Shockley-Read-Hall model) and broad density of states (DOS) catalyst and solution models. Interfacial electron transfers are all modeled with second-order reaction kinetics.

### 2.4.1 Electron transfer model

For transfer between subsystems 1 and 2, we write  $d_i(\epsilon)$  for an electron donor species and  $a_i(\epsilon)$  for an electron acceptor species in subsystem  $i$  and electron energy  $\epsilon$ . At each value of  $\epsilon$ , the basic reaction is



with the reaction proceeding to the right representing positive current from subsystem 1 to 2. The current, proportional to the total reaction rate, is computed by integrating the rate densities over the electron energy  $\epsilon$ .

The donor and acceptor distributions can be written as the product of an electronic DOS function  $g_i(\epsilon)$  and an occupancy probability (Fermi-Dirac) function  $f_i(\epsilon)$ , where  $f_i(\epsilon) = 1/(1 + e^{\epsilon - E_i})$ ;

$$d_i(\epsilon) = g_i(\epsilon)f_i(\epsilon) \quad a_i(\epsilon) = g_i(\epsilon)[1 - f_i(\epsilon)] \quad (7)$$

The current integral is then

$$J_{1,2} = q \int k_{1,2}(\epsilon) g_1(\epsilon)g_2(\epsilon)[f_1(\epsilon) - f_2(\epsilon)] d\epsilon \quad (8)$$

The DOS function used for the semiconductor and catalyst are constants; for the surface states, an impulse function [ $g_{ss}(\epsilon) = N_{ss}\delta(\epsilon - E_{ss}^0)$ ]; and for the solution, the large- $\lambda$  limit of the Marcus-Gerischer DOS<sup>37</sup>

$$d_{sol}(\epsilon) = ce^{-(\epsilon-E_{sol})/2} \quad a_{sol}(\epsilon) = ce^{-(E_{sol}-\epsilon)/2} \quad (9)$$

We define  $s$  and  $s^+$  for the neutral and oxidized surface state concentrations, respectively. We define  $c_{ss}$  and  $c_{ss}^+$  for the neutral and oxidized occupation of catalyst sites at energy  $E_{ss}^o$ .

#### 2.4.2 Interfacial currents

The reaction of semiconductor holes and electrons with surface states is described by,

$$J_{vb,ss} = \bar{J}_{vb,ss} \left( \frac{p_s s}{\bar{p}_s \bar{s}} - \frac{s^+}{\bar{s}^+} \right) \quad (10)$$

$$J_{cb,ss} = \bar{J}_{cb,ss} \left( \frac{s}{\bar{s}} - \frac{n_s s^+}{\bar{n}_s \bar{s}^+} \right) \quad (11)$$

Reaction of surface states with catalyst and solution must consider that the surface states are at an electrostatic potential  $+V_H$  with respect to the catalyst and solution (see supporting information E.S2); this shift puts the surface state energy at  $E_{ss}^o = \bar{E}_{ss}^o + V_H$ . The current then depends on the surface state concentration and the catalyst occupancy at energy  $E_{ss}^o$ :

$$J_{ss,cat} = \bar{J}_{ss,cat} \left( \frac{s^+ c_{ss}}{\bar{s}^+ \bar{c}_{ss}} - \frac{s c_{ss}^+}{\bar{s} \bar{c}_{ss}^+} \right) \quad (12)$$

Current flow from surface states to the solution is

$$J_{ss,sol} = \bar{J}_{ss,sol} \left( \frac{s^+}{\bar{s}^+} e^{\Delta V_H/2} - \frac{s}{\bar{s}} e^{-\Delta V_H/2} \right) \quad (13)$$

where  $\Delta V_H$  represents deviation from equilibrium for the Helmholtz potential.

The expressions we used previously<sup>23</sup> to model the current between semiconductor and ion-permeable catalyst are modified to account for the electrostatic potential drop between the semiconductor surface and the catalyst:

$$J_{vb,cat} = \bar{J}_{vb,cat} \left( \frac{p_s}{\bar{p}_s} - e^{-\Delta V_H - E_{cat}} \right) \quad (14)$$



$$J_{cb,cat} = \bar{J}_{cb,cat} \left( e^{\Delta V_H + E_{cat}} - \frac{n_s}{\bar{n}_s} \right) \quad (15)$$

The catalyst-solution current is modeled by

$$J_{cat,sol} = \bar{J}_{cat,sol} \left( e^{\frac{E_{cat}}{2}} - e^{-\frac{E_{cat}}{2}} \right) \quad (16)$$

which does not depend on  $V_H$  because the catalyst and solution always remain at the same electrostatic potential. These interfacial current expressions are all derived by evaluating the current integral Eq. (9); see supporting information E.S4 for explicit derivations and exchange current definitions.

## 2.5 Solution to the model equations

There are four variables in the model:  $p_s$ ,  $E_{ss}$ ,  $E_{cat}$ , and  $V_H$ . To obtain a solution, four equations are required - the electroneutrality condition

$$q_{sc} + q_{ss} = q_H \quad (17)$$

and the subsystem current continuity conditions

$$J_{vb,ss} + J_{cb,ss} = J_{ss,cat} + J_{ss,sol} \quad (18)$$

$$J_{vb,cat} + J_{cb,cat} = J_{ss,cat} + J_{cat,sol} \quad (19)$$

$$J_p = J_{vb,ss} + J_{vb,cat} \quad (20)$$

where  $J_p$  is defined in Eq. (4). Solving this system presents numerical challenges in that variables may vary by many orders of magnitude. The method we adopted is to numerically approximate the equilibrium Helmholtz potential and open-circuit voltage, begin the numerical solution at this applied bias with all potentials set to zero, then scan the applied bias in small increments away from there, using the previous solution as an initial guess for the next step. More details and a

Mathematica implementation of this algorithm are included in the supporting information sections E.S8 and E.S14.

### 3 Results and Discussion

#### 3.1 Non-ideal photodiodes

The addition of depletion recombination decreases the maximum current obtainable from the semiconductor under otherwise ideal conditions (i.e. fast OER kinetics at the surface states and/or catalyst). Before discussing the roles of surface states and catalyst, we analyze the deviation of the semiconductor response from its ideal behavior.

The ideal photodiode equation is a simple model that describes the  $J(V)$  behavior obtained from an ideal system (fast hole transfer from the semiconductor and fast OER kinetics),

$$J_{id} = J_G - \bar{J}_{cb,sol} e^{-V} \quad (21)$$

which results from assuming a constant forward hole current  $J_G$  (ignoring depletion recombination), quasiequilibrium of electrons in the semiconductor, and quasiequilibrium of the surface states and catalyst with the solution, where  $\bar{J}_{cb,sol} = \bar{J}_{cb,ss} + \bar{J}_{cb,cat}$  is the effective exchange current. It provides a simple means of estimating  $V_{oc}$ ,

$$V_{oc}^{(0)} \approx -\ln\left(\frac{J_G}{\bar{J}_{cb,sol}}\right) \quad (22)$$

However, in the presence of depletion layer recombination, the hole current must be modified according to the generalized Gärtner model, Eq. (4). This gives the “non-ideal” photodiode equation,

$$J_{n-id} = \frac{J_G}{1 + (\bar{J}_R/\bar{J}_{vb,sol})e^{-V}} - \bar{J}_{cb,sol} e^{-V} \quad (23)$$

which is shown in Figure E.1 for various values of  $\bar{J}_R/\bar{J}_{vb,sol}$ . This is the highest current obtainable from the semiconductor in the presence of depletion recombination. Including this effect leads to a shift of  $V_{oc} \approx V_{oc}^{(0)} + V_{oc}^{(1)}$ , where

$$V_{oc}^{(1)} = -\ln \left[ \left( \sqrt{\frac{1}{4} + \frac{J_G \bar{J}_R}{1 + \bar{J}_{vb,sol} \bar{J}_{cb,sol}}} - \frac{1}{2} \right) \cdot \left( \frac{\bar{J}_{vb,sol} \bar{J}_{cb,sol}}{J_G \bar{J}_R} \right) \right] \quad (24)$$

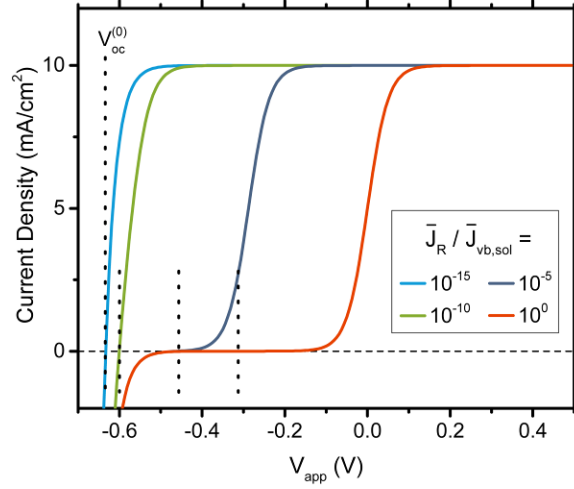


**Figure E.1. Response for a “non-ideal” photodiode.** The limiting current obtainable from a fast catalyst, for different values of  $\bar{J}_R/\bar{J}_{vb,sol}$  (marked).

Note that the decrease in current is not due to changes in band bending; it is due only to increased recombination in the depletion region.

### 3.2 Basic transfer models

We begin by investigating the transfer mechanisms of two simplified systems: sem|cat|sol (no surface states) and sem|ss|sol (no catalyst). We show that these correspond to the adaptive and metallic models we previously defined in our simulation work.<sup>23</sup>

#### 3.2.1 Adaptive catalysts — no surface states

First, we examine the model without surface states. The catalyst potential shifts to accommodate slower catalysts (smaller  $\bar{J}_{cat,sol}$ ), until depletion recombination sets in and decreases the hole current, as can be seen in Figure E.2. With high values of  $\bar{J}_{cat,sol}$ ,  $E_{cat}$  remains close to  $E_{sol}$ . As  $\bar{J}_{cat,sol}$  decreases, the catalyst potential shifts to increase the reaction rate and compensate for the slower kinetics. However, at sufficiently low  $\bar{J}_{cat,sol}$  values, the attainable current is limited by the rate of hole transfer out of the semiconductor (i.e. where  $E_{cat}$  approaches  $E_{p,s}$ ). When the surface hole density becomes sufficiently large, depletion recombination leads to a much slower

$E_{cat}$  increase for any positive  $\Delta V_{app}$ ; this in turn limits  $E_{cat}$  and therefore limits the total current at a given  $V_{app}$ .

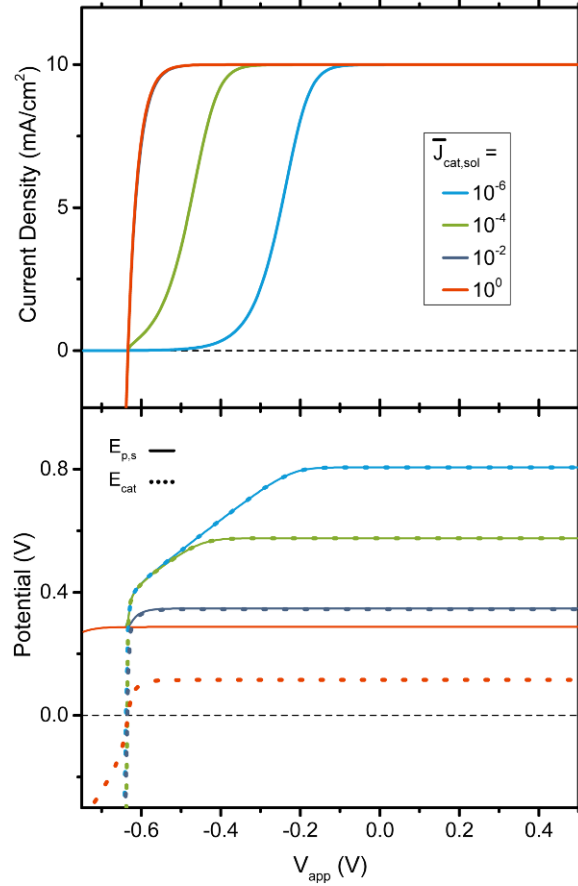


**Figure E.2. Adaptive catalyst model. (top)  $J(V)$  curves for varying values of  $\bar{J}_{cat,sol}$ . (bottom)  $E_{p,s}$  and  $E_{cat}$  corresponding to the curves above.**

The key potentials can be quantified. When  $V_{app}$  is high enough to obtain  $J = J_G$ ,  $E_{cat}$  levels off to a constant value,

$$E_{cat}[J_G] \approx 2 \ln \left( \frac{J_G}{\bar{J}_{cat,sol}} \right) \quad (24)$$

However, the bias at which this potential is reached is limited by depletion recombination. When depletion recombination occurs, the maximum  $E_{cat}$  at bias  $V$  is

$$E_{cat}[max] \approx V + \ln\left(\frac{J_G}{\bar{J}_R}\right) \quad (25)$$

When depletion recombination occurs, the current will not reach  $J_G$  until the bias reaches

$$V_{app}[J_G] = \ln\left(\frac{J_G^3}{\bar{J}_R \bar{J}_{cat,sol}^2}\right) \quad (26)$$

At high values of  $\bar{J}_{cat,sol}$ , the surface hole concentration is determined by whatever is necessary to pass current  $J_G$  from the valence band to the catalyst,

$$E_p[min] = \ln\left(\frac{J_G}{\bar{J}_{vb,cat}}\right) \quad (27)$$

However, when the catalyst is slow, a greater hole concentration is necessary to reach  $J_G$ . In this case  $E_{p,s}$  tends to  $E_{cat}[J_G]$ ; in fact, from interpolation between the minimum value and  $E_{cat}$  we can write

$$E_{p,s} \approx \ln\left[\frac{J_G}{\bar{J}_{vb,cat}} + \left(\frac{J_G}{\bar{J}_{cat,sol}}\right)^2\right] \quad (28)$$

A crucial aspect of adaptive catalysts, that allows them to respond so effectively to a low  $\bar{J}_{cat,sol}$ , is that  $E_{cat}$  can swing very quickly from negative to positive values near  $V_{oc}$ . Indeed,  $E_{cat}$  ( $V_{app} > V_{oc}$ ), sans depletion recombination is

$$E_{cat}[V_{app}] \approx 2\ln\left(\frac{J_G - \bar{J}_{cb,cat}e^{-V_{app}}}{\bar{J}_{cat,sol}}\right) \quad (29)$$

This function swings very rapidly from negative values to  $E_{cat}[J_G]$  as  $V_{app}$  passes through  $V_{oc}$ , as reflected in Figure E.2. The results are analogous to the simulation work in our previous publication<sup>23</sup>, but here we note that the depletion recombination is analytically treated. This allows us to explicitly assign the performance limitation, due to depletion recombination, to the region of decreased slope in Figure. E.2 (bottom).

### 3.2.2 Unscreened metallic surface states – no catalyst

In many systems with surface states, particularly those with lower redox potentials ( $E_{SS}^0 < E_{sol}$ ), the states will always be partially filled. When this excess charge cannot be screened by ions (as with surface species embedded in the semiconductor rather than surface-attached species), they will produce a substantial Helmholtz potential. Consequently, band bending in the semiconductor is reduced, leading to more electron and less hole current.

The presence of the surface states causes the system to act in many ways analogously to dense metallic Schottky junctions. For these, a large density of states resides at an electrochemical potential which is essentially controlled by the electrostatic potential  $V_H$ . This is the same physical situation as found for impermeable catalysts, which also contain a large quantity of unscreened charge states and hence can only be affected by a change in the electrostatic potential drop between the catalyst and the solution.

The equilibrium Helmholtz potential  $\bar{V}_H$  is always greater than  $\bar{E}_{SS}^0$ , the amount depending on  $N_{SS}$ . This potential is essentially lost to the system, in that the equilibrium barrier height is reduced by  $\bar{V}_H$ . This leads to a shift in  $V_{oc}$  and the  $J(V)$  response, as seen in Figure E.3 (top). Hence, these systems behave in the same way as those with a dense metallic catalyst whose Fermi level differs from the solution potential by the amount  $\bar{V}_H$ .

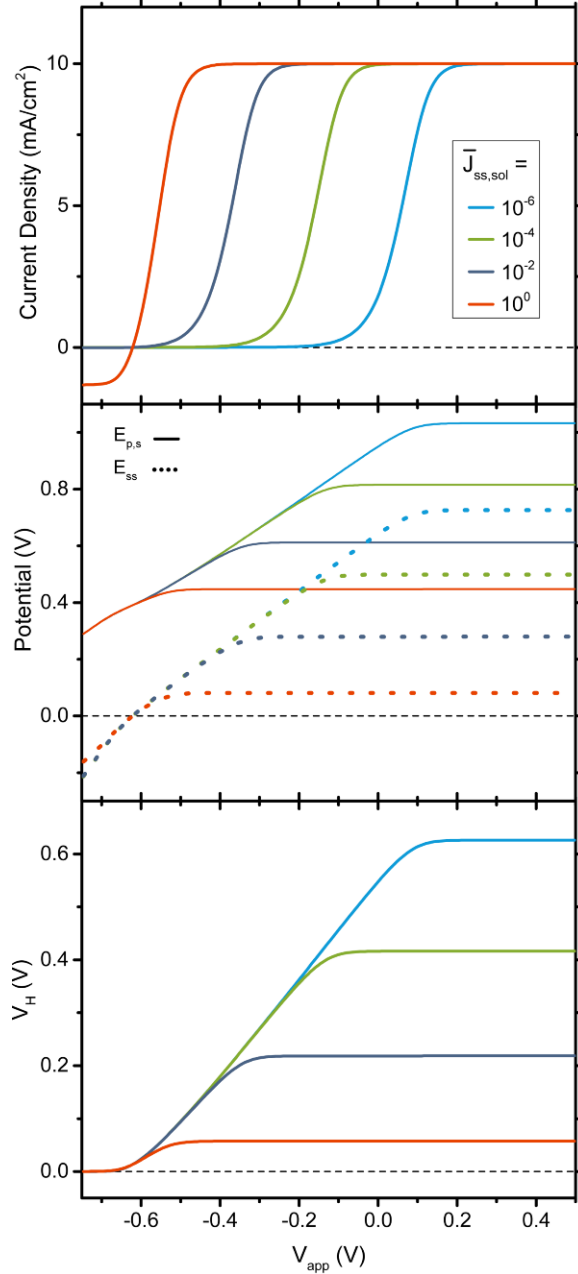


**Figure E.3. Metallic surface state behavior.** (top)  $J(V)$  curves for varying values of  $\bar{J}_{ss,sol}$ . (middle)  $E_{p,s}$  and  $E_{ss}$  corresponding to the curves above. (bottom)  $V_H$  the corresponding to the same.

The decreased band bending in systems with metallic behavior leads to an earlier onset of electron current as  $\bar{J}_{ss,sol}$  decreases, because of the greater electrostatic potential required to drive the reaction. Before the current reaches  $J_G$ , we have

$$V_H \approx V_{app} + \ln\left(\frac{J_G}{\bar{J}_{cb,ss}}\right) = V_{app} + V_{oc} \quad (30)$$

In this regime,

$$E_{ss} \approx E_{ss}^o - V_H + \ln\left(\frac{N_{ss}}{c_H V_H} - 1\right) \approx V + V_{oc} - \bar{V}_H + \ln[E_{ss}^o(V + V_{oc})] \quad (31)$$

This small deviation from  $V + V_{oc} - \bar{V}_H$  is visible in Figure E.3 (middle), and represents the minor deviation from our previous impermeable catalyst model. It is a result of the interaction between charge neutrality and catalyst kinetics.

In other respects, it behaves like the metallic model, except that the transfer coefficient in this case is 1 instead of 1/2 due to the localized DOS. The potential at  $J = J_G$  is

$$E_{ss} = E_{ss}^o + \ln\left(\frac{\bar{J}_{ss,sol} e^{-\Delta V_H} (1 + e^{E_{ss}^o})}{J_G} - 1\right) \quad (32)$$

and the bias required to reach this current is

$$V = \bar{V}_H + \ln\left[\frac{\bar{J}_{ss,sol} \bar{J}_{cb,ss}}{J_G^2} \left(\frac{s^+}{\bar{s}^+}\right)\right] \quad (33)$$

In supporting information E.S7 we derive a model for the surface state mediated recombination current ( $J_r^{ss}$ ). Recombination increases as  $\bar{J}_{ss,sol}$  decreases, because the smaller  $V_{sc}$  promotes electron current (supporting information E.S11). Note that there is substantial recombination current even when the total current is near zero; in this regime, the electron current is balanced by the hole current, so all of it results in surface recombination.

### 3.3 Full transfer models

We now study the interaction between the surface states and catalyst overlayer by examining the system where  $\bar{J}_{ss,sol} = 10^{-2} \text{ mA cm}^{-2}$ , from the unscreened surface state (metallic) model above (Figure E.3), and adding a catalyst overlayer to it. We discuss two behavior regimes to demonstrate the interaction effects: a regime in which the catalyst operates primarily in series with the surface states and one in which it operates in parallel.



### 3.3.1 Series behavior — surface-state mediated transfer

First, we investigate a “series” catalyst, one where charge transfer between the surface states and catalyst is facile. Here we assume that  $\bar{J}_{ss,cat}$  is large, so that the surface states and catalyst are at quasiequilibrium. This is reflected in the equality of Fermi levels,  $E_{ss} = E_{cat}$ , as evident in Figure E.4 (middle). Because quasiequilibrium exists we term this surface state-mediated transfer.<sup>38</sup>

The results are shown in Figure E.4. With a slow catalyst (sky blue curve), the result is essentially the same as that obtained in the metallic model (Figure E.3). As  $\bar{J}_{cat,sol}$  is increased, the total current tends toward the limiting curve of high  $\bar{J}_{cat,sol}$  in the adaptive model.

Since the catalyst is at quasiequilibrium with the surface states, and functions in series with them, the catalyst effectively increases the rate of transfer from surface states to solution, i.e. increases the effective value of  $\bar{J}_{ss,sol}$ :

$$\bar{J}_{ss,sol}[eff] = e^{\Delta V_H} J_G S^+ \left( 1 + \frac{e^{E_{cat}}}{e^{E_{ss}^o}} \right) \quad (34)$$

In the metallic model, slow  $\bar{J}_{ss,sol}$  values resulted in surface state mediated recombination. Here, the quicker catalysts “harvest” some of the holes and prevent recombination by transfer into the solution. For slower catalysts, the surface states act as a “hole sink” (Figure E.4 – bottom), serving as recombination centers for conduction band electrons and catalyst holes.

The driving force for catalysis is dependent on the ratio of  $\bar{J}_{ss,sol}$  to  $\bar{J}_{cat,sol}$  (supporting information E.S13). With the lowest value of  $\bar{J}_{cat,sol}$ , the current is all produced by the surface states. In the next (green) curve, the catalyst is carrying nearly 1/4<sup>th</sup> of the total current, the rest provided by the surface states. As  $\bar{J}_{cat,sol}$  increases further, however, practically all the current is carried by the catalyst, and the curves tend toward the ideal photodiode curve, with the barrier height reduced by  $\bar{V}_H$  as discussed in Sec 3.2.2.

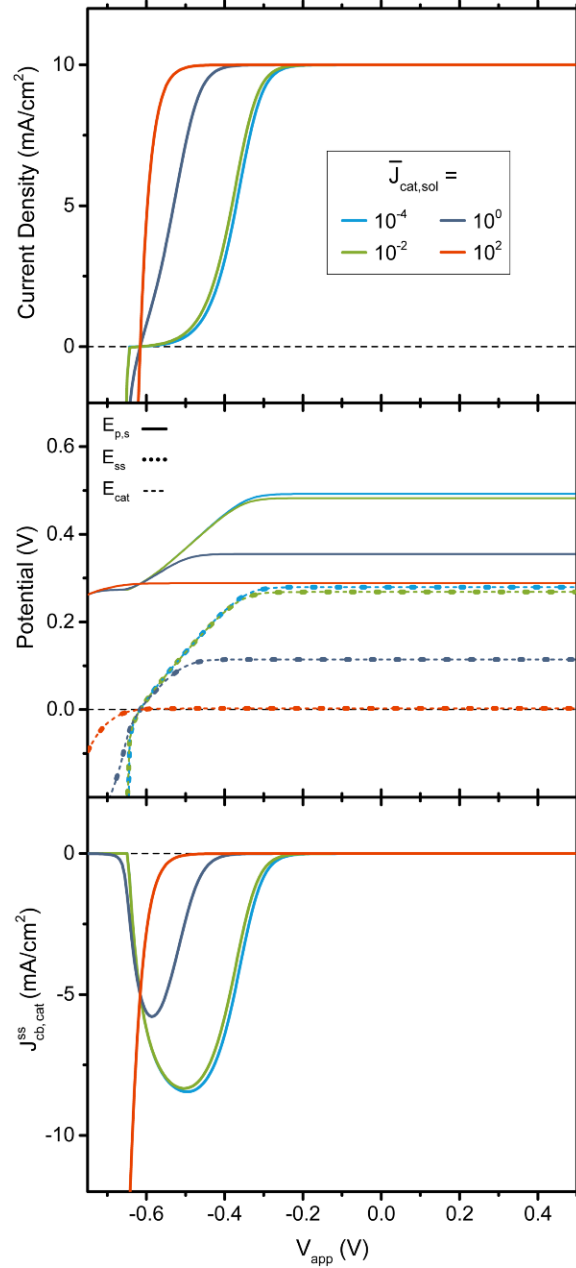


**Figure E.4. Full model – series behavior where  $\bar{J}_{cat,sol}$  is fixed at  $10^{-2} \text{ mA}\cdot\text{cm}^{-2}$ .** (top)  $J(V)$  curves for varying values of  $\bar{J}_{cat,sol}$ . (middle)  $E_{p,s}$ ,  $E_{cat}$  and  $E_{ss}$  corresponding to the curves above. (bottom) Surface state mediated current between the cb and catalyst. Derived in supporting information E.S7.

The maximum attainable  $V_{oc}$  for this system is still limited by the equilibrium Helmholtz potential  $\bar{V}_H$ . Because the catalyst is effectively only increasing the rate of transfer from surface states to solution, there is no mechanism by which it can alter  $\bar{V}_H$ . So while the catalyst can increase

the effective exchange current between surface states and solution, thereby increasing the total current, it cannot increase the attainable photovoltage or  $V_{oc}$ .

### 3.3.2 Parallel effect — compensating for $V_H$

We now discuss “parallel” effects of the catalyst, where ss-cat transfer is negligible, but semiconductor-catalyst transfer is comparable to the rate of semiconductor-surface state transfer.

The total current  $J$  is shown in Figure E.5 (top). With a small value of  $\bar{J}_{cat,sol}$ , the system behaves like the parent curve in the metallic model. However, even with a low value of  $\bar{J}_{cat,sol}$ , a small current is passed through the catalyst (supporting information E.S12). Comparing the  $\bar{J}_{cat,sol} = 10^{-2}$  curve in the parallel model against the series model reveals higher performance in the parallel model (Figures E.4 and E.5 – top). This occurs because, without quasiequilibrium between the surface states and catalyst (Figure E.5 – middle), the surface states no longer act as a hole sink. Instead, in the slower two curves catalysis is predominantly driven through the surface states (supporting information E.S12). Whereas in the quicker curves, the catalyst harvests most holes and then never equilibrates with the surface state Fermi level. For this latter behavior, the system acts as in the adaptive catalyst model (Sec 3.2.1), where  $E_{cat}$  remains below  $E_{p,s}$  for sufficiently quick kinetics (Figure E.5 – middle).

When catalyst kinetics are slow, the accumulation of holes in the surface states leads to surface state mediated recombination (Figure E.5 – bottom). These curves approach the limit given by the parent curve in the metallic model (supporting information E.S11). The surface states result in a unique effect in that the catalyst Fermi level behaves as if it were dependent on the Helmholtz potential. As the surface states fill, the Helmholtz potential shifts both  $E_{p,s}$  and  $E_{ss}$  to higher potentials. Since the surface states cannot deload the catalyst, sufficiently slow catalysts will remain in quasiequilibrium with  $E_{p,s}$  and will also experience this potential shift.

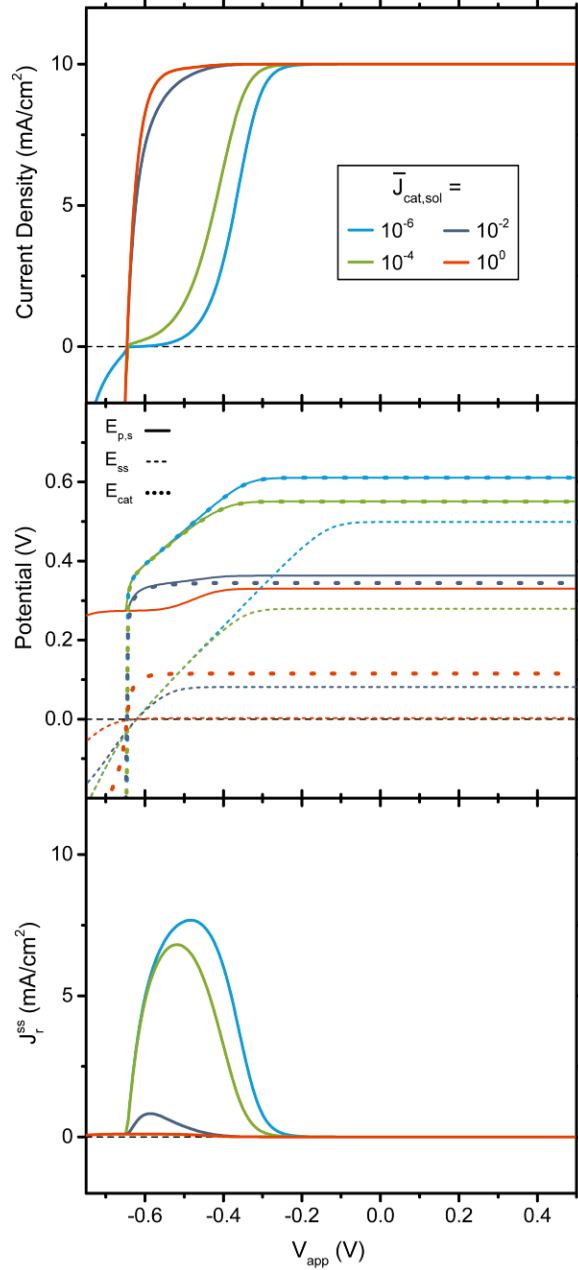


**Figure E.5. Full model – parallel behavior where  $\bar{J}_{cat,sol}$  is fixed at  $10^{-2} \text{ mA}\cdot\text{cm}^{-2}$ . (top)  $J(V)$  curves for varying values of  $\bar{J}_{cat,sol}$ . (middle)  $E_{p,s}$ ,  $E_{cat}$  and  $E_{ss}$  corresponding to the curves above. (bottom) Surface state mediated recombination. Derived in supporting information E.S7.**

When catalyst kinetics are quick, the system circumvents the  $\bar{V}_H$  limitation from the metallic model. Despite the existence of a non-negligible Helmholtz potential (supporting information E.S12), since the catalyst need not equilibrate with the surface states, it circumvents the  $\bar{V}_H$  limitation by transitioning to a potential where current continuity is achieved. As in the

adaptive model, this transition is limited by depletion recombination when  $E_{p,s}$  is sufficiently large (supporting information E.S12) Thus, unlike the series regime, parallel catalyst behavior can improve the attainable photovoltage or  $V_{oc}$ , but this affect is limited by depletion recombination.

#### 4 Conclusion

We have developed a simple analytical model for predicting the impacts of surface states on photoanodes. This work is an improvement, over our previous modeling efforts, on three accounts: (1) The analytical solution is solved in a trivial amount of time (seconds) compared to the days oftentimes required for differential equation based numerical methods.<sup>23</sup> (2) The modeling approach is sufficiently simplistic such that investigators can adapt it without already possessing extensive computer programing knowledge. (3) The results corroborate our previously defined “adaptive” and “metallic” models while also accounting for the additional complexity of surface states.

We have defined two regimes for surface state behavior. For surface states behaving in series with the catalyst, the surface states will tend to act as a “hole sink”. As the catalyst is oxidized, its quasiequilibrium condition with the surface states requires that it simultaneously charge the surface states. This surface state filling increases surface state mediated recombination, increases the Helmholtz potential, and limits both  $E_{p,s}$  and  $E_{cat}$ . Presence of surface states result in an increased  $V_{app}$  requirement to reach  $J_G$ , as compared to a photoanode with no surface states and an equivalent  $\bar{J}_{cat,sol}$ .

For surface states behaving in parallel with the catalyst,  $J(V)$  performance compares more favorably to the equivalent system without surface states. Although a Helmholtz electrostatic increase is also realized in this system, the catalyst Fermi level is not directly limited by surface state recombination. Growth in the catalyst Fermi level is predominantly inhibited by depletion recombination, as in the adaptive model. For this reason, at  $\bar{J}_{cat,sol} = 10^{-2}$  mA cm<sup>-2</sup>, the parallel system exhibits near ideal-diode  $J(V)$  behavior, whereas the series model exhibits a significant cathodic shift. In effect, surface states which act in parallel can be compensated for by a sufficiently fast adaptive catalyst. The fast catalyst enables the system to ignore the performance reducing effects that would otherwise be caused by the increased Helmholtz potential.

In real devices, these two behavior regimes operate in tandem - the degree depending on the  $\bar{J}_{ss,cat}$  exchange current. For a photoanode with sufficient surface states, a catalytically poor catalyst coating may outperform a catalytically superior coating, simply by limiting  $\bar{J}_{ss,cat}$ . In terms of the proposed mechanisms (introduction), a catalyst with poor OER kinetics tends to confer no

benefit to the system. However, we note that this would change if the equilibrium band bending was influenced by the addition of the overlayer and/or if addition chemically passivated surface states. Without these effects, the addition of the oxide overlayer improves the current only when catalyst kinetics are sufficiently large. This improves the current (in the series model) by increasing transfer from the surface states to the solution, and improves the  $V_{oc}$  (in the parallel model) by effectively bypassing the Helmholtz potential.

## CHAPTER IV: IDENTIFYING NANOSCALE PHENOMENA AT PHOTOELECTROCHEMICAL INTERFACES: THE PINCH-OFF EFFECT

In the previous chapter analytical expressions were developed which ultimately describe charge transport through semiconductor/catalyst/solution interfaces. Charge transport can also be examined experimentally with the previously described dual-working-electrode (DWE) technique. A key strength of the DWE technique is that the semiconductor/catalyst interfacial behavior can be monitored during photoanode operation. That is, the bias across the interface and the current passing through it are directly observable. These observations are valuable because the semiconductor/catalyst interface is thought to play a significant role in charge separation. In this chapter, the DWE technique is applied to understand the semiconductor/catalyst interface of two model systems which exhibit unexpected oxygen evolution performance. In the first model system, photoanodes comprised of a 3-nm-thick Ni film evaporated onto n-Si exhibit significantly better photocurrent onsets ( $\sim 300$  mV) than photoanodes with a 20 nm Ni film. In the second model system, photoanodes formed from a 5-s electrodeposition of Ni nanoislands onto n-Si exhibit significantly better photocurrent onsets ( $\sim 300$  mV) than photoanodes with a 60-s electrodeposition. The difference in onset is surprising because, in each case, the photoanodes with more electrocatalyst on the surface exhibit significantly diminished photocurrent onset potentials.

The results of these two studies indicate that the “pinch-off” effect explains the unexpected photocurrent onset behavior. The pinch-off effect is a phenomena in which semiconductor/catalyst junctions with poor charge selectivity (i.e. low barrier heights) become more selective through interaction with adjacent high barrier regions. In the first body of work, published in *Energy and Environmental Science*, the thinnest Ni films age during photoelectrochemical cycling to produce a heterogenous interface. Some regions of this interface retain the original n-Si/Ni character (low barrier) while other areas evolve to n-Si/SiO<sub>x</sub>/NiOOH interfaces (larger barrier). Charge primarily travels through the n-Si/Ni interfaces but the selectivity is enhanced via pinch-off caused by the n-Si/SiO<sub>x</sub>/NiOOH interfaces. In the second body of work, currently in review at *Nature Materials*, the pinch-off effect is more rigorously analyzed by using potential-sensing electrochemical atomic force microscopy (PS-EC-AFM) to directly examine the selectivity of single nanojunctions formed between n-Si and variably-sized Ni islands. During photoelectrochemical cycling a portion of the Ni island is converted to Ni(OH)<sub>2</sub>/NiOOH and this forms a high barrier n-Si/SiO<sub>x</sub>/NiOOH interface surrounding the n-Si/Ni interface. By PS-EC-AFM the photovoltages produced by individual nano-interfaces are shown to increase as the island radii decreases, a result consistent with analytical descriptions of the pinch-off effect. Discovering that the pinch-off effect is responsible for the

unexpected oxygen evolution performance in these two cases suggests that the effect could be used to design improved photoanodes.

Section A, Junction Behavior of n-Si Photoanodes Protected by Thin Ni Elucidated from Dual Working Electrode Photoelectrochemistry, contains co-authored material published as: Laskowski, F. A. L.; Nellist, M. R.; Venkatkarthick, R.; & Boettcher, S. W. Junction Behavior of n-Si Photoanodes Protected by Thin Ni Elucidated from Dual Working Electrode Photoelectrochemistry. *Energy & Environmental Science*, 10(2), 570579 (2017).

Section B, Nanoscale Semiconductor/Catalyst Interfaces in Photoelectrochemistry, contains co-authored material currently under review as: Laskowski F. A. L.; Oener, S. Z.; Nellist M. R.; Gordon, A. M.; Bain, D. C.; Fehrs, J. L.; Boettcher S.W. Nanoscale Semiconductor/Catalyst Interfaces in Photoelectrochemistry, Under Review at *Nature Materials*.

Prof. Boettcher and I conceived of the projects. I performed and directed experiments. I collected data with help from S. Oener, D. Bain, M. Nellist, and A. Gordon. I analyzed data with help from the aforementioned, as well as R. Venkatkarthick and J. Fehrs. I wrote the papers with help from Prof. Boettcher and editorial assistance from all authors.

## Paper F

### Junction Behavior of n-Si Photoanodes Protected by Thin Ni Elucidated from Dual Working Electrode Photoelectrochemistry

Forrest A. L. Laskowski, Michael R. Nellist, Radhakrishnan Venkatkarthick, and Shannon W. Boettcher\*

#### Broader Context

Si is a desirable photoanode material for use in photoelectrochemical water-splitting devices. However, Si self-passivates during the oxygen evolution half reaction and requires a protection layer to maintain high photoanodic efficiency. Thin evaporated metallic Ni layers have been reported to protect Si while also enhancing the kinetics for oxygen evolution. Maximizing performance of these and related protected/catalyzed semiconductors requires a fundamental understanding of the semiconductor | catalyst | solution interface. We use dual-working-electrode (DWE) photoelectrochemistry measurements to directly measure the interface's electronic properties *in situ* during operation. By controlling the Ni thickness (3, 5, and 20 nm), we confirm that favorable shifts in photocurrent onset are correlated with thinner protection layers.



Photoelectrochemical DWE measurements are used to test various prevailing hypotheses for the origin of this behavior. We find evidence that increased photovoltage is due to the development of a spatially inhomogeneous buried junction wherein high barrier regions arise via adventitious SiO<sub>2</sub> growth. Thinner protection layers more readily promote this behavior by facilitating solution permeation to the n-Si | Ni interface. Repeated electrochemical cycling of thicker catalyst layers can achieve similar behavior and improve the photocurrent onset by as much as 300 mV. The results are discussed in the context of the general design principles for metal-insulator-semiconductor protected photoanodes.

Tandem photoelectrochemical water splitting devices rely on integration of a photoanode and a photocathode for solar energy conversion to a storable chemical fuel such as H<sub>2</sub> gas. These photoelectrodes must be simultaneously efficient and stable over the required device lifetime to meet cost targets. To date, efficiency losses at the photoanode have been considered the limiting factor in fabricating an efficient tandem cell. Si is a near-ideal solar material, which could be employed in an efficient photoanode to overcome these limitations. However, Si self-passivates under oxygen evolution conditions, forming an electronically insulating oxide. Recent work has demonstrated that ultrathin Ni metal layers can protect n-Si photoanodes and simultaneously enhance catalytic activity for the oxygen-evolution half-reaction. Sufficiently thin Ni protection layers have been shown to yield enhanced photocurrent onsets, and thus performance, by providing an anomalously large photovoltage relative to thicker layers. Using new dual-electrode photoelectrochemical techniques, we provide a fundamental picture of the operational mechanisms of these devices while highlighting the underlying design principles and tradeoffs. This mechanistic insight is important in future device design for protected and catalyzed semiconductor photoelectrodes.

## 1. Introduction

Solar water splitting to produce H<sub>2</sub> allows for the direct capture and storage of solar energy. Identification of materials that are both stable and efficient remains a key challenge, particularly for the oxygen evolution half reaction (OER). Stable photoanode materials, such as Fe<sub>2</sub>O<sub>3</sub> or TiO<sub>2</sub>, suffer from low photovoltages, photocurrents, or both, that severely limit water-splitting efficiency.<sup>1</sup> Use of traditional high-quality semiconductors, such as Si or GaAs, is limited by inherent material instabilities in aq. electrolyte or under OER conditions.<sup>2-7</sup> To address stability limitations, protective films which segregate unstable semiconductors from solution have been developed.<sup>5,8-14</sup> Ideally, protective films facilitate charge transport without impeding photoanode efficiency; in practice, films can introduce optical losses and electrical series resistance. The

addition of new layers can further affect interfacial recombination processes (e.g. at defects) and interfacial band alignment, and these effects could be spatially heterogeneous. To improve protected photoanodes the fundamental understanding of light-absorbing semiconductors in series with OER catalysts must be expanded to account for the various effects of the protection layer.

Photoanode protection strategies can generally be grouped into four categories: thin “tunnel” insulators<sup>11,14-16</sup>, thick “leaky” insulators<sup>13,14</sup>, thin conductive oxides<sup>4,9,17-25</sup>, or thin metals<sup>12,23,26-28</sup>. Efficiency losses introduced by the protection layer affect all these categories, but to varying degrees. For thin tunnel oxides, parasitic optical losses are small compared to losses from tunneling resistance as the protective film thickness increases. As thicker protection layers afford better stability, tunnel oxide protection research has focused on minimizing charge extraction barriers and series resistance through the oxide layer.<sup>11,13,29</sup> For thick “leaky” oxides, series-resistance voltage losses are reduced, but the presence of conductive defect states appears to influence the junction voltage for n-Si heterojunctions.<sup>11,30,31</sup> Continued research on “leaky” oxides has focused on tuning the junction properties to control the illuminated open circuit potential ( $V_{oc}$ ).<sup>31</sup> Work on thin conductive oxides and thin metal protection layers has largely focused on passivation of interface states responsible for Fermi level pinning in heterojunctions and recombination losses in buried homojunctions.<sup>8,30,32-35</sup> Various barrier height ( $\phi_b$ ) tuning strategies have been explored for heterojunctions in order to limit dark-current recombination losses.<sup>12,18,21,25</sup> The optical reflectivity and absorption properties of the protection layers have been non-trivial sources of light loss and improving optical transmittance is an area of continued research.<sup>22,35</sup>

To better understand the fundamental interface-energetics and charge-transfer-kinetics aspects of protection layers we investigate the metallic nickel (Ni) coated n-Si photoanodes first studied by Kenney *et al.*<sup>28</sup> The Ni appears to simultaneously serve as a protection layer, electrocatalyst for oxygen evolution (when oxidized), and some type of charge-separating heterojunction to the n-Si. These photoanodes exhibit dynamic photoelectrochemical (PEC) response and a high photovoltage at sufficiently thin Ni coatings ( $\leq 5$  nm) relative to thicker coatings. The origin of the photovoltage increase for thin films remains unclear but various explanations have been suggested, including: a solution-equilibrated  $\phi_b$  increase due to incomplete screening from the Ni metal<sup>28,36,37</sup>, the development of an “adaptive” junction<sup>8</sup> (discussed in more detail below), and decreased optical losses for thin films<sup>3</sup>. Research on a similar architecture, wherein metallic Co was electrodeposited as a protection layer, suggests that sufficiently thin layers may enable an SiO<sub>x</sub> mediated surface-state passivation effect and the development of high barrier regions.<sup>12</sup>

We seek to identify the primary cause(s) of the apparent changes in interface energetics and/or charge-transfer kinetics. A major consideration in doing so is evaluation of the junction behavior for the n-Si | Ni architecture. Establishing whether the photoanode behaves in the so-called “adaptive” regime or buried regime is one key to designing improved devices.<sup>38-40</sup> So-called adaptive junctions are those where the changes in electrochemical potential of the catalyst under operational conditions (i.e. due to photo-oxidation) lead to changes in the semiconductor | catalyst interface energetics (e.g. increases in the effective interface  $\phi_b$ ).<sup>40</sup> In buried junctions the energetics are fixed by a solid-state interface and invariant under operational conditions (e.g. a solid state *pn* junction or Schottky diode, coated with catalytic material). Junction characterization, however, is difficult with conventional PEC techniques which conflate information about the catalyst, semiconductor, and protection layer into the combined photoelectrode current-voltage response.

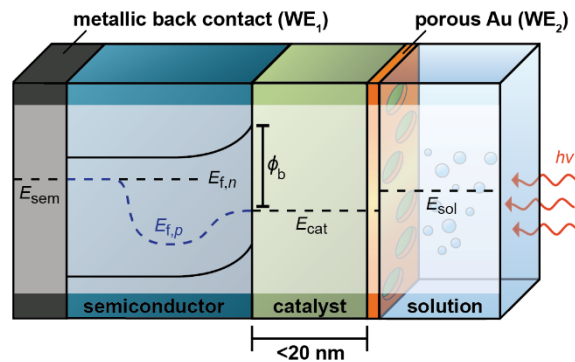


**Figure F.1. Schematic depicting a n-type photoanode protected with a catalyst material and a second working electrode for DWE measurements.** Fermi levels are labeled for the bulk semiconductor ( $E_{sem}$ ), the hole quasi Fermi level ( $E_{f,p}$ ), the electron quasi Fermi level ( $E_{f,n}$ ), the catalyst Fermi level ( $E_{cat}$ ), and the solution potential ( $E_{sol}$ ). The primary working electrode ( $WE_1$ ) controls/senses the semiconductor potential while the secondary working electrode ( $WE_2$ ) controls/senses the catalyst potential.  $WE_2$  is deposited as a thin, 10 nm gold layer which results in an electrolyte-porous but electronically interconnected surface. The effective electronic barrier height ( $\phi_b$ ) between semiconductor and catalyst is labeled for clarity.

Dual-working-electrode (DWE) PEC techniques enable separation of catalyst, semiconductor, and interface effects from the overall photoelectrode response.<sup>39</sup> Measurements are made using a second working electrode ( $WE_2$ ) that independently probes the catalyst potential (or the current flowing through the catalyst) *in situ*, during PEC operation, while the semiconductor potential/current is simultaneously monitored/controlled through the first working electrode ( $WE_1$ ).

The technique was used previously on model TiO<sub>2</sub> single-crystal electrodes which provided a well-defined and stable semiconductor | catalyst junction.<sup>38,39</sup> The DWE experiments demonstrated that electrocatalysts deposited on TiO<sub>2</sub> can yield either buried or adaptive junction behavior, depending on catalyst preparation. Electrolyte-permeable catalyst layers, arising from electrodeposition of Ni oxyhydroxide or hydrated iridium oxide, produced adaptive junctions with high photovoltages, consistent in magnitude with the TiO<sub>2</sub> flat band position and bandgap.<sup>38,41</sup> Electrolyte impermeable layers composed, for example, of annealed nanocrystalline IrO<sub>2</sub>, produce buried junctions that had small and static barrier heights, resulting in low photovoltages. The presence of such distinct junction behaviors based on catalyst permeability indicates that control of the semiconductor | catalyst interface is a critical design principle for enhancing photoanode performance.<sup>8,40</sup>

Here we use DWE photoelectrochemistry to systematically probe interface energetics and efficiency loss mechanisms in Ni protected n-Si photoanodes. We establish that resistive and optical losses are not instrumental in producing the anomalously high photovoltage of sufficiently thin Ni protection layers relative to thicker ones. While potential cycling under illumination consistently improves photoanode response, concomitant with oxidation of the Ni layer to form Ni(Fe)OOH, DWE experiments reveal that even the conditioned devices do not behave as adaptive junctions. The data suggest that these devices are, in fact, spatially inhomogenous buried junctions. These results are generally useful in understanding n-Si protection strategies and are applicable for enhancing photoanodes reliant on transition metal and/or thin conductive-oxide protection.

## 2. Methods

### 2.1 Photoanode Fabrication and Electrochemical Characterization

P-doped [100] n-Si wafers (resistivity  $\sim 0.1$  ohm $\cdot$ cm) were cleaned by sonication in isopropyl alcohol (IPA) for 10 min, dried under N<sub>2</sub>, and diced into 1  $\times$  1 cm squares. Ni films were deposited onto the squares, without etching the native oxide, by thermal evaporation at  $\sim 0.1$  Å s<sup>-1</sup> from an Al<sub>2</sub>O<sub>3</sub>-coated W boat (Kurt Lesker) using Ni powder (Alfa Aesar  $\sim 120$  mesh). Ohmic contact was achieved via wetting the back surface with Ga-In eutectic, placing a Sn-Cu wire within the eutectic, and fixing both in place with epoxy (Loctite Hysol 1C). The Sn-Cu wire was then threaded through a 3.5-mm-diameter glass tube and the n-Si chip was affixed to one end with epoxy. A standard activation protocol was used, unless otherwise noted, to achieve reproducible electrochemical behavior. Electrodes were electrochemically cycled 50 times at 100 mV s<sup>-1</sup>. For each cycle the anodic sweep was terminated 200 mV past the Ni(OH)<sub>2</sub> oxidation peak and the cathodic sweep was terminated 200 mV negative of the NiOOH reduction peak. This range was found to be ideal across all experimental configurations; notably, cycling procedures with more

anodic sweeps appeared to promote bubble-mediated mechanical exfoliation of the Au WE<sub>2</sub> contact for DWE devices.

For long-term cycling experiments an additional layer of Ni was electrodeposited to increase stability of the Au WE<sub>2</sub> contact. This was accomplished by photodeposition under 1 sun illumination in a 0.1 M NiCl<sub>2</sub> / 1.0 M potassium-borate (K-borate) solution. During illumination, an anodic current (0.1 mA cm<sup>-1</sup>) was passed through each electrode for 2 min and the electrodes were then cycled 50 times as described as the standard activation above. Electrodes were removed from the NiCl<sub>2</sub> solution before characterization.

Application of the WE<sub>2</sub> contact is challenging. Au layers must be sufficiently thin as to allow solution to reach the electrode; a relatively smooth deposition surface is therefore required to retain lateral electrical contact across the Au film. Additionally, ultrathin Ni layers used in this study increase the likelihood of direct shorting from the Au WE<sub>2</sub> layer to the Si. Prior to Au deposition Ni coated wafers were plasma cleaned for 10 min and thermally annealed for 5 min at 150 °C on a hot plate. Electrodes were then electrochemically cycled as described above and rinsed with 18.2 MΩ·cm water. The Au WE<sub>2</sub> was then deposited on a subset of the samples (~ 2 Å s<sup>-1</sup>). The optimal Au thickness for WE<sub>2</sub> was found to be ~ 10 nm. Samples were tested for shorting (i.e. direct Au contact to n-Si) with dry two-electrode current-voltage measurements (see supporting information (SI) Section F.S1 for additional details). Despite recent reports of Au mediated catalytic enhancement, we note no significant enhancement to the OER kinetics upon deposition of the Au contact.<sup>42</sup> This discrepancy is likely due to the thicker Ni(OH)<sub>2</sub> layers generated in our study, where ~19 monolayer equivalents are calculated via redox integration for the devices protected by 3 nm of Ni. However, parasitic optical absorption by the Au causes the limiting photocurrent densities to decrease. Comparison of limiting photocurrent densities before and after Au application reveals a transmittance through the thin Au of 54% ± 1%.

Electrochemical characterization was conducted using a BioLogic SP200 bipotentiostat. Electrodes were characterized in a three-neck flask containing 50 mL of aq. 1 M potassium borate (K-borate) buffered to pH ~9.5. For photo-electrochemical characterization, a solar simulator (Abet Technologies, model 10500) was calibrated to deliver ~1 sun AM1.5G illumination at the electrode surface. A Pt counter electrode and an Ag/AgCl reference electrode were used to collect cyclic voltammetry data without *iR* compensation. Prior to characterization the cells were sparged with O<sub>2</sub> flow for 10 min; mild stirring was used during characterization.

For Fe-free studies a previously described procedure was used to produce Fe-free K-borate electrolyte.<sup>43</sup> In short, 2 g of 0.99% Ni(NO<sub>3</sub>)<sub>3</sub> was dissolved in 4 mL of 18.2 Ω·ohm H<sub>2</sub>O and then precipitated with 20 mL of semiconductor grade KOH. The solution was agitated for 10 min,

centrifuged at 7000 rpm for 5 min, and the supernatant was decanted. Two more wash cycles were employed to remove nitrates; in each 20 mL of 18.2  $\Omega$ -ohm H<sub>2</sub>O and 2 mL of KOH were added to the precipitate, it was redispersed, agitated for 10 min, centrifuged at 7000 rpm, and decanted. K-borate buffer was added to the Ni(OH)<sub>2</sub> powder, agitated for 10 min, and the solution was left to sit for 24 h. The solution was then centrifuged at 7000 rpm for 5 min and the supernatant was collected for use as electrolyte. To prevent possible Fe leaching associated with glass electrochemical cells, a custom HDPE cell was employed with a quartz window. Electrodes fabricated for Fe-free experiments used hot glue in place of epoxy (due to Fe leeching from the latter).<sup>44</sup> Fe incorporation experiments were accomplished by addition of 10  $\mu$ L of 0.1 M Fe(NO<sub>3</sub>)<sub>2</sub> (to 50 mL of Fe-free K-borate present in the electrochemical cell) followed by gentle stirring for  $\sim$ 10 s.

Measurement of precise photocurrent onset potential shifts is experimentally challenging due to the proximity of the NiOOH anodic redox peak. To overcome this, photocurrent onset shifts were calculated at a current density where the onset slope was clearly distinguishable from the anodic redox peak. The specific current density used is explicitly stated for each measurement.

## 2.2 Material Characterization

Elemental and oxidation state composition analysis was accomplished via X-ray photoelectron spectroscopy (XPS) using an ESCALAB 250 ThermoScientific with an Al K $\alpha$  monochromated source (150 W, 20 eV pass energy, 500  $\mu$ m spot size). Depth profiles were performed with an Ar sputter (2 keV, 3  $\mu$ A, 5 s step<sup>-1</sup>, 4 mm<sup>2</sup> spot). Peaks were fit using ThermoScientific Avantage 4.75 software and cross referenced to the NIST database. Scanning electron microscopy (SEM) analysis was accomplished with a Zeiss Ultra SEM (5 keV, 30  $\mu$ m aperture). Atomic force microscopy (AFM) data was collected with a Bruker Dimension Icon using tapping mode and a Tespa v2 probe (scan rate 1 Hz, 512 lines). Nanoscope v1.5 software was employed for 1<sup>st</sup> order flattening of all AFM data.

## 3. Results and Discussion

### 3.1 Photoelectrode and Junction Behavior as a Function of Ni Thickness

To understand the n-Si | Ni interface and photoelectrode response, we first measured the photoelectrode properties as a function of the Ni film thickness (Figure F.2). As the film thickness increases from 3 to 20 nm, the light-limited photocurrent density decreases and the photocurrent onset shifts anodic (i.e. the photovoltage generated by the n-Si | Ni interface decreases). The

decrease in photocurrent is easily explained by increased parasitic optical absorption as the Ni layer increases in thickness (illumination is incident on the system from the catalyst side of the device).

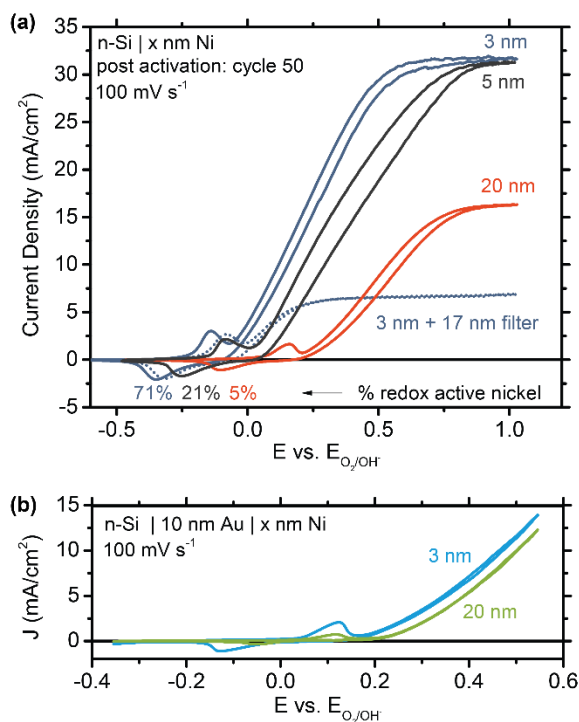


**Figure F.2. Comparison of WE1 and WE2 for devices with varied Ni thickness. (a)** Illuminated cyclic voltammetry comparison of 3, 5, and 20 nm thermally deposited Ni films on n-Si. An optical filter, comprised of 17 nm of Ni deposited on a transparent quartz slide, is placed between the 3 nm coated photoanode and the light source. **(b)** Illuminated photocurrent onsets of n-Si with 10 nm Au deposited prior to the 3 nm and 20 nm thick Ni layers. Both experiments were performed under 100 mW cm<sup>-2</sup> of AM1.5G solar simulation in pH 9.5 K-borate buffer.

The shift in onset potential, however, cannot be explained by the decreased optical transmission through the Ni protection layer for thicker films. The photoelectrodes with 20 nm Ni show a ~340 mV anodic shift in the onset potential relative to those with 3 nm Ni (when measured at 2.5 mA cm<sup>-2</sup> photocurrent density). The ideal diode equation, however, predicts only a ~60 mV decrease in junction photovoltage for each order-of-magnitude decrease in photocurrent. When the light intensity is reduced on the photoelectrode with 3 nm Ni by use of an inline optical filter (consisting of 17 nm of deposited Ni metal film on quartz), only a small ~60 mV shift in onset potential is observed (when measured at 2.5 mA cm<sup>-2</sup> photocurrent density) for a ~6-fold decrease in photocurrent. These experiments demonstrate that the fundamental junction properties of the n-

Si | Ni interface – and thus ability to generate photovoltage – depend sensitively on the thickness of the Ni layer.

The voltammetry in Figure F.2 features the characteristic wave associated with, nominally, nickel hydroxide/oxyhydroxide redox,  $\text{Ni}(\text{OH})_2 + \text{OH}^- \rightarrow \text{NiOOH} + \text{H}_2\text{O} + \text{e}^-$ . The position of the wave in Figure F.2a depends on the thickness of the Ni layer protecting the n-Si electrode, consistent with the above conclusion that photovoltage generated by the n-Si | Ni interface is dependent on the Ni thickness. For the 3 nm, 5 nm and 20 nm thick Ni films, the integrated intensity corresponds to ~ 71, 21, and 5 % of the total Ni atoms in the film, respectively. This measurement therefore illustrates that for the thin films, the majority of the initial metallic Ni film is oxidized to NiOOH during operation; while for the 5 and 20 nm films significant areas of metallic Ni remain, and likely producing a buried n-Si | Ni junction (see below). This finding is consistent with X-ray photoelectron spectroscopy (XPS) elemental depth profile showing persistent metallic Ni trapped below an outer oxidized Ni layer after 5 h of continuous PEC operation.<sup>28</sup>

To confirm that OER onset shift is largely dictated by junction properties, control samples were fabricated where a 10 nm Au interlayer was deposited between the Ni and n-Si (Figure F.2b). In doing so, the interface is controlled by the n-Si | Au Schottky junction and energetic losses associated with the bulk catalyst layer are distinguishable from Ni-thickness-dependent junction effects. The n-Si | Au with 20 nm Ni exhibits an anodic onset shift of ~50 mV at 2.5 mA cm<sup>-2</sup> relative to the n-Si | Au sample with 3-nm Ni. This shift is attributed to parasitic optical absorption in the thicker Ni that lowers the minority carrier injection level and thus photovoltage (in agreement with the optical filter experiment shown in Figure F.2a). Both electrodes have similar shaped photocurrent onset profiles, indicating no significant difference in the electrical resistance of the catalyst layer, in contrast to thin oxide protected photoanodes where charge extraction barriers and series resistance can be significant.<sup>11,13,29</sup> These control samples corroborate the previous analysis, indicating that the ~340 mV onset shift between n-Si photoanodes protected with 3 nm and 20 nm Ni coating is due to changes in the details of the photovoltage-generating n-Si | Ni interface.

### 3.2 Effect of electrochemical “activation”

The observations that the 3 nm Ni layers generate higher photovoltage and also exhibit ~70% redox-active Ni species (oxidized to NiOOH under operating conditions) suggest that oxidation of the protection layer is linked to increased performance. To test this hypothesis, we studied the junction properties as a function of electrochemical activation (Figure F.3). Samples were fabricated with 5 nm Ni and 10 nm of (electrolyte-permeable) Au as a top contact to serve as



WE<sub>2</sub>. NiOOH was then photodeposited on top of the Au to improve long-term stability during cycling and DWE experiments by slowing the apparent delamination of the Au top contact.

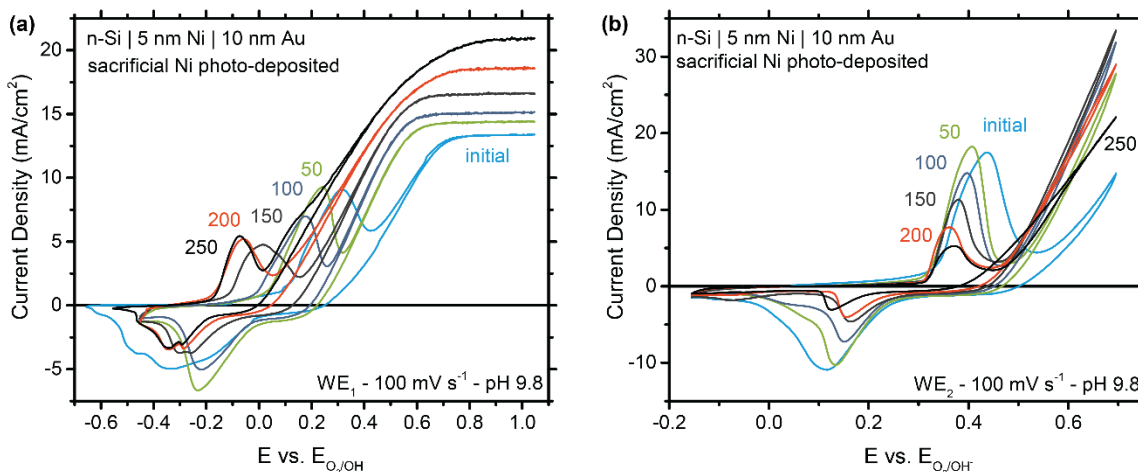


**Figure F.3. Illuminated cycling of n-Si protected with 5 nm Ni in pH 9.8 K-borate buffer.** To fully capture catalyst activation, the electrodes were not pre-activated in this experiment. **(a)** Cycling of WE<sub>1</sub> results in a ~300 mV OER onset shift. **(b)** Illuminated catalyst WE<sub>2</sub> response on the same electrode exhibits little change after the initial 50 cycles. The integrated charge in the Ni redox waves measured at both WE<sub>1</sub> and WE<sub>2</sub> are similar for the first 200 cycles (after which the sample begins to degrade). For example, at cycle 50 both cathodic waves measured at WE<sub>1</sub> and WE<sub>2</sub> both yield 17 mC of charge. This suggests both WE<sub>1</sub> and WE<sub>2</sub> are interrogating the entire catalyst film.

The illuminated photoanode performance improves notably over the first 250 CV cycles (Figure F.3a), with the photocurrent onset potential shifting by ~300 mV and the light-limited photocurrent increasing by a factor of 1.5. The change in photocurrent density is attributed to partial dissolution of the photo-deposited NiOOH/Ni(OH)<sub>2</sub>, which parasitically absorbs light. The change in photocurrent onset could be due to two factors, (1) increased catalytic activity as the Ni is electrochemically conditioned to form Ni(Fe)OOH, and/or (2) increased junction photovoltage induced by the same oxidation of Ni.<sup>43,45,46</sup> Using the DWE approach we can differentiate between these two possibilities. Figure F.3b shows the voltammetric response of WE<sub>2</sub>, which is directly connected to the catalyst layer. After the first 50 cycles the electrocatalytic current onset measured directly through WE<sub>2</sub> reaches a nominal steady state, while the photocurrent onset measured through WE<sub>1</sub> continues to shift cathodically. Of the ~300 mV shift measured via WE<sub>1</sub> at 10 mA cm<sup>-2</sup>, only ~110 mV can be explained by the increased catalytic activity measured through WE<sub>2</sub>.

This finding reveals that most of the activity enhancement when cycling arises from an increase in junction photovoltage. The increased junction photovoltage is further corroborated by the cathodic shift in the oxidation peaks through WE<sub>1</sub> (Figure F.3a) and the absence of a comparable shift through WE<sub>2</sub> (Figure F.3b).

To confirm this result, control devices were again fabricated by depositing a 10 nm Au interlayer between the n-Si and Ni (see SI Section S2). For the control samples, the catalyst activity measured through WE<sub>2</sub> once again saturates after 50 cycles and little shift in the Ni redox wave potential is observed. When illuminated J-E curves are measured through the semiconductor (WE<sub>1</sub>), no significant shifts in the photocurrent onset or Ni redox wave potential are found. These observations are consistent with the expected behavior of the buried n-Si | Au junction in series with the Ni-based catalyst layer and further indicate that the cathodic shifts in photocurrent onset are produced specifically by changes to the n-Si | Ni junction.

After long-term cycling, the performance of all the Ni-protected photoanodes declines (see SI Sections S2 and S3). For n-Si with 5-nm Ni this begins at ~350 cycles. On samples with only 2 nm of Ni the deactivation occurs over the first 20 cycles. During the deactivation process the Ni redox peaks split successively further apart with cycling and decrease in intensity, while the slope of the photocurrent onset decreases. These observations are consistent with oxidation of the underlying n-Si to form a SiO<sub>2</sub> layer that blocks current flow by presenting a large series resistance. n-Si protected only with Ni (oxy)hydroxide catalysts deposited by cathodic electrodeposition or photo-assisted anodic electrodeposition, which are known to be completely electrolyte permeable, also degraded quickly, within 10 CV cycles (see SI Section S3). Furthermore, related work on PEC ageing of n-Si photoanodes protected with Ni has revealed pinhole formation in thin ~2 nm protection layers and pitting behavior in thicker ~10 nm protection layers.<sup>3</sup> In both instances, after sufficient PEC ageing, the growth of interfacial SiO<sub>2</sub> was apparent by XPS elemental depth profiling and more-prevalent in areas with pinholes/pitting.

The results discussed above suggest that photovoltage increases are connected to increased Ni porosity and/or thin adventitious SiO<sub>2</sub> growth. Thicker Ni films on n-Si do not fully activate, and therefore the photoelectrodes with such films appear to be limited by the small n-Si | Ni Schottky barrier.<sup>47,48</sup> Ni films that are too thin (e.g. 2 nm), or catalysts consisting only of electrolyte permeable Ni (oxy)hydroxide, generate relatively large photovoltages but cannot protect the electrode from oxidation. Intermediate thickness Ni films (3-5 nm) provide a degree of protection, while simultaneously providing for large photovoltages.

### 3.3 Elucidation of junction behavior through dual working electrode photoelectrochemistry

Understanding the junction behavior (e.g. adaptive, buried, or mixed) for the n-Si with optimal Ni thickness of 3-5 nm may provide general insight into interface design for catalyzed/protected photoanode devices. To distinguish between these junction behaviors, and to identify the source of photocurrent onset enhancement, we employ DWE PEC techniques (first demonstrated on TiO<sub>2</sub> model systems<sup>39</sup>). To test for the presence of adaptive behavior in the n-Si with 3 nm of Ni, the catalyst potential  $E_{\text{cat}}$  (sensed with WE<sub>2</sub>) is measured as a function of the semiconductor potential  $E_{\text{sem}}$  controlled by WE<sub>1</sub> (Figure F.4). The measured response shows three distinct regions, discussed in detail below.

At low potentials (i.e. cathodic of -0.25 V vs.  $E_{\text{O}_2/\text{OH}^-}$ ) the apparent  $E_{\text{cat}}$  is not affected by changes in  $E_{\text{sem}}$ . Illumination also has no effect on the measured catalyst potential and  $E_{\text{cat}}$  slowly drifts cathodic with time. This behavior is consistent with the surface of the Ni catalyst being converted to Ni(OH)<sub>2</sub>/NiOOH during activation. When WE<sub>1</sub> is poised between -0.7 and -0.25 V vs.  $E_{\text{O}_2/\text{OH}^-}$ , the catalyst layer remains in the reduced Ni(OH)<sub>2</sub> form because the photovoltage generated by the junction is not sufficient to drive the oxidation to (nominally) NiOOH. Ni(OH)<sub>2</sub> is highly electrically resistive and thus WE<sub>2</sub> is electrically isolated from the semiconductor surface and remains unable to measure a meaningful catalyst potential.

At  $E_{\text{sem}} = \sim -0.2$  V vs.  $E_{\text{O}_2/\text{OH}^-}$ ,  $E_{\text{cat}}$  rapidly increases to  $\sim -0.25$  V vs.  $E_{\text{O}_2/\text{OH}^-}$ , a potential that is sufficient to oxidize the catalyst to electrically conductive NiOOH.<sup>43,45,46</sup> A  $\sim 440$  mV interface photovoltage is directly measured between the electrically conductive Ni/NiOOH and the n-Si. When  $E_{\text{sem}}$  is between -0.2 and +0.2 vs.  $E_{\text{O}_2/\text{OH}^-}$ ,  $E_{\text{cat}}$  changes linearly with  $E_{\text{sem}}$  with a slope of  $\sim 1$ . This suggests a type of buried-junction behavior which will be discussed in detail below.

For  $E_{\text{sem}} > 0.25$  vs.  $E_{\text{O}_2/\text{OH}^-}$ ,  $E_{\text{cat}}$  saturates at  $\sim 0.55$  vs.  $E_{\text{O}_2/\text{OH}^-}$ . This is consistent with the constant photocurrent measured in this potential regime. Because current through the semiconductor and catalyst systems must be conserved, a constant photocurrent through WE<sub>1</sub> leads to a constant catalytic current and thus constant  $E_{\text{cat}}$  as measured with WE<sub>2</sub>.

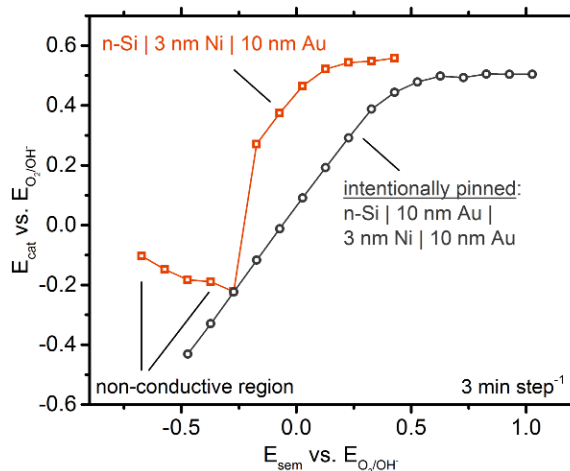


**Figure F.4. Catalyst electrochemical potential sensing via WE2.** Illuminated ( $100 \text{ mW cm}^{-2}$ ) chronoamperometry experiments for n-Si protected with 3 nm Ni (red) and intentionally buried with 10 nm Au + 3 nm Ni (black). Samples were activated in pH 9.8 K-borate buffer. Data was recorded after a 3 min equilibration at each constant potential.

The samples are compared to intentionally buried controls where 10 nm Au is deposited between the n-Si and Ni layers (Figure F.4 – dark grey curve). From  $-0.5$  to  $+0.3 \text{ V vs. } E_{\text{O}_2/\text{OH}^-}$ ,  $E_{\text{cat}}$  is a linear function of  $E_{\text{sem}}$  indicating that any potential changes applied to  $\text{WE}_1$  drop predominantly at the catalyst | solution interface – as expected for a buried junction device.<sup>39,49</sup> At more-positive  $E_{\text{sem}}$ ,  $E_{\text{cat}}$  again saturates, as the photocurrent becomes constant and the applied potential drops across the buried junction instead of the catalyst | solution interface. The limiting  $E_{\text{cat}}$  for the control samples is lower than for the n-Si | Ni samples because the additional light-blocking Au layer results in lower saturated photocurrent. The fact that no “non-conductive” catalyst region is observed suggests pinholes that provide electrical conductivity between the two Au layers for this control sample. The fact that the both intentionally buried control sample and the n-Si with 3 nm of Ni exhibit the same linear  $E_{\text{cat}}$  vs.  $E_{\text{sem}}$  response over the region where the catalyst is conductive suggest the n-Si | Ni junction is behaving as a buried system.<sup>39</sup> By contrast, simulations show that an adaptive junction would typically produce a switching behavior (slope of  $E_{\text{cat}}$  vs.  $E_{\text{sem}} \gg 1$ ) over a narrow  $\text{WE}_1$  potential range before saturating, as is observed for the  $\text{TiO}_2/\text{NiOOH}$  junction.<sup>38,39,49</sup>

To further understand the nature of the buried junction we measured the dark  $J$ - $E$  response of the junction directly (Figure F.5).  $E_{\text{cat}}$  is held fixed versus the reference through  $\text{WE}_2$ , while  $E_{\text{sem}}$  is swept linearly through  $\text{WE}_1$ . For  $E_{\text{cat}} = 0.0$  and  $0.1 \text{ V vs. } E_{\text{O}_2/\text{OH}^-}$ , the catalyst is reduced and

electrically insulating, yielding the  $J$ - $E$  curves that are highly resistive in both scan directions. For  $E_{\text{cat}} = 0.3, 0.4,$  and  $0.5$  V vs.  $E_{\text{O}_2/\text{OH}^-}$ , the catalyst is oxidized and electrically conductive. The current voltage curves are highly rectifying, but their magnitude and shape in both forward and reverse bias are nearly identical for these  $E_{\text{cat}}$ . This behavior demonstrates that the interface  $\phi_b$  (i.e. energetics) is unaffected by changes in catalyst potential and further suggests that the junction is buried, in contrast to that observed for adaptive junctions such as  $\text{TiO}_2/\text{NiOOH}$ .<sup>38,39</sup>

The intentionally buried control samples with Au in between the Ni and n-Si were also tested (see SI Figure F.S3). As expected, these samples exhibited buried junction behavior where the  $J$ - $E$  curves remained independent of  $E_{\text{cat}}$  for all applied potentials when normalized to the junction voltage. The same buried-junction behavior was observed when electrolyte-impermeable  $\text{IrO}_x$  was deposited on the  $\text{TiO}_2$ .<sup>39</sup>

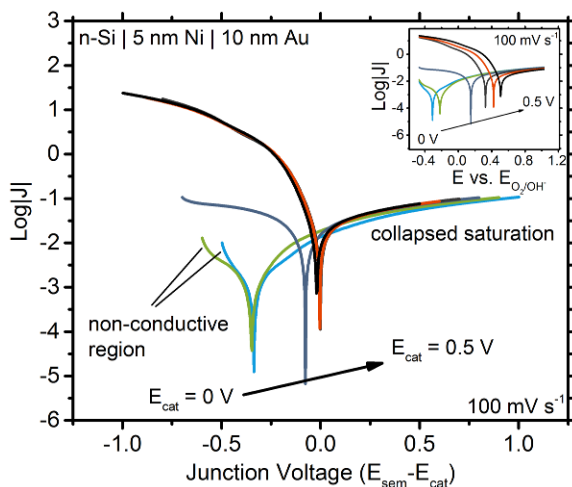


**Figure F.5. Dark  $J$ - $V$  characteristics for the 5 nm n-Si photoanodes.** The inset shows the same data but with  $E_{\text{sem}}$  referenced to the solution potential as the x-axis.

### 3.4 In-situ Tuning of Catalyst Activity to Assess Interface Properties

Fe cation impurities in electrolyte media have been shown to dramatically increase the OER activity of Ni-based catalysts.<sup>43</sup> This effect provides a method for changing the catalyst activity in situ, for the same electrode, without significantly affecting other junction properties. For a buried-junction photoelectrode, reduction of the catalyst overpotential corresponds directly to cathodic shifts in the catalyzed photoelectrode three-electrode  $J$ - $E$  behavior, while for an adaptive junction this is not typically the case.<sup>38,49</sup> Here, DWE electrodes with 3 nm of Ni deposited were cycled (as per the activation protocol) in Fe-free electrolyte until the  $\text{WE}_2$  catalyst activity saturated

(typically after  $\sim 50$  cycles). Voltammograms were collected through  $WE_1$  under illumination beginning one cycle before Fe was introduced. Voltammograms were also collected through  $WE_2$  before and after Fe incorporation. Fe incorporation cathodically shifts the photocurrent onset potential by  $\sim 120$  mV when measured through  $WE_1$  at  $10 \text{ mA/cm}^2$  (Figure F.6). Similarly, when measured through  $WE_2$  the onset dark catalytic onset shifted by  $\sim 100$  mV at  $10 \text{ mA/cm}^2$  (see SI Section S5 for additional information). These results indicate that the photocurrent onset of the activated n-Si | Ni system is enhanced almost entirely through increased activity of the catalyst and not via a change in junction dynamics. Direct measurements of the junction photovoltage before and after Fe incorporation confirm that the photovoltage is unaffected by Fe incorporation. These results are expected for a photoanode in which the critical junction is buried and ion-impermeable, with the Fe thus only modulating the catalyst activity. We note that different behavior was found for similar experiments on adaptive  $\text{TiO}_2$  | Ni(Fe)OOH junctions.<sup>38</sup>

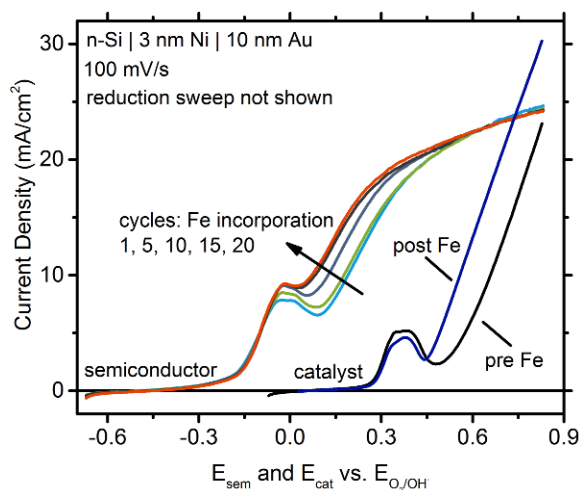


**Figure F.6. Illuminated PEC response due to Fe incorporation as measured through the semiconductor electrode and the catalyst electrode ( $100 \text{ mW cm}^{-2}$ ).** Data through the semiconductor electrode was collected continuously; Fe was introduced at the beginning of cycle 1 (where cycle 1 is the first cycle after the activation protocol). Data through the catalyst electrode was collected before and after the semiconductor CVs.

### 3.5 Physical picture of junction behavior

The data and analysis presented above can be used to develop a physical picture for the Ni-coated n-Si system. For thick Ni layers, the behavior is consistent with the presence of a buried junction (generating a small photovoltage) in series with surface oxidized Ni (nominally Ni(Fe)OOH) serving as the OER catalyst. For very thin films ( $\sim 2$  nm Ni) or for films composed of

directly (photo)electrodeposited NiOOH, the n-Si rapidly passivates and no stable photoelectrode response is observed. For intermediate layer thicknesses (3-5 nm of Ni) both comparatively large photovoltages and relatively stable responses are exhibited. All the DWE PEC analyses indicate that samples with 3-5 nm Ni form buried junctions with the underlying n-Si, despite the catalyst layer being largely comprised of redox active and thus electrolyte-permeable Ni(Fe)OOH after activation. XPS depth profile analysis of these samples, after activation, show the presence of residual metallic Ni as well as nickel silicides (see SI Section S6). Simultaneous examination of the Si regional spectra, indicates that the metallic Ni is in close proximity with the n-Si (SI Figure F.S9).

These data are consistent with a picture where (1) protective metallic Ni regions are retained despite electrochemical cycling, providing low resistance pathways for photo-generated hole collection, and (2) the remainder of the surface is passivated n-Si | SiO<sub>2</sub> | Ni(Fe)OOH resulting in an interface  $\phi_b$  increase relative to the pre-cycled samples. Such an interface might be considered a spatially “inhomogeneous” buried junction. Evidence for junction inhomogeneity is observed for many of the photoelectrodes with 3-5 nm Ni (see SI Section S7 for additional information). For example, in Figure F.6, light-limited photocurrent does not saturate at a constant value as  $E_{sem}$  is raised to more-anodic potentials. The sloped photocurrent in reverse bias is not accounted for by the dark voltammetry (which show negligible dark current) and generally becomes more pronounced with continued cycling. This effect can be explained if the majority of the n-Si surface is comprised of a sufficiently thick SiO<sub>2</sub> layer that prevents hole transfer to the catalyst. All the photocurrent must thus travel to regions of retained Ni metal where it can be collected (likely across a much thinner native oxide layer). Collecting photocurrent to these small regions and driving it across a resistive contact likely leads to additional voltage losses and produces potential-dependent “saturated” photocurrents.

In the above physical picture, increased photovoltage may be explained by the “pinch-off” effect. With sufficient spatial heterogeneity, carrier depletion required to reach charge neutrality in the high-barrier regions can spill into the low-barrier regions and increase the local built in potential ( $V_{bi}$ ). Although current still travels through the low-barrier regions of retained Ni metal islands, the added band bending effectively increases the  $\phi_b$  of this current pathway. The low-barrier region is then said to exhibit a pinched-off “saddle point” because the resulting  $\phi_b$  vs. distance profile of the region is a non-constant “saddle” buoyed between two high-barrier regions. The effective barrier height ( $\phi_{b,eff}$ ) of the spatially heterogeneous contact is greater than the  $\phi_b$  generated by homogenous contact of the low-barrier materials.<sup>50-53</sup> Suppression of dark conduction current, due to the increase in  $\phi_{b,eff}$ , results in a photocurrent onset shift to more cathodic potentials. This physical picture,

where the cathodic shift in the photocurrent onset is mediated by an inhomogeneous buried junction, is also in agreement with recent Co | n-Si work where inhomogeneous barriers were proposed to arise given sufficiently thin electrodeposited metallic Co.<sup>12</sup>

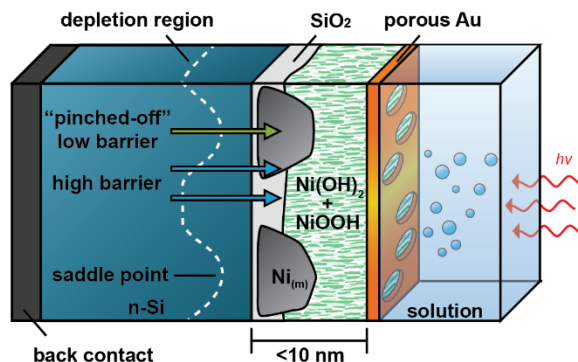


**Figure F.7. Schematic of ultrathin Ni protection on n-Si.** Adventitious SiO<sub>2</sub> passivates the edges of Ni regions producing higher photovoltages via the pinch-off effect.

The development of high-barrier-height regions is likely a byproduct of Ni oxidation and SiO<sub>2</sub> formation during OER conditions. The pre-activated junction is expected to be pinned by the metallic Ni work function and/or by any interface defect states introduced during thermal evaporation of Ni.<sup>48</sup> As the photoanode is cycled, the majority of the Ni oxidizes and adventitious SiO<sub>2</sub> forms where semiconductor-solution contact occurs. Adventitious SiO<sub>2</sub> can then suppress pinning by spatially separating the Ni from the n-Si, causing the n-Si Fermi level to equilibrate with defect states in the SiO<sub>2</sub>. Adventitious SiO<sub>2</sub> may also passivate shallow defect states responsible for pinning the n-Si Fermi level. Discerning between these possibilities is difficult. However, both are similar in that they produce a higher  $\phi_b$  by decreasing relatively shallow Fermi level pinning. Interface defect pinning has recently been reported in a number of NiO<sub>x</sub>-based TCO protection strategies on n-Si photoanodes. Passivation of these defects with a thin Al<sub>2</sub>O<sub>3</sub> interlayer<sup>33</sup>, and separately with a thin SiO<sub>x</sub>/CoO<sub>x</sub> bilayer<sup>9,21,35</sup>, was demonstrated to significantly enhance the respective photovoltages. Similarly, recent work relying on TiO<sub>2</sub> and Ir metal protection has shown that defect-heavy SiO<sub>2</sub> layers may limit attainable photovoltages.<sup>29,30</sup>

The process of adventitious SiO<sub>2</sub> growth has been examined by Han *et al.* in their study on PEC ageing of Ni protected n-Si photoanodes.<sup>3</sup> Over 6.5 days of continuous PEC activity using n-Si coated with ~5 nm of Ni, they document progressive increases in surface roughness (consistent with transformation to Ni(OH)<sub>2</sub>/NiOOH), the formation of large holes in the Ni film, and a 0.4 nm increase in interfacial SiO<sub>2</sub> thickness. In parallel analysis with ~2 nm Ni protection layers and 24 h



of continuous PEC testing, they document the formation of solution-permeable pinholes (ultimately leading to complete passivation) and a 1.2 nm increase in interfacial SiO<sub>2</sub> thickness. In our assessment, the decreased lifetime and the increased adventitious SiO<sub>2</sub> growth exhibited by their ~2 nm Ni protected devices is attributable to the ease with which solution can reach the n-Si | Ni junction. For thinner protection layers, solution not only permeates over a quicker timeframe but also through more areas of the film. For our results, this ease of solution permeability explains why thinner depositions exhibit higher photovoltages after shorter durations of PEC testing. Adventitious SiO<sub>2</sub> growth more readily occurs through thinner protection layers and rapidly produces high-barrier pinched-off Ni regions (schematic in Figure F.7). This interpretation is supported by AFM and SEM analysis (SI Figures F.S14 and F.S15, respectively) on the electrode before and after PEC cycling that show increased morphological heterogeneity and surface roughness. It is also supported by XPS depth profiling, which confirms the presence of persistent metallic Ni near the n-Si | Ni interface after cycling (SI Figures F.S9, F.S10, and F.S12).

Our analysis is thus different than that of other contemporary junction behavior hypotheses, where photocurrent onset improvements are thought to arise as a result of semiconductor equilibration with the solution Fermi level.<sup>28,36,37</sup> In this view, a high  $V_{bi}$  occurs when the solution is only partially screened by a sufficiently thin/porous Ni protection layer. Since the semiconductor passivates upon solution contact, photocurrent must still travel through Ni before reaching the solution, even in regions of partial screening. Pinholes in the Ni that could give rise to partial screening, by allowing solution-semiconductor contact, likely passivate with SiO<sub>2</sub>. To identify the extent of n-Si electronic equilibration with the solution Fermi level, open circuit photovoltages were measured with two different redox electrolytes: 100:1 and 1:100 ferri:ferro cyanide (10 mM). Despite spanning a solution potential range of ~240 mV the measured open circuit photovoltages were statistically identical ( $436 \pm 21$  mV and  $445 \pm 9$  mV for the 1:100 and 100:1 solutions, respectively). Since solution potential does not significantly affect the open circuit photovoltage, we conclude that partial solution screening does not occur. If partial screening were occurring, we would also expect to observe some adaptive character as the Ni(OH)<sub>2</sub>/NiOOH phase equilibrates with the semiconductor. Lack of adaptive behavior corroborates the open circuit photovoltage data and suggests that increased  $\phi_b$  is not caused by incomplete Ni screening.

Our electrochemical analysis also contrasts with suggestions that improved photocurrent onset is caused by the development of adaptive behavior given sufficiently thin protection layers.<sup>8</sup> Instead, our results indicate that the device behaves as a buried junction for all Ni protection-layer thicknesses tested. Results compare well to work on Co-protected n-Si by Hill *et al.* wherein photocurrent onset enhancements were attributed to SiO<sub>x</sub> mediated surface state passivation and

the development of spatially inhomogeneous high-barrier regions.<sup>12</sup> They speculate that high-barrier regions arise when n-Si electronically equilibrates with redox active CoOOH located on the edges of nanometer scale Co islands. Using the DWE approach, we demonstrate that the analogous equilibration with NiOOH does not take place for Ni-protected n-Si. Results in Figures F.4, F.5, and F.6 all depict buried-junction behavior, indicating that  $\phi_b$  is independent of the Ni(OH)<sub>2</sub>/NiOOH Fermi level.

## Conclusions

We used a number of DWE PEC techniques to analyze the junction behavior of n-Si protected by thin Ni coatings. This work therefore provides for the first time a direct measurement of the catalyst | semiconductor junction behavior in-situ for a small bandgap photoelectrode, building substantially on our previous initial report of using DWE PEC to study catalyzed TiO<sub>2</sub> model systems. We found that, contrary to previous hypotheses, the improved photocurrent onset potential at sufficiently thin Ni coatings is not due to the presence of adaptive junction behavior or incomplete screening effects. Across all Ni thicknesses studied, the photoanodes solely exhibited buried-junction behavior. Devices with sufficiently thin Ni layers, i.e. those with improved photocurrent onset, displayed characteristics consistent with a spatially heterogeneous junction. We suggest that the formation of high-barrier regions is due to *in situ* adventitious SiO<sub>2</sub> growth, which decreases shallow Fermi-level pinning, and that low barrier regions are due to remaining metallic Ni contacting the Si. This hypothesis is supported by PEC data as well XPS depth profiling that shows both oxidized and reduced Ni species in the film (SI Figure F.S9). Although direct measurement of the pinch-off effect is experimentally difficult, future directions could employ Auger depth profile spectroscopy and/or in-situ current-sensing electrochemical atomic force microscopy (EC-AFM) to spatially resolve and correlate pinched-off-region chemical features and electronic properties, respectively.<sup>54,55</sup>

The inability to observe adaptive junction behavior on Ni-protected n-Si photoanodes is likely broadly applicable to catalyzed Si photoanodes where the catalyst layer is in direct contact with the Si. If the catalyst layer is electrolyte permeable, and thus allows the formation of an adaptive junction where catalyst charging modulates the effective interface barrier height, then the Si surface oxidizes to prevent current flow and the device quickly loses functionality. If the catalyst layer retains metallic or dense-oxide components in contact with Si, then it forms a buried junction whose interface properties are unlikely to be optimal for generating a high photovoltage in Si.

In light of these findings, it appears that Si photoanode design should focus on engineering buried junctions for high photovoltage output while engineering low resistance electrical contact

to the catalyst layer. A number of recent examples that follow this approach have been reported in the literature.<sup>9,11,14,19,21,29</sup> Other viable approaches might make use of engineered micro or nanopatterning of the charge-collecting contacts (that are electrically in contact with the catalyst layer), while leaving the rest of the surface passivated behind a thick chemically inert oxide that passivates the Si surface to recombination and to corrosion, similar in design to the so-called point-contact photovoltaic cell.<sup>56,57</sup>

## Paper G

### Nanoscale Semiconductor/Catalyst Interfaces in Photoelectrochemistry

Forrest A. L. Laskowski, Sebastian Z. Oener, Michael R. Nellist, Adrian M. Gordon, David C. Bain, Jessica L. Fehrs, Shannon W. Boettcher\*

#### 1. Introduction

Semiconductor structures (e.g. films, wires, particles) used in photoelectrochemical devices are often decorated with nanoparticles that catalyze fuel-forming reactions, such as water oxidation, hydrogen evolution, or carbon-dioxide reduction. For high performance, the catalyst nanoparticles must form charge-carrier-selective contacts with the underlying light-absorbing semiconductor, facilitating either hole or electron transfer while inhibiting collection of the opposite carrier. Despite the key role that such selective contacts play in photoelectrochemical energy conversion and storage, the underlying nanoscale interfaces are poorly understood because it is challenging to directly measure their properties, especially under operating conditions. Using an n-Si/Ni photoanode model system and potential-sensing atomic-force microscopy, we measure interfacial electron-transfer processes and map the photovoltage generated during photoelectrochemical oxygen evolution at nanoscopic semiconductor/catalyst interfaces. We discover interfaces where the hole-selectivity of low-Schottky-barrier n-Si/Ni contacts is enhanced via a nanoscale size-dependent pinch-off effect produced when surrounding high-barrier regions develop during device operation. These results thus demonstrate both the ability to make nanoscale *operando* measurements of contact properties under practical photoelectrochemical conditions and illustrate a design principle to control the flow of electrons and holes across catalyst/semiconductor junctions broadly relevant to different photoelectrochemical devices.

Nanoscale interfaces play a central role in devices for photoelectrochemical energy conversion and storage. Catalyst nanoparticles are often sparsely deposited onto photoactive

semiconductors such that they selectively collect either electrons or holes, drive fuel-forming reactions at low overpotentials, and minimally block incoming light<sup>1-3</sup>. The properties of the resulting semiconductor/catalyst nanojunctions are likely heterogeneous and vary substantially based on surface treatment, deposition method, particle size, or with electrochemical conditioning<sup>4,5</sup>. Additionally, heterogeneous nanoscale interfaces may be formed during device operation from initially homogeneous interfaces. For example, Ni catalyst films on n-Si photoanodes are thought to transform into isolated nanojunctions during photoelectrochemical operation<sup>6,7</sup>. Heterogeneous nanoscale catalyst/semiconductor interfaces are difficult to characterize electrically, especially with the required nanoscale resolution under relevant photoelectrochemical conditions. While the properties of uniform planar semiconductor/metal interfaces (Schottky contacts) have been studied in detail and provide a valuable reference<sup>8</sup>, large changes in interfacial electrical behavior occur as the contact dimensions approach or become smaller than the semiconductor depletion width ( $\sim 10 - 1000$  nm)<sup>9</sup>.

Techniques have been developed for mapping heterogeneous interfacial properties in photovoltaic and (photo)electrochemical systems. Nanoscale open-circuit-voltage mapping of solid-state photovoltaics is possible via Kelvin-probe force microscopy (KPFM)<sup>10</sup>. The application of KPFM, or related electrochemical-force microscopies<sup>11</sup>, to (photo)electrochemical systems are challenged by the presence of practical electrolyte concentrations<sup>12</sup>. Photoconductive atomic-force microscopy (AFM) has been used to illustrate heterogeneous electrical-transport properties in semiconductor photoelectrodes<sup>13</sup>, but the measurements are performed ex-situ and the details of how nanoscale electrocatalysts interface with the semiconductor remain unexplored. Scanning-electrochemical microscopy (SECM)<sup>14,15</sup> and scanning-electrochemical-cell microscopy (SECCM)<sup>16</sup> can map catalytic reaction rates by monitoring product formation but do not directly provide information on the electrical properties of underlying semiconductor/catalyst interfaces. Scanning electrochemical potential microscopy can be used to measure potential gradients through electrical double layers or map constant-potential surfaces. However, it is challenging to map non-constant surface potentials on most experimental systems because the measurement conflates potential with topography<sup>17,18</sup>. Recently, we developed a potential-sensing electrochemical AFM (PS-EC-AFM) technique to measure the surface potential of continuous metal-oxyhydroxide catalyst films on metal-oxide photoelectrodes, showing how the oxyhydroxides behaved as both hole-collecting layers and catalysts for water oxidation<sup>6,19</sup>.

Here we use PS-EC-AFM to spatially resolve the interfacial electronic properties of nanoscale semiconductor/catalyst interfaces. As a model system, we study nominally hemispherical Ni nanocontacts electrodeposited onto n-Si, following work by Loget *et al.*<sup>20</sup>. The n-Si/Ni interface

has been studied extensively as a “stabilized” photoanode for water oxidation under neutral-to-basic conditions<sup>6,7,21-23</sup>. Generally n-Si photoelectrodes with thinner Ni films or smaller Ni nanoparticles perform better (following electrochemical conditioning) than those with higher Ni loading<sup>22,23</sup>. Here we find that electrodeposition of Ni nanoparticles on n-Si leads to low-Schottky-barrier ( $\sim 0.61$  V) contacts which under dry conditions yield photovoltages of only  $\sim 300$  mV, independent of the Ni nanoparticle size. After photoelectrochemical potential cycling, the surfaces of the Ni nanocontacts convert into nickel (oxy)hydroxide (i.e. Ni(OH)<sub>2</sub> or NiOOH). Further ex-situ electrical measurements of the semiconductor/catalyst junction are not possible because the catalyst resting state, Ni(OH)<sub>2</sub>, is electrically insulating. During photoelectrochemical oxygen evolution, the Ni(OH)<sub>2</sub> is oxidized to electrically conducting NiOOH. *Operando* photovoltages measured on individual nanoscale n-Si/Ni/NiOOH junctions by PS-EC-AFM dramatically increase with cycling and show a strong dependence on nanocontact size. We explain the size dependence quantitatively by the pinch-off effect<sup>9,24,25</sup>, where the oxidized (high-work-function) NiOOH induces a large depletion region surrounding the n-Si/Ni interface during operation that increases the effective n-Si/Ni interface barrier and enhances hole selectivity<sup>22,23,26</sup>. This finding not only represents the first direct nanoscale measurement of the pinch-off effect in a photoelectrochemical system<sup>27</sup>, but also illustrates a potentially useful contact behavior where minority carrier selectivity<sup>28</sup> is enhanced, *during operation*, by oxidation of an electrochemically-active surrounding region. Such pinch-off or surface-gating effects are relevant to any semiconductor-based solar-energy-conversion devices involving nanoscale elements<sup>29</sup>.

## 2. Photoelectrochemistry of n-Si decorated with Ni nanoislands

The photoelectrochemical behavior of semiconductor photoanodes typically depends on the amount of catalyst deposited. We study n-Si photoanodes (with dopant density of  $5 - 8 \cdot 10^{15}$  cm<sup>-3</sup>) onto which Ni-metal islands have been deposited from 0.01 M NiCl<sub>2</sub> in aq. 0.1 M H<sub>3</sub>BO<sub>3</sub> at -1.5 V vs. Ag/AgCl for 5, 15, or 60 s. The photoelectrochemical response of these photoanodes, after 50 cyclic voltammograms (CVs) in aq. 1 M KOH under  $\sim 1$  sun illumination, is shown in Figure G.1a. This photoelectrochemical activation converts the outer portion of the Ni to Ni(OH)<sub>2</sub>/NiOOH. Fe impurities that catalyze the OER are incorporated from the electrolyte and are assumed to be present in all catalysts studied<sup>30</sup>. The formation of the Ni (oxy)hydroxide is apparent from the increasing size of the Ni redox wave at potentials negative of the photocurrent onset (Figure G.1a) and from cross-sectional transmission-electron microscopy (Fig. G.1b, Supplementary Section G.1). Samples prepared with a 5-s deposition produced photoanodes with the most-negative photocurrent-onset potentials (i.e. the highest photoanode performance) and

spatially-distributed Ni nanoislands with radii ranging from 35-150 nm (Fig. G.1b and 1c). The 15-s and 60-s depositions produce successively larger Ni islands (Fig. G.1c). The thicker Ni leads to more-positive photocurrent-onset potentials as well as lower photocurrents due to parasitic light absorption.

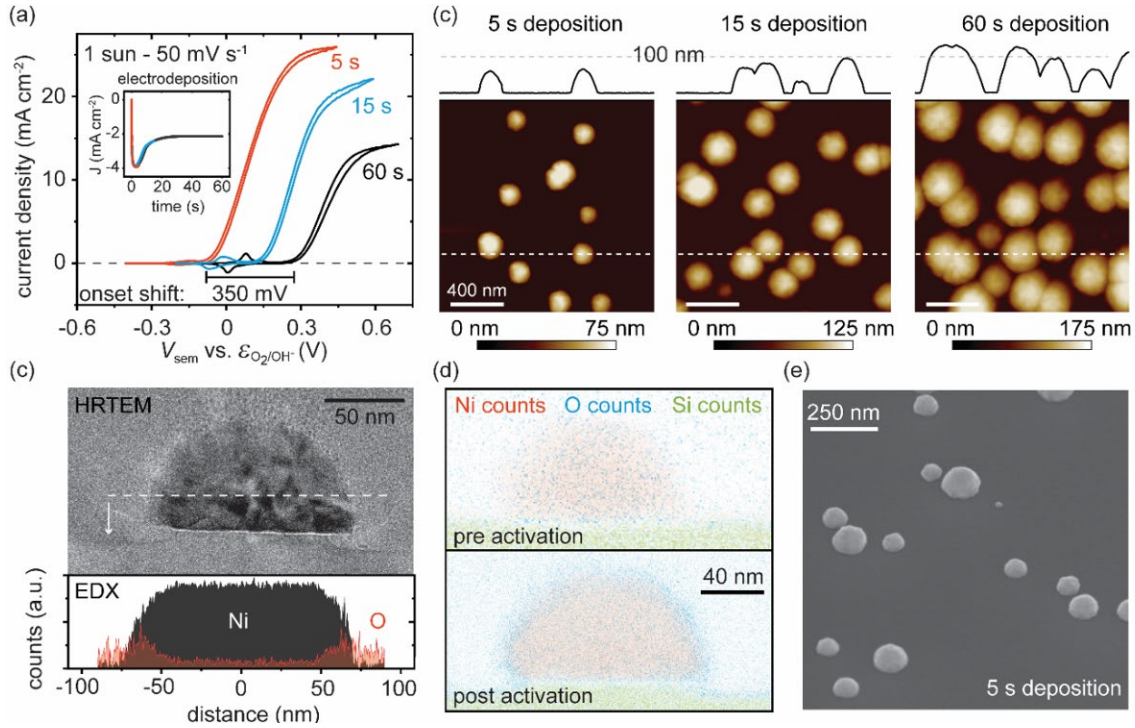


**Figure G.1. Characteristics of photoanodes fabricated by electrodepositing Ni nanoislands onto n-Si.** (a) Photoelectrochemical data for n-Si/Ni collected at  $50 \text{ mV s}^{-1}$  in 1 M KOH under  $100 \text{ mW cm}^{-2}$  AM1.5G illumination (one sun) after 50 CVs to activate the photoelectrode. The photocurrent onset, defined at  $1 \text{ mA cm}^{-2}$ , is improved by  $\sim 350 \text{ mV}$  for the 5-s Ni deposition relative to the 60-s one. The inset depicts characteristic chronoamperometry data for a 5, 15, and 60-s deposition. (b) AFM data collected immediately after 5, 15 and 60-s depositions with height line scans shown above each image. The results are characteristic of each specific surface, although regions of larger/smaller islands can sometimes be found. For the 5-s deposition, the Ni-island radii ranged from 35 to 150 nm. (c) High-resolution transmission electron microscopy (TEM) images and the associated energy-dispersive x-ray (EDX) analysis line scan data show that activation of the n-Si/Ni photoelectrode converts the Ni surface to  $\text{Ni}(\text{OH})_2/\text{NiOOH}$ . (d) EDX composition maps shown before (top) and after (bottom) photo-anodic activation of n-Si with 5 s of Ni deposition. The maps illustrate the conversion of Ni to  $\text{Ni}(\text{OH})_2/\text{NiOOH}$ . Additional elemental maps for non-

activated and activated islands are in Supplementary Section G.1. **(e)** Scanning electron microscope (SEM) image (at 45°) characteristic of a 5-s Ni deposition.

The Schottky barrier heights at individual n-Si/Ni nanocontacts were measured *ex situ* (i.e. in air) via conductive AFM prior to photoelectrochemical activation. A representative area was topographically imaged, single Ni nanocontacts were brought into contact with the conductive AFM tip (0.5 V piezo-deflection voltage), and dark  $J$ - $V$  curves were collected (Figure G.2a, inset). The barrier heights were calculated from the exchange-current density,  $J_0 = A^*T^2(e^{-q\phi_b/kT})$  where  $A^*$  is the effective Richardson constant,  $T$  is the temperature,  $q$  is the elementary charge, and  $k$  is the Boltzmann constant, by extrapolating the linear forward-bias region of the dark  $\ln |J|$ - $V$  curves to the  $y$ -intercept (ideality factors are in Supplementary Section G.2). The fits show that the barrier height is independent of Ni-island size (Figure G.2a) with a value ( $0.61 \pm 0.01$  V) near that of bulk n-Si/Ni contacts ( $\sim 0.58$  V)<sup>31</sup>.

The illuminated  $V_{oc}$  of each nanocontact was measured under  $\sim 5$ -sun-equivalent flux using a 690-nm laser contained in the AFM unit (Supplementary Section G.3). The  $V_{oc}$  values of  $310 \pm 10$  mV show little dependence on island size and agree with the calculated  $V_{oc}$  of 284 mV for a 0.61 V n-Si/Ni Schottky barrier under the experimental illumination (Figure G.2b). These barrier-height and  $V_{oc}$  results indicate that size-dependent interface behavior is not present for the as-deposited nanocontacts and thus cannot alone explain the photocurrent-onset potential differences with Ni deposition time (Figure G.1a).

We next studied the nanocontacts under photoelectrochemical conditions. Conductive AFM cantilevers in which the entire tip was isolated from the solution by a dielectric layer except for the apex<sup>32</sup> were used (inset of Figure G.2c). The custom AFM photoelectrochemistry cell and measurement details are presented in Supplementary Section G.3. Under illumination the semiconductor back ohmic contact was biased at a potential such that the catalyst particles were held in the electrically conductive NiOOH state while few bubbles were produced (i.e. near the photocurrent onset potential; vigorous bubble generation interferes with the AFM measurement). The surface was then topographically imaged and the photovoltage, i.e. the difference between the measured AFM tip potential and the potential applied to the semiconductor ohmic contact ( $V_{ph} = V_{tip} - V_{sem}$ ), was measured individually on each island. Photovoltages were collected both before and after activation with 50 photoanodic CV cycles (Figures G.2c and G.2d, this activation was used because, even for the smallest islands, most of the original metallic Ni remains and the nanoislands retain a well-defined hemispherical shape). Notably, the photovoltages are not only

substantially larger (in some cases  $> 500$  mV) than those measured under dry ex-situ conditions but they also depend on contact area (taken to be the two-dimensional geometric area in the AFM topography image) and increase with activation time. These results indicate a size-dependent mechanism for enhancing the Ni-nanocontact hole selectivity that is operative only in the presence of the OER-active NiOOH surface layer.

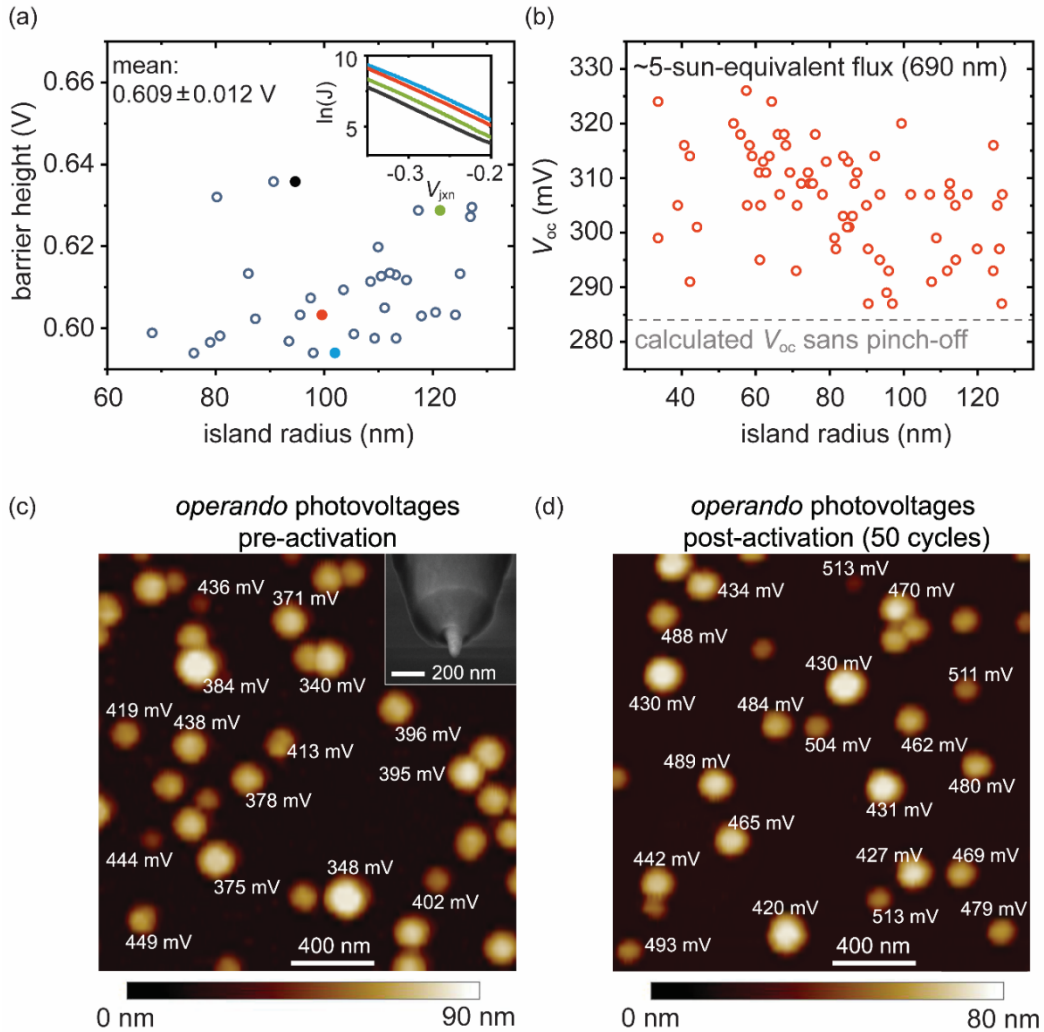


**Figure G.2. Characterization of n-Si/Ni photoelectrodes obtained from the 5-s deposition.** (a) n-Si/Ni barrier heights collected ex-situ from electrodes without activation show no dependence on Ni nanocontact radius. The inset shows  $\ln|J|$ - $V$  curves for the four colored points. (b)  $V_{oc}$  measurements extracted *ex situ*, under  $\sim 5$ -sun-effective illumination (690 nm), from electrodes without activation also show no significant dependence on Ni nanocontact radius. (c) *Operando* photovoltages collected using PS-EC-AFM prior to significant electrochemical activation, by landing the AFM tip on individual nanocontacts. The inset shows an SEM image of the PS-EC-



AFM Pt nanoelectrode tip. **(d)** *Operando* photovoltages collected at a different location after cycling the electrode under illumination from -0.35 to 0.35 V vs.  $\epsilon_{\text{O}_2/\text{OH}^-}$  50 times.

### 3. Analytical Model of Size-Dependent Photovoltages – The Pinch-off Effect

The experimentally observed size-dependent photovoltage can be explained by the “pinch-off” effect<sup>25</sup>, which occurs when an interface has spatially heterogeneous electrostatic barrier heights with low-barrier patches (here  $\phi_{\text{b}}^{\text{Ni}}$ ) surrounded by a higher-barrier background  $\phi_{\text{b}}^0$  (Figure G.3a). Pinch-off occurs when the depletion region induced by the adjacent higher-barrier region overlaps with the patch’s depletion region (i.e. with decreasing contact size the contact’s selectivity is increasingly dominated by the work function of its surrounding). For the system studied here, the electron conductivity decreases resulting in an increased photovoltage due to reduced recombination at the more-hole-selective contact. This model has been invoked to explain low-temperature deviations from ideal Schottky junction transport models<sup>8</sup> and used to control contact selectivity in nanowire-type devices by utilizing high/low-work-function layers acting as a surface gate.<sup>29</sup> In electrochemistry, the pinch-off effect has been used to explain the macroscopic behavior of intentionally patterned semiconductor photoelectrodes<sup>23,27</sup>; the effect, however, has never been studied by examining individual pinched-off nanocontacts.

We fit the experimental size-dependent photovoltage data to an analytical pinch-off model with a circular patch geometry (see Figure G.3a for model schematic and Supplementary Section G.4 for additional discussion).<sup>9,24,25</sup> The expression for the current through the nanocontact is given by a modified ideal-diode equation

$$I_{\text{patch}} = A^*T^2C_a \left( e^{\frac{-q\phi_{\text{b}}^0}{kT} + C_b} \right) \left( e^{\frac{qV_{\text{app}}}{nkT}} - 1 \right) \quad (1)$$

where  $C_a$  represents the effective contact area and  $C_b$  a decrease in the barrier height relative to the background barrier  $\phi_{\text{b}}^0$ . The exact forms of these perturbations are dependent on the dopant density ( $N_{\text{D}}$ ), band bending ( $V_{\text{bb}}$ ), nanocontact radii ( $r$ ), and  $\Delta$ , the difference between  $\phi_{\text{b}}^{\text{Ni}}$  and  $\phi_{\text{b}}^0$ :

$$C_a = \frac{4\pi kT}{9q} \left( \frac{3\Delta r^2}{4} \right)^{1/3} \left( \frac{\epsilon_{\text{s}}}{qN_{\text{D}}V_{\text{bb}}} \right)^{2/3} \quad (2)$$

$$C_b = \frac{q}{kT} \left( \frac{3q\Delta r^2 V_{\text{bb}} N_{\text{D}}}{4\epsilon_{\text{s}}} \right)^{1/3} \quad (3)$$

The photovoltage data was assessed by assuming a patch barrier height of  $\phi_b^{\text{Ni}} = 0.61$  V (the average n-Si/Ni contact barrier height) and then fitting the background barrier ( $\phi_b^0$ ) to the analytical model using to reproduce the contact-size dependence (Supplementary Section G.4). The fits indicate  $\phi_b^0 = 0.82$  V for the n-Si/Ni sample prior to intentional activation and  $\phi_b^0 = 0.91$  V after photoelectrochemical activation (Figure G.3b). The chemical nature of this high-barrier region and the feasibility of the extracted  $\phi_b^0$  values are discussed in the subsequent section.

Pinch-off increases minority-carrier selectivity by reducing the flow of majority carriers that lead to recombination in the contact. Significant pinch-off behavior is expected when  $\frac{\Delta}{V_{\text{bb}}} > \frac{2r}{W}$ , where  $W$  is the depletion-region thickness<sup>33</sup>. For  $\phi_b^0$  of 0.82 V and 0.91 V with  $\phi_b^{\text{Ni}} = 0.61$  V, significant pinch-off is predicted for contacts with radii below  $\sim 110$  and  $140$  nm, respectively. The Ni particles studied here have radii between 30 and 150 nm. To illustrate the effect of pinch-off on carrier selectivity we plot the calculated conduction-band-potential ( $E_{\text{CB}}$ ) profile as a function of both the distance from the center of a 60-nm-radius Ni nanocontact and the depth into the semiconductor (Figure G.3c). The junction is shown poised at open circuit under 1 sun illumination (corresponding to photoelectrochemical conditions where the back contact of the semiconductor is held at a potential near the photocurrent onset). A pinched-off “saddle point” in the conduction-band energy with a maximum value near 0.8 V and a confined cross section relative to the 120-nm Ni-particle diameter (Figure G.3b) is apparent. This increased barrier (relative to the macroscopic barrier of 0.61 V) results in a lower electron conductivity and hence improved hole-selectivity and reduced recombination. The pinch-off effect thus leads to photovoltages that are not only dependent on the contact’s work function, but also its size, its geometry, and the work function of the surrounding medium.

The pinch-off model can explain the observed current-potential data for the n-Si/Ni oxygen-evolving photoanodes (Figure G.1a). The experimental data is modeled by solving current continuity for the modified diode expression in series with a circuit element representing the catalyst driving the OER. The OER potential drop is obtained from a Butler-Volmer expression based on the measured OER activity of Ni electrodeposited on Pt (see Supplementary Section G.4). The model is consistent with the experimental data for electrodes with 5-s depositions when the diode expression represents uniform Ni catalyst nanocontacts that have radii of 60 nm and 15% surface coverage (we observed 10-20% experimentally). The result suggests that, at least near the photocurrent onset, the current is primarily passed through surface islands smaller than the average

( $80 \pm 25$  nm radii) that have larger effective barrier heights. This model illustrates that the photocurrent-onset-potential shift observed for the small particles is completely accounted for by enhanced hole selectivity due to the pinch-off effect. The 60-s deposition produces Ni particles too large to leverage pinch off and thus the photoelectrode response in that case is consistent with the bulk n-Si/Ni Schottky junction driving charge separation (Figure G.3d).

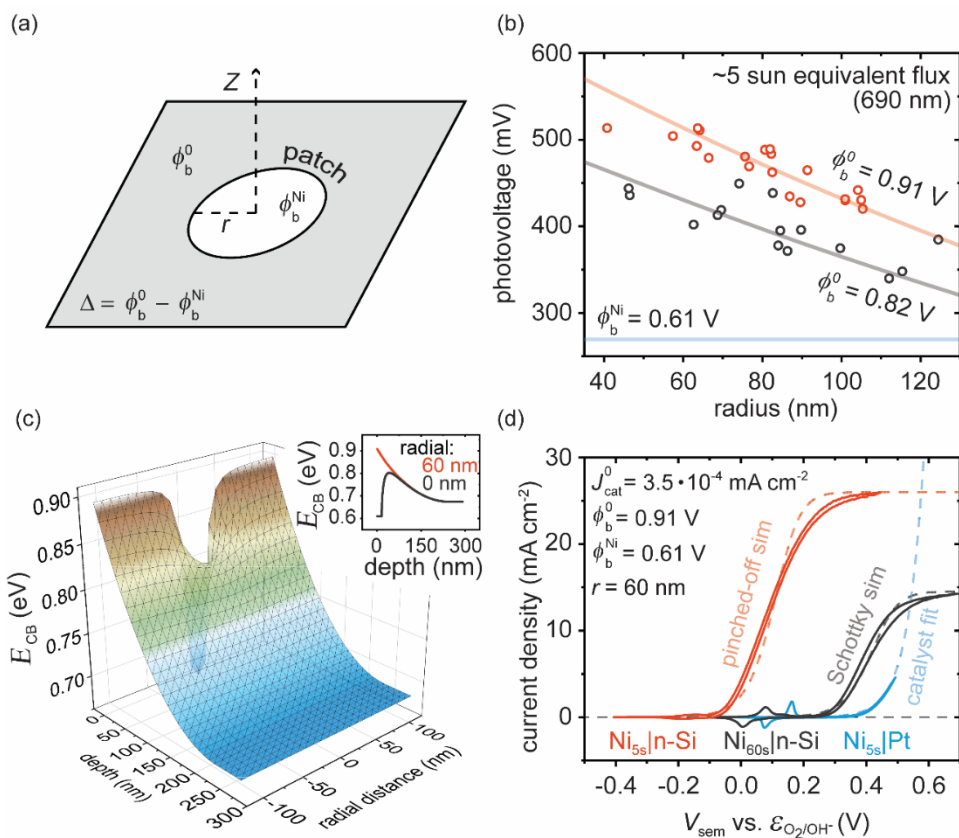


**Figure G.3. Simulations showing how the pinch-off model explains performance enhancements with catalyst nanocontacts.** (a) Tung's model<sup>33</sup> for the circular patch geometry is used where a small barrier  $\phi_b^{\text{Ni}} = 0.61$  V representing the n-Si/Ni contact is surrounded by a region with larger barrier height  $\phi_b^0$ . (b) With  $\phi_b^{\text{Ni}} = 0.61$  V the pinch-off model indicates a surrounding barrier of 0.82 V and 0.91 V for the non-activated and activated interfaces, respectively. The surrounding barrier height ( $\phi_b^0$ ) is the only fitting parameter. (c) The conduction-band energy ( $E_{\text{CB}}$ ) is plotted at  $V_{\text{oc}}$  under 1 sun illumination for a 60-nm-radius island with  $\phi_b^0 = 0.91$ . The inset shows a cross-section of the barrier through the center of the island (radial distance = 0 nm) and at the edge of the island (radial distance = 60 nm). A pinched-off saddle point occurs with an effective barrier near 0.8 V – a value significantly larger than the average 0.61 V barrier height measured ex situ. (d) The macroscopic voltammetry is consistent with that predicted by the pinch-off model.

The photoelectrochemical data for n-Si with 5 s of Ni deposition is consistent with  $\phi_b^0 = 0.91$  V, assuming uniform islands with 60-nm radii covering 15% of the surface.

#### 4. Chemical Identity of the High-Barrier Region

Although the model shows that the photovoltage trend with nanocontact size can be explained by pinch-off, this requires the presence of a high-barrier region surrounding the n-Si/Ni contact. Since the experimentally measured dry barrier heights and illuminated  $V_{oc}$  values are independent of the Ni nanocontact size (Figure G.2a and G.2b) such a region is not present prior to photoelectrochemical activation. The activation process results in oxidation of any exposed Si to  $\text{SiO}_x$  and converts a portion of the Ni to  $\text{Ni}(\text{OH})_2/\text{NiOOH}$ . To evaluate the barrier height in surface regions only covered by the  $\text{SiO}_x$  layer (and not  $\text{NiOOH}$  or Ni) we performed Mott-Schottky impedance analysis in a ferro/ferricyanide electrolyte (aq. 1 M KCl, 0.05 M  $\text{K}_3\text{Fe}(\text{CN})_6$ , and 0.35 M  $\text{K}_4\text{Fe}(\text{CN})_6$ ) on bare n-Si photoanodes. The ferro/ferricyanide solution potential sets the barrier height at the n-Si/electrolyte interface to  $\sim 0.7$  V (larger than the n-Si/Ni barrier height of  $\sim 0.6$  V). Anodic cycling of the n-Si leads to the growth of a  $\text{SiO}_x$  passivation layer. Subsequent Mott-Schottky analysis shows that the  $\text{SiO}_x$  layer lowers the barrier height to  $\sim 0.5$  V (Supplementary Section G.5). This data indicates that  $\text{SiO}_x$  cannot be responsible for setting the proposed large background barrier height around the Ni islands.

Another possible mechanism is that oxidized catalyst with a large work function induces the large background barrier. To evaluate the barrier height of the  $\text{Ni}(\text{OH})_2/\text{NiOOH}$  on n-Si, we fabricated dual-working-electrode devices by (i) depositing a 2-nm-thick uniform Ni-metal layer on the n-Si via electron-beam evaporation, (ii) photodepositing additional Ni (oxy)hydroxide from saturated  $\text{NiCl}_2$  solution in 1 M K-borate buffer (pH 9.5) by applying 0.625 V vs.  $\mathcal{E}_{\text{O}_2/\text{OH}^-}$  under one-sun illumination for 30 s, (iii) photoelectrochemically cycling the electrode in 1 M K-borate buffer until no photocurrent was evident (which oxidized remaining Ni metal and the n-Si surface), and (iv) depositing a 10-nm-thick porous Au contact layer on the catalyst surface (Figure G.4a and Supplementary Section G.6). The Au contact on these metal-oxide-semiconductor-type devices was biased, in an electrochemical cell, to hold the catalyst layer in either its reduced,  $\text{Ni}(\text{OH})_2$ , or oxidized,  $\text{NiOOH}$ , form while impedance spectroscopy was performed at a series of DC biases between the Au and back semiconductor contact (Figure G.4b). Mott-Schottky<sup>26</sup> analysis of the extracted bias-dependent depletion capacitances yield the dopant densities consistent with the manufacturer specifications ( $5 - 8 \cdot 10^{15} \text{ cm}^{-3}$ ) and show that the interfacial barrier depends on the redox state of the catalyst (Figure G.4b inset). When the Au top contact is poised to hold the catalyst

in the  $\text{Ni}(\text{OH})_2$  state, the barrier height is 0.65 V. When the catalyst is oxidized (i.e. in the OER-active state) the barrier is 1.04 V, similar to the large background barrier heights indicated by the fit to the analytical pinch-off model (Figure G.3b). Figures G.4c, 4B.4d, and 4B.4e depict the band-bending and barrier-height differences between Ni,  $\text{Ni}(\text{OH})_2$ , and  $\text{NiOOH}$  contacts to n-Si, respectively. This result is conceptually similar to so-called “adaptive junctions” where the barrier height of a contact to an n-type semiconductor is enhanced during operation as the electrolyte-permeable contact is converted to a higher oxidation state by accumulated holes.<sup>34,35</sup> The result is also consistent with n-Si/ $\text{Al}_2\text{O}_3$ /Pt/Ni photoanodes where the barrier height was increased by 0.23 V upon oxidation of the Ni catalyst, although the thin Pt layer was noted to partially screen the effect.<sup>36</sup>

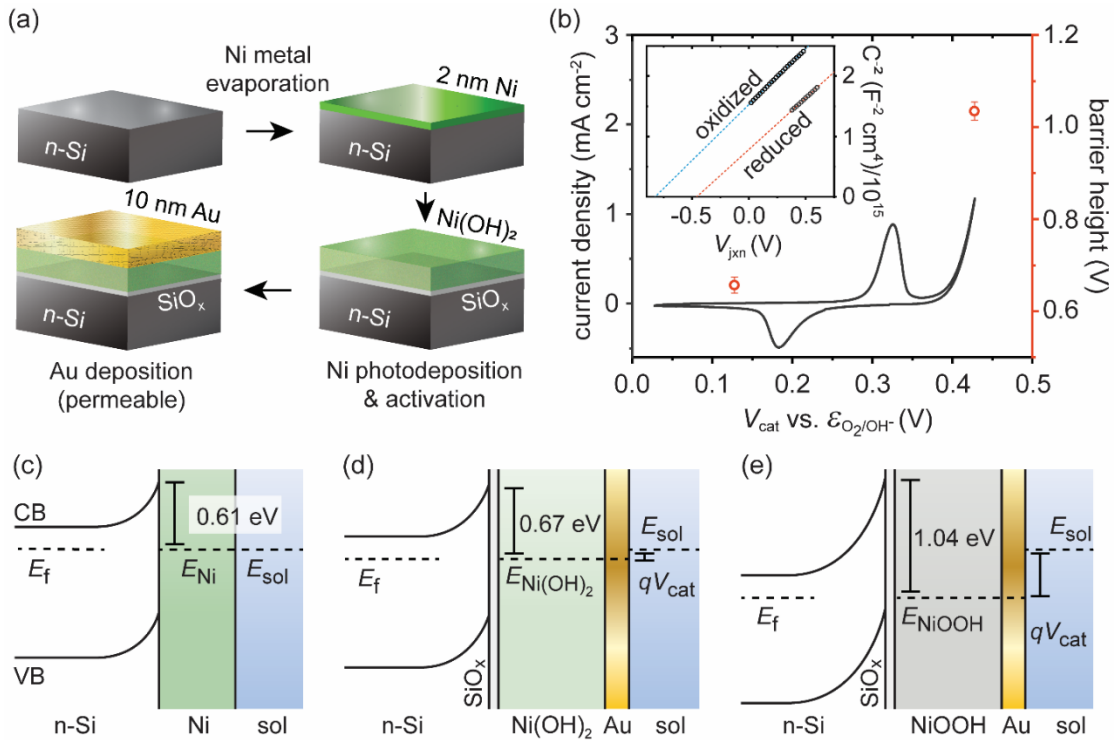


**Figure G.4. Dual-working-electrode (DWE) device measurements show that high-barrier contacts are formed from the oxidized  $\text{NiOOH}$  during operation.** (a) The schematic illustrates how DWE devices are fabricated. Connections to the backside of the n-Si and to the Au layer are used to perform impedance experiments while the  $\text{Ni}(\text{OH})_2/\text{NiOOH}$  layer is potentiostatically held in either its reduced ( $V_{\text{cat}} = 0.125$  V vs.  $\epsilon_{\text{O}_2/\text{OH}^-}$ ) or oxidized ( $V_{\text{cat}} = 0.425$  V vs.  $\epsilon_{\text{O}_2/\text{OH}^-}$ ) state. (b) The voltammograms show the  $\text{Ni}(\text{OH})_2/\text{NiOOH}$  redox behavior as it is cycled through the Au secondary working electrode at  $20$   $\text{mV s}^{-1}$  in  $1$  M K-borate buffer at pH 9.5. Mott-Schottky analysis on the impedance data collected between the Au and semiconductor back contact (inset) shows that

oxidation Ni(OH)<sub>2</sub> to NiOOH causes the barrier height to increase from 0.66 V to 1.04 V. Band-bending diagrams, as deduced from Mott-Schottky analysis, are shown for **(c)** metallic Ni, **(d)** Ni(OH)<sub>2</sub>, and **(e)** NiOOH contacts to the n-Si. The barrier heights increase as the Ni is successively oxidized to higher oxidation states. The symbols  $E_f$ ,  $E_{Ni}$ ,  $E_{Ni(OH)_2}$ ,  $E_{NiOOH}$  and  $E_{sol}$  represent the electrochemical potential for the semiconductor, Ni, Ni(OH)<sub>2</sub>, NiOOH and solution ( $E_{sol} = q\varepsilon_{O_2/OH^-}$ ), respectively. The magnitude of  $qV_{cat}$  is depicted in (d) and (e) and corresponds to the data points in panel (b). See Supplementary Section G.6 for further discussion.

The above results are consistent with the n-Si/Ni photoanodes exhibiting an emergent pinch-off phenomenon. After photoanodic generation of NiOOH, high-barrier regions on the n-Si are produced because the work function of NiOOH ( $> 5.3$  eV)<sup>37</sup> is larger than that of metallic Ni (5.0 eV). The large barrier is also consistent with the Ni(OH)<sub>2</sub>/NiOOH redox potential ( $\sim 1.35$  V vs. RHE) being  $> 1$  V more positive than the flat-band potential of n-Si ( $\sim 0.25$  V vs. RHE)<sup>38</sup>. The improved photocurrent onset potentials for activated devices with smaller Ni particles (5-s deposition) are therefore due to low-barrier n-Si/Ni interfaces “pinched-off” by high-barrier n-Si/SiO<sub>x</sub>/NiOOH interfaces (Figure G.5). The pinched off n-Si/Ni junctions form hole-selective contacts and suppress majority-carrier electron transfer to the catalyst, compared to non-pinched-off analogues, while maintaining direct low-resistance electrical connection between the Ni and n-Si. Photoanodes decorated with large islands (e.g. radii  $> 140$  nm) or those that have not been activated to form the NiOOH layer (Supplementary Figure G.S7) show poor performance due to the lack of this pinch-off phenomena improving the Ni nanocontact hole selectivity. Continued activation (beyond 50 cycles) further improves the photocurrent onset until the underlying n-Si is oxidized when the Ni is completely converted to electrolyte-permeable NiOOH, blocking all current flow (Supplementary Section G.7). This improvement is attributed to increased Ni oxidation which enhances pinch-off by decreasing the n-Si/Ni contact area. The extent of NiOOH necessary to produce pinch-off is discussed in Supplementary Section G.8 and supported by COMSOL finite-element simulations of the nanoscale junction.

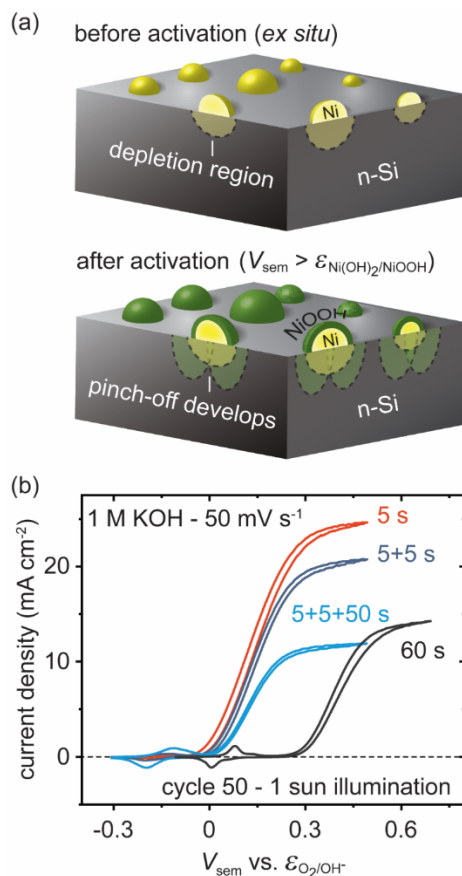


**Figure G.5. n-Si/Ni nanocontacts produce a pinched-off junction after activation.** (a) Schematic illustrating the depletion regions produced by the surface contacts before and after activation. Although the initial depletion region is small, the conversion of surface Ni to NiOOH produces a larger depletion region which causes the n-Si/Ni contact to become pinched-off and increase in hole selectivity. The necessary extent of conversion required to produce pinch-off is discussed in Supplementary Section G.8. Simulation shows that the NiOOH likely extends on the surface beyond the clearly evident shell. (b) The pinch-off hypothesis is corroborated by examining devices with cumulative 60-s electrodepositions where the pinched-off junction is intentionally retained. By halting the electrodeposition after 5 and 10 s to perform activation cycles that generate an interfacial SiO<sub>x</sub>, the photocurrent onset remains near that of the devices with 5 s of Ni electrodeposition.

To further test the pinch-off hypothesis we deposited Ni for 5 s, oxidized the Si and Ni surface via 50 photoelectrochemical potential cycles, then electroplated Ni for an additional 55 s (Figure G.5b). These devices showed a photocurrent-onset potential ~250 mV more positive than n-Si/Ni fabricated with a continuous 60-s Ni electrodeposition (Supplementary Section G.9). The

light-limited photocurrent and integrated redox peaks for the samples, however, are similar indicating a comparable Ni surface area. These results are explained by the fact that the potential cycling step oxidizes the underlying Si surface in regions where Ni has not been deposited and subsequent Ni deposition serves only to grow the existing Ni nanoparticles without increasing n-Si/Ni contact area. The pinched-off junction is thus maintained.

## 5. Pinch-off in Photoelectrode Devices

Our direct measurements of pinch-off explain previous observations for a variety of catalyst-coated semiconductor photoelectrodes. Kenny *et al.* found that 2-nm-thick Ni layers on n-Si show a photocurrent onset 200 mV more negative than 5-nm-thick layers.<sup>21</sup> This difference cannot be explained by resistive losses through the thicker catalyst layer or parasitic light loss.<sup>7</sup> The data is readily explained, however, by electrochemical activation of the 2-nm Ni film which produces nanoscale low-barrier semiconductor/metal contacts pinched-off by high-barrier semiconductor/oxide/metal-oxyhydroxide contacts<sup>7</sup>. Similar observations have been noted for devices where catalyst nanocontacts were intentionally deposited. Loget *et al.* noted a ~200 mV improvement in photocurrent-onset potential after 40 photoelectrochemical conditioning cycles when comparing n-Si coated with Ni nanoislands ( $59 \pm 17$  nm diameter) to n-Si coated with a uniform Ni film.<sup>20</sup> Xu *et al.* found a similar improvement in photocurrent onset, without activation, when NiOOH was photodeposited after initial Ni-metal island formation.<sup>39</sup> Annealing the Ni metal nanoparticles to oxidize their surface has also been shown to improve photocurrent onset without requiring electrochemical cycling.<sup>40</sup> For n-Si/Co photoanodes the barrier height was found to be a function of Co coverage with low coverage (i.e. coalesced islands of  $21 \pm 8$  nm in diameter) yielding photoanodes with a 360-mV improvement in photocurrent onset relative to uniform Co films (pinch-off was also hypothesized and rationalized in this work, but not analyzed via direct measurement).<sup>26</sup> For p-GaAs photocathodes, the better HER performance was achieved by using small Pt nanoparticles 10 nm in diameter, relative to 90-nm particles.<sup>41</sup> p-Si nanowires decorated with NiCoSe<sub>x</sub> nanoparticles show a 110 mV improvement in the flat-band potential relative to a planar NiCoSe<sub>x</sub>/p-Si.<sup>42</sup> For particulate semiconductors, size-dependent photocatalytic activity has been observed for particulate n-TiO<sub>2</sub> decorated with Au nanoparticles, with the smallest nanoparticles being the most active.<sup>43</sup> The above results are likely due to pinch-off where the high-barrier region is attributed either to contact with oxidized catalyst or with the electrolyte.

The insight illustrated here may be useful in designing improved devices by engineering nanocontact selectivity. Although high-performance selective contacts to Si can be achieved by



forming doped-semiconductor homo/heterojunctions,<sup>44</sup> for some applications carrier-selective junctions formed by depositing electrochemically stable contacts may be useful.<sup>45</sup> This approach is difficult, however, because of the lack of materials that form carrier-selective heterojunctions while remaining stable and electrically conductive under electrochemical conditions. An alternative strategy might focus on depositing stable/conductive nanocontacts before engineering the surrounding surface to induce selectivity via pinch-off (see Supplementary Section G.9). For emerging photoelectrode materials, particularly oxides<sup>1</sup> such as BiVO<sub>4</sub> or photoactive particulate semiconductors like TiO<sub>2</sub> and SrTiO<sub>3</sub><sup>46,47</sup>, designing carrier-selective contacts is even more difficult. This challenge might be addressed by using sufficiently small catalytic contacts and engineering the surrounding surface (which does not need to provide catalytic sites nor collect charge) to induce a large interface electrostatic barrier. The redox activity of such a selectivity-inducing material might be leveraged to improve selectivity during operation.

## 6. Conclusions

Understanding and controlling the selective flow of electron and holes is critical in the design of efficient photoelectrochemical devices. We provide the first example of spatially resolved potential measurements on electronically isolated nanoscale features in operating photoelectrochemical systems. This capability enables the interfacial behavior of nanoscale contacts to semiconductor photoelectrodes to be directly interrogated. By translating the approach to polycrystalline thin-film<sup>13</sup> or nanostructured<sup>48</sup> photoelectrodes coated with nanoparticle catalyst particles, heterogeneity in the underlying semiconductor properties could be probed through their effect on the photovoltage measured at individual nanoparticle semiconductor/catalyst contacts. The technique should further enable studies of catalyst-contact properties in particulate photoelectrochemical systems where both anode and cathode catalyst are dispersed on the same semiconductor particle<sup>47,49</sup>. We further provide the first measurement of pinch-off achieved by characterizing individual nanocontacts in photoelectrochemical devices. For photoelectrochemical devices, the pinch-off effect has only been experimentally studied previously via macroscopic current-voltage measurements utilizing intentionally nanofabricated monodisperse contacts and a reversible redox couple.<sup>27</sup> The pinch-off phenomena studied here provide evidence that the effect can be utilized, possibly in a wide range of semiconductor and catalyst systems, to create photoelectrochemical devices with high efficiency.

The ability to measure local surface potentials with PS-EC-AFM could be useful in other areas. The technique and data interpretation are straightforward, with measurements only reliant on electrochemical-potential equilibration between the AFM tip and the feature of interest. Nanoscale-

resolved surface-potential sensing is perhaps useful in measuring heterogeneity of processes in fuel-cell/electrolyzer catalyst-ionomer structures<sup>50</sup> and intercalation/deintercalation phenomena in battery electrodes<sup>51,52</sup>. The technique might aid biological research, where potential measurements in physiologically relevant electrolyte is challenging<sup>12,53</sup>, by allowing direct measures of bacterial<sup>53</sup> and membrane surface potentials<sup>54</sup>. The technique could also be adapted to apply potential to nanoscale features instead of sensing potential. It may be possible to locally study charge-transfer processes and extract basic parameters related to conductivity, catalytic rates, and double-layer capacitance on isolated nanoscale features in operating (photo)electrochemical systems.

## CHAPTER V: CONCLUSIONS

The impacts of these works on the photoelectrochemical energy conversion field largely remain to be seen. However, at the time of writing, the dual-working-electrode (DWE) technique has been adopted by at least four other groups. Potential-sensing electrochemical atomic force microscopy (PS-EC-AFM) has yet to be adopted but represents a significant improvement over DWE analysis because it can measure nanoscale semiconductor|catalyst interfaces. Many current efforts in photoelectrochemical water splitting (e.g. those employing nanowire semiconductors and overall water splitting particulates) could foreseeably benefit from nanoscale potential sensing. Currently the main limitation of the PS-EC-AFM technique is slow data collection, where a topographical image must be captured prior to sensing the potential at a single location. Future iterations of the approach might look to sense surface potentials in tandem with the initial topology mapping.

The analytical descriptions of charge transport across the semiconductor|catalyst interface presented herein are far simpler than traditional numerical modeling approaches. The analytical equations should make prediction and modeling of semiconductor|catalyst interfacial behavior much easier for researchers. The equations also provide significant insight on how semiconductor surface states (often invoked to qualitatively explain unexpected behavior) affect charge transport through the semiconductor|catalyst interface.

Finally, an understanding of how the “pinch-off” effect can influence photoelectrochemical devices was largely absent from the literature base prior to this work. The “pinch-off” effect likely underpins numerous results in the literature base, as discussed in Chapter 4, and this knowledge should aid investigators in better interpreting results. Intentional application of the “pinch-off” effect to enhance carrier selectivity may be useful for designing more efficient photoelectrodes. For oxide semiconductors (e.g.  $\text{BiVO}_4$  &  $\text{Fe}_2\text{O}_3$ ), where charge separating homojunctions are difficult to fabricate, “pinch-off” engineering to create selective heterojunctions is a promising alternative.

## APPENDICES

### APPENDIX A. SUPPORTING INFORMATION FOR PAPER C

#### Transient Photocurrents on Catalyst-Modified n-Si Photoelectrodes: Insight from Dual-Working Electrode Photoelectrochemistry

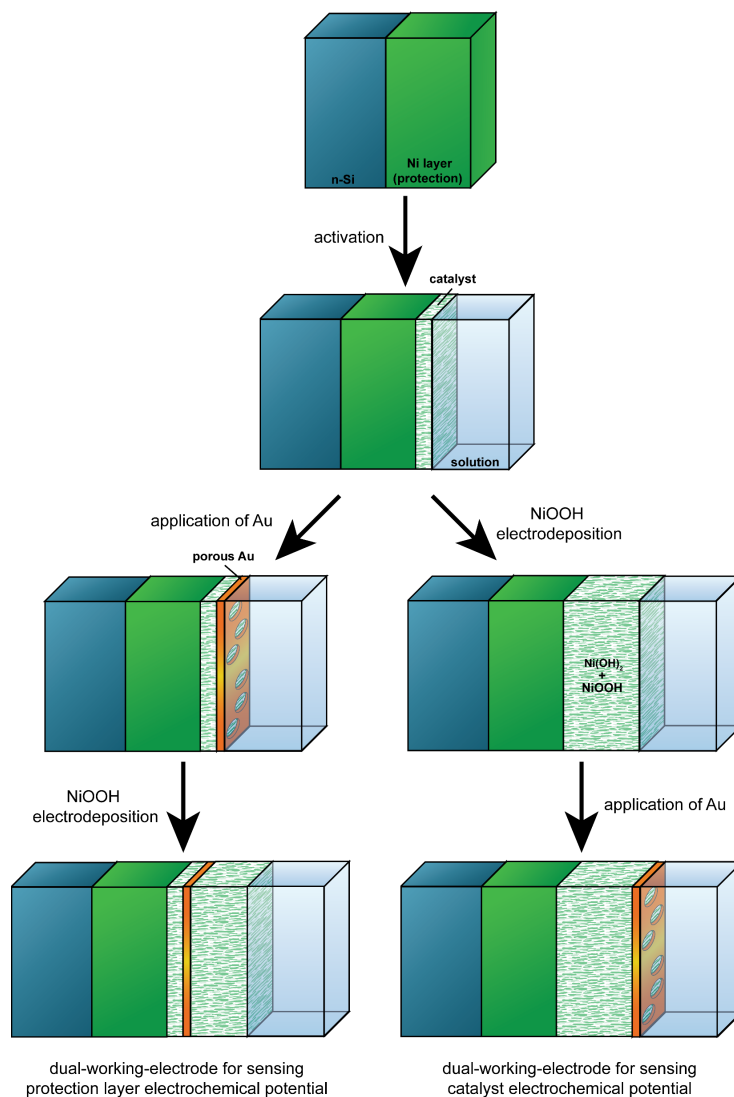


**Figure C.S1. Two dual-working-electrode (DWE) deposition strategies.** Both strategies begin by activating the metallic Ni protection layer via electrochemically cycling 50 times through potentials that span the redox wave under  $\sim 1$  sun illumination. For a DWE that senses the protection layer electrochemical potential (depicted by the left fork), the thin porous Au contact is

deposited immediately after activation. The NiOOH layer is sufficiently thin such that areas of contact form between the metallic Ni and the Au film. Additional NiOOH is then electrodeposited (photo-assisted) on top of the Au contact. For a DWE that senses the catalyst electrochemical potential (depicted by the right fork), the additional NiOOH catalyst is deposited prior to the porous Au layer. This prevents the Au film from contacting the protection layer.

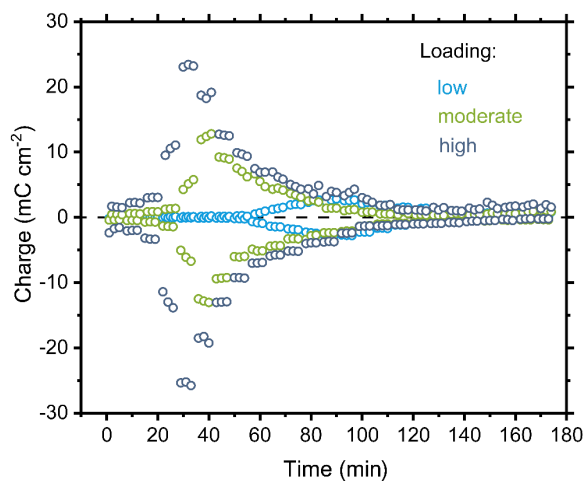


**Figure C.S2. Transient integration comparison between the different extents of catalyst loading.** All data is collected on the same electrode with NiOOH loading sequentially increased via photo-assisted electrodepositions. Increasing the amount of redox active catalyst results in transients with larger charge integrals.

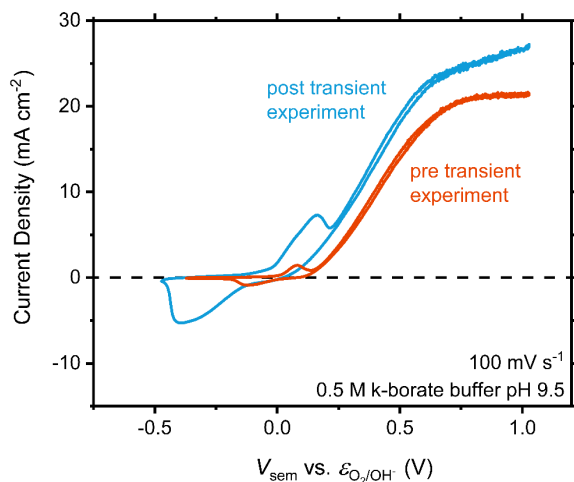


**Figure C.S3. Comparison of electrode activity before and after the first transient experiment.** Cyclic voltammograms are collected on the same electrode as in Figure C.1 of the main text. The transient experiment results in a cathodic shift of oxygen evolution onset and an increase in the

redox peak integrations. The data indicates that the transient experiment ages the electrode and converts some of the protection layer to redox active NiOOH/Ni(OH)<sub>2</sub>. The cathodic onset shift is attributed to an increase in the photovoltage. Increased photovoltage also explains the cathodic shift in the region of large integrated transient charge for Figure C.1 and Figure C.S2.

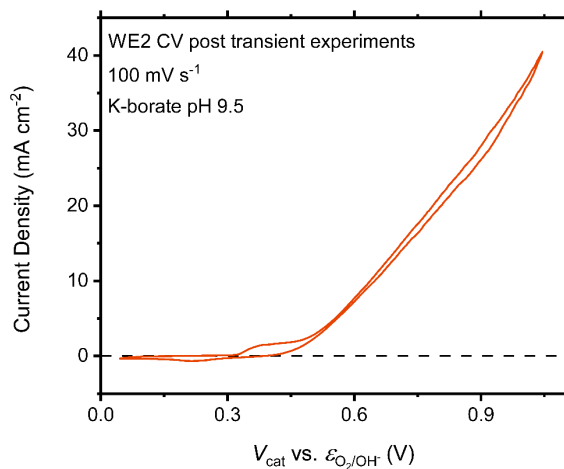


**Figure C.S4. Cyclic voltammogram through the WE<sub>2</sub> contact after transient experiments showing position of the oxidation and reduction waves for the catalyst.** The data is from the same electrode as in Figure C.3 of the main text; i.e. WE<sub>2</sub> is in direct contact with the outer catalyst layer. Note that redox integration is small here, most likely due to mechanical exfoliation of the Au contact during the experiment. Onset of catalyst oxidation occurs at  $\sim 0.3$  vs.  $\epsilon_{\text{O}_2/\text{OH}^-}$  while reduction occurs at  $\sim 0.25$  vs.  $\epsilon_{\text{O}_2/\text{OH}^-}$ .

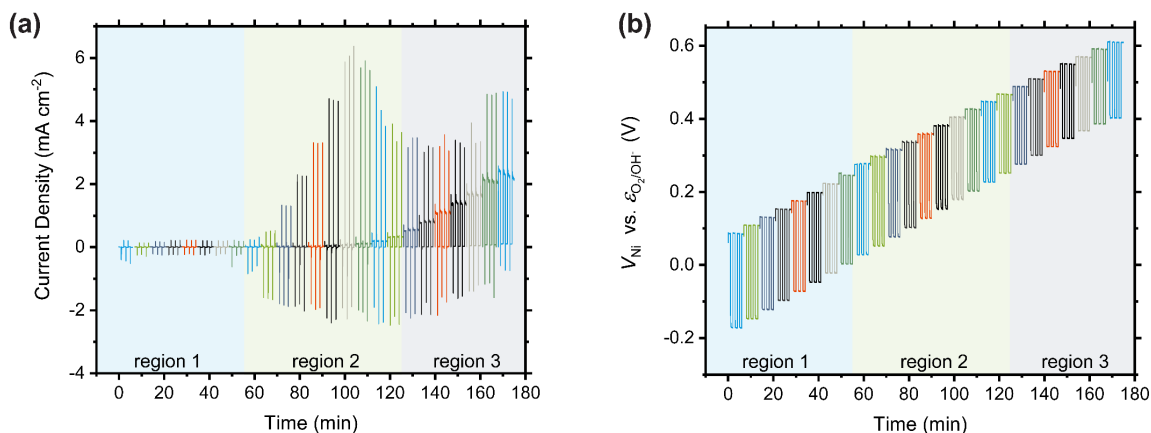


**Figure C.S5. Full transient behavior for the electrode used to sense the protection layer electrochemical potential (from Figure C.5).** (a) The photocurrent transients as a function of time. The regions of transient activity are denoted as in Figure C.3 of the main text. These are

assigned by examining the redox integration in Figure C.S7. **(b)**  $V_{Ni}$  response during transient experiments. The voltage sensed by WE<sub>2</sub> always responds to changes in the applied potential or light condition. This indicates that the porous Au layer is in contact with the protection layer and is not influenced by the catalyst's conductivity transitions.

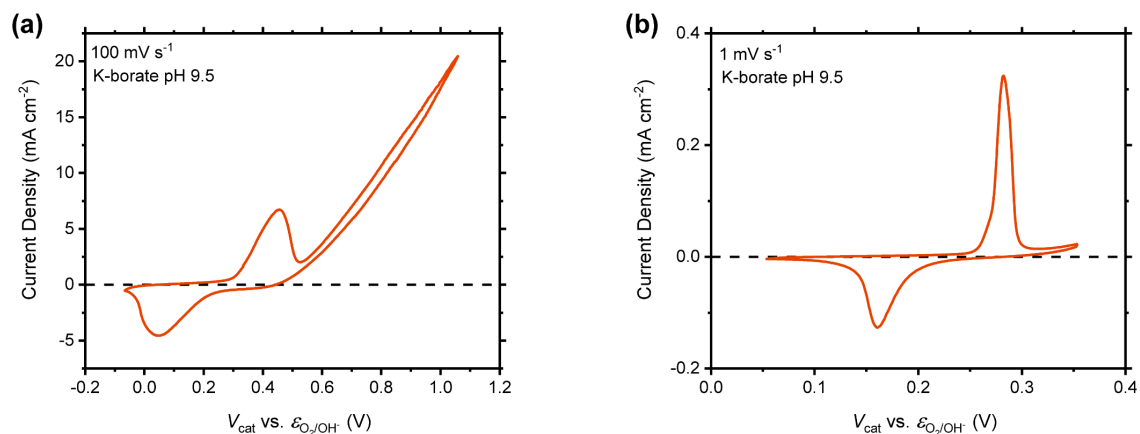


**Figure C.S6. Cyclic voltammogram through the WE<sub>2</sub> contact after transient experiments.**

The data is from the same electrode as in Figure C.5 of the main text; i.e. WE<sub>2</sub> is in direct contact with the Ni protection layer. **(a)** Data collected at 100 mV s<sup>-1</sup> shows that onset of oxidation occurs at ~ 0.3 vs. ε<sub>O<sub>2</sub>/OH<sup>-</sup></sub> while reduction occurs at ~ 0.2 vs. ε<sub>O<sub>2</sub>/OH<sup>-</sup></sub>. **(b)** Data collected at 1 mV s<sup>-1</sup> approximates steady-state behavior and shows that redox states exist over a 40-50 mV range. This range is comparable with the region of diminished decay in Figures C.5b and C.5c.

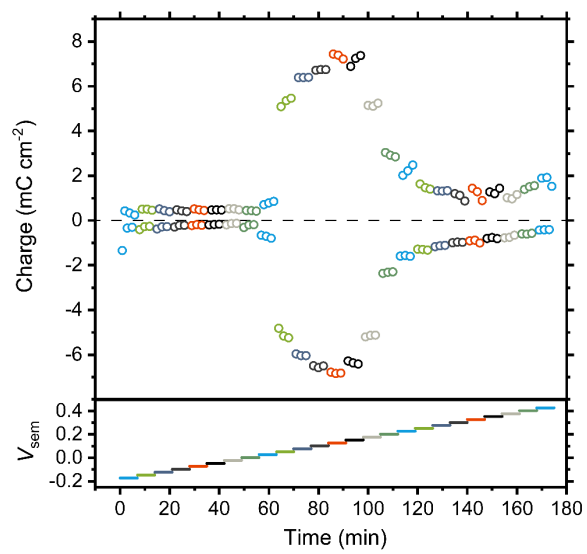


**Figure C.S7. Integration of the photocurrent transients from Figure C.5 of the main text.** Behavior is very similar to the transients from Figure C.2, where a region of increased integrated transient charge occurs. The region with increased integration is defined as “region 2”. The bottom pane shows  $V_{\text{sem}}$  vs.  $\epsilon_{\text{O}_2/\text{OH}^-}$  as a function of time.



## APPENDIX B. SUPPORTING INFORMATION FOR PAPER D

### Behavior of Catalyst-Modified n-Si Photoelectrodes in the Presence of a Sacrificial Hole Scavenger: Insight from Dual-Working Electrode Photoelectrochemistry

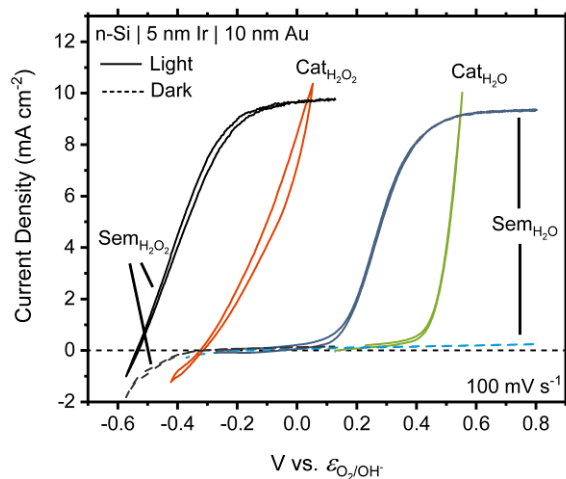


**Figure D.S1. Comparison of electrochemical behavior for a n-Si | Ir photoanode with and without a 0.5 M H<sub>2</sub>O<sub>2</sub> hole scavenger.** All experiments were performed on the same electrode without altering its position relative to the 1 sun solar simulator source. The curves labeled with the H<sub>2</sub>O subscript indicate experiments without hole scavenger presence, whereas the H<sub>2</sub>O<sub>2</sub> subscript indicates hole scavenger presence. Curves labeled “Sem” indicate that cyclic voltammetry data was collected by applying the potential to the semiconductor back-contact. Curves labeled “Cat” indicate that the data was collected by applying the potential to the secondary Au contact. The two dashed curves represent the Sem behavior in the dark and show that leakage current is minimal. The difference in OER onset for the SemH<sub>2</sub>O and CatH<sub>2</sub>O is the photoanodes photovoltage. The results show that the photovoltage is retained once H<sub>2</sub>O<sub>2</sub> is introduced. In this case, the H<sub>2</sub>O<sub>2</sub> acts to enhance charge injection without holding the catalyst in a reduced, insulating state.

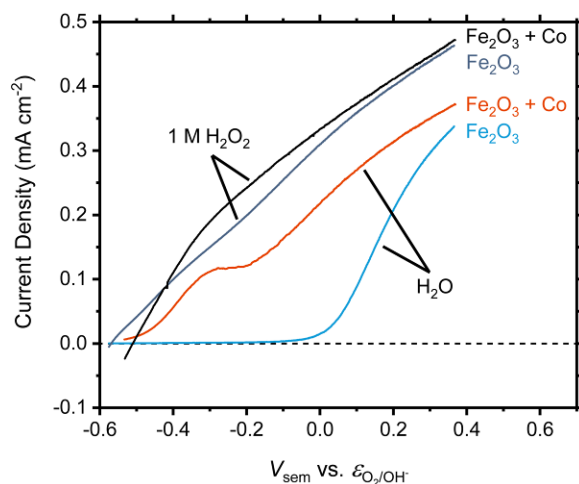


**Figure D.S2. Comparison of  $\text{H}_2\text{O}_2$  and  $\text{H}_2\text{O}$  oxidation responses before and after Co-Pi deposition on a  $\text{Fe}_2\text{O}_3$  photoanode.** All linear sweep voltammograms are collected on the same electrode, in 1 M potassium phosphate buffer (pH 9.5), without repositioning between experiments. Co-Pi deposition was achieved by draining the electrolyte, introducing a  $\text{CoCl}_2$  solution into the 3-neck electrochemical cell and performing a photo-assisted (1 sun) deposition. During the 10 min photo-assisted deposition the potentiostat maintained chronopotentiometry at  $10 \mu\text{A cm}^{-2}$ . The solution was then drained, rinsed, and refilled with the potassium phosphate buffer. The results show differences in the hole scavenged behavior before and after Co-Pi electrodeposition. At sufficiently cathodic potentials ( $V_{\text{sem}} < -0.5$  vs. vs.  $\epsilon_{\text{O}_2/\text{OH}^-}$ ), the bare photoanode exhibits higher current densities. Whereas at more anodic potentials Co-Pi decorated photoanode exhibits higher current densities. These results suggest that the catalyst is not merely an inactive spectator. It may be that the increased activity at anodic potentials is due to catalyst-mediated passivation of surface states which would otherwise act as recombination centers. The decreased activity at cathodic potentials could then be explained in catalytic active area; the reduced Co-Pi catalyst blocks some of the surface area that was available prior to catalyst deposition.

## APPENDIX C. SUPPORTING INFORMATION FOR PAPER E

### Theory and Simulation for the Effects of Surface States on Charge Transport in Photoelectrochemical Devices

#### Section E.S1 Notation and Modeling Conventions

##### Section E.S1.1 Notation

The semiconductor surface is at  $x = 0$ , and the semiconductor extends in the negative  $x$  direction, so that positive currents represent net current into the solution. The total semiconductor width is assumed to be large relative to the depletion width so that the bulk semiconductor corresponds to  $x \sim -\infty$ . Electron and hole densities in the semiconductor are labeled  $n$  and  $p$ , respectively, with a subscript  $s$  indicating the value at the surface ( $x = 0$ ). Current density is labeled  $J$  and has two subscripts corresponding to transfer between two subsystems, except where indicated. The subsystems are labeled vb (valence band), cb (conduction band), sc (semiconductor), ss (surface states), cat (catalyst), and sol (solution). The electrostatic potential is labeled  $\phi$  and the total electrostatic potential drop across the entire system is  $V$ . The total electrostatic potential is portioned into two sub-components, that in the semiconductor depletion region ( $V_{sc}$ ) and the Helmholtz potential ( $V_H$ ). Electrochemical potentials (quasi-Fermi levels) of the subsystems are labeled  $E$  with a subscript indicating the subsystem, except for  $E_C$ ,  $E_V$  which represent the conduction and valence band edge energies, and  $E_n$ ,  $E_p$  which represent the electron and hole quasi-Fermi levels. The energy level (standard potential) of the surface states is  $E_{ss}^o$ . Overbars (e.g.  $\bar{n}$ ) generally indicate equilibrium quantities; in the case of current densities, overbars indicate exchange currents (i.e. the unidirectional equilibrium currents rather than the total equilibrium current, which is zero). In the case of  $\bar{E}_{ss}^o$  the overbar denotes the standard surface state potential in the absence of the Helmholtz potential. The equilibrium electron  $\bar{n}$  and hole  $\bar{p}$  concentrations without subscripts indicate the bulk concentrations. Standard symbols are used for physical constants:  $k$ ,  $T$ ,  $q$ ,  $\varepsilon$ , indicate the Boltzmann constant, absolute temperature, magnitude of elementary charge, and vacuum permittivity, respectively. Material parameters are the hole diffusion coefficient ( $D_p$ ), effective density of states constants for the conduction and valence bands ( $N_C$  and  $N_V$ ), semiconductor absorption coefficient ( $\alpha$ ), and the semiconductor diffusion length ( $\delta$ ). A few quantities are computed from these parameters: the semiconductor Debye length  $\lambda \equiv \sqrt{\varepsilon\varepsilon_0 kT/q^2 N_d}$ , where  $N_d$  is the donor density semiconductor ( $N_d \approx \bar{n}$  for an n-type semiconductor);

and the semiconductor hole diffusion length  $\delta \equiv \sqrt{D_p k_R / \bar{n}}$  where  $k_R$  is the second-order recombination rate constant.

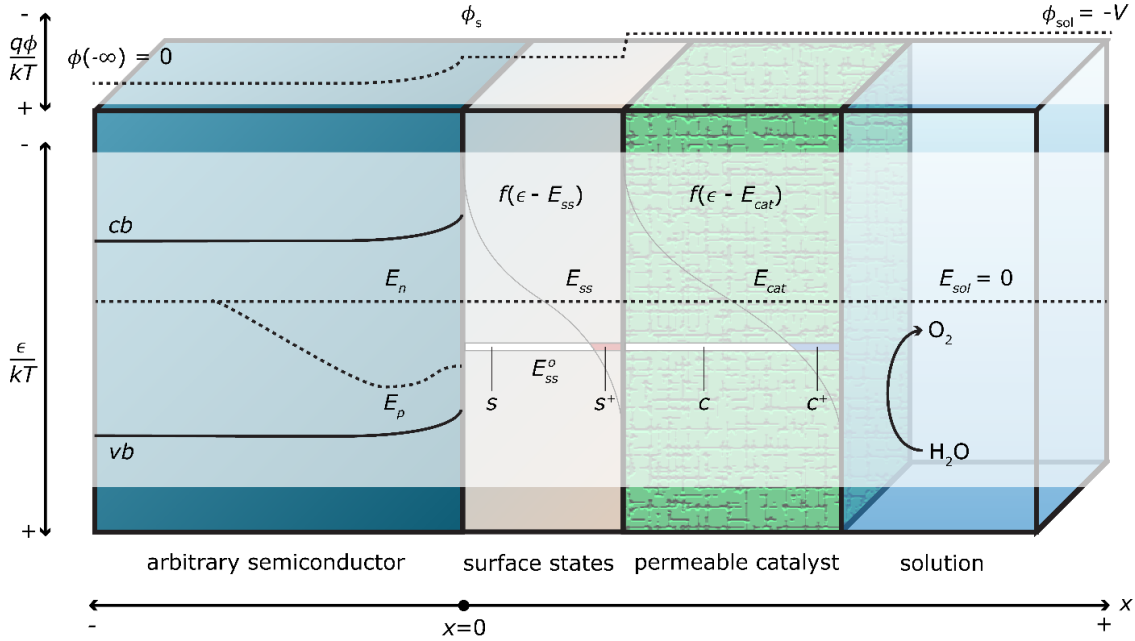


**Figure E.S1. Model schematic depicting a semiconductor/surface states/catalyst/solution interface.** Terms and parameters are described in detail in the paragraph above.

All quantities are written in physical units except for energies and potentials, which are treated as unitless quantities that have been reduced by the thermal energy  $kT$  (for energies) or the thermal voltage  $kT/q$  (for potentials). Because of this variable reduction, there are many equations in this work that appear to treat potentials and energies as though they have the same units - the reader should keep in mind that in physical units there exists a proportionality factor of  $q$ .

### Section E.S1.2 Model Conventions

All energies are referenced to the solution potential  $E_{sol} \equiv 0$ , and the sign convention is chosen to produce a hole energy scale, so that more positive potentials are more oxidizing. The electrostatic potential is referenced to the bulk semiconductor,  $\phi(-\infty) \equiv 0$ , so that the electrostatic potential in the solution is  $\phi_{sol} = -V$ . Note that energies and electric potentials are referenced to opposite ends of the system ( $x = \infty$  for energies,  $x = -\infty$  for potentials); this assignment facilitates modeling. Relating energies in combined solid state-electrochemical systems can be challenging because of the different energy scales used; for a thorough exposition on understanding energy diagrams, we refer the reader to the work of Bisquet,<sup>1</sup> which uses similar notation to ours.

For the isolated semiconductor (i.e. with flat bands),  $E_n = E_p = \bar{E}_{sc}$ ,  $E_C = \bar{E}_C$ , and  $E_V = \bar{E}_V$ . The carrier concentrations are given by

$$\bar{n} = N_C e^{\bar{E}_C - \bar{E}_{sc}} \quad \bar{p} = N_V e^{\bar{E}_{sc} - \bar{E}_V} \quad (\text{S1.1})$$

After equilibration with the rest of the system, the band positions shift according to:

$$E_C(x) = \bar{E}_C + (\phi(x) - \phi_{sol}) \quad E_V(x) = \bar{E}_V + (\phi(x) - \phi_{sol}) \quad (\text{S1.2})$$

where  $\phi(x) - \phi_{sol}$  is the electrostatic potential offset from solution to semiconductor at position  $x$ , defined as a positive quantity. The bulk carrier concentrations remain at their pre-equilibrium values. Quasi-Fermi levels and carrier concentrations are then related by:

$$n(x) = \bar{n} e^{-E_n(x) + \phi(x)} \quad p(x) = \bar{p} e^{E_p(x) - \phi(x)} \quad (\text{S1.3})$$

The Helmholtz potential is defined as the difference in potential between the semiconductor surface and the solution,  $V_H \equiv \phi_s - \phi_{sol}$ , where  $\phi_s$  is the potential at the semiconductor surface ( $x = 0$ ). The potential drop in the semiconductor depletion region is defined as the difference in potential between the bulk semiconductor and the semiconductor surface,  $V_{sc} \equiv \phi(-\infty) - \phi_s = -\phi_s$ . The total electrostatic potential drop at equilibrium is  $\bar{V} \equiv -\bar{E}_{sc}$ , which is equivalent to  $\bar{V} \equiv \bar{V}_H + \bar{V}_{sc}$ . The applied bias is defined as a deviation from the equilibrium value,  $V_{app} \equiv V - \bar{V}$ ; this can also be expressed as a difference in electrochemical potentials,  $V_{app} \equiv E_{sc} - E_{sol}$ . The surface electron and hole concentrations are therefore given by:

$$n_s = \bar{n} e^{-E_{n,s} - V_{sc}} \quad p_s = \bar{p} e^{E_{p,s} + V_{sc}} \quad (\text{S1.4})$$

Or alternatively, expressed in terms of the Helmholtz potential drop, by:

$$n_s = \bar{n} e^{-E_{n,s} - (V - V_H)} \quad p_s = \bar{p} e^{E_{p,s} + (V - V_H)} \quad (\text{S1.5})$$

### E.S1.3 Complete List of Model/Paper Terms

$x$	distance coordinate
$x = -\infty$	bulk semiconductor position
$x = 0$	semiconductor surface position
$\phi$	electrostatic potential
$\phi_s$	electrostatic potential at the semiconductor surface
$\phi_{sol}$	electrostatic potential in the solution
$V_H$	Helmholtz potential drop
$V_{sc}$	potential drop in semiconductor depletion region
$V$	total potential drop ( $V = V_{sc} + V_H = -\phi_{sol}$ )
$V_{app}$	externally applied bias ( $V_{app} = E_{sem} - E_{sol}$ )
$\bar{V}_H$	Helmholtz potential drop at equilibrium
$\bar{V}_{sc}$	potential drop in semiconductor depletion region at equilibrium
$\bar{V}$	total potential drop at equilibrium
$\Delta V_H$	Helmholtz potential deviation from equilibrium ( $\Delta V_H = V_H - \bar{V}_H$ )
$\Delta V_{sc}$	semiconductor depletion region potential deviation from equilibrium
$n, p$	charge carrier concentrations
$n_s, p_s$	charge carrier concentration at the semiconductor surface
$p_w$	hole concentration at depletion width edge
$p^+(x)$	hole concentration deviation from quasi-equilibrium
$\bar{n}, \bar{p}$	charge carrier concentrations at equilibrium
$\bar{n}_s, \bar{p}_s$	charge carrier equilibrium concentration at semiconductor surface
$c, c^+$	reduced and oxidized catalyst states
$\bar{c}, \bar{c}^+$	reduced and oxidized catalyst states at equilibrium
$c_{ss}, c_{ss}^+$	catalyst states occupancy at the surface state formal potential
$\bar{c}_{ss}, \bar{c}_{ss}^+$	equilibrium catalyst states occupancy at the surface state formal potential
$s, s^+$	reduced and oxidized surface state concentrations at equilibrium
$\bar{s}, \bar{s}^+$	reduced and oxidized surface state concentrations at equilibrium

$E_{sc}$	semiconductor bulk Fermi level
$\bar{E}_{sc}$	semiconductor bulk Fermi level - isolated semiconductor
$E_p, E_n$	quasi-Fermi levels
$E_{p,s}, E_{n,s}$	quasi-Fermi levels at the semiconductor surface
$\bar{E}_p, \bar{E}_n$	equilibrium quasi-Fermi levels
$\bar{E}_{p,s}, \bar{E}_{n,s}$	equilibrium quasi-Fermi levels at the semiconductor surface
$E_V, E_C$	valence and conduction band energies
$\bar{E}_V, \bar{E}_C$	valence and conduction band energies – isolated semiconductor
$E_{ss}$	surface state Fermi level
$\bar{E}_{ss}$	equilibrium surface state Fermi level
$E_{ss}^o$	surface state standard potential - also isoenergetic transfer level
$\bar{E}_{ss}^o$	surface state standard potential - neglecting $V_H$
$E_{cat}$	catalyst Fermi level
$\bar{E}_{cat}$	equilibrium catalyst Fermi level
$E_{sol}$	solution Fermi level (set to 0 by model definition)
$J_{vb,ss}$	valence band to surface state current density
$J_{cb,ss}$	conduction band to surface state current density
$J_{vb,cat}$	valence band to catalyst current density
$J_{cb,cat}$	conduction band to catalyst current density
$J_{ss,cat}$	surface state to catalyst current density
$J_{ss,sol}$	surface state to solution current density
$J_{cat,sol}$	catalyst to solution current density
$\bar{J}_{vb,ss}, \bar{J}_{cb,ss}, \bar{J}_{vb,cat},$ $\bar{J}_{cb,cat}, \bar{J}_{ss,cat}, \bar{J}_{ss,sol},$ $\bar{J}_{cat,sol}$	equilibrium exchange currents for each current density
$k_{vb,ss}, k_{cb,ss},$ $k_{vb,cat}, k_{cb,cat},$	2 <sup>nd</sup> order rate constant for each transfer process

$k_{ss,cat}, k_{ss,sol}, k_{cat,sol}$	
$J_G$	Gärtner current
$\bar{J}_R$	depletion recombination current
$J_p$	total hole current (transfer from vb to ss plus from vb to cat)
$J_r^{ss}$	surface state recombination current
$J_{vb,cat}^{ss}$	surface state mediated current density from valence band to catalyst
$J_{vb,sol}^{ss}$	surface state mediated current density from valence band to solution
$J_{cb,cat}^{ss}$	surface state mediated current density from conduction band to catalyst
$J_{cb,sol}^{ss}$	surface state mediated current density from conduction band to solution
$N_V, N_C$	effective DOS for the valence and conduction bands
$N_{ss}$	DOS for the surface states at $E_{ss}^0$
$N_D$	semiconductor dopant density
$C_H$	Helmholtz capacitance
$q_{sc}$	excess charge in semiconductor depletion region
$q_{ss}$	excess charge in surface states
$q_H$	excess charge in Helmholtz layer
$k_B$	Boltzmann constant
$T$	absolute temperature
$q$	elementary charge
$\varepsilon$	vacuum permittivity
$\varepsilon_0$	vacuum permittivity constant
$D_p$	hole diffusion coefficient
$\delta$	hole diffusion length
$\lambda$	Debye length
$k_R$	second order recombination rate constant
$w$	depletion width
$\alpha$	absorption coefficient
$\Phi$	incident photon flux



$\Phi_{bulk}$	incident photon flux absorbed in bulk of semiconductor
$\Phi_{dep}$	incident photon flux absorbed in semiconductor depletion region
$G(x)$	generation at position $x$
$R(x)$	recombination at position $x$
$a_i$	acceptor state in subsystem $i$
$d_i$	donor state in subsystem $i$
$g_i(\epsilon)$	DOS as a function of energy $\epsilon$ – subsystem $i$
$f_i(\epsilon)$	Fermi-Dirac occupancy probability as a function of energy $\epsilon$ – subsystem $i$

**Table E.S1 Definition for all terms found in the charge transport modeling.**

### Section E.S2 Charge Neutrality Treatment and Electrostatics

The electrostatic potential drops across the semiconductor depletion region  $V_{sc} \equiv -\phi_s$  and the Helmholtz layer drop  $V_H \equiv \phi_s - \phi_{sol}$  are determined by the electroneutrality, i.e. by equality of charge on either side of the semiconductor-solution interface:

$$q_{sc} + q_{ss} = q_H \quad (S2.1)$$

where  $q_{sc}$  is the excess charge in the depletion region of the semiconductor,  $q_{ss}$  is that in the semiconductor surface states, and  $q_H$  is that in the Helmholtz layer. The sum of the potential drops should equal the total potential drop across the entire system,

$$V_{sc} + V_H = V \quad (S2.2)$$

With a small amount of surface charge  $q_{ss}$ , ions in the Helmholtz layer compensate the charge in the depletion region  $q_{sc}$ ; because the electrolyte concentration is generally much higher than the dopant density, the Helmholtz potential drop is typically quite small in the absence of surface charge. When sufficient charge accumulates in the surface states ( $q_{ss} \gg q_{sc}$ ), more ions will be needed to balance the charge, and the Helmholtz potential drop is increased. Since the catalyst charge is distributed throughout the ion-permeable catalyst layer, ions from the solution can balance the catalyst charge outside of the Helmholtz layer, so we can assume that the catalyst charge does not influence the interfacial charge neutrality condition [Eq. S2.1].

An important consequence of the Helmholtz potential is that it shifts the energy of the surface states  $E_{ss}^o$  relative to the solution. Denoting by  $\bar{E}_{ss}^o$  the value of  $E_{ss}^o$  in the absence of a Helmholtz potential, we have  $E_{ss}^o = \bar{E}_{ss}^o + V_H$ .

Using the depletion layer approximation,<sup>2</sup> the charge in the semiconductor depletion region, assuming  $V_{sc} > 0$ , is

$$q_{sc} = qN_D w \quad (\text{S2.3})$$

To write  $q_{sc}$  in terms of  $V_{sc}$  we first define the dopant density  $N_D$

$$N_D = \frac{\epsilon k_B T}{q^2 \lambda^2} \quad (\text{S2.4})$$

and the depletion width  $w$  as

$$w = \sqrt{\frac{2\epsilon V_{sc}}{qN_D}} \quad (\text{S2.5})$$

Substitution of  $N_D$  into the expression for  $w$  yields

$$w = \lambda \sqrt{2V_{sc}} \sqrt{\frac{q}{kT}} \quad (\text{S2.6})$$

which we substitute into the abrupt depletion approximation to yield an expression for  $q_{sc}$

$$q_{sc} = qN_D \lambda \sqrt{2V_{sc}} \sqrt{\frac{q}{k_B T}} \approx qN_D \lambda \sqrt{2V_{sc}} \quad (\text{S2.7})$$

The excess charge in the surface states is determined by the surface state electrochemical potential  $E_{ss}$  and the surface state DOS function,  $g_{ss}$

$$q_{ss} = q \int g_{ss}(\epsilon) f(\epsilon - E_{ss}) d\epsilon \quad (\text{S2.8})$$

Since the surface states are treated mono-energetically – only existing at  $E_{ss}^o$ , the DOS function,  $g_{ss}(\epsilon)$ , is represented using a delta-Dirac expression

$$g_{ss}(\epsilon) = N_{ss}\delta(\epsilon - E_{ss}^o) \quad (\text{S2.9})$$

Occupancy (excess holes in the surface states) is expressed via the following Fermi-Dirac expression

$$f(\epsilon - E_{ss}) = \frac{1}{1 + e^{\epsilon - E_{ss}}} \quad (\text{S2.10})$$

Substitution of S2.9 and S2.10 into S2.8 yields the  $q_{ss}$  expression

$$q_{ss} = qN_{ss} \frac{1}{1 + e^{E_{ss}^o - E_{ss}}} \quad (\text{S2.11})$$

The Helmholtz region is essentially a capacitor in which one electrode is the semiconductor surface and the other is the layer of ions in the Helmholtz plane, with a neutral region between them. The excess charge in the Helmholtz layers is expressed in terms of the Helmholtz capacitance ( $C_H$ )

$$q_H = C_H V_H \quad (\text{S2.12})$$

Substitution of S2.7, S2.11, and S2.12 into S2.1 yields the complete charge neutrality equation

$$qN_D \lambda \sqrt{2V_{sc}} + qN_{ss} \frac{1}{1 + e^{E_{ss}^o - E_{ss}}} \approx C_H V_H \quad (\text{S2.13})$$

Equation (S2.13) determines the division of the total electrostatic potential  $V$  into  $V_{sc}$  and  $V_H$  in terms of the parameters and the surface state potential  $E_{ss}$ . At equilibrium  $E_{ss} = 0$ , and the equilibrium potential drops  $\bar{V}_{sc}$  and  $\bar{V}_H$  are constants determined by the parameters. Figure E.S2 shows  $\bar{V}_H$  as a function of  $N_{ss}$  for  $\bar{E}_{ss}^o = -0.25$  to  $0.5$  V. To examine the limits of behavior we must rewrite  $E_{ss}^o$  in terms of  $V_H$

$$qN_D\lambda\sqrt{2V_{sc}} + qN_{ss}\frac{1}{1 + e^{\bar{E}_{ss}^o + V_H - E_{ss}}} \approx C_H V_H \quad (\text{S2.14})$$

If  $V_H$  is assumed to be negligible in the absence of surface states, consistent with a high electrolyte concentration relative the semiconductor dopant density, then the following simplification can be made in the presence of surface states

$$qN_{ss}\frac{1}{1 + e^{\bar{E}_{ss}^o + V_H - E_{ss}}} \approx C_H V_H \quad (\text{S2.15})$$

At the limit where  $N_{ss} \rightarrow 0$ , the  $\bar{E}_{ss}^o$  term dominates in the Fermi-Dirac expression and equation S2.15 can be solved to reveal that  $\bar{V}_H$  depends linearly on  $N_{ss}$ :

$$\bar{V}_H \approx \frac{qN_{ss}}{C_H} \quad (\text{S2.16})$$

When  $N_{ss}$  is large,  $\bar{V}_H$  surpasses  $\bar{E}_{ss}^o$  - the surface state energy has been shifted all the way past the solution potential - and its dependence on  $N_{ss}$  becomes much weaker,

$$\bar{V}_H \approx \ln\left(\frac{qN_{ss}}{\bar{E}_{ss}^o C_H}\right) - \bar{E}_{ss}^o \quad (\text{S2.17})$$

This limit is shown in dotted lines for  $\bar{E}_{ss}^o = -0.5$  V. In this case, there are enough surface states that, if they remained filled, would produce a very large potential; the system acts to move the surface state energy  $E_{ss}^o$  sufficiently positive to minimize the potential by emptying states. Under applied bias, this principal continues to work and acts to keep the Helmholtz potential roughly constant; this is known as the *Fermi level pinning* regime. Since this effect occurs when  $\bar{V}_H$  reaches  $\bar{E}_{ss}^o$ , we will be in the pinning regime approximately when:

$$N_{ss} > -\frac{C_H \bar{E}_{ss}^o}{q} \quad (\text{S2.18})$$

Note that the above analysis requires that  $\bar{E}_{SS}^o < 0$  and that the contribution from the depletion layer can be neglected.

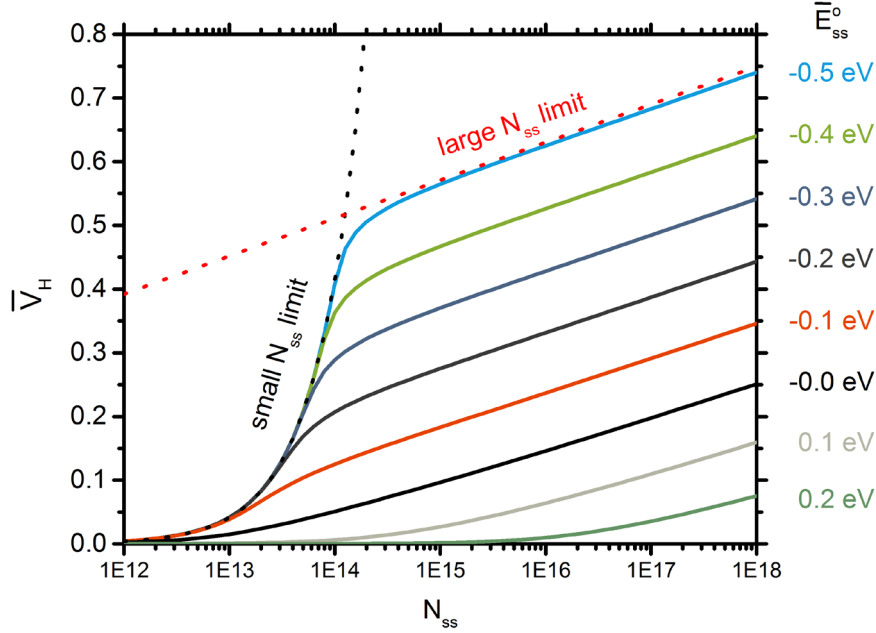
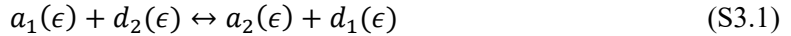


**Figure E.S2.** Equation S2.13 solved for equilibrium Helmholtz potential at various values of  $\bar{E}_{SS}^o$ . The small and large  $N_{SS}$  limits, corresponding to equations S2.16 and S2.17, are shown in black and red, respectively.

### Section E.S3 Occupancy Expressions

To build an electron transfer model we first define the concentration of oxidized and neutral species in each subsystem. We write  $d_i(\epsilon)$  for an electron donor species and  $a_i(\epsilon)$  for an electron acceptor species in subsystem  $i$  and energy  $\epsilon$ . At each value of  $\epsilon$ , the basic reaction is



The donor and acceptor distributions can be written as the product of an electronic density of states (DOS) function  $g_i(\epsilon)$  and an occupancy probability (Fermi-Dirac) function  $f_i(\epsilon)$ , where  $f_i(\epsilon - E_i) = 1/(1 + e^{\epsilon - E_i})$ , such that

$$d_i(\epsilon) = g_i(\epsilon)f_i(\epsilon - E_i) \quad a_i(\epsilon) = g_i(\epsilon)f_i(E_i - \epsilon) \quad (\text{S3.2})$$

The DOS function used for the semiconductor and catalyst are constants. For the surface states, a delta dirac function is employed to produce a mono-energetic model [ $g_{ss}(\epsilon) = N_{ss}\delta(\epsilon - E_{ss}^o)$ ]. For the solution, we use the large reorganization energy ( $\lambda_R$ ) limit of the Marcus-Gerischer DOS<sup>3</sup>

$$d_{sol}(\epsilon) = c_{sol}e^{(E_{sol}-\epsilon)/2} \quad a_{sol}(\epsilon) = c_{sol}e^{(\epsilon-E_{sol})/2} \quad (S3.3)$$

Here,  $c_{sol}$  is

$$c_{sol} = \sqrt{\frac{[D][A]}{4\pi\lambda_R k_B T}} e^{-\lambda_R/4} \quad (S3.4)$$

where [D] and [A] are total concentrations of donor and acceptor species in solution.

We write  $s$  and  $s^+$  for the neutral and oxidized surface state concentrations, respectively

$$s = N_{ss}f(E_{ss} - E_{ss}^o) \quad s^+ = N_{ss}f(E_{ss}^o - E_{ss}) \quad (S3.5)$$

and  $c_{ss}$  and  $c_{ss}^+$  for the fraction of neutral and oxidized catalyst sites at energy  $E_{ss}^o$ ,

$$c_{ss} = f(E_{cat} - E_{ss}^o) \quad c_{ss}^+ = f(E_{ss}^o - E_{cat}) \quad (S3.6)$$

Note here that the catalyst occupation expressions are evaluated at  $E_{ss}^o$  because the catalyst is assumed to be isoenergetic with the surface states. For modeling purposes, it is convenient to write these expressions in terms of the Helmholtz potential. Doing so produces the following expressions

$$s = N_{ss} \frac{1}{1+e^{E_{ss}-\bar{E}_{ss}^o-V_H}} \quad s^+ = N_{ss} \frac{1}{1+e^{\bar{E}_{ss}^o+V_H-E_{ss}}} \quad (S3.7)$$

and

$$c_{ss} = \frac{1}{1+e^{E_{cat}-\bar{E}_{ss}^o-V_H}} \quad c_{ss}^+ = \frac{1}{1+e^{\bar{E}_{ss}^o+V_H-E_{cat}}} \quad (S3.8)$$

Equilibrium values occur where  $E_{ss} = 0$ ,  $E_{cat} = 0$ , and  $V_H = \bar{V}_H$ . Solving for the equilibrium concentrations gives rise to the following expressions

$$\bar{s} = N_{ss} \frac{1}{1+e^{-E_{ss}^0 - \bar{v}_H}} \quad \bar{s}^+ = N_{ss} \frac{1}{1+e^{E_{ss}^0 + \bar{v}_H}} \quad (\text{S3.9})$$

and

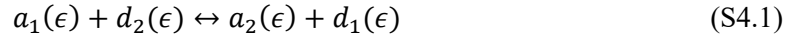
$$\bar{c}_{ss} = \frac{1}{1+e^{-E_{ss}^0 - \bar{v}_H}} \quad \bar{c}_{ss}^+ = \frac{1}{1+e^{E_{ss}^0 + \bar{v}_H}} \quad (\text{S3.10})$$

The equations in S3.7 – S3.10 are used in developing current density equations based on 2<sup>nd</sup> order kinetic expressions (Section E.S4).

## Section E.S4 Modeling Current Densities – 2nd Order Kinetic Expressions

### Section E.S4.1 General Scheme

The model for interfacial electron transfer is based on simple second-order reaction kinetics. Recall that for transfer between subsystems 1 and 2, the reaction at each value of  $\epsilon$  is



with the reaction proceeding to the right representing positive current from subsystem 1 to 2. The current, proportional to the total reaction rate, is computed by integrating the rate densities over the energy range  $\epsilon$ , such that

$$J_{1,2} = q \int k_{1,2}(\epsilon) [a_1(\epsilon)d_2(\epsilon) - a_2(\epsilon)d_1(\epsilon)] d\epsilon \quad (\text{S4.2})$$

Substitution of the occupancy expressions gives the current integral

$$J_{1,2} = q \int k_{1,2}(\epsilon) g_1(\epsilon)g_2(\epsilon) [f_1(\epsilon) - f_2(\epsilon)] d\epsilon \quad (\text{S4.3})$$

Note that for the purposes of modeling we formulate each expression in terms of a deviation from the equilibrium state. This is accomplished by strategically defining the exchange currents.

### Section E.S4.2 $J_{ss,cat}$

For the current from surface states to the catalyst  $J_{ss,cat}$ , transfer only occurs at  $\epsilon = E_{ss}^0$  and so the integral evaluates to

$$J_{ss,cat} = k_{ss,cat}(s^+c_{ss} - sc_{ss}^+) \quad (\text{S4.4})$$

To formulate a meaningful exchange current we use the relationship  $\bar{c}_{ss}/\bar{c}_{ss}^+ = \bar{s}/\bar{s}^+ = e^{E_{ss}^0 + \bar{V}_H}$  to write

$$J_{ss,cat} = k_{ss,cat}\bar{s}^+\bar{c}_{ss}^+e^{E_{ss}^0 + \bar{V}_H} \left( \frac{s^+c_{ss}}{\bar{s}^+\bar{c}_{ss}} - \frac{sc_{ss}^+}{\bar{s}\bar{c}_{ss}^+} \right) \quad (\text{S4.5})$$

This expresses  $J_{ss,cat}$  in terms of a deviation from equilibrium and simplifies to

$$J_{ss,cat} = \bar{J}_{ss,cat} \left( \frac{s^+c_{ss}}{\bar{s}^+\bar{c}_{ss}} - \frac{sc_{ss}^+}{\bar{s}\bar{c}_{ss}^+} \right) \quad (\text{S4.6})$$

where

$$\bar{J}_{ss,cat} = k_{ss,cat}\bar{s}^+\bar{c}_{ss}^+e^{E_{ss}^0 + \bar{V}_H} \quad (\text{S4.7})$$

is the exchange current - a constant.

### Section E.S4.3 $J_{vb,cat}$ and $J_{cb,cat}$

In our previous work on adaptive junctions, current between the semiconductor and catalyst was modeled as a function of the deviation from the equilibrium carrier concentration and a perturbation to the barrier height

$$J_{jxn} = k_p(p_s - \bar{p}_s e^{qV_{cat}/kT}) - k_n(n_s - \bar{n}_s e^{-qV_{cat}/kT}) \quad (\text{S4.8})$$

In this work, we simplify the expression into the two constituent currents:



$$J_{vb,cat} = \bar{J}_{vb,cat} \left( \frac{p_s}{\bar{p}_s} - e^{E_{cat} - \Delta V_H} \right) \quad (\text{S4.9})$$

$$J_{cb,cat} = \bar{J}_{cb,cat} \left( e^{\Delta V_H - E_{cat}} - \frac{n_s}{\bar{n}_s} \right) \quad (\text{S4.10})$$

where

$$\bar{J}_{vb,cat} = k_{vb,cat} \bar{p}_s \quad (\text{S4.11})$$

and

$$\bar{J}_{cb,cat} = k_{cb,cat} \bar{n}_s \quad (\text{S4.12})$$

Note here that Helmholtz terms are introduced to account for the realignment of  $E_{cat}$  relative to the band edges, when sufficient surface state filling has occurred. The  $E_{cat}$  term is technically a deviation from its equilibrium value, but the equilibrium value is set to zero in this model.

#### Section E.S4.4 $J_{ss,sol}$

For the current from surface states to the solution  $J_{ss,sol}$ , the initial integral is

$$J_{ss,sol} = q \int k_{ss,sol} N_{ss} c_{sol} \delta(\epsilon - E_{ss}^0) \left[ [f_{ss}(\epsilon - E_{ss})] e^{\epsilon/2} - [f_{ss}(E_{ss} - \epsilon)] e^{-\epsilon/2} \right] d\epsilon \quad (\text{S4.13})$$

Once integrated this becomes

$$J_{ss,sol} = k_{ss,sol} c_{sol} \left[ s^+ e^{E_{ss}^0/2} - s e^{-E_{ss}^0/2} \right] \quad (\text{S4.14})$$

The substitution  $E_{ss}^0 = \bar{E}_{ss}^0 + \bar{V}_H + \Delta V_H$  is made to facilitate the development of a meaningful exchange current, and the expression is then rewritten

$$J_{ss,sol} = k_{ss,sol} c_{sol} \left[ s^+ (e^{\bar{E}_{ss}^0/2}) (e^{\bar{V}_H/2}) (e^{\Delta V_H/2}) - s (e^{-\bar{E}_{ss}^0/2}) (e^{-\bar{V}_H/2}) (e^{-\Delta V_H/2}) \right] \quad (\text{S4.15})$$

By factoring out  $e^{-\bar{E}_{ss}^0/2}$ ,  $e^{-\bar{V}_H/2}$  and  $\bar{s}$ , we further simplify to

$$J_{ss,sol} = k_{ss,sol} c_{sol} \bar{s} e^{-\bar{E}_{ss}^0/2} e^{-\bar{V}_H/2} \left[ \frac{s^+ (e^{\bar{E}_{ss}^0}) (e^{\bar{V}_H}) (e^{\Delta V_H/2})}{\bar{s}} - \frac{s (e^{-\Delta V_H/2})}{\bar{s}} \right] \quad (\text{S4.16})$$

Using the relationship  $\frac{\bar{s}}{\bar{s}^+} = e^{\bar{E}_{ss}^0 + \bar{V}_H}$  we can write

$$J_{ss,sol} = k_{ss,sol} c_{sol} \sqrt{\bar{s}\bar{s}^+} \left[ \frac{s^+}{\bar{s}^+} e^{\Delta V_H/2} - \frac{s}{\bar{s}} e^{-\Delta V_H/2} \right] \quad (\text{S4.17})$$

Thus, we arrive at

$$J_{ss,sol} = \bar{J}_{ss,sol} \left[ \frac{s^+}{\bar{s}^+} e^{\Delta V_H/2} - \frac{s}{\bar{s}} e^{-\Delta V_H/2} \right] \quad (\text{S4.18})$$

where

$$\bar{J}_{ss,sol} = k_{ss,sol} c_{sol} \sqrt{\bar{s}\bar{s}^+} \quad (\text{S4.19})$$

#### Section E.S4.5 $J_{cat,sol}$

For the current from catalyst to the solution  $J_{cat,sol}$ , the initial integral is

$$J_{cat,sol} = k_{cat,sol} \int N_{cat} c_{sol} [f(\epsilon - E_{cat}) e^{\epsilon/2} - f(E_{cat} - \epsilon) e^{-\epsilon/2}] d\epsilon \quad (\text{S4.20})$$

After integration this evaluates to

$$J_{cat,sol} = k_{cat,sol} N_{cat} c_{sol} [I_f(\epsilon - E_{cat}) - I_b(E_{cat} - \epsilon)] \quad (\text{S4.21})$$

where the functions  $I_f$  and  $I_b$  are defined:

$$I_f(\epsilon - E_{cat}) = \int_{-\infty}^{\infty} \frac{e^{\epsilon/2}}{1 + e^{\epsilon - E_{cat}}} \quad (\text{S4.22})$$

$$I_b(E_{cat} - \epsilon) = \int_{-\infty}^{\infty} \frac{e^{-\epsilon/2}}{1 + e^{E_{cat} - \epsilon}} \quad (\text{S4.23})$$

To simplify these integral functions, the substitution  $\epsilon = \epsilon + E_{cat}$  can be employed (note that this is a valid substitution because the full energy range is still integrated despite the substitution)

$$I_f(\epsilon - E_{cat}) = \int_{-\infty}^{\infty} \frac{e^{(\epsilon + E_{cat})/2}}{1 + e^{\epsilon}} = \pi e^{E_{cat}/2} \quad (\text{S4.24})$$

$$I_b(E_{cat} - \epsilon) = \int_{-\infty}^{\infty} \frac{e^{-(\epsilon + E_{cat})/2}}{1 + e^{-\epsilon}} = \pi e^{-E_{cat}/2} \quad (\text{S4.25})$$

The finalized expression then becomes

$$J_{cat,sol} = \bar{J}_{cat,sol} \left( e^{\frac{E_{cat}}{2}} - e^{-\frac{E_{cat}}{2}} \right) \quad (\text{S4.26})$$

where

$$\bar{J}_{cat,sol} = k_{cat,sol} N_{cat} c_{sol} \pi \quad (\text{S4.27})$$

#### Section E.S4.6 $J_{vb,ss}$ and $J_{cb,ss}$

The reaction of semiconductor holes and electrons with surface states is modeled using the quasi-second order expressions:

$$J_{vb,ss} = \bar{J}_{vb,ss} \left( \frac{p_s s}{\bar{p}_s \bar{s}} - \frac{s^+}{\bar{s}^+} \right) \quad (\text{S4.28})$$

$$J_{cb,ss} = \bar{J}_{cb,ss} \left( \frac{s}{\bar{s}} - \frac{n_s s^+}{\bar{n}_s \bar{s}^+} \right) \quad (\text{S4.29})$$

Note here that the 1<sup>st</sup> order terms are consistent with the assumption that the concentrations of valence band electrons and conduction band holes are not meaningfully altered under realistic operating conditions.

### Section E.S5 Gärtner Generalization – Full Derivation

In deriving the generalized Gärtner model we explicitly write each step to show the similarity to Gärtner’s original formulation.<sup>4</sup> The generalizations we make allow for (1) a non-zero value of the hole concentration at the edge of the depletion region (corresponding to relaxing Gärtner’s original assumption of fast surface kinetics), and (2) recombination in the depletion region, which requires approximating the hole concentration profile in this region. Extensive analyses of the minority carrier profiles and depletion region recombination have been conducted by Albery et. al.;<sup>5,6</sup> for comparison purposes the error in our treatment is explored in subsequent section (E.S6). Our method and results are closely related to those of El Guibaly et. al.<sup>7</sup> but we use simple second-order recombination rather than trap-mediated recombination.

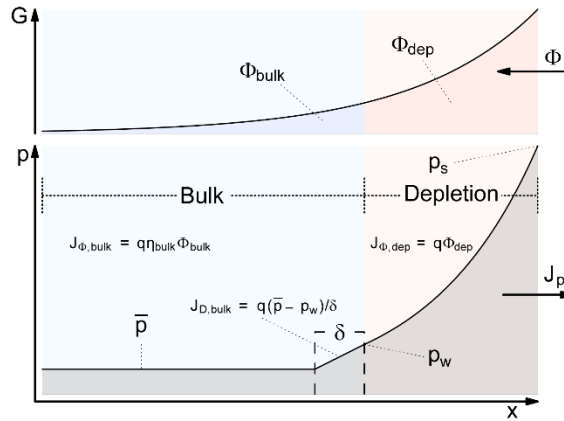


**Figure E.S3. Hole concentration profile and the currents generated by the generalized Gärtner model.**

Figure E.S3 shows quantities relevant to the derivation of the generalized Gärtner model. The incoming photon flux  $\Phi$  is split into a portion that is absorbed in the depletion region,  $\Phi_{\text{dep}}$ , and in the bulk,  $\Phi_{\text{bulk}}$ , so that  $\Phi = \Phi_{\text{dep}} + \Phi_{\text{bulk}}$ . The semiconductor interface is at  $x = 0$  and the inside of

the depletion region is at  $x = -w$ , where  $w$  is the depletion region width. The generated carriers per unit time is

$$G(x) \equiv \Phi \alpha e^{\alpha x} \quad (\text{S5.1})$$

Recombination is assumed to follow a simple second-order law

$$R(x) \equiv k_R n p \quad (\text{S5.2})$$

The electrons are assumed to be at quasiequilibrium throughout the semiconductor, so that

$$n(x) = \bar{n} e^{\phi} \quad (\text{S5.3})$$

The hole distribution in the bulk will be computed explicitly below. In the depletion region, the transport equations can be solved to relate the hole concentration profile  $p(x)$  to the concentration at the edge of the depletion region  $p_w$ ,

$$p(x) = p_w e^{-\phi} + p^\dagger(x) \quad (\text{S5.4})$$

where

$$p^\dagger(x) = e^{-\phi(x)} \int_{-w}^x \theta(x') e^{\phi(x')} dx' \quad (\text{S5.5})$$

$$\theta(x) = -F_p + \int_x^0 G(x') - R(x') dx' \quad (\text{S5.6})$$

$$\phi(x) = -\frac{(x+w)^2}{2\lambda^2} \quad (\text{S5.7})$$

$$w = \lambda \sqrt{2V} \quad (\text{S5.8})$$

Note that  $p^\dagger$  represents the deviation from quasiequilibrium. We assume that  $p^\dagger = 0$  which is equivalent to assuming that the holes are at quasiequilibrium throughout the depletion region. Thus, the following simplification is made

$$p(x) \approx p_w e^{-\phi} \quad (\text{S5.9})$$

The error in using this approximation is on the order of  $\lambda/\delta$ ; this approximation therefore holds when the Debye length is much smaller than the diffusion length. In the subsequent section (E.S6) it is shown that, even when this assumption is relaxed, the current takes the same form in that it is linear in  $J_G$  and  $p_w$ .

The time dependent continuity equation for holes is

$$\frac{dp}{dt} = -\frac{1}{q} \frac{dJ_p}{dx} + G(x) - R(x) \quad (\text{S5.10})$$

Evaluation at steady state ( $dp/dt = 0$ ) produces

$$\frac{1}{q} \frac{dJ_p}{dx} = G(x) - R(x) \quad (\text{S5.11})$$

After integrating across the depletion region, this can be represented via the form

$$J_p = J_{bulk} + J_{\phi,dep} - J_{R,dep} \quad (\text{S5.12})$$

where  $J_p = J(0)$  is the total hole current passing through the surface,  $J_{bulk} = J(-w)$  is the hole current from the bulk to the depletion region,  $J_{\phi,dep}$  is current from holes generated in the depletion region,

$$J_{\phi,dep} \equiv q\Phi_{dep} = q \int_{-w}^0 G dx = q\Phi(1 - e^{-\alpha w}) = q \int_{-w}^0 \Phi \alpha e^{\alpha x} dx = q\Phi(1 - e^{-\alpha x}) \quad (\text{S5.13})$$

and  $J_{R,dep}$  is current due to recombination in the depletion region

$$J_{R,dep} \equiv q \int_{-w}^0 R dx = q \int_{-w}^0 k_R \bar{n} p_w dx = q k_R w \bar{n} p_w \quad (S5.14)$$

$J_{\text{bulk}}$  is obtained by assuming that there is no field in the bulk and that the electron concentration remains unperturbed from its equilibrium value  $\bar{n}$ . Therefore, in the bulk the hole continuity equation is

$$-\frac{d^2 p}{dx^2} = \frac{\Phi \alpha e^{\alpha x}}{D_p} - \frac{p - \bar{p}}{\delta^2} \quad (S5.15)$$

By substituting  $\frac{d^2 p}{dx^2} = P''$  and  $\Phi \alpha e^{\alpha x} = g(x)$  we simplify to

$$D_p p'' - (p - \bar{p}) \frac{D_p}{\delta^2} + g(x) = 0 \quad (S5.16)$$

Solving the second order differential equation, with the boundary conditions  $p(-\infty) = \bar{p}$  and  $p(-w) = p_w$ , yields:

$$p = \frac{-e^{x\alpha} \alpha \delta^2 \Phi - D_p \bar{p} + D_p \alpha^2 \delta^2 \bar{p}}{D_p (-1 + \alpha \delta)(1 + \alpha \delta)} + e^{\frac{w+x}{\delta}} \left( -\frac{-e^{-w\alpha} \alpha \delta^2 \Phi - D_p \bar{p} + D_p \alpha^2 \delta^2 \bar{p}}{D_p (-1 + \alpha \delta)(1 + \alpha \delta)} + p_w \right) \quad (S5.17)$$

The derivative of p with respect to position yields,

$$p' = \frac{-e^{x\alpha} \alpha^2 \delta^2 \Phi}{D_p (-1 + \alpha \delta)(1 + \alpha \delta)} + \frac{e^{\frac{w+x}{\delta}}}{\delta} \left( -\frac{-e^{-w\alpha} \alpha \delta^2 \Phi - D_p \bar{p} + D_p \alpha^2 \delta^2 \bar{p}}{D_p (-1 + \alpha \delta)(1 + \alpha \delta)} + p_w \right) \quad (S5.18)$$

Substitution of  $\bar{p} = \left( \frac{-D_p \bar{p} + D_p \alpha^2 \delta^2 \bar{p}}{D_p (-1 + \alpha \delta)(1 + \alpha \delta)} \right)$  enables simplification to

$$p' = \frac{-e^{x\alpha}\alpha^2\delta^2\Phi}{D_p(-1+\alpha\delta)(1+\alpha\delta)} + \frac{e^{\frac{w+x}{\delta}}}{\delta} \left( \frac{e^{-w\alpha}\alpha\delta^2\Phi}{D_p(-1+\alpha\delta)(1+\alpha\delta)} - \bar{p} + p_w \right) \quad (\text{S5.19})$$

which is further simplified to

$$p' = \frac{-e^{x\alpha}\alpha^2\delta^2\Phi + e^{-w\alpha}e^{\frac{w+x}{\delta}}\alpha\delta\Phi}{D_p(-1+\alpha\delta)(1+\alpha\delta)} - e^{\frac{w+x}{\delta}}\frac{(\bar{p} - p_w)}{\delta} \quad (\text{S5.20})$$

Since no field exists in the bulk semiconductor, only diffusion is treated. The diffusive current can be calculated by solving  $-qD_p p'(x)$  at the edge of the depletion layer:

$$-qD_p p'(-w) = \frac{q\alpha\delta\Phi e^{-w\alpha}}{(1+\alpha\delta)} + \frac{qD_p(\bar{p} - p_w)}{\delta} \quad (\text{S5.21})$$

Solving with boundary conditions  $p(-\infty) = \bar{p}$  and  $p(-w) = p_w$  gives the solution for  $J_{bulk} \equiv q(dp/dx)(w)$ ,

$$J_{bulk} = J_{\Phi,bulk} + J_{D,bulk} \quad (\text{S5.22})$$

The current due to generation in the bulk is

$$J_{\Phi,bulk} = q\eta_{bulk}\Phi_{bulk} \quad (\text{S5.23})$$

where

$$\Phi_{bulk} = \Phi e^{-\alpha w} \quad \eta_{bulk} = \frac{\alpha\delta}{1+\alpha\delta} \quad (\text{S5.24})$$

Here  $\eta_{bulk}$  is the fraction of charges generated in the bulk that reach the edge of the depletion region before recombining. The diffusion current term is



$$J_{D,bulk} = qD_p \frac{\bar{p} - p_w}{\delta} \quad (S5.25)$$

which is the current due to diffusion across one diffusion length just inside the bulk region, as depicted in Figure E.S3. The concentration profile shown here is a schematic one; in reality, the hole concentration varies throughout the bulk and in general has a nonlinear profile that is dependent on the magnitude of generation and recombination, but the diffusional current is mathematically equivalent to the simple conceptual illustration in the figure. Note that the original Gärtner model assumes  $p_w = 0$ .

We substitute these results into Eq. S5.12, and make the following simplifications to relate our results to the Gärtner model:

$$J_p = J_{bulk} + J_{\Phi,dep} - J_{R,dep} \quad (S5.12)$$

Substitution of Eq. S5.13, S5.14 and S5.22, into S5.12 produces

$$J_p = q\Phi e^{-\alpha w} \frac{\alpha\delta}{1 + \alpha\delta} + q\Phi(1 - e^{-\alpha w}) + qD_p \frac{\bar{p} - p_w}{\delta} - qk_R \bar{n} p_w w \quad (S5.26)$$

The expression is simplified by factoring out  $\Phi$ ,

$$J_p = q\Phi \left( e^{-\alpha w} \frac{\alpha\delta}{1 + \alpha\delta} + (1 - e^{-\alpha w}) \right) + qD_p \frac{\bar{p} - p_w}{\delta} - qk_R \bar{n} p_w w \quad (S5.27)$$

further simplified via a common denominator,

$$J_p = q\Phi \left( \frac{\alpha\delta e^{-\alpha w}}{1 + \alpha\delta} - \frac{(1 + \alpha\delta)e^{-\alpha w}}{1 + \alpha\delta} + 1 \right) + qD_p \frac{\bar{p} - p_w}{\delta} - qk_R \bar{n} p_w w \quad (S5.28)$$

and rearranged to demonstrated cancellation of the first two terms,

$$J_p = q\Phi \left( \frac{\alpha\delta e^{-\alpha w}}{1 + \alpha\delta} - \frac{\alpha\delta e^{-\alpha w}}{1 + \alpha\delta} - \frac{e^{-\alpha w}}{1 + \alpha\delta} + 1 \right) + qD_p \frac{\bar{p} - p_w}{\delta} - qk_R \bar{n} p_w w \quad (S5.29)$$

Finally, we substitute the original Gärtner current expression  $J_G = q\Phi\left(1 - \frac{e^{-\alpha w}}{1 + \alpha\delta}\right) + qD_p\frac{\bar{p}}{\delta}$ ,

$$\begin{aligned} J_p &= -q\Phi\left(1 - \frac{e^{-\alpha w}}{1 + \alpha\delta}\right) + qD_p\frac{\bar{p} - p_w}{\delta} - qk_R w \bar{n} p_w \\ &= J_G - q\left(\frac{D_p}{\delta} + k_R w \bar{n}\right) p_w \end{aligned} \quad (\text{S5.30})$$

This result is the original Gärtner current  $J_G$  minus an extra term proportional to  $p_w$  that describes additional recombination losses due to the hole transport limitation. The first term,  $qD_p p_w / \delta$ , is the amount of current fed back into the bulk, where the holes recombine, and the second term,  $qk_R w \bar{n} p_w$ , is the amount of current lost due to recombination in the depletion region.

In the original Gärtner model the diffusion current  $qD_p \bar{p} / \delta$  is typically not the major contribution to the total current because of the relatively small value of  $\bar{p}$ ; however, if the kinetics are slow and there is a large buildup of holes in the depletion region, there may be enough of a back current that  $p_w$  exceeds  $\bar{p}$ , leading to a net negative diffusion current. If  $p_w$  becomes large enough, the diffusion current may eventually eclipse the generation current; when this occurs, we say that the current becomes limited by the hole transport. Depending on the relative values of  $D_p / \delta$  and  $k_R w \bar{n}$ , a large  $p_w$  may also limit the hole current via recombination in the depletion region.

To couple this to the boundary conditions, we need to be able to relate  $p_w$  to  $p_s$ . Using the quasiequilibrium assumption for the hole concentration profile Eq. S5.9, we have  $p_s = p_w e^{V_{sc}}$ , and we may write S5.30 in terms of  $p_s$

$$J_p = J_G - q\left(\frac{D_p}{\delta} + k_R w \bar{n}\right) \frac{p_s}{e^{V_{sc}}} \quad (\text{S5.31})$$

A recombination current at equilibrium can then be defined by factoring out  $\frac{e^{\bar{V}_{sc}}}{\bar{p}_s}$

$$J_p = J_G + qe^{\bar{V}_{sc} - V_{sc}} \frac{p_s}{\bar{p}_s} \left(\frac{-D_p}{\delta} - qk_R \bar{n} w\right) \bar{p}_s e^{-\bar{V}_{sc}} \quad (\text{S5.32})$$

We arrive at the final analytical solution – the generalized Gärtner model:

$$J_p = J_G - \bar{J}_R e^{\bar{V}_{sc} - V_{sc}} \frac{p_s}{\bar{p}_s} \quad (\text{S5.33})$$

where

$$\bar{J}_R = q \left( \frac{D_p}{\delta} + k_R w \bar{n} \right) \bar{p}_s e^{-\bar{V}_{sc}} \quad (\text{S5.34})$$

is the depletion recombination current. Note that due to the appearance of  $w$ , this quantity is not exactly constant, but can be treated as such for practical purposes. We generally refer to this term as “depletion recombination” but note that it accounts for two more specific sub-processes: (1) holes passing from the depletion region back into the bulk and (2) holes recombining within the depletion region itself.

By using this approximation and the common assumption<sup>8,9</sup> that surface electrons are at quasi-equilibrium with the bulk

$$n_s = \bar{n} e^{-V_{sc}} \quad (\text{S5.35})$$

the numerical simulation can be dispensed with and the semiconductor transport, generation, and recombination processes can be described analytically.

### Section E.S6 Gärtner Generalization – Error Discussion

Here we illustrate that the error in our generalization of the Gärtner model is proportional to  $\lambda/\delta$  and is therefore valid when the Debye length is much smaller than the diffusion length. We also show that when this assumption is relaxed, the current takes a form similar to the generalization in that it is linear in  $J_G$  and  $p_w$ . Berz has also given an analysis of the validity of the quasiequilibrium assumption<sup>10</sup> using a different method. It is important to note that this assumption changes the form of the depletion region recombination current relative to other classical treatments.

We start with the hole continuity equation,

$$\frac{dp}{dt} = 0 = -\frac{dF_p(x)}{dx} + G(x) - R(x) \quad (\text{S6.1})$$

and integrate once,

$$F_p(x) = F_p - \int_x^0 G(x) - R(x) dy \quad (\text{S6.2})$$

Here  $F_p \equiv F_p(0)$ , and

$$F_p(x) = -\mu_p \frac{d\phi}{dx} p - D_p \frac{dp}{dx} \quad (\text{S6.3})$$

Solving this last equation with the boundary condition  $p(-w) \equiv p_w$  yields,

$$p(x) = e^{-\phi} (p_w - p^\dagger(x)) \quad (\text{S6.4})$$

where

$$p^\dagger(x) = D_p^{-1} \int_{-w}^x F_p(y) e^{\phi(y)} dy \quad (\text{S6.5})$$

Note that the electrostatic potential is defined

$$\phi(x) = -\frac{(x+w)^2}{2\lambda^2} \quad (\text{S6.6})$$

and the depletion width defined as

$$w = \lambda\sqrt{2V} \quad (\text{S6.7})$$

A generation integral is defined,

$$I_G(x) \equiv \int_x^0 G(y) dy = \int_x^0 \Phi e^{\alpha y} dy = \Phi(1 - e^{\alpha x}) \quad (\text{S6.8})$$

and a recombination integral, given  $n(x) = \bar{n}e^\phi$ , is defined,

$$\begin{aligned}
I_R(x) &\equiv \int_x^0 R(y)dy \\
&= k_R \bar{n} \int_x^0 p_w - p^\dagger dx \\
&= k_R \bar{n} \left( -p_w x - \int_x^0 p^\dagger dx \right)
\end{aligned} \tag{S6.9}$$

This integral requires additional work as it depends on  $p^\dagger$ . The first term of  $F_p(x)$  gives rise to the resistance integral

$$F_p \int_{-w}^x e^{\phi(y)} dy = F_p \lambda \sqrt{\pi/2} \operatorname{erf} \left( \frac{w+x}{\sqrt{2}\lambda} \right) \tag{S6.10}$$

The full generation integral is then expressed

$$\begin{aligned}
&\int_{-w}^x e^{\phi(y)} I_G(y) dy \\
&= \Phi \lambda \sqrt{\pi/2} \left\{ \operatorname{erf} \left( \frac{w+x}{\sqrt{2}\lambda} \right) \right. \\
&\quad \left. - e^{-\alpha w + \alpha^2 \lambda^2 / 2} \left[ \operatorname{erf} \left( \frac{\alpha \lambda}{\sqrt{2}} \right) + \operatorname{erf} \left( \frac{w+x}{\sqrt{2}\lambda} - \frac{\alpha \lambda}{\sqrt{2}} \right) \right] \right\}
\end{aligned} \tag{S6.11}$$

and the full recombination integral is expressed

$$\begin{aligned}
&\int_{-w}^x e^{\phi(y)} I_R(y) dy \\
&= -k_R \bar{n} p_w \lambda \left[ \lambda \left( 1 - e^{-\frac{(w+x)^2}{2\lambda^2}} \right) - w \sqrt{\frac{\pi}{2}} \operatorname{erf} \left( \frac{w+x}{\sqrt{2}\lambda} \right) \right] \\
&\quad - k_R \bar{n} \int_{-w}^x e^{\phi(y)} \int_y^0 p^\dagger(z) dz dy
\end{aligned} \tag{S6.12}$$

Now we calculate  $p_s$  with the following approximations:  $V$  is sufficiently large so that the  $\text{erf}\left(\frac{\alpha\lambda}{\sqrt{2}}\right)$  terms are effectively equal to 1, and the product  $\alpha\lambda \approx 0$ , since the Debye length can be assumed much shorter than the absorption length. To calculate the final integral, we let  $p^\dagger$  be constant throughout the depletion regions, such that  $p^\dagger = p_s^\dagger$ . This is justifiable because the exact functions above become effectively constant a few Debye lengths away from the edge of the region. This leads to

$$p_s^\dagger \approx \frac{\lambda\sqrt{\pi/2}}{D_p} [F_p - \Phi(1 - e^{-\alpha w})] + \frac{\lambda(w\sqrt{\pi/2} - \lambda)}{\delta^2} (p_w - p_s^\dagger) \quad (\text{S6.13})$$

Since

$$p_w - p_s^\dagger = p_s e^{-V_{sc}} \quad (\text{S6.14})$$

we simplify to

$$p_s^\dagger \approx \frac{\lambda\sqrt{\pi/2}}{D_p} [F_p - \Phi(1 - e^{-\alpha w})] + \frac{\lambda(w\sqrt{\pi/2} - \lambda)}{\delta^2} p_s e^{-V_{sc}} \quad (\text{S6.15})$$

To write  $p_w$  in terms of  $p_s$  we use the following relationship

$$p_w = p_s e^{-V_{sc}} + p_s^\dagger \quad (\text{S6.16})$$

to arrive at

$$p_w \approx \frac{\lambda\sqrt{\pi/2}}{D_p} [F_p - \Phi(1 - e^{-\alpha w})] + \left[ 1 + \frac{\lambda(w\sqrt{\pi/2} - \lambda)}{\delta^2} \right] p_s e^{-V_{sc}} \quad (\text{S6.17})$$

We now take the main result of the generalized Gärtner model,

$$J_p = J_G - q \left( \frac{D_p}{\delta} + k_R w \bar{n} \right) p_w \quad (\text{S6.18})$$

and substitute for  $p_w$  to obtain,

$$J_p = \frac{J_G - \frac{qD_p}{\delta} \left(1 + \frac{w}{\delta}\right) \left[1 + \frac{\lambda(w\sqrt{\pi/2} - \lambda)}{\delta^2}\right] p_s e^{-V_{sc}} + q\sqrt{\pi/2} \frac{\lambda}{\delta} \left(1 + \frac{w}{\delta}\right) \Phi(1 - e^{-\alpha w})}{1 + \sqrt{\pi/2} \frac{\lambda}{\delta} \left(1 + \frac{w}{\delta}\right)} \quad (\text{S6.19})$$

We compare this to the solution which assumes hole quasiequilibrium,

$$J_p = J_G - q \left( \frac{D_p}{\delta} + k_R w \bar{n} \right) \frac{p_s}{e^{V_{sc}}} \quad (\text{S6.20})$$

There are three new terms that occur when the hole profile is allowed to deviate from quasiequilibrium. The first is a term ( $X_F$ ) in the denominator

$$X_F = \sqrt{\pi/2} \frac{\lambda}{\delta} \left(1 + \frac{w}{\delta}\right) \quad (\text{S6.21})$$

This term represents a decrease in hole density due to the resistance of charge transport through the depletion region. The second ( $Y_R$ ) is a new term in the numerator

$$Y_R = \frac{\lambda(w\sqrt{\pi/2} - \lambda)}{\delta^2} p_s e^{-V_{sc}} \quad (\text{S6.22})$$

This term represents the decrease in hole density due to recombination. The third term ( $Y_G$ ) is also in the numerator,

$$Y_G = q\sqrt{\pi/2} \frac{\lambda}{\delta} \left(1 + \frac{w}{\delta}\right) \Phi(1 - e^{-\alpha w}) \quad (\text{S6.23})$$

and represents the increase in hole density due to generation.

These new terms are proportional to  $\lambda/\delta$ . This means that ignoring these terms and assuming hole quasiequilibrium is equivalent to assuming that the recombination length is much larger than the Debye length,  $\delta \gg \lambda$ . It is important to note that even when this assumption is relaxed, the form of  $J_p$  remains the same in that it is linear in  $J_G$  and  $p_s e^{-V_{sc}}$ . Thus, from a modeling standpoint, including these effects would be equivalent to altering the values of  $J_G$  and the coefficient of  $p_s e^{-V_{sc}}$ .

### Section E.S7 Surface State Mediated Transfer Model

Our surface state model is closely related to the Shockley-Read-Hall (SRH) recombination model as we have used a single energy level DOS for the surface states. However, because we allow for transfer between the surface states, catalyst, and solution, the steady-state occupancy of the surface states is different from that predicted by the SRH model. Some of the positive charge injected into the surface states does not participate in recombination but instead proceeds further to oxidize the catalyst and/or solution; this effect has been discussed before by van Maekelbergh<sup>11</sup> and is called *surface state-mediated transfer*. The results of this section are not required for solution of the model equations, but illuminate the relationship between our model and the SRH model and quantify the effect of surface state-mediated transfer.

The occupancy of the surface states is determined by applying current equality through them;

$$J_{vb,ss} + J_{cb,ss} = J_{ss,cat} + J_{ss,sol} \quad (S7.1)$$

where

$$J_{vb,ss} = \bar{J}_{vb,ss} \left( \frac{p_s s}{\bar{p}_s \bar{s}} - \frac{s^+}{\bar{s}^+} \right) \quad (S7.2)$$

$$J_{cb,ss} = \bar{J}_{cb,ss} \left( \frac{s}{\bar{s}} - \frac{n_s s^+}{\bar{n}_s \bar{s}^+} \right) \quad (S7.3)$$

$$J_{ss,cat} = \bar{J}_{ss,cat} \left( \frac{s^+ c_{ss}}{\bar{s}^+ \bar{c}_{ss}} - \frac{s c_{ss}^+}{\bar{s} \bar{c}_{ss}^+} \right) \quad (S7.4)$$



$$J_{ss,sol} = \bar{J}_{ss,sol} \left[ \frac{s^+}{\bar{s}^+} (e^{\Delta V_H/2}) - \frac{s}{\bar{s}} (e^{-\Delta V_H/2}) \right] \quad (S7.5)$$

Solving for  $s^+$  and calculating the currents permits one to write them in the form

$$J_{vb,ss} = J_r^{ss} + J_{vb,cat}^{ss} + J_{vb,sol}^{ss} \quad (S7.6)$$

$$J_{cb,ss} = -J_r^{ss} + J_{cb,cat}^{ss} + J_{cb,sol}^{ss} \quad (S7.7)$$

Here,  $J_r^{ss}$  represents the surface state recombination current, and the others represent surface state-mediated transfers, i.e. the current passed through the surface states from the semiconductor into the catalyst and solution. These currents are

$$J_r^{ss} = u_{ss} \bar{J}_{vb,ss} \bar{J}_{cb,ss} \left( \frac{p_s n_s}{\bar{p}_s \bar{n}_s} - 1 \right) \quad (S7.8)$$

$$J_{vb,cat}^{ss} = u_{ss} \bar{J}_{vb,ss} \bar{J}_{ss,cat} \left( \frac{p_s c}{\bar{p}_s \bar{c}} - \frac{c^+}{\bar{c}^+} \right) \quad (S7.9)$$

$$J_{vb,sol}^{ss} = u_{ss} \bar{J}_{vb,ss} \bar{J}_{ss,sol} \left( \frac{p_s}{\bar{p}_s} e^{\Delta V_H/2} - e^{-\Delta V_H/2} \right) \quad (S7.10)$$

$$J_{cb,cat}^{ss} = u_{ss} \bar{J}_{cb,ss} \bar{J}_{ss,cat} \left( \frac{c}{\bar{c}} - \frac{n_s c^+}{\bar{n}_s \bar{c}^+} \right) \quad (S7.11)$$

$$J_{cb,sol}^{ss} = u_{ss} \bar{J}_{cb,ss} \bar{J}_{ss,sol} \left( e^{\Delta V_H/2} - \frac{n_s}{\bar{n}_s} e^{-\Delta V_H/2} \right) \quad (S7.12)$$

where

$$u_{ss} = \frac{1}{\bar{s}^+} \left[ \bar{J}_{vb,ss} \left( \frac{\bar{s}}{\bar{s}^+} + \frac{p_s}{\bar{p}_s} \right) + \bar{J}_{cb,ss} \left( \frac{n_s \bar{s}}{\bar{n}_s \bar{s}^+} + 1 \right) + \bar{J}_{ss,cat} \left( \frac{\bar{s} c}{\bar{s}^+ \bar{c}} + \frac{c^+}{\bar{c}^+} \right) + \bar{J}_{ss,sol} \left( \frac{\bar{s}}{\bar{s}^+} e^{\Delta V_H/2} + e^{-\Delta V_H/2} \right) \right]^{-1} \quad (S7.13)$$

Eq. S7.8 is analogous to the main result of the SRH model, but is modified by the factor  $u_{ss}$ , which decreases when charge is transferred through the surface states instead of recombining. This factor essentially partitions the current into the surface states between recombination and further transfer out of the states. It is important to note that the presence of the catalyst can decrease the recombination current relative to a system without catalyst by moving charge out of the surface states and into the catalyst or solution. This acts to lower the surface state energy ( $E_{ss}$ ) hence reducing the states and leaving fewer holes in the surface states to recombine with electrons from the conduction band. The transfer currents (Eqs. S7.9 – S7.12) take the form of second-order rate expressions for direct transfer between semiconductor, catalyst, and solution, with more complicated “exchange currents” that depend on the applied bias through the factor  $u_{ss}$ .

We note also that the same analysis can be applied to the catalyst, which can function both as a recombination center and as an intermediary by which charge can be passed from the semiconductor to the solution, in the same way that surface states can. However, because of the non-monoenergetic DOS of the catalyst, the analysis is more involved, but the basic mechanisms and conclusions are the same.

### Section E.S8 Analytical Solution to Model Equations – Solving for $p_s$

Four equations are required to solve the model; electro neutrality holds that the charge in the Helmholtz layer must be balanced by charge in the semiconductor and surface states:

$$q_{sc} + q_{ss} = q_H \quad (\text{S8.1})$$

Current from the semiconductor to the surface states must equal current from the surface states to the solution:

$$J_{vb,ss} + J_{cb,ss} = J_{ss,cat} + J_{ss,sol} \quad (\text{S8.2})$$

Current into the catalyst, from the semiconductor and surface states, must equal current from the catalyst to the solution:

$$J_{vb,cat} + J_{cb,cat} + J_{ss,cat} = J_{cat,sol} \quad (\text{S8.3})$$

The hole current ( $J_p$ ) is equivalent to the current from the valance band to the surface states and from the valance band to the catalyst:

$$J_p = J_{vb,ss} + J_{vb,cat} \quad (\text{S8.4})$$

Eqs. S8.5, S8.6 and S8.7 can be applied to this final equation to solve the surface hole concentration:

$$J_p = J_G - \bar{J}_R e^{\bar{v}_{sc} - V_{sc}} \frac{p_s}{\bar{p}_s} \quad (\text{S8.5})$$

$$J_{vb,ss} = \bar{J}_{vb,ss} \left( \frac{p_s s}{\bar{p}_s \bar{s}} - \frac{s^+}{\bar{s}^+} \right) \quad (\text{S8.6})$$

$$J_{vb,cat} = \bar{J}_{vb,cat} \left( \frac{p_s}{\bar{p}_s} - e^{E_{cat} - \Delta V_H} \right) \quad (\text{S8.7})$$

Substituting into Eq. S8.4 yields:

$$J_G - \bar{J}_R e^{\bar{v}_{sc} - V_{sc}} \frac{p_s}{\bar{p}_s} = \bar{J}_{vb,ss} \left( \frac{p_s s}{\bar{p}_s \bar{s}} - \frac{s^+}{\bar{s}^+} \right) + \bar{J}_{vb,cat} \left( \frac{p_s}{\bar{p}_s} - e^{E_{cat} - \Delta V_H} \right) \quad (\text{S8.8})$$

We redistribute to isolate like terms

$$J_G + \bar{J}_{vb,ss} \frac{s^+}{\bar{s}^+} + \bar{J}_{vb,cat} e^{E_{cat} - \Delta V_H} = \bar{J}_R e^{\bar{v}_{sc} - V_{sc}} \frac{p_s}{\bar{p}_s} + \bar{J}_{vb,ss} \frac{p_s s}{\bar{p}_s \bar{s}} + \bar{J}_{vb,cat} \frac{p_s}{\bar{p}_s} \quad (\text{S8.9})$$

and factor out  $\frac{p_s}{\bar{p}_s}$

$$J_G + \bar{J}_{vb,ss} \frac{s^+}{\bar{s}^+} + \bar{J}_{vb,cat} e^{E_{cat} - \Delta V_H} = \frac{p_s}{\bar{p}_s} \left( \bar{J}_R e^{\bar{v}_{sc} - V_{sc}} + \bar{J}_{vb,ss} \frac{s}{\bar{s}} + \bar{J}_{vb,cat} \right) \quad (\text{S8.10})$$

Isolating  $\frac{p_s}{\bar{p}_s}$  gives the analytical solution to the surface hole concentration ( $p_s$ )

$$\frac{p_s}{\bar{p}_s} = \frac{J_G + \bar{J}_{vb,ss} \frac{S^+}{S^-} + \bar{J}_{vb,cat} e^{E_{cat} - \Delta V_H}}{\left( \bar{J}_R e^{\bar{V}_{sc} - V_{sc}} + \bar{J}_{vb,ss} \frac{S}{\bar{S}} + \bar{J}_{vb,cat} \right)} \quad (S8.11)$$

### Section E.S9 Ideal and Non-ideal Photodiode Derivation

The Gärtner model assumes that there is perfect hole conductivity and therefore neglects the behavior of holes in the depletion region. Ideal behavior is constructed by assuming that hole current is equivalent to the Gärtner current, and overall current is that minus the electron current

$$J_{ideal} = J_G - \bar{J}_{cb,sol} e^{-V} \quad (S9.1)$$

To solve for the  $V_{oc}$  we set  $J_{ideal} = 0$

$$V_{oc} \approx -\ln\left(\frac{J_G}{\bar{J}_{cb,sol}}\right) \quad (S9.2)$$

The generalized Gärtner model can be applied to account for depletion layer recombination. Doing so complicates the expression for hole current

$$J_p = J_G - \bar{J}_R e^{\bar{V}_{sc} - V_{sc}} \frac{p_s}{\bar{p}_s} \quad (S9.3)$$

For the non-ideal current expression, we modify the Gärtner model by introducing a first order rate constant into the reverse current:

$$J_{non-ideal} = J_G - k_1 \bar{J}_R e^{\bar{V}_{sc} - V_{sc}} \frac{p_s}{\bar{p}_s} - \bar{J}_{cb,sol} e^{-V} \quad (S9.4)$$

This allows us to write the following simplification,

$$J_{non-ideal} = \frac{J_G}{1 + \frac{\bar{J}_R e^{\bar{V}_{sc} - V_{sc}}}{\bar{J}_{vb,sol}}} - \bar{J}_{cb,sol} e^{\bar{V}_{sc} - V_{sc}} \quad (S9.5)$$

where

$$\bar{J}_{vb,sol} = k_1 \frac{J_G}{p_s/\bar{p}_s} - \bar{J}_R e^{\bar{V}_{sc} - V_{sc}} \quad (S9.6)$$

The non-ideal photodiode equation is solved for the  $V_{oc}$  by setting  $J_{non-ideal} = 0$ ,

$$V_{oc} = -\ln\left(\sqrt{\frac{J_G \bar{J}_R}{\bar{J}_{cb,sol} \bar{J}_{vb,sol}} + \frac{1}{4}} - \frac{1}{2}\right) + \ln\left(\frac{\bar{J}_R}{\bar{J}_{vb,sol}}\right) \quad (S9.7)$$

### Section E.S10 Model Results – Only Catalyst (no surface states)

The model can be compared to our previously employed differential equations based simulation if surface states are neglected.<sup>12</sup> As expected, the catalyst potential shifts quickly at  $V_{oc}$  to accommodate slower catalysts. Once catalysis becomes sufficiently slow (small  $\bar{J}_{cat,sol}$ ) depletion recombination limits device performance by limiting the maximum  $E_{p,s}$  (and consequently  $V_{cat}$ ) achievable at any given  $V_{app}$ . This can be seen in the shallower  $E_{cat}$  vs.  $V_{app}$  transition slope for the slowest two catalysts in Figure E.S4(d).

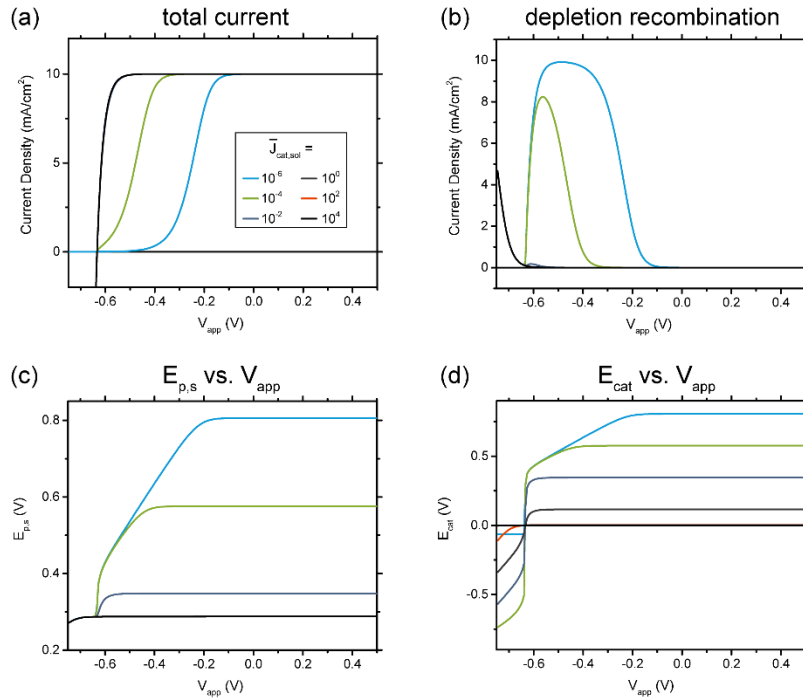


**Figure E.S4. Simulation results for the system without surface states.** Exchange currents for this simulation are,  $\bar{J}_{vb,cat} = 10^{-4}$ ,  $\bar{J}_{cb,cat} = 10^{-10} \text{ mA cm}^{-2}$ . The simulation is solved for  $\bar{J}_{cat,sol} = [10^{-6}, 10^{-4}, 10^{-2}, 10^0, 10^2, 10^4]$ .

These results are similar to the differential equation based model in that they predict slow catalysts can be compensated by increases in  $E_{cat}$ . While the limit of this behavior is determined by recombination in the depletion region, for both models, this model provides an analytical solution to the limitation.

### **Section E.S11 Model Results – Only Surface States (no catalyst)**

A system with only surface states acts similar to the buried “metallic” junctions defined in our previous work.<sup>12</sup> Since the monoenergetic surface state level cannot shift relative to the semiconductor bands (no internal charge screening), this system relies on a Helmholtz potential to drive oxidation. This is the same physical situation as found for impermeable catalysts, which also contain a large quantity of unscreened charge states and hence can only be affected by a change in the electrostatic potential drop between the catalyst and the solution.

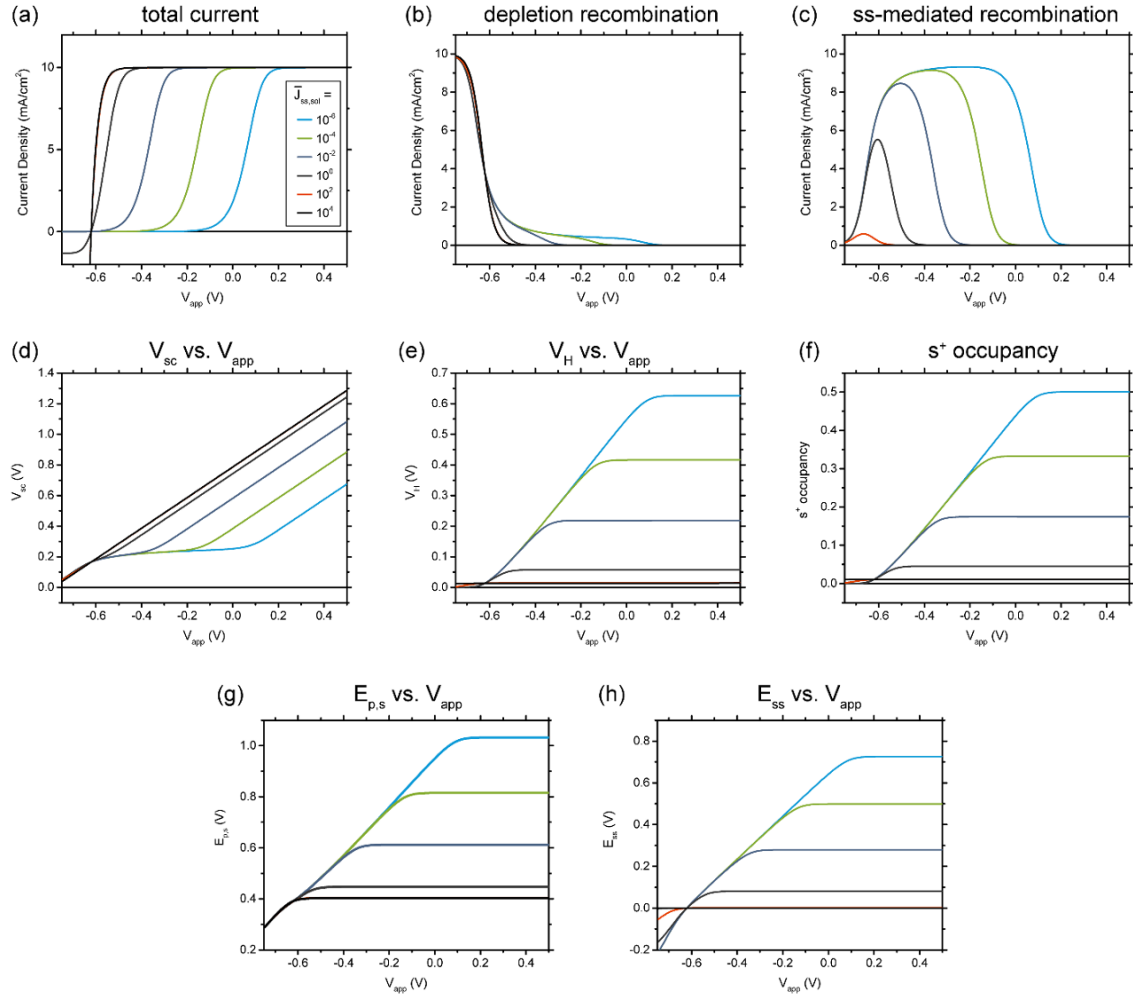


**Figure E.S5. Simulation results for the system without surface states.** Exchange currents for this simulation are  $\bar{J}_{vb,ss} = 10^{-6}$ ,  $\bar{J}_{cb,ss} = 10^{-10}$  mA cm<sup>-2</sup>. The simulation is solved for  $\bar{J}_{ss,sol} = [10^{-6}, 10^{-4}, 10^{-2}, 10^0, 10^2, 10^4]$ .

For slow oxidation kinetics (small  $\bar{J}_{ss,sol}$ ) charge builds up in the surface states (Figure E.S5f) and produces a sizeable Helmholtz drop (Figure E.S5e). Surface state charging also increases surface state mediated recombination (Figure E.S5c), which accounts for the cathodic shift in the J-V behavior relative to curves for quicker oxidation kinetics (Figure E.S5a).

## Section E.S12 Model Results – Parallel behavior

For models containing both surface states and catalyst states there are two primary behavior regimes. If electronic communication between the surface states and catalyst states is poor ( $\bar{J}_{ss,cat}$  is small) we say that the system behaves in parallel. Whereas, good communication gives rise to series behavior. We examine the parallel behavior in this SI section and the series behavior in the subsequent section. We note that series behavior is more likely to for real systems.

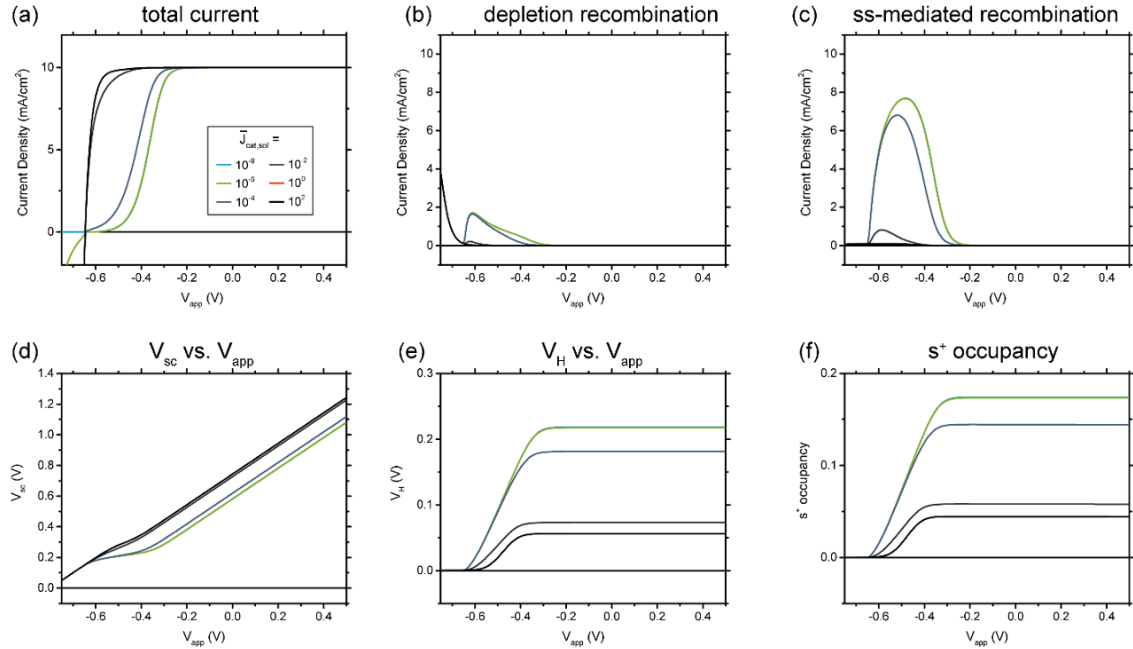


**Figure E.S6. Simulation results for model exhibiting parallel behavior ( $\bar{J}_{ss,cat} = 0$ ).** Exchange currents for this simulation are  $\bar{J}_{vb,ss} = 10^{-6}$ ,  $\bar{J}_{cb,ss} = 10^{-10}$ ,  $\bar{J}_{vb,cat} = 10^{-4}$ ,  $\bar{J}_{cb,cat} = 10^{-10}$ ,  $\bar{J}_{ss,sol} = 10^{-2}$ , and  $\bar{J}_{ss,cat} = 0$  mA cm<sup>-2</sup>. The simulation is solved for  $\bar{J}_{cat,sol} = [10^{-8}, 10^{-6}, 10^{-4}, 10^{-2}, 10^0]$ .

This model shows two regions of behavior. In the first, for large  $\bar{J}_{cat,sol}$  values, J-V characteristics collapse to the same limit given by the pure catalyst model in S10 (Figure E.S6a). This occurs because transfer from the valance band to the catalyst dominates which allows the system to act as if the surface states do not exist. Surface state occupancy remains low for these curves (Figure E.S6f). Once catalysis becomes sufficiently slow the second behavior region sets in. In this region, a larger surface hole concentration is needed to further oxidize the catalyst (Figure E.S7a). However, the increase in  $p_s$  promotes surface state filling (Figure E.S6f), resulting in an



increased Helmholtz drop (Figure E.S6e) and the promotion of direct oxidation from the surface states (Figure E.S7d). The result is that  $J_{ss,sol}$  becomes the dominant driver of current while  $J_{cat,sol}$  becomes negligible. The cathodic shift in the J-V behavior when moving from the 1<sup>st</sup> to the 2<sup>nd</sup> region is accounted for by surface state mediated recombination (Figure E.S6c) As the surface states fill they become recombination centers while simultaneously driving the OER. This recombination is also why the  $E_{cat}$  vs.  $V_{app}$  slope diminishes for the slower  $\bar{J}_{cat,sol}$  values (Figure E.S7c). The recombination precludes the surface hole quasi Fermi level from charging the catalyst to a potential necessary for OER.

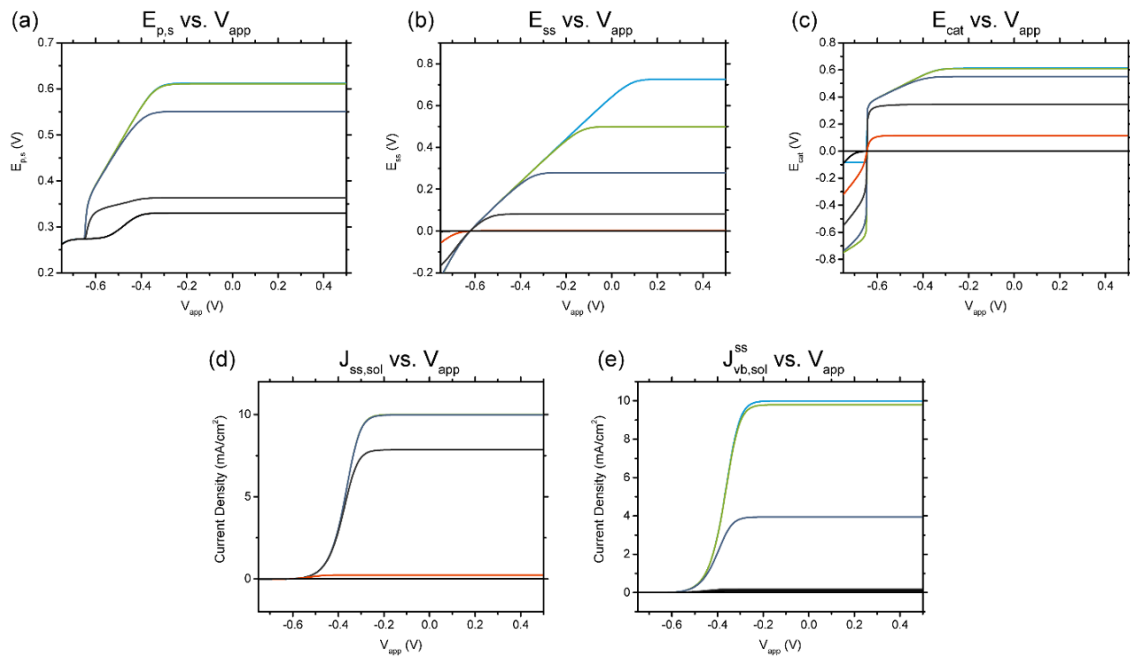


**Figure E.S7. Additional simulation results for model exhibiting parallel behavior ( $\bar{J}_{ss,cat} = 0$ ).** Colors correspond to those in Figure E.S6.

## Section E.S13 Model Results – Series behavior

Here we describe the behavior of a model containing both surface states and catalyst states where these elements behave in series with each other. That is, where  $\bar{J}_{ss,cat}$  is sufficiently large to allow electronic communication between the surface states and catalyst.

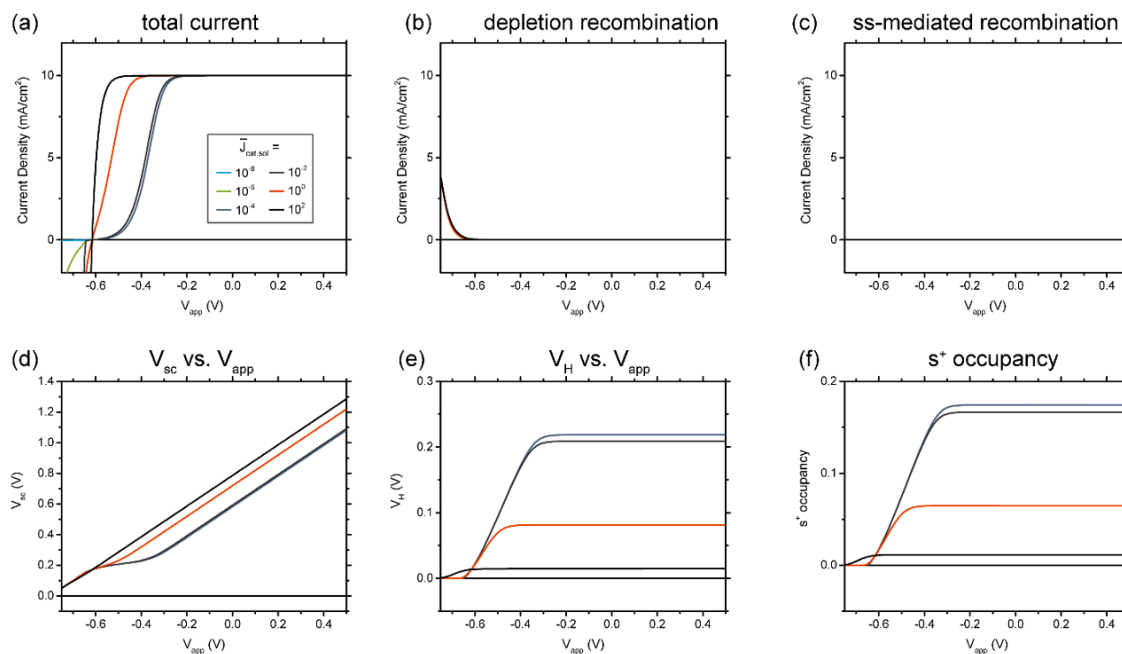


**Figure E.S8. Simulation results for model exhibiting parallel behavior.** Exchange currents for this simulation are  $\bar{J}_{vb,ss} = 10^{-6}$ ,  $\bar{J}_{cb,ss} = 10^{-10}$ ,  $\bar{J}_{vb,cat} = 10^{-4}$ ,  $\bar{J}_{cb,cat} = 10^{-10}$ ,  $\bar{J}_{ss,sol} = 10^{-2}$ , and  $\bar{J}_{ss,cat} = 10^5 \text{ mA cm}^{-2}$ . The simulation is solved for  $\bar{J}_{cat,sol} = [10^{-8}, 10^{-6}, 10^{-4}, 10^{-2}, 10^0, 10^2]$ .

Like the parallel model, results here exhibit two distinct regions of behavior. In the first, for large  $\bar{J}_{cat,sol}$  values, J-V characteristics collapse to the same limit given by the pure catalyst model in S10 (Figure. E.S8a). Unlike the parallel model, the transition to the second region (where the J-V curves have shifted cathodically) occurs much earlier here (at higher values of  $\bar{J}_{cat,sol}$ ). The earlier transition is due to back transfer of holes from the catalyst to the surface states (Figure E.S9e). This transfer occurs because the catalyst and surface states are now at quasi-equilibrium with each other (Figures E.S9b & E.S9c) and so the surface states act as a hole “sink” even when they cannot drive the OER themselves. The “sink” behavior means that the 2<sup>nd</sup> region exhibits an increase in the surface state occupancy and in the Helmholtz drop (Figures E.S8e & E.S8f). The

latter effect increases the ability for surface states to directly drive the OER (Figure E.S9d). Interestingly, the cathodic J-V shift when moving from the 1<sup>st</sup> to 2<sup>nd</sup> region is not explained by either depletion recombination or surface state mediated recombination (Figures E.S8b & E.S8c). Examining the conduction band to catalyst surface state mediated transfer ( $J_{cb,cat}^{ss}$ ) reveals the cause of this shift. Ultimately, recombination still occurs in the surface states, but the recombination is not direct – electrons from the conduction band recombine with holes back-transferring from the catalyst (Figure E.S9f).

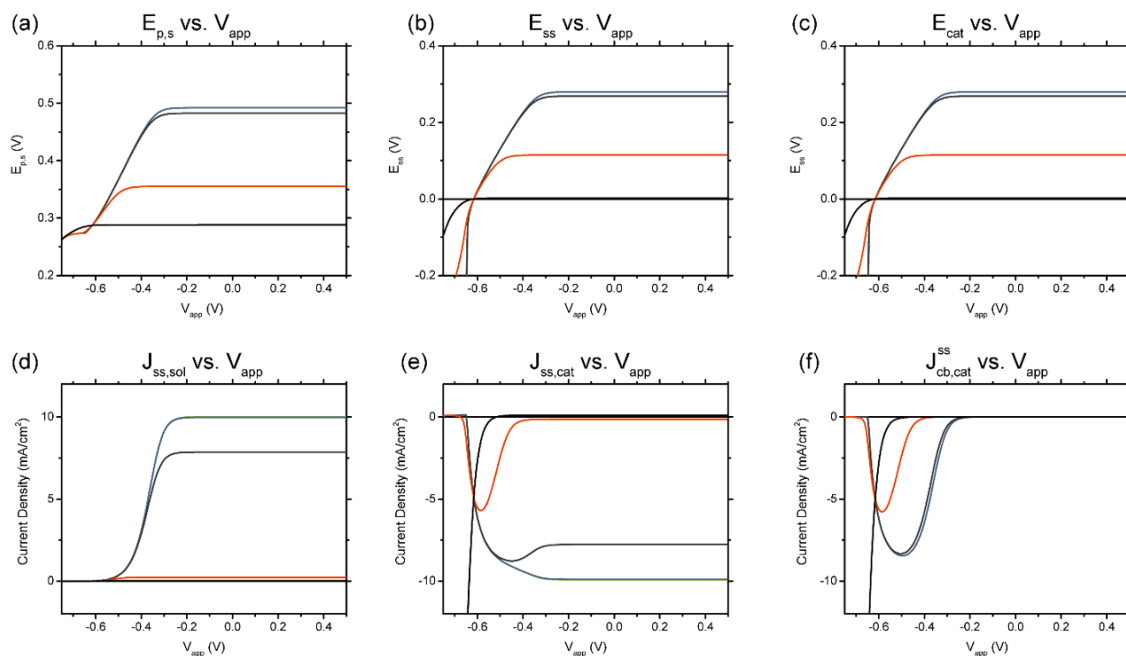


**Figure E.S9. Additional simulation results for model exhibiting parallel behavior.** Colors correspond to those in Figure E.S8.

## Section E.S14 Full Model – Mathematica

To facilitate comprehension, the Mathematica files are broken into four core components, (1) “Model Initialization and Logic”, (2) “Solving the Model”, (3) “Current Expression and Datasets”, and (4) “Plotting Functions”. The first and second components include all the model logic and the computational solve for the system of four equations. The final two components are purely cosmetic, in that they are used to generate datasets and then plot them. Note that teal code is Mathematica’s comment notation, these sections are incorporated to help the reader understand the subsequent code blocks.

```
(* Variables Defined:
s is s (surface state concentration),
sp is s' (oxidized surface state concentration),
sq is S,
spq is S',
c is c (catalyst states),
cq is c,
cp is c',
cpq is c',
ess is Ess (surface state energy),
esso is Eoss (formal energy sans helmholtz drop),
vh is VH,
vh0 is VH,
ec is Ecat,
p is ps/ps,
v is Vapp,
jg is JG (Gärtner Current),
jd is JR (Depletion recombination exchange current),
jps is Jb,ss,
jns is Jb,ss,
jpc is Jb,cat,
jss is Jss,sol,
jsc is Jss,cat,
jnc is Jb,cat,
jcs is Jcat,sol,
ass is alpha (reaction coordinate),
vo is V,
cs is Cs,
nss is Ns (surface state DOS),
nd is Nb (semiconductor dopant density),
ch is CH (helmholtz capacitance)
*)

(*Substitutions list for s, s', S, S', c, c', c, c'*)
subs = (s → 1 / (1 + E-(-esso - vh + ess)), sp → 1 / (1 + E-(-ess + esso + vh)), sq → 1 / (1 + E-(-esso - vh0)), spq → 1 / (1 + E-(+vh0 + esso)),
c → 1 / (1 + E-(-esso - vh + ec)), cp → 1 / (1 + E-(-ec + esso + vh)), cq → 1 / (1 + E-(-esso - vh0)), cpq → 1 / (1 + E-(esso + vh0)));

(*Solving Jb,ss + Jb,cat = JG for p *)
jps (ps / sq - sp / spq) + jpc (p - E-(ec - vh + vh0)) = jg - jd E-(-v + vh - vh0) p /. subs // Simplify;
subs = Join[subs, Solve[%, p] // Flatten]; (*Adds p to substitution list*)

(*
The three primary equations
#1 Jb,ss + Jb,cat = Jss,sol + Jss,cat
#2 Jb,cat + Jb,cat + Jss,cat = Jcat,sol
#3 qsc + qss = qH
*)
eqn =
{jps (ps / sq - sp / spq) + jns (s / sq - E-(-v + vh - vh0) sp / spq) =
jss (sp / spq E-(ass (vh - vh0)) - s / sq E-(- (1 - ass) (vh - vh0))) + jsc ((sp c) / (spq cq) - (s cp) / (sq cpq)),
jpc (p - E-(ec - vh + vh0)) + jnc (E-(-ec + vh - vh0) - E-(-v + vh - vh0)) + jsc ((sp c) / (spq cq) - (s cp) / (sq cpq)) = jcs (E-(ec / 2) - E-(-ec / 2)),
nd * Sqrt[Abs[(v + vo - vh)]] + cs nss sp = ch vh} /. subs // Simplify;

(*Solving for Voc*)
eqn /. subs /. {ec → 0, ess → 0, vh → vh0, jd → jd} // Simplify;
voc = v /. Solve[%, {v}][[2]] /. C[1] → 0;
```

Figure E.S10. Model code section 1. Model initialization and key equations.

```

(*Constant Substitutions: Jvb,ss, Jcb,ss, Jvb,cat, Jcb,cat, Jss,sol, Jss,cat, Jg, Jdr, Nl, Nss, E0ss, Vg, ass, Cl, Cs*)
const = {jps → 1*^6, jns → 1*^10, jpc → 1*^4, jnc → 1*^10, jss → 1*^2, jsc → 0*10^5, jg → 10, jd → 1*^-17, nd → 1*^0, nss → 1*^5,
  esso → 4, vo → 32, ass → 1/2, ch → 200, cs → 1*^-1} // N;

(*Determine VH and add to Constant Substitutions*)
AppendTo[const, FindRoot[eqn[[3]] /. subs /. {ess → 0, v → 0, vh → vh0} /. const, {vh0, 0}][[1]];

(*
Block solves the analytical expressions at various values of Jcat,sol
pmin and pmax are the boundary exponent values and dp is the transition between them, such that:
Jcat,sol = {10pmin, 10pmin+dp, 10pmin+2dp, ..., 10pmax-dp, 10pmax}
Outputs into the list: "data"
*)
pmin = -10;
pmax = 4;
dp = 2;
einc = 0.0;
np = (pmax - pmin) / dp;
out = {};
eqc = eqn /. const;
Legend = Range[pmin, pmax, dp];
var = jcs;
For[ip = pmin, ip ≤ pmax, ip += dp,
Block[{jcs = 10^ip},
varv = voc /. const;
vmax = 20;
vmin = -30;
nv = 200;
dv = (vmax - vmin) / nv;
data = {{varv, FindRoot[eqc /. v → varv, {ess, 0}, {ec, 0}, {vh, vh0 /. const}] // Quiet, var}};
varv += dv;
For[, varv < vmax, varv += dv,
AppendTo[data,
{varv, FindRoot[eqc /. v → varv, {ess, -einc + ess /. Last[data][[2]]}, {ec, -einc + ec /. Last[data][[2]]},
{vh, 0 einc + vh /. Last[data][[2]]}, MaxIterations → 300] // Quiet, var}};
];
varv = voc - dv /. const;
AppendTo[data, {varv, FindRoot[eqc /. v → varv, {ess, ess /. data[[1, 2]]}, {ec, ec /. data[[1, 2]]}, {vh, vh /. data[[1, 2]]} // Quiet, var}};
varv -= dv;
For[, varv > vmin, varv -= dv,
AppendTo[data,
{varv, FindRoot[eqc /. v → varv, {ess, einc + ess /. Last[data][[2]]}, {ec, 0 einc + ec /. Last[data][[2]]}, {vh, -0 einc + vh /. Last[data][[2]]} //
Quiet, var}};
];
data = SortBy[data, First];
];
AppendTo[out, data];
]

```

Figure E.S11. Model code section 2. Current continuity equations and logic used to solve the model.

```

(*Explicit expressions for J_tot, J_ss,sol, J_cat,sol, J_ss,cat, J_cb,cat, J_ub,cat, J_cb,ss, J_ub,ss, S', E_p,s, J_g, J_dr, and J_R*)
jexp = jss (sp / sq) E^(ass (vh - vh0)) - s / sq E^(-(1 - ass) (vh - vh0)) + jcs (E^(ec / 2) - E^(-ec / 2)) / . subs // Simplify;
jssexp = jss (sp / sq) E^(ass (vh - vh0)) - s / sq E^(-(1 - ass) (vh - vh0)) / . subs // Simplify;
jcatexp = jcs (E^(ec / 2) - E^(-ec / 2)) / . subs // Simplify;
jscexp = jsc ((sp c) / (sq cq) - (s cp) / (sq cpq)) / . subs // Simplify;
jncexp = jnc (E^(-ec + vh - vh0) - E^(-v + vh - vh0)) / . subs // Simplify;
jpcexp = jpc (p - E^(ec - vh + vh0)) / . subs // Simplify;
jnsexp = jns (s / sq - E^(-v + vh - vh0) sp / sq) / . subs // Simplify;
jpsexp = jps (ps / sq - sp / sq) / . subs // Simplify;
spexp = sp / . subs // Simplify;
epexp = Log(p) + vh - vh0 / . subs // Simplify;
jgexp = jg - jd E^(-v + vh - vh0) p / . subs // Simplify;
jdepexp = jd E^(-v + vh - vh0) p / . subs // Simplify;
jrexp =
  jps jns (p E^(-v + vh - vh0) - 1) (1 / sq)
  (jps (sq / sq + p) + jns (E^(-v + vh - vh0) sq / sq + 1) + jsc ((sq / sq) (c / cq) + (cp / cpq)) + jss (E^((vh - vh0) / 2) (sq / sq) + E^(-(vh - vh0) / 2))) ^
  (-1) / . subs // Simplify;
jrvbcatexp =
  jps jsc (p c / cq - cp / cpq) (1 / sq)
  (jps (sq / sq + p) + jns (E^(-v + vh - vh0) sq / sq + 1) + jsc ((sq / sq) (c / cq) + (cp / cpq)) + jss (E^((vh - vh0) / 2) (sq / sq) + E^(-(vh - vh0) / 2))) ^
  (-1) / . subs // Simplify;
jrvbsolexp =
  jps jss (p E^((vh - vh0) / 2) - E^(-(vh - vh0) / 2)) (1 / sq)
  (jps (sq / sq + p) + jns (E^(-v + vh - vh0) sq / sq + 1) + jsc ((sq / sq) (c / cq) + (cp / cpq)) + jss (E^((vh - vh0) / 2) (sq / sq) + E^(-(vh - vh0) / 2))) ^
  (-1) / . subs // Simplify;
jrcbcatexp =
  jns jsc (c / cq - (cp / cpq) E^(-v + vh - vh0)) (1 / sq)
  (jps (sq / sq + p) + jns (E^(-v + vh - vh0) sq / sq + 1) + jsc ((sq / sq) (c / cq) + (cp / cpq)) + jss (E^((vh - vh0) / 2) (sq / sq) + E^(-(vh - vh0) / 2))) ^
  (-1) / . subs // Simplify;
jrcbsolexp =
  jns jss (E^((vh - vh0) / 2) - E^(-v + vh - vh0) E^(-(vh - vh0) / 2)) (1 / sq)
  (jps (sq / sq + p) + jns (E^(-v + vh - vh0) sq / sq + 1) + jsc ((sq / sq) (c / cq) + (cp / cpq)) + jss (E^((vh - vh0) / 2) (sq / sq) + E^(-(vh - vh0) / 2))) ^
  (-1) / . subs // Simplify;

(*Expressions evaluated with the data list and stored in new lists*)
jdata = {#[1] / 40, jexp / . subs / . const / . var -> #[3] / . #[2]} &/@ # &/@ out;
jssdata = {#[1] / 40, jssexp / . subs / . const / . var -> #[3] / . #[2]} &/@ # &/@ out;
jcatdata = {#[1] / 40, jcatexp / . subs / . const / . var -> #[3] / . #[2]} &/@ # &/@ out;
jscdata = {#[1] / 40, jscexp / . subs / . const / . var -> #[3] / . #[2]} &/@ # &/@ out;
jncdata = {#[1] / 40, jncexp / . subs / . const / . var -> #[3] / . #[2] / . v -> #[1]} &/@ # &/@ out;
jpcdata = {#[1] / 40, jpcexp / . subs / . const / . var -> #[3] / . #[2] / . v -> #[1]} &/@ # &/@ out;
jnndata = {#[1] / 40, jnsexp / . subs / . const / . var -> #[3] / . #[2] / . v -> #[1]} &/@ # &/@ out;
jpndata = {#[1] / 40, jpsexp / . subs / . const / . var -> #[3] / . #[2] / . v -> #[1]} &/@ # &/@ out;
jgdata = {#[1] / 40, jgexp / . subs / . const / . var -> #[3] / . #[2] / . v -> #[1]} &/@ # &/@ out;
jdrdata = {#[1] / 40, jdepexp / . subs / . const / . var -> #[3] / . #[2] / . v -> #[1]} &/@ # &/@ out;
jrddata = {#[1] / 40, jrexp / . subs / . const / . var -> #[3] / . #[2] / . v -> #[1]} &/@ # &/@ out;
jrvbcadata = {#[1] / 40, jrvbcatexp / . subs / . const / . var -> #[3] / . #[2] / . v -> #[1]} &/@ # &/@ out;
jrvbsoldata = {#[1] / 40, jrvbsolexp / . subs / . const / . var -> #[3] / . #[2] / . v -> #[1]} &/@ # &/@ out;
jrcbcadata = {#[1] / 40, jrcbcatexp / . subs / . const / . var -> #[3] / . #[2] / . v -> #[1]} &/@ # &/@ out;
jrcbsoldata = {#[1] / 40, jrcbsolexp / . subs / . const / . var -> #[3] / . #[2] / . v -> #[1]} &/@ # &/@ out;

essdata = {#[1] / 40, (ess) / 40 / . #[2]} &/@ # &/@ out;
ecdata = {#[1] / 40, (ec) / 40 / . #[2]} &/@ # &/@ out;
vhdata = {#[1] / 40, vh / 40 / . #[2]} &/@ # &/@ out;
vscdata = {#[1] / 40, (v + vo - vh) / 40 / . subs / . const / . var -> #[3] / . #[2] / . v -> #[1]} &/@ # &/@ out;
epdata = {#[1] / 40, (epexp) / 40 / . subs / . const / . var -> #[3] / . #[2] / . v -> #[1]} &/@ # &/@ out;
spdata = {#[1] / 40, spexp / . subs / . const / . var -> #[3] / . #[2] / . v -> #[1]} &/@ # &/@ out;

```

Figure E.S12. Model code section 3. Current output expressions and data frames.

```

(*All plotting functions*)
imsiz = {500, 400};

jrplot = ListPlot[jrdata, PlotRange -> {-5, 12}, Joined -> True, PlotLabel -> "Jss,recombination", ImageSize -> imsiz, Frame -> True,
  FrameLabel -> {"J (mA/cm2)", None}, {"V", None}], LabelStyle -> Directive[13];
jplot = ListPlot[jdata, PlotRange -> {-5, 12}, Joined -> True, PlotLabel -> "Jtot", ImageSize -> imsiz, Frame -> True,
  FrameLabel -> {"J (mA/cm2)", None}, {"V", None}], LabelStyle -> Directive[13];
PlotLegends -> Placed[LineLegend[Legend, LabelStyle -> {GrayLevel[0.3], Bold, 18}, LegendLabel -> "Jcat,sol = 103", LegendLayout -> {"Row", 4},
  LegendFunction -> Framed], {0.8, 0.35}];
jssplot = ListPlot[jssdata, PlotRange -> {-5, 12}, Joined -> True, PlotLabel -> "Jss,sol", ImageSize -> imsiz, Frame -> True,
  FrameLabel -> {"J (mA/cm2)", None}, {"V", None}], LabelStyle -> Directive[13];
jcatplot = ListPlot[jcatdata, PlotRange -> {-5, 12}, Joined -> True, PlotLabel -> "Jcat,sol", ImageSize -> imsiz, Frame -> True,
  FrameLabel -> {"J (mA/cm2)", None}, {"V", None}], LabelStyle -> Directive[13];
jscplot = ListPlot[jscdata, PlotRange -> {-12, 12}, Joined -> True, PlotLabel -> "Jss,cat", ImageSize -> imsiz, Frame -> True,
  FrameLabel -> {"J (mA/cm2)", None}, {"V", None}], LabelStyle -> Directive[13];
jncplot = ListPlot[jncdata, PlotRange -> {-12, 12}, Joined -> True, PlotLabel -> "Jcb,cat", ImageSize -> imsiz, Frame -> True,
  FrameLabel -> {"J (mA/cm2)", None}, {"V", None}], LabelStyle -> Directive[13];
jpcplot = ListPlot[jpcdata, PlotRange -> {-12, 12}, Joined -> True, PlotLabel -> "Jvb,cat", ImageSize -> imsiz, Frame -> True,
  FrameLabel -> {"J (mA/cm2)", None}, {"V", None}], LabelStyle -> Directive[13];
jnsplot = ListPlot[jnsdata, PlotRange -> {-12, 12}, Joined -> True, PlotLabel -> "Jcb,ss", ImageSize -> imsiz, Frame -> True,
  FrameLabel -> {"J (mA/cm2)", None}, {"V", None}], LabelStyle -> Directive[13];
jpsplot = ListPlot[jpsdata, PlotRange -> {-5, 12}, Joined -> True, PlotLabel -> "Jvb,ss", ImageSize -> imsiz, Frame -> True,
  FrameLabel -> {"J (mA/cm2)", None}, {"V", None}], LabelStyle -> Directive[13];
jdrplot = ListPlot[jdrdata, PlotRange -> {-5, 12}, Joined -> True, PlotLabel -> "Jdr", ImageSize -> imsiz, Frame -> True,
  FrameLabel -> {"J (mA/cm2)", None}, {"V", None}], LabelStyle -> Directive[13];
jgpplot = ListPlot[jgpdata, PlotRange -> {-5, 12}, Joined -> True, PlotLabel -> "JG", ImageSize -> imsiz, Frame -> True,
  FrameLabel -> {"J (mA/cm2)", None}, {"V", None}], LabelStyle -> Directive[13];
jrvcatplot = ListPlot[jrvcatdata, PlotRange -> {-10, 12}, Joined -> True, PlotLabel -> "(JSS)vb,cat", ImageSize -> imsiz,
  Frame -> True, FrameLabel -> {"J (mA/cm2)", None}, {"V", None}], LabelStyle -> Directive[13];
jrvcatsolplot = ListPlot[jrvcatsoldata, PlotRange -> {-10, 12}, Joined -> True, PlotLabel -> "(JSS)vb,sol", ImageSize -> imsiz,
  Frame -> True, FrameLabel -> {"J (mA/cm2)", None}, {"V", None}], LabelStyle -> Directive[13];
jrvcatsolplot = ListPlot[jrvcatsoldata, PlotRange -> {-10, 12}, Joined -> True, PlotLabel -> "(JSS)cb,cat", ImageSize -> imsiz,
  Frame -> True, FrameLabel -> {"J (mA/cm2)", None}, {"V", None}], LabelStyle -> Directive[13];
jrvcatsolplot = ListPlot[jrvcatsoldata, PlotRange -> {-10, 12}, Joined -> True, PlotLabel -> "(JSS)vb,sol", ImageSize -> imsiz,
  Frame -> True, FrameLabel -> {"J (mA/cm2)", None}, {"V", None}], LabelStyle -> Directive[13];

essplot = ListPlot[essdata, PlotRange -> All, Joined -> True, PlotLabel -> "Ess", ImageSize -> imsiz, Frame -> True,
  FrameLabel -> {"E (V)", None}, {"V", None}], LabelStyle -> Directive[13];
ecplot = ListPlot[ecdata, PlotRange -> All, Joined -> True, PlotLabel -> "Ecat", ImageSize -> imsiz, Frame -> True,
  FrameLabel -> {"E (V)", None}, {"V", None}], LabelStyle -> Directive[13];
vnpplot = ListPlot[vndata, PlotRange -> All, Joined -> True, PlotLabel -> "Vn", ImageSize -> imsiz, Frame -> True, FrameLabel -> {"V", None}, {"V", None}],
  LabelStyle -> Directive[13];
vscplot = ListPlot[vscdata, PlotRange -> All, Joined -> True, PlotLabel -> "Vsc", ImageSize -> imsiz, Frame -> True,
  FrameLabel -> {"V", None}, {"V", None}], LabelStyle -> Directive[13];
epplot = ListPlot[epdata, PlotRange -> All, Joined -> True, PlotLabel -> "Ep,s", ImageSize -> imsiz, Frame -> True,
  FrameLabel -> {"E (V)", None}, {"V", None}], LabelStyle -> Directive[13];
spplot = ListPlot[spdata, PlotRange -> All, Joined -> True, PlotLabel -> "S", ImageSize -> imsiz, Frame -> True,
  FrameLabel -> {"Occupancy", None}, {"V", None}], LabelStyle -> Directive[13];

GraphicsGrid[({jplot, jrplot, jdrplot}), PlotLabel -> "Relevant Currents", Frame -> True, FrameStyle -> Thick]
Print["\n"]
GraphicsGrid[({epplot, essplot, ecplot}), {vscplot, vnpplot, spplot}], PlotLabel -> "Energies and Potentials", Frame -> True,
  FrameStyle -> Thick]
Print["\n"]
GraphicsGrid[({jpcplot, jncplot, jscplot}), {jcatplot}], PlotLabel -> "Jvb,cat + Jcb,cat + Jss,cat = Jcat,sol", Frame -> True,
  FrameStyle -> Thick]
Print["\n"]
GraphicsGrid[({jpsplot, jnsplot}), {jssplot, jscplot}], PlotLabel -> "Jvb,ss + Jcb,ss = Jss,sol + Jss,cat", Frame -> True, FrameStyle -> Thick]
Print["\n"]
GraphicsGrid[({jpsplot, jpcplot}), {jgpplot}], PlotLabel -> "Jvb,ss + Jvb,cat = JG,generalized", Frame -> True, FrameStyle -> Thick]
Print["\n"]
GraphicsGrid[({jrvcatplot, jrvcatsolplot}), {jrvcatsolplot, jrvcatsolplot}], PlotLabel -> "Surface State Transfer Currents",
  Frame -> True, FrameStyle -> Thick]

```

Figure E.S13. Model code section 4. Plotting functions.

## APPENDIX D. SUPPORTING INFORMATION FOR PAPER F

### Junction Behavior of n-Si Photoanodes Protected by Thin Ni Elucidated from Dual Working Electrode Photoelectrochemistry

#### Section F.S1

The electrical conductivity through the photoelectrochemical (PEC) activated Ni film is largely dependent on the state of the near-solution Ni species. If the surface Ni is in the Ni(OH)<sub>2</sub> phase it will behave as an insulator and impede charge transfer. When the catalyst is oxidized to NiOOH, it exhibits much higher conductivity.<sup>1-3</sup> The electrical junction behavior of the composite dual working electrode (DWE) is dependent on what state the Ni is in prior to performing the Au thermal deposition to form the WE<sub>2</sub> contact.

A significant concern in depositing 10 nm of Au on 3 and 5 nm Ni films is the development of direct n-Si | Au shorting. To evaluate this concern, we produced DWE photoanodes wherein the redox active Ni is isolated as Ni(OH)<sub>2</sub> prior to Au evaporation. Devices created in this manner can be evaluated for shorting by examining the dark ex-situ J-V characteristics before and after Ni(OH)<sub>2</sub> solution oxidation (Figure F.S1). Without n-Si | Au shorting, the J-V characteristics exhibit poor conductivity which becomes rectifying only once the Ni(OH)<sub>2</sub> is electrochemically oxidized to NiOOH. Devices were re-reduced after performing in-situ DWE experiments; these J-V characteristics exhibit good agreement with the initial film which indicates WE<sub>2</sub> stability and sustained lack of shorting. Such “short-free” devices are suitable for further interface analysis.

We note that devices where the Ni is electrochemically oxidized to NiOOH, directly prior to Au depositions, tend to exhibit electrical conductivity despite electrochemical re-reduction (to Ni(OH)<sub>2</sub>). We speculate that this is caused by small regions of previously redox-active NiOOH being isolated from solution by the thin gold layer. In effect, these regions of Ni are never able to fully re-reduce and thus remain conductive despite the majority of the film being converted to Ni(OH)<sub>2</sub>. Electrodes produced in this manner are useful in that the junction photovoltage can be sensed at all relevant potentials through WE<sub>2</sub> (discussed more below).



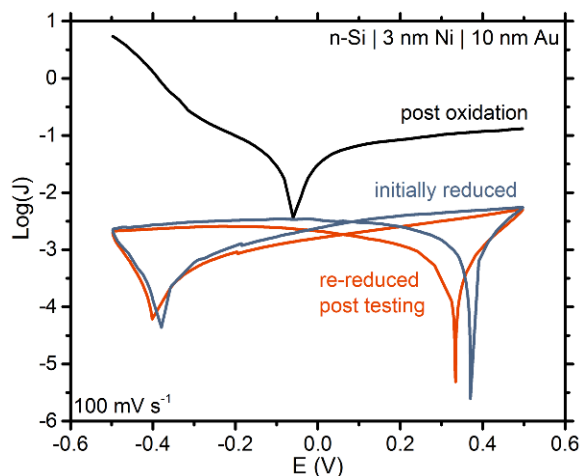


**Figure F.S1. Shorting test for photoelectrodes.** Dark, *ex-situ* JV characteristics for a DWE photoanode with Ni(OH)<sub>2</sub> isolation. Catalyst films were isolated as Ni(OH)<sub>2</sub> by supplying a reducing potential for 10 min (200 mV cathodic of the reduction peak potential) and to NiOOH by supplying an oxidizing potential for 10 min (200 mV anodic of the oxidation peak potential).

## Section F.S2

To examine electrode activity as a function of (long-term) cycling we photo-deposited additional Ni before evaporation of the Au WE<sub>2</sub>. This improved the cycling longevity of the DWE electrode. Such photodeposition of sacrificial Ni is also useful in that it consistently prevents n-Si | Au shorting (which is often observed for the thinner layers). We examine the 5 nm devices because they exhibit an intermediate photovoltage enhancement relative to the 3 and 20 nm devices. During a typical experiment, WE<sub>1</sub> was cycled 49 times through the oxidation and reduction peak without significantly entering the OER region. On the 50<sup>th</sup> cycle a more extended CV was swept to include the OER region and then WE<sub>2</sub> was cycled once to examine the catalyst activity independent of the semiconductor. After 250 cycles it becomes apparent that WE<sub>2</sub> losses significant contact with the catalyst. This conclusion is consistent with the diminishing redox peaks, likely indicating the dissolution or detachment of sacrificial catalyst.

Figure F.S2 expands on the data in Figure F.3 of the text, and demonstrates the continued effects of this process on both working electrodes. Results show that OER onset significantly improves over 250 cycles when measured from WE<sub>1</sub> but only improves over the first 50 cycles when measured from WE<sub>2</sub>. Additionally, the improvement onset potential measured through WE<sub>2</sub> (i.e. catalyst) is ~100 mV while that measured through WE<sub>1</sub> (i.e. semiconductor ohmic contact) is ~400 mV.

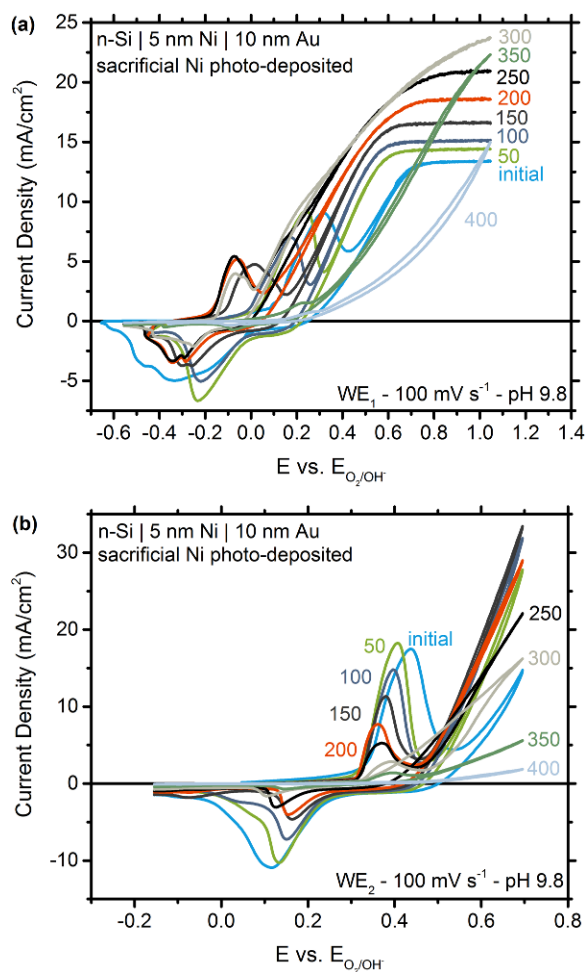


**Figure F.S2. Comparison of WE1 and WE2 with extended ageing.** (a) Illuminated cycling experiments through WE<sub>1</sub> on n-Si | 5 nm Ni | 10 nm Au DWE photoanodes. (b) Illuminated cycling experiments through WE<sub>2</sub> on n-Si | 5 nm Ni | 10 nm Au DWE photoanodes. Same device as Figure F.S2a. Both experiments were performed under 100 mW cm<sup>-2</sup> of AM1.5G solar simulation in a pH 9.8 K-borate buffer.

Because sacrificial catalyst loss is apparent during cycling experiments we controlled for this effect by intentionally “pinning” the junction. To accomplish this a 10 nm Au interlayer was deposited between the n-Si and 5 nm Ni layer. CV experiments were conducted in an identical manner to those in Figure F.S2. Sacrificial Ni loss was also noticed in this instance but no change in the illuminated OER onset was seen when measured through WE<sub>1</sub>. Additionally, the redox peak locations remained largely unaffected by continued cycling, when measured through both WE<sub>1</sub> and WE<sub>2</sub>. Whereas in the n-Si | 5 nm Ni junction the redox peaks moved mostly in step with the OER onset increases, when measured through WE<sub>1</sub>. This data is consistent with the expected behavior

of the buried n-Si | Au junction and shows that the cathodic shifts in photocurrent onset are produced specifically by changes to the n-Si | Ni junction.

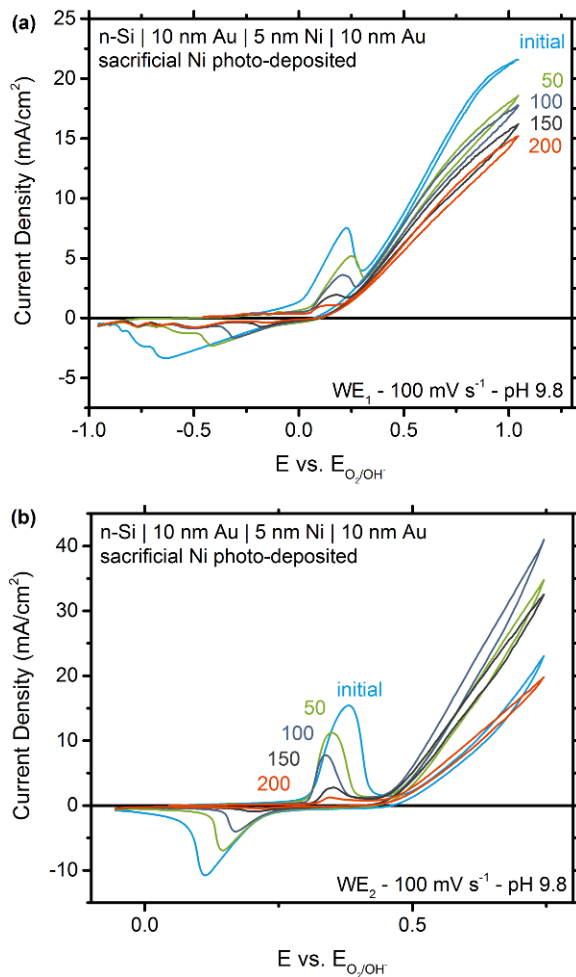


**Figure F.S3. Dual-working-electrode technique applied to Au control. (a)** Illuminated cycling experiments through WE<sub>1</sub> on n-Si | 10 nm Au | 5 nm Ni | 10 nm Au DWE photoanodes. **(b)** Illuminated cycling experiments through WE<sub>2</sub> on n-Si | 10 nm Au | 5 nm Ni | 10 nm Au DWE photoanodes. Same device as Figure F.S3a. Both experiments were performed under 100 mW cm<sup>-2</sup> of AM1.5G solar simulation in a pH 9.8 K-borate buffer.

### Section F.S3

Thermal evaporation of ~2 nm Ni on n-Si results in photoanodes which decay back to bare n-Si response within ~20 CVs (Figure F.S4). Limited lifetime is attributed to passivation via holes in the thermally evaporated film and oxidation of the underlying Si surface.

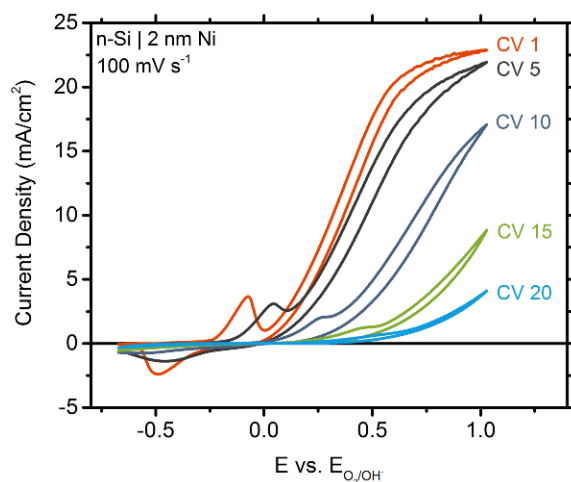


**Figure F.S4. Illuminated degradation of an n-Si photoanode protected with 2 nm metallic Ni.** The data was collected under  $100 \text{ mW cm}^{-2}$  of solar simulation in a pH 9.8 K-borate buffer.

Similarly, cathodic electrochemical deposition of  $\text{Ni}(\text{OH})_2$ , accomplished by maintaining a current density of  $-0.1 \text{ mA cm}^{-2}$  for 10 min in a 0.1 M, pH 7  $\text{NiSO}_4$  solution, fail to protect photoanodes at all due to the electrolyte permeability of the catalyst layer (Figure F.S5). Deposition was sufficiently thick as to be visible by eye.

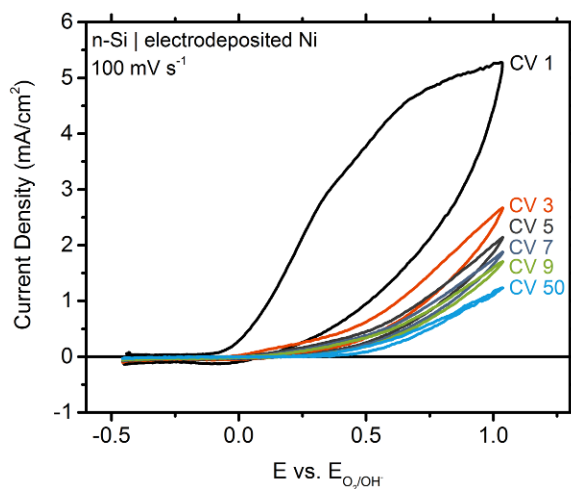


**Figure F.S5. Illuminated degradation of an n-Si photoanode protected with electrochemically deposited Ni.** The voltammetry presented shows initial limited photoelectrode performance which degrades rapidly within  $\sim 10$  cycles. Electrolyte permeable electrochemically deposited Ni (oxy)hydroxide cannot protect the Si surface. The data was collected under  $100 \text{ mW cm}^{-2}$  of solar simulation in a pH 9.8 K-borate buffer.

## Section F.S4

Dark linear sweep voltammograms (LSVs) on control devices (i.e. with direct Au|Si Schottky contact) exhibited the expected behavior for a buried Schottky junction. When normalized to the junction voltage ( $E_{\text{sem}} - E_{\text{cat}}$ ) the reverse saturation current remained invariant despite stepping the potential at WE<sub>2</sub> through a 500 mV range. In the forward bias regime (negative voltage in Figure F.S6), when normalized to the junction voltage, curves also collapsed upon each other at all WE<sub>2</sub> potentials. The devices display rectifying behavior, consistent with well-established Schottky diode theory.<sup>4</sup>

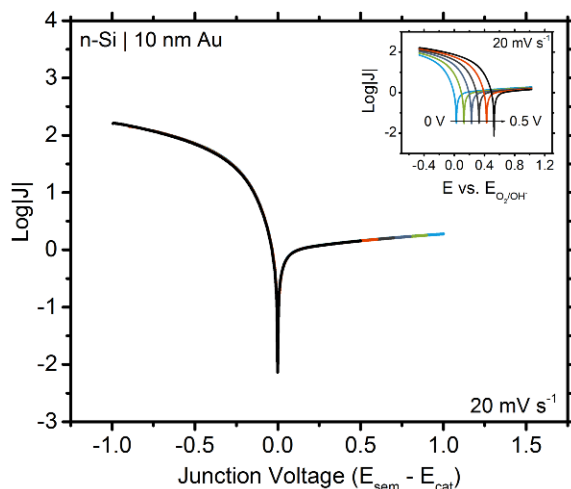


**Figure F.S6. Dark in-situ LSV characteristics for an intentionally buried n-Si | Au junction.** Results are normalized to the junction voltage to examine reverse saturation current – a function of barrier height. The data was collected in a pH 9.5 K-borate buffer.

For DWE junction experiments the chemical state of the Ni during deposition of the secondary Au working electrode is an important consideration. The porous Au can either be deposited on surface Ni isolated as NiOOH or as Ni(OH)<sub>2</sub>. Isolation in the Ni(OH)<sub>2</sub> state is useful in that it allows for identification of direct shorting from the Au to the n-Si (discussed above). However, Ni(OH)<sub>2</sub> is insulating and will produce a switching behavior in the DWE measurements when oxidized to conductive NiOOH. Isolation in the NiOOH phase eliminates the switching behavior, but n-Si | Au shorting cannot be identified. Both situations are discussed in SI section S1.

To understand better the interface character, we reproduced the DWE experiments with the Ni isolated in the NiOOH phase. Results are then compared to control devices wherein the junction is intentionally pinned; that is, where 10 nm of Au is thermally evaporated before Ni evaporation (Figure F.S6). The control devices behave as expected for a buried junction; rectifying behavior is

exhibited and each curve is nearly identical when normalized to the junction voltage. For DWE photoanodes where the Ni is isolated as NiOOH prior to gold evaporation, the LSVs depict buried junction behavior with a substantially reduced conductivity switch effect between Ni(OH)<sub>2</sub> and NiOOH (Figure F.S7). In both the devices with 3 nm and 5 nm of Ni, the forward bias region is effected by the in-situ transition from Ni(OH)<sub>2</sub> to NiOOH. In each case increases in conductivity appear to modestly enhance the current response. Interestingly this effect is more pronounced on the 3 nm Ni protected photoanodes perhaps as a result of fewer NiOOH regions protected by Au. However, examination of the reverse bias region in each case reveals an invariant current response, which is an indication of an invariant barrier height as the potential of the catalyst layer is changed. *The data further supports our hypothesis that protected Si photoanodes in the size regimes explored exhibit buried-junction behavior.*

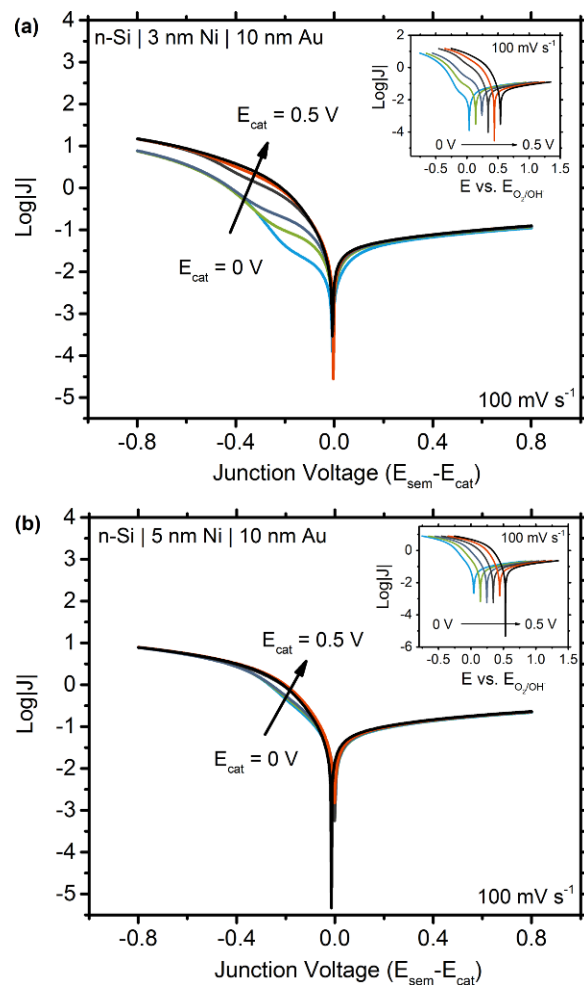


**Figure F.S7. Dark in-situ LSV characteristics for n-Si photoanodes protected with 3 and 5 nm of Ni.** (a) Dark in-situ LSV characteristics for a DWE n-Si | 3 nm Ni | Au junction. In these devices the Au layer was deposited after isolating the Ni in the conductive NiOOH form. (b) Dark in-situ LSV characteristics for a DWE n-Si | 5 nm Ni | Au junction. For both data sets  $E_{\text{cat}}$  is varied via  $\text{WE}_2$  in steps of 100 mV through the entire Ni redox region, while current voltage curves across the interface are collected for each  $E_{\text{cat}}$  by sweeping  $E_{\text{sem}}$  ( $\text{WE}_1$ ). The data was collected in a pH 9.5 K-borate buffer.

### Section F.S5

To better distinguish the Ni redox peak from the OER region, slower LSVs at  $10 \text{ mV s}^{-1}$  were collected before and after Fe incorporation. The offset between the two is  $\sim 99 \text{ mV}$  at  $2.5 \text{ mA/cm}^2$ , consistent with the  $\sim 100 \text{ mV}$  shift measured through  $\text{WE}_2$  at  $100 \text{ mV s}^{-1}$ .

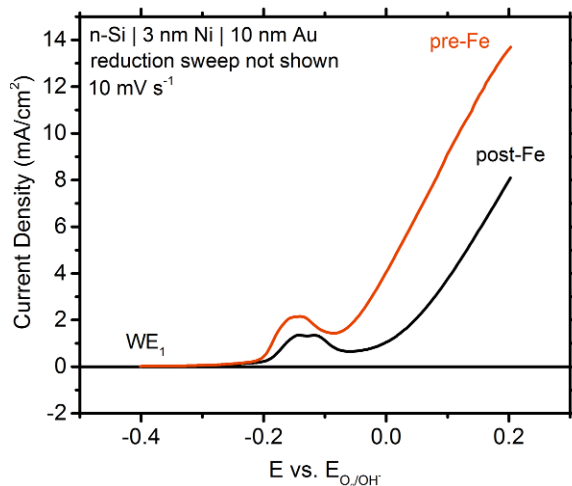


**Figure F.S8. Illuminated  $10 \text{ mV s}^{-1}$  LSVs collected through  $\text{WE}_1$  before and after Fe incorporation.** Results are similar to  $100 \text{ mV s}^{-1}$  LSVs but better resolve the redox peak and OER onset. The data was collected under  $100 \text{ mW cm}^{-2}$  of solar simulation in a pH 9.8 K-borate buffer.

### Section F.S6

XPS was used to identify the elemental composition and oxidation states of n-Si protected with 3 nm of Ni before and after electrochemical cycling. The raw data was shifted such that the adventitious carbon 1s peak was centered at a binding energy of 284.8 eV. A depth profile, via Ar ion sputtering (2 keV, 3  $\mu\text{A}$ ), was conducted in 5 s increments to determine compositional changes as a function of depth. For the *post-cycled* electrodes (Figure F.S9) XPS data shows that the surface is primarily composed of nominally Ni hydroxide/oxyhydroxide (Figure F.S9a). However, the depth profile indicates that residual metallic Ni persists under this layer and becomes the dominant Ni species after 20 s of Ar ion sputtering. Interestingly, this layer later gives way to an XPS spectrum consistent with NiSi, demonstrating direct contact between Si and Ni, even in the electrochemically cycled device. The Si regional spectra (Figure F.S9b) illustrates that the  $\text{SiO}_2$  layer has been milled through after  $\sim 75\text{s}$  of cumulative Ar ion sputtering.



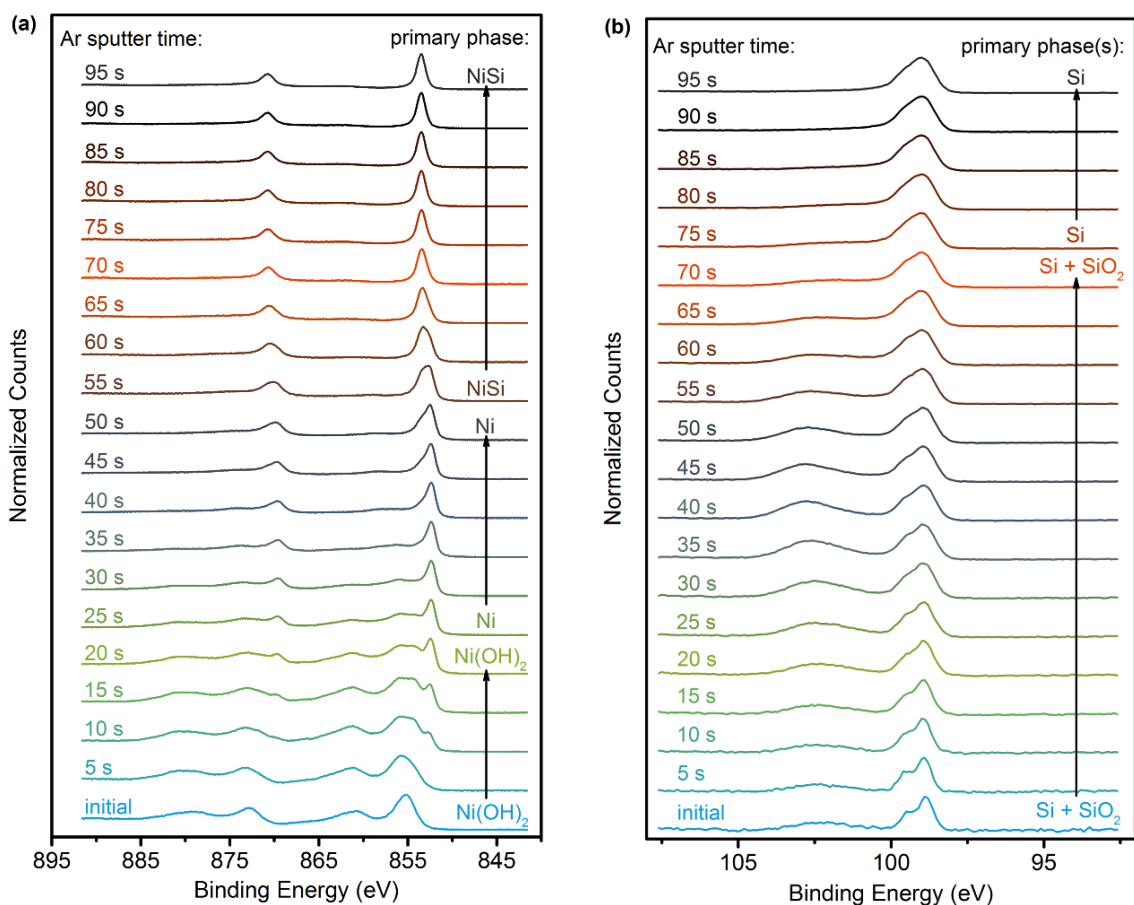


**Figure F.S9. XPS spectra of n-Si protected with 3 nm of Ni after electrochemical cycling. (a)** The Ni region of the XPS profile exhibits a transition from Ni(OH)<sub>2</sub> to Ni to NiSi. **(b)** The Si region of the XPS profile exhibits increased SiO<sub>2</sub> character for the first 35 s before it completely diminishes after 75 s. This is consistent with a depth profile which has passed through a Si oxide layer consisting of the native oxide and any oxidized regions formed during electrochemical cycling.

Peaks were identified using the ThermoScientific Avantage 4.75 software, comparisons to Mullins et al. monochromated K $\alpha$  spectra, and comparisons to the NIST XPS Database 20, version 4.1 binding energies.<sup>5,6</sup> Select spectra are taken from Figure F.S9a above and labeled in more detail below (Figure F.S10).

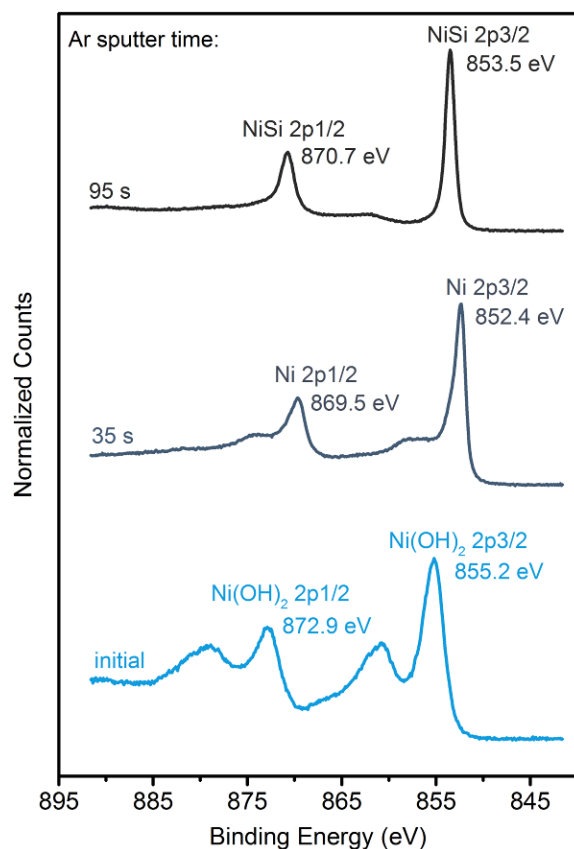


**Figure F.S10. Select sputter times selected from Figure F.S9a to identify key peak positions.** Peak locations and general shapes were compared to monochromated K $\alpha$  spectra from Mullins et al. and the NIST XPS database.

As-deposited samples not subject to electrochemical cycling exhibit a metallic Ni peak before depth profiling (Figure F.S11).

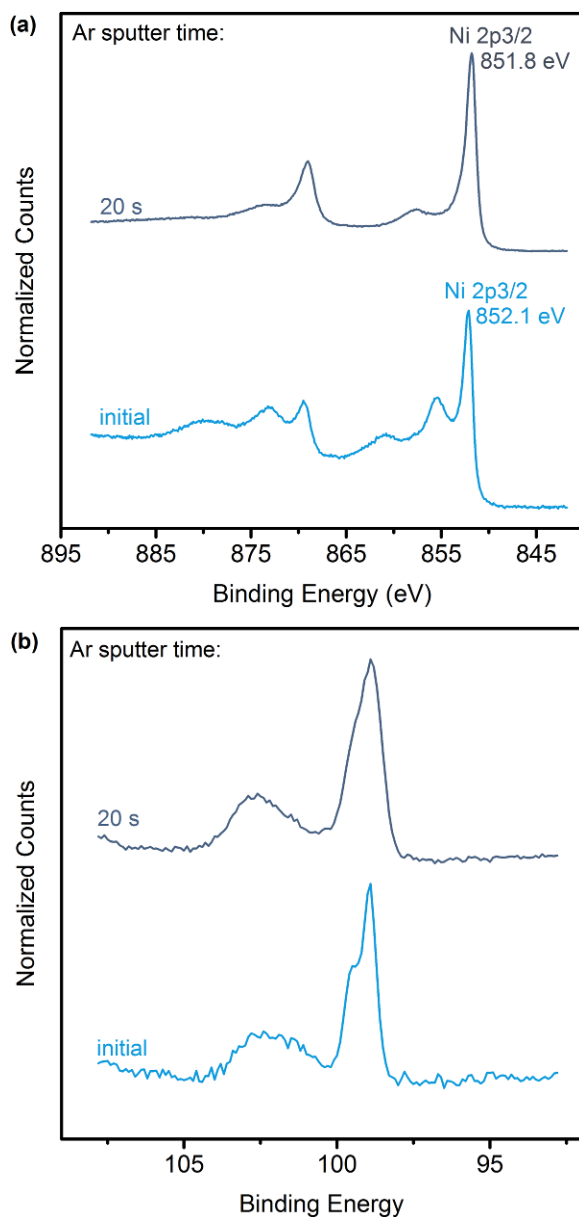


**Figure F.S11. XPS spectra at select sputter times for control samples of n-Si protected with 3 nm of Ni without electrochemical cycling. (a) the regional Ni spectra and (b) the regional Si spectra.**

Reduction of Ni(OH)<sub>2</sub> to metallic Ni by Ar ion sputtering has been documented in other systems.<sup>7</sup> A control sample, fabricated by electrodepositing Ni(OH)<sub>2</sub> onto an Au/Ti-coated glass slide, was used to examine the extent of Ni(OH)<sub>2</sub> reduction from this process (Figure F.S12). During the first three sputter steps (identical conditions as above) the Ni regional spectrum changes

significantly as a shoulder grows into the Ni 2p 3/2 peak – consistent with the presence of metallic Ni. However, for subsequent sputter steps the spectrum remains largely unchanged – consistent with establishment of a steady state ratio of metallic Ni to Ni(OH)<sub>2</sub> as the Ar ion milling removes material. In the Ni-protected n-Si samples, analyzed after electrochemical cycling, a transition to purely metallic Ni is observed - this indicates the presence of metallic Ni before sputtering. *The metallic Ni observed in the cycled photoelectrodes is thus not an artifact from Ar ion sputtering.*

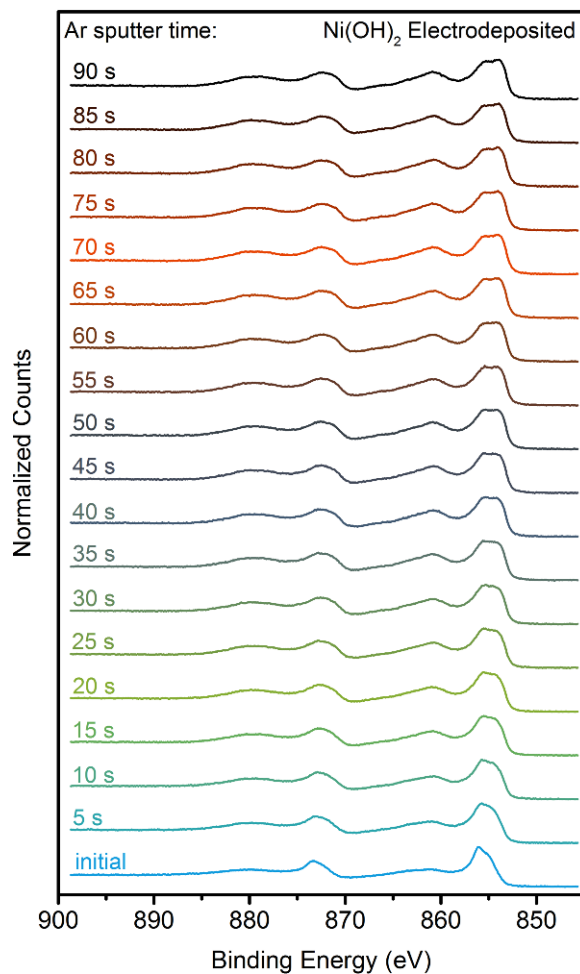


**Figure F.S12. XPS spectra of Ni(OH)<sub>2</sub> electrodeposited (-2 mA for 60 s in a 0.1 Ni(NO<sub>3</sub>)<sub>2</sub> solution) onto Au, after electrochemical cycling.** The Ni region of XPS profile shows the conversion of some Ni(OH)<sub>2</sub> to metallic Ni and the establishment of a steady state ratio between the two species.

## Section F.S7

### **Non-saturated photocurrent and cleaning procedure dependence.**

The majority (95%+) of electrodes fabricated with the simple IPA cleaning procedure exhibit non-constant photocurrent in the saturated regime. As discussed in the main text, this behavior can be attributed to the pinch-off effect, arising from a spatially heterogeneous junction. Interestingly, altering the cleaning procedure by adding a 1 min HF buffered oxide etch (BOE) followed by a 10 min Radio Corporation of America (RCA) SC-2 clean, produces constant photocurrent in the saturated regime. However, this change in photocurrent behavior is accompanied by a significantly diminished photocurrent onset and reduced redox peak integration (Figure F.S13). It appears that the altered cleaning procedure leads to a more-conformal coating which then reduces the electrolyte's ability to permeate to the semiconductor | catalyst junction. Lack of permeation is apparent from the reduced redox integration. In turn, spatial barrier height heterogeneity decreases (as indicated by the saturated photocurrent profile at sufficiently anodic potential) and better photocurrent onset potentials are precluded because the pinch-off effect is no longer a dominant process.

This view is supported by AFM analysis which depicts smoother films, post-Ni deposition, when the altered cleaning procedure is used. Additionally, the photocurrent onset of the 3 nm devices deposited with the altered cleaning procedure compares favorably with the devices protected by 20 nm of Ni in Figure F.2 of the main text. *The data further supports our hypothesis that sufficient spatial barrier height heterogeneity allows the interface to generate larger photovoltages.*

A further consideration in employing the altered cleaning procedure is the possible alleviation of shallow defect states responsible for Fermi level pinning (as discussed in the main paper). Growth of a more conformal and dense SiO<sub>2</sub> layer, via the RCA SC-2 clean, may accomplish this goal and result in a larger photovoltage. However, if this effect is present it is ultimately obscured by the apparent photovoltage loss associated with precluding development of spatially heterogeneous barrier heights.

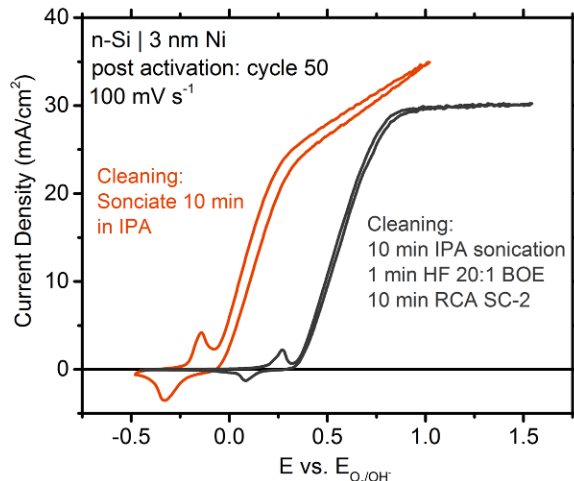


**Figure F.S13. Comparison of illuminated CVs for n-Si protected with 3 nm Ni after activation protocol.** The more rigorous cleaning procedure (black curve) results in a decreased onset potential and diminished redox integration. The data was collected under  $100 \text{ mW cm}^{-2}$  of solar simulation in a pH 9.8 K-borate buffer.

### Section F.S8

Material characterization with AFM reveals a relatively smooth surface for electrodes imaged directly after 3 nm Ni evaporation (Figure F.S14a). We identify the surface speckles as adventitious particulate contamination incorporated during the fabrication process. This view is supported by the lack of these defects in films where additional cleaning procedures were used (1 min 20:1 HF BOE and 10 min RCA SC2) and by the quick disintegration of these features during SEM imaging. After the standard PEC activation protocol, films roughen and develop island features  $> 100 \text{ nm}$  in diameter and particulate contamination generally persists (Figure F.S14b). This is consistent with oxidation of the majority of the film to Ni (oxy)hydroxide.

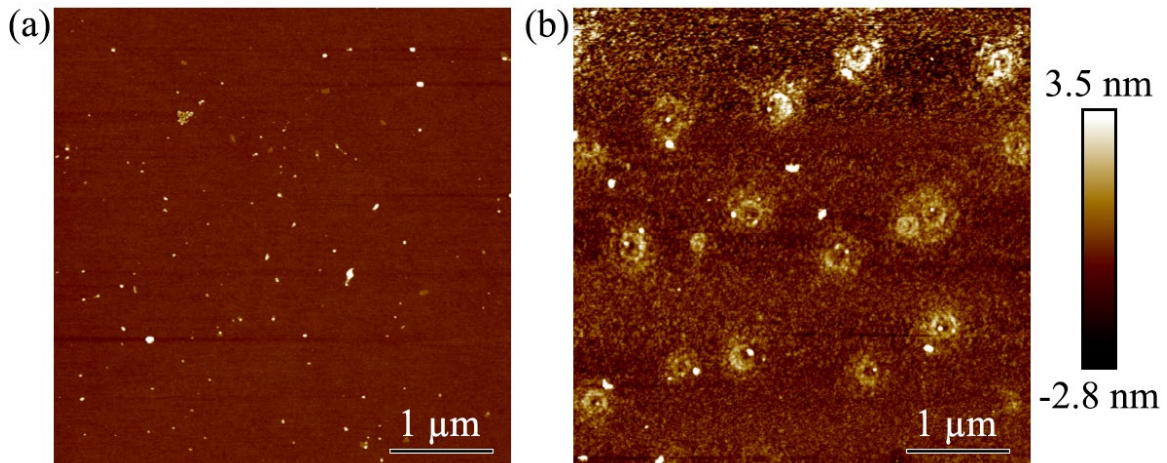


**Figure F.S14.** AFM images of n-Si protected with 3 nm of Ni. (a) before electrochemical cycling and (b) after electrochemical cycling.

Imaging the films after the activation protocol with SEM also reveals the island features (Figure F.S15). We hypothesize that incomplete Ni protection, caused by the oxidation to Ni (oxy)hydroxides, leads to rapid passivation ( $\text{SiO}_2$  growth) in most areas of the film, consistent with the XPS spectra shown earlier.

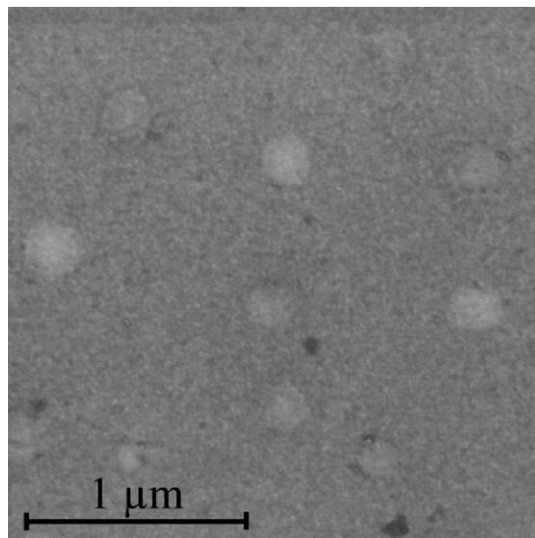


**Figure F.S15.** SEM image of n-Si protected with 3 nm of Ni after electrochemical cycling.

**APPENDIX E. SUPPORTING INFORMATION FOR PAPER G**

**Nanoscale catalyst/semiconductor interfaces in photoelectrochemistry**

	<b>Term</b>	<b>Description</b>	<b>Value and/or Units</b>
Coordinates	$Z$	Depth into semiconductor orthogonal to semiconductor surface plane	nm
	$R$	Radial distance from center of patch, taken along or parallel to the semiconductor surface plane	nm
Independent Variables	$\phi_b^0$	Barrier height for region surrounding patch	V
	$r$	Radius of the nanoscale contact patch	nm
	$A$	Patch area	nm <sup>2</sup>
	$I_{\text{photo}}$	Photocurrent	mA
	$J_{\text{photo}}$	Photocurrent density	mA cm <sup>-2</sup>
	$E_{\text{sem}}$	Semiconductor energy referenced to $E_{\text{sol}}$	eV
	$E_{\text{cat}}$	Catalyst energy referenced to $E_{\text{sol}}$	eV
	$V_{\text{jxn}}$	Applied potential across the n-Si/Ni diode: $qV_{\text{jxn}} = E_{\text{sem}} - E_{\text{cat}}$	V
	$V_{\text{sem}}$	Voltage drop between the bulk semiconductor and solution: $qV_{\text{sem}} = E_{\text{sem}} - E_{\text{sol}}$	V
	$V_{\text{cat}}$	Voltage drop between the catalyst and the solution: $qV_{\text{cat}} = E_{\text{cat}} - E_{\text{sol}}$	V
	$V_{\text{tip}}$	Voltage drop between the AFM tip and the solution $qV_{\text{tip}} = E_{\text{tip}} - E_{\text{sol}}$	V
	$ff$	Filling factor - fraction of surface covered by islands	unitless
Constants	$N_D$	Dopant Density	$5.25 \cdot 10^{15} \text{ cm}^{-3}$
	$V_n$	Potential difference between conduction band and Fermi level	0.217 V



	$\epsilon_s$	Static permittivity of Si	$12.8.854 \cdot 10^{-14} \text{ F cm}^{-1}$
	$A^*$	Richardson constant	$120,000 \text{ mA cm}^{-2} \text{ K}^{-2}$
	$k$	Boltzmann constant	$1.381 \cdot 10^{-19} \text{ cm}^2 \text{ kg s}^{-1} \text{ K}^{-1}$
	$q$	Elementary charge	$1.602 \cdot 10^{-19} \text{ C}$
	$T$	Temperature	298.15 K
	$\phi_b^{\text{Ni}}$	Barrier height for n-Si/Ni contact	0.61 V
	$\mathcal{E}_{\text{O}_2/\text{OH}^-}$	Thermodynamic potential for oxygen evolution, used as the reference potential	defined as 0 V
	$E_{\text{sol}}$	Solution energy, taken as the reference energy	$q\mathcal{E}_{\text{O}_2/\text{OH}^-}$
	$J_{\text{cat}}^0$	Catalyst exchange-current density	$3.5 \cdot 10^{-7} \text{ A cm}^{-2}$
	$\alpha$	Charge transfer coefficient	0.5
Dependent Expressions and Values	$V_{\text{bb}}$	Band bending in semiconductor depletion region	V
	$V_{\text{bi}}$	Built-in potential for the semiconductor depletion region in the dark at equilibrium	V
	$\Delta$	Difference in barrier between patch and surrounding region ( $\phi_b^0 - \phi_b^{\text{Ni}}$ )	V
	$C_a$	Area adjustment term used in Tung model	unitless
	$C_b$	Barrier height modification term used in Tung model	V
	$E_{\text{CB}}$	Conduction band energy referenced to the majority carrier Fermi level in the bulk of the semiconductor (unless otherwise noted)	eV
	$E_{\text{metal}}$	Metal Fermi energy	eV
	$I_{\text{patch}}$	Patch current	mA
	$I_{\text{cat}}$	Catalyst current	mA
	$V_{\text{oc}}$	Open circuit potential	mV
	$\gamma$	Patch model region parameter <sup>1</sup> $\gamma = \left( \frac{3\Delta r^2}{4} \right)^{1/3}$	$\text{V}^{1/3} \cdot \text{cm}^{2/3}$

**Table G.S1 List of all variables, dependent expressions, coordinates and constants for pinch-off model.**

### Section 1. Model System Fabrication & Characterization

Fabrication of n-Si photoanodes with Ni nanocontacts was adapted from the electrodeposition-based reports of Loget et al.<sup>2</sup> Phosphorous-doped n-Si [100] (0.65 - 0.95 ohm-cm) wafers (University Wafer) were diced into 1 cm × 1 cm squares and sequentially sonicated for 10 min each in acetone, isopropyl alcohol, and water (18.2 MΩ-cm). The n-Si squares were placed in

boiling piranha (~100 °C – 3:1 by volume conc. aq. H<sub>2</sub>SO<sub>4</sub> : 30% aq. H<sub>2</sub>O<sub>2</sub> – both from Fisher Chemical) for 30 min and then vigorously rinsed with water (18.2 MΩ cm) before being dried under N<sub>2</sub>. An ohmic contact was established to the backside of each n-Si square by applying two drops of Ga-In eutectic (≥99.99%, Sigma Aldrich), scratching within the Ga-In with a diamond scribe to ensure contact, and then affixing one end of a Sn-Cu wire (~25 cm length – 30 AWG – McMaster Carr) within the eutectic using hot glue (SureBonder Mini). The Sn-Cu wire was fed through a glass tube (7 mm diameter) and constructed into an electrode suitable for side-illumination with the n-Si backside and adjacent Sn-Cu wire insulated by hot glue. The Ni electrodeposition solution (aq. 0.01 M NiCl<sub>2</sub> + 0.1 M H<sub>3</sub>BO<sub>3</sub>) was produced fresh for each batch of electrodes by dissolving NiCl<sub>2</sub>·6H<sub>2</sub>O (99.9%, Sigma Aldrich) and H<sub>3</sub>BO<sub>3</sub> (≥99.5%, Sigma Aldrich) in water (18.2 MΩ·cm) and sonicating until dissolution was complete (typically 10 min). Immediately prior to deposition, electrodes were submerged in a buffered hydrofluoric acid etching solution (20:1 buffered oxide etch, J. T. Baker) for 2 min and then rinsed with water (18.2 MΩ cm). For deposition of the Ni islands, the electrode, a Pt wire coil serving as a counter electrode, and a commercial Ag/AgCl reference electrode (BASi MF-2052) were placed in the NiCl<sub>2</sub>-based deposition solution and -1.5 V vs.  $\mathcal{E}_{\text{Ag/AgCl}}$  was applied for 5, 15, or 60 s using a BioLogic SP200 potentiostat (Figure G.S1).

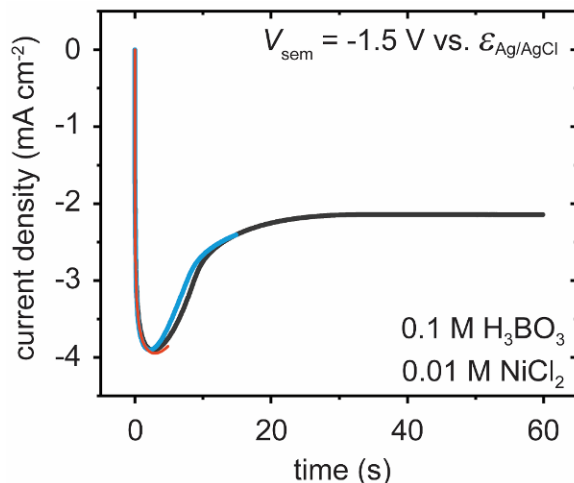


**Figure G.S1. Typical chronoamperometry data for electrodepositions used to produce photoanodes with n-Si/Ni nanocontacts.** In a 0.01 M NiCl<sub>2</sub> + 0.1 M H<sub>3</sub>BO<sub>3</sub> aq. solution -1.5 V vs.  $\mathcal{E}_{\text{Ag/AgCl}}$  was applied for 5, 15, or 60 s. Only electrodes which exhibited the deposition character shown here (initial spike in current which relaxes to a steady-state value) were selected for further study.

The photoanodes' photoelectrochemical behavior was tested in both 1 M KOH and a 1 M potassium borate buffer (K-borate) adjusted to pH 9.5. Characterization was conducted in 1 M KOH to illustrate the photoelectrochemical activity in an environment where oxygen evolution catalysis is facile. However, 1 M K-borate buffer was selected for *operando* studies with the PS-EC-AFM to decrease any etching of the Si surface that might occur between initial topographical characterization and photovoltage measurement as well as to preserve the longevity of the EC-AFM tips. For photoelectrode characterization, the electrodes were activated via 50 voltammogram cycles in either electrolyte solution under  $100 \text{ mW cm}^{-2}$  of solar simulation (Abet Technologies model 10500) using the Ag/AgCl reference and Pt counter electrodes. The activation potential range varied based on Ni-deposition time but was always conducted at  $50 \text{ mV s}^{-1}$  with one endpoint cathodic of the catalyst's reduction peak, nominally  $\text{NiOOH} + \text{e}^- + \text{H}_2\text{O} \rightarrow \text{Ni(OH)}_2 + \text{OH}^-$ , and the other endpoint positioned in the light-limited photocurrent range. Photocurrent-onset potentials (vs.  $\mathcal{E}_{\text{O}_2/\text{OH}^-}$ ) and the magnitude of the light-limiting photocurrent were comparable for electrodes with the same electrodeposition time, irrespective of the electrolyte solution. Photocurrent onset slopes were steeper when electrodes were measured in the 1 M KOH solution, consistent with the higher OER activity and electrolyte conductivity relative to measurements in the buffered solution.

The n-Si/Ni nanocontacts were physically characterized before and after activation with scanning electron microscopy (SEM) and cross-sectional transmission electron microscopy (TEM, Figure G.S2). SEM images (FEI Helios 600 DualBeam) of photoanodes with 5 s of Ni electrodeposition reveal a distribution of hemispherical islands ranging from 40 to 140 nm in diameter. It was noted that smaller islands with less separation could typically be found near the edge of the photoelectrode surface. Cross-sectional TEM (FEI Titan 80-200 TEM/STEM with ChemiSTEM) collected before (Figure G.S2b) and after (Figure G.S2c) activation in 1 M KOH revealed that the Si surface etches 10-15 nm during activation. High annular angular dark field (HAADF) images (Figure G.S2d) revealed some diminished density of material at the edges of the Ni islands near the n-Si/Ni interface. Energy dispersive x-ray analysis (EDX) data collected via ChemiSTEM (Figure G.S3) reveals increased oxygen concentration around the Ni island edge after activation which is consistent with the conversion of Ni to  $\text{Ni(OH)}_2/\text{NiOOH}$ .

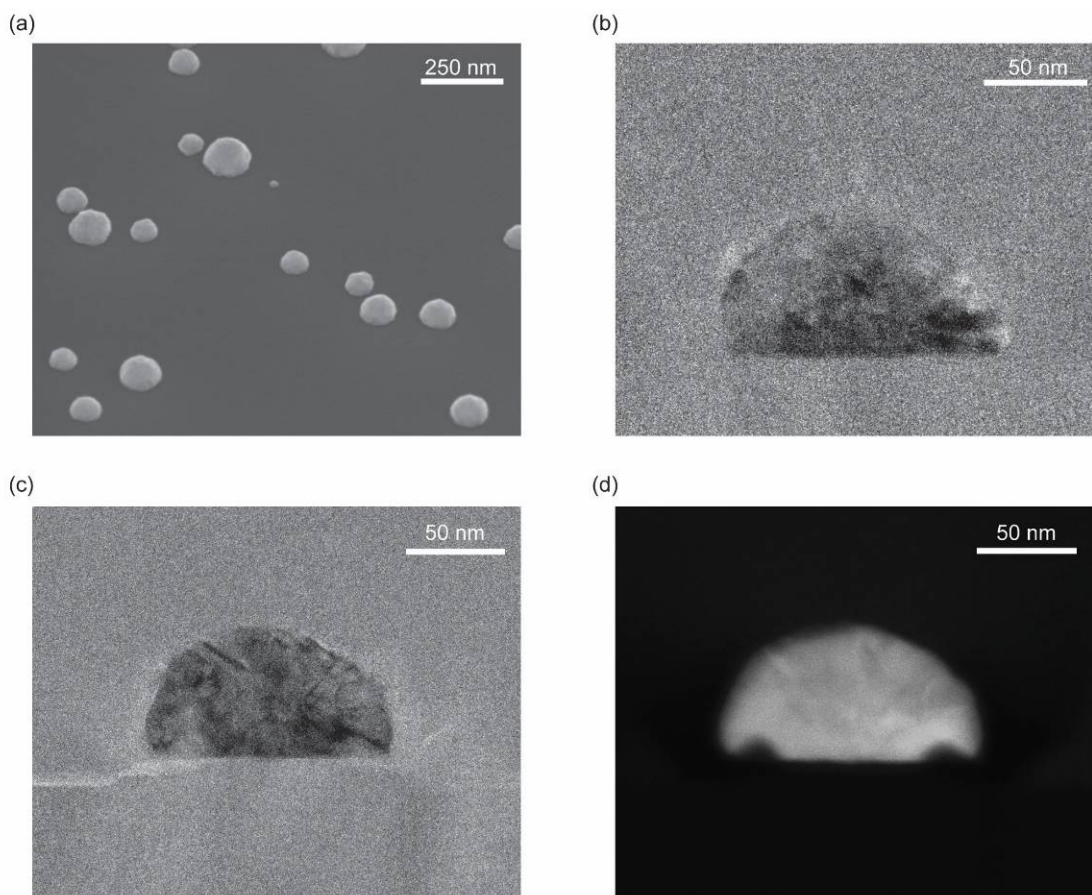


**Figure G.S2. SEM, cross-sectional TEM, and high-angle annular dark field (HAADF) TEM images for Ni nanoislands electrodeposited for 5 s on n-Si.** (a) SEM image collected on a FEI Helios 600 DualBeam at 5 kV at a 45° angle. The selected location illustrates a typical spread and size distribution for Ni particles, although larger and smaller particles can be found across the surface. (b) Cross-sectional TEM collected on a FEI TITAN 80-200 before activation. (c) Cross-sectional TEM collected after a 50-cycle activation in 1 M KOH. Si etching is apparent. (d) HAADF image corresponding to the same island in panel c.

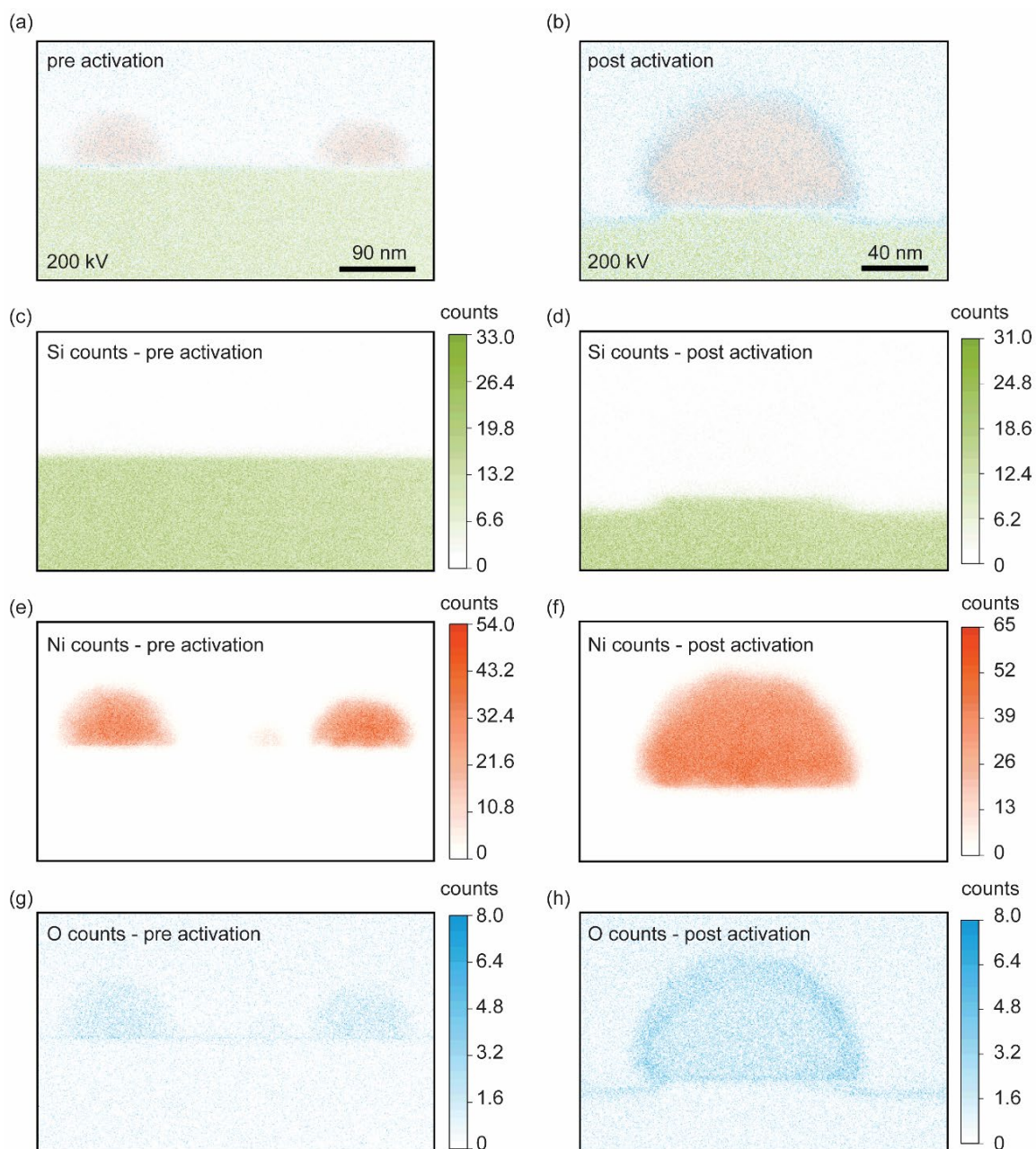


**Figure G.S3. EDX composition maps collected using ChemiSTEM mode on a FEI TITAN 80-200 TEM/STEM for islands before and after activation in 1 M KOH.** The composite image for Ni, Si, and O counts prior to activation (a) and after activation (b) are displayed in the top panel. The isolated Si (c), Ni (e), and O (g) counts collected before activation are displayed in the left column. The isolated Si (d), Ni (f), and O (h) counts collected after activation are displayed in the right column. The EDX results demonstrate that a portion of the Ni island is oxidized during electrochemical activation, consistent with the observed increase in the Ni redox wave.

## Section 2. Ideality Factor

Dry current-voltage data was collected for nanocontacts formed by 5 s of Ni electrodeposition using conducting AFM. Ideality factors ( $n$ ) were calculated from the dry current-voltage behavior by fitting the slope ( $m$ ) of the  $\ln(J)$  vs.  $V$  plot with the expression

$$m = \frac{q}{nkT} \quad (\text{S1.1})$$

Ideality factors generally increased as the contact size became smaller (Figure G.S4), although this was not accompanied by an increase in the barrier height (Figure G.2a).

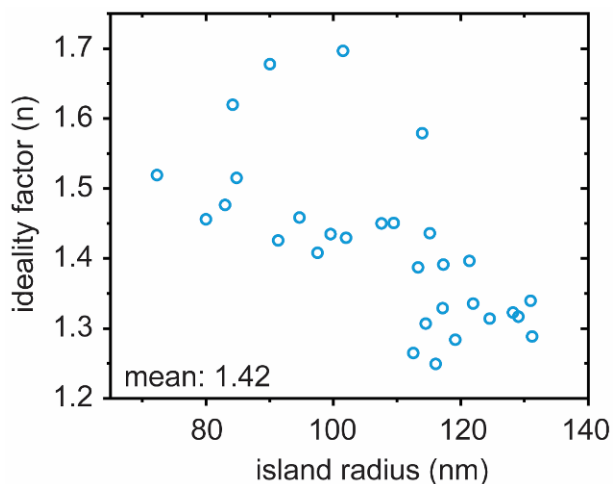


**Figure G.S4. Ideality factors extracted from the dark J-V curves measured through single nanoislands via AFM.** The same  $\ln(J)$  vs.  $V$  data was used to calculate barrier heights in Figure G.2a of the main text.

## Section 3. *Operando* Potential-Sensing Electrochemical Atomic-Force Microscopy

*Operando* potential sensing was achieved using commercial PeakForce SECM probes on a custom-modified Bruker Dimensional Icon AFM. Photoelectrodes were dissected, immediately following Ni electrodeposition, by using a razor blade to remove hot glue insulation. A custom cell was designed where the dissected n-Si square chip was affixed to a Kel-F baseplate featuring a hole to accommodate the ohmic back contact. Epoxy (Hysol Loctite 9460) was used to affix the photoanode and insulate the ohmic contact from electrolyte. A groove was machined around the photoanode mounting area which accommodated a Pt-coil counter electrode and a standard Ag/AgCl reference electrode (Pine Research). During experiments the cell was filled with 1 M K-

borate (pH 9.5) such that the photoanode was covered by at least 1 mm of solution. A Bio-Logic SP300 potentiostat was used with the working electrode connection attached to the photoanode's ohmic contact and the counter-electrode potential-sensing lead attached to the backside of the PeakForce SECM probe (through a strain-release module) to monitor the tip potential. The built-in AFM laser (power: 1 mW, illumination area:  $\sim 8 \cdot 10^{-4} \text{ cm}^2$ , wavelength: 690 nm) which tracks with the AFM tip was used as a local illumination source. The surface was then imaged in PeakForce Tapping mode to identify suitable areas for photovoltage measurements (ideally where most Ni nanoparticles could be well-resolved from adjacent particles). After identifying a suitable area, bias was applied to the photoanode to oxidize the  $\text{Ni}(\text{OH})_2$  shell while simultaneously producing no bubbles. This was accomplished either by setting a chronoamperometry condition (typically  $V_{\text{sem}} = 0.7 \text{ V vs. Ag/AgCl}$ ) or chronopotentiometry condition (typically  $I = 1 \mu\text{A}$ ). Once a stable bias was maintained, islands were landed upon using the Bruker software's point-and-shoot function and the surface potential was recorded. An example raw data set and corresponding topography image is shown (Figure G.S5), corresponding to the data in Figure G.2d of the main paper.

We also note Pt is known to dissolve under large positive biases. We have not noticed tip failure due to Pt dissolution through our studies here at the relatively mild positive potentials sensed at the catalyst surface. Repeated topographical imaging with the Pt tips does, however, result in loss of the electrically conductive Pt coating and failure of the tip as a potential probe.

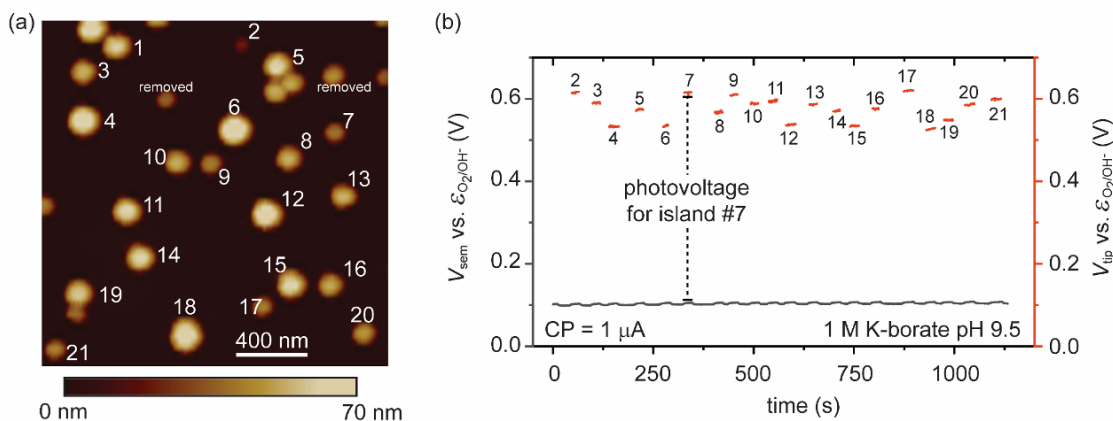


**Figure G.S5. Raw *operando* photovoltage data corresponding to Figure G.2d in main manuscript.** (a) The AFM topography image was collected with the SECM AFM tip prior to using point-and-shoot mode. Two islands were removed from the surface when the tip contacted them during subsequent scans (as indicated in the labels). (b) A chronopotentiometry condition ( $I = 1 \mu\text{A}$ ) was applied and resulted in a near-steady applied potential ( $V_{\text{sem}} \sim 0.11 \text{ V vs. } \epsilon_{\text{O}_2/\text{OH}^-}$ ). The islands were landed on sequentially (from 1 to 21) and the resulting tip potential ( $V_{\text{tip}}$ ) was recorded.

**Light Source for Photovoltage Measurements.** The Bruker AFM's built-in laser was used as a constant illumination source for the *in situ* photovoltage experiments. The laser is a monochromatic 690 nm source with a power of 1 mW and an illumination area of approximately  $8 \cdot 10^{-4} \text{ cm}^2$ . The illumination intensity is compared to the AM 1.5 G flux absorbable by Si (leading to a theoretical limiting photocurrent density of  $43.8 \text{ mA cm}^{-2}$ ) to give a  $\sim 15$ -sun-equivalent flux. During operation the AFM cantilever partially obscures the incident beam. A Si photodiode (Thorlabs UDT UV-005) was used to determine that  $\sim 65\%$  of the incident light is obscured during measurement, leading to a  $\sim 5$ -sun-effective-illumination flux. Due to cantilever shadowing, we note that any measured Ni island is not under direct illumination. However, the bulk diffusion length of carriers in these Si wafers is several hundred microns. Further, the AFM's built-in laser is housed within the same apparatus where the cantilever is mounted and thus the incident illumination profile remains constant relative to the tip position. Thus, all measured nanocontacts experience a near-identical photogenerated minority carrier flux to the interface. The incident illumination could be better controlled in future iterations of the *operando* AFM cell by using fiber optics to illuminate at a shallow angle relative to the semiconductor surface. Back illumination is also possible, but this will limit the minority carrier generation near the surface and will likely be non-viable for materials with direct band gaps.

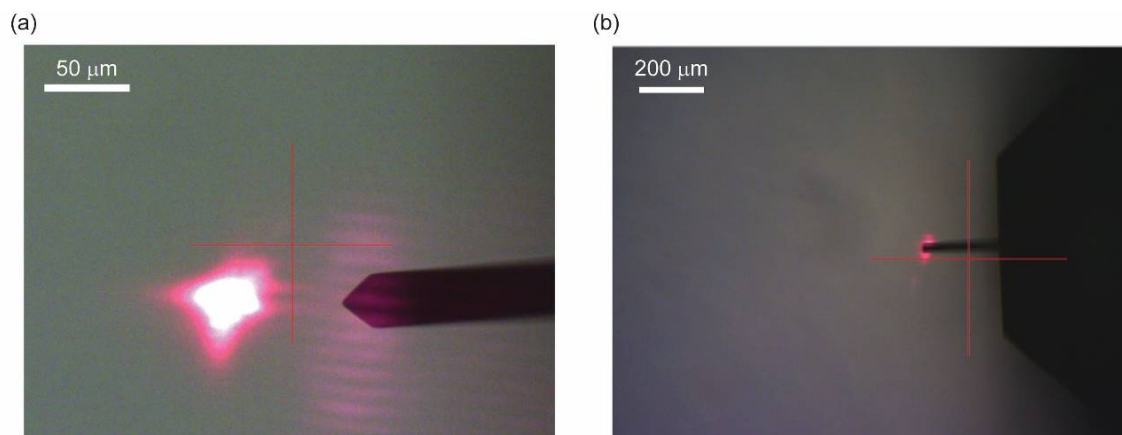


**Figure G.S6. Built-in laser alignment for the Bruker AFM.** (a) Laser illumination shown *ex situ*, next to a SCM-PIT v2 commercial conducting AFM tip. This tip was used for the *ex situ* *J-V* characterization of islands. (b) Laser illumination shown during *operando* measurements with the Peakforce SECM probe partially obstructing the incident beam. Characterization with a standard Si photodiode (Thorlabs UDT UV-005) reveals that  $\sim 65\%$  of the incident beam is obstructed. Thus



a  $\sim 5$ -sun-equivalent illumination flux is incident on the surface in the  $\sim 8 \cdot 10^{-4}$  cm<sup>2</sup> illumination area.

**Nanoisland Dimension Corrections.** The radii of the nanoislands throughout this work are calculated from the topographical AFM data assuming a circular n-Si/Ni contact area. The radii are then corrected to account for AFM tip broadening and the activation process which decreases the Ni volume via conversion to Ni(OH)<sub>2</sub>/NiOOH. To correct for the AFM tip broadening a series of AFM topographical images were compared to the same regions as measured by SEM. Examination of 50 islands revealed that the AFM measurement artificially increased the radii by 4 nm ( $\pm 3$  nm) relative to the SEM measurement (Figure G.S7). To compensate for the activation process the cathodic redox peak on the 50<sup>th</sup> cycle was integrated and compared to the charge passed during deposition. This comparison, assuming that all the deposition current reduced Ni<sup>2+</sup> salts to Ni metal on the electrode surface, reveals that 5.7% ( $\pm 1\%$ ) of the Ni has converted to Ni(OH)<sub>2</sub>/NiOOH by the 50<sup>th</sup> activation cycle. This is equivalent to a 2% decrease in the radii of the Ni islands.

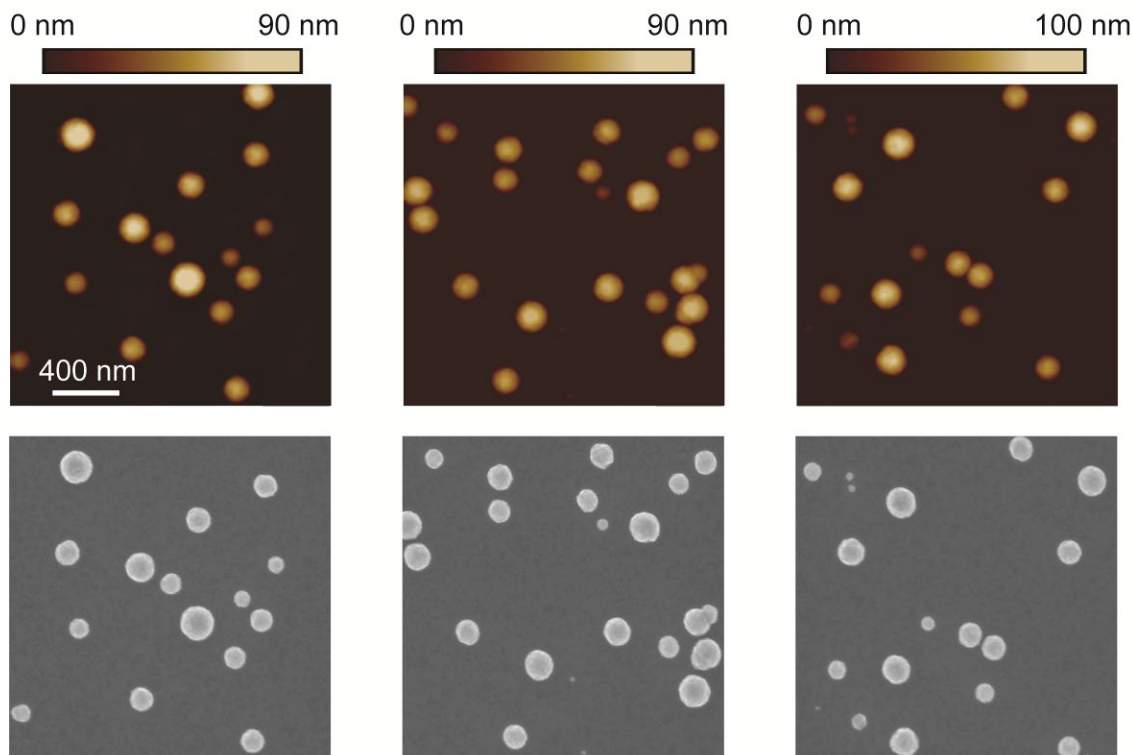


**Figure G.S7. Comparison of AFM island dimensions to those measured by SEM.** Each top panel AFM topographical image corresponds to the same area as measured by a FEI Helios 600 DualBeam SEM at 5 kV in the bottom panel. Island areas were analyzed using the threshold

imaging mode of ImageJ. Radii were calculated assuming the n-Si/Ni contact area is circular, revealing that AFM-tip-induced broadening artificially increases the radii by 4 nm ( $\pm 1$ ). AFM-extracted radii were corrected to account for this broadening throughout the paper.

#### Section 4. Analytical Model for Pinch-off

The Tung analytical pinch-off model<sup>1,3</sup> is used to interpret the *operando* photovoltage results. We employ the patch-geometry solution wherein a circular patch with a low barrier height ( $\phi_b^{\text{Ni}}$ ) is surrounded by a larger barrier region ( $\phi_b^0$ ). Current-voltage behavior is modeled via the modified ideal-diode expression

$$I_{\text{patch}} = A^*T^2C_a e^{\frac{-q\phi_b^0}{kT} + C_b} \left( 1 - e^{\frac{qV_{\text{jxn}}}{kT}} \right) \quad (\text{S1.1})$$

where the effective-area modification ( $C_a$ ) and barrier-height modification ( $C_b$ ) are

$$C_a = \frac{4\pi kT}{9q} \left( \frac{3\Delta r^2}{4} \right)^{1/3} \left( \frac{\epsilon_s}{qN_D V_{\text{bb}}} \right)^{2/3} \quad (\text{S1.2})$$

$$C_b = \frac{q}{kT} \left( \frac{3q\Delta r^2 V_{\text{bb}} N_D}{4\epsilon_s} \right)^{1/3} \quad (\text{S1.3})$$

and the ideality factor is taken to be the average experimental value ( $n = 1.42$ ). For  $V_{\text{oc}}$  modeling the expression is multiplied by the patch area and modified to include a photocurrent density term ( $J_{\text{photo}}$ ). With  $J_{\text{patch}} = 0$  the expression is then solved for  $V_{\text{jxn}} = V_{\text{oc}}$ .

$$J_{\text{patch}} = 0 = AA^*T^2C_a \left( e^{\frac{-q\phi_b^0}{kT} + C_b} \right) \left( 1 - e^{\frac{qV_{\text{jxn}}}{nkT}} \right) + J_{\text{photo}} \quad (\text{S1.4})$$

For modeling the aggregate photoelectrochemical data, the photocurrent term is taken to be the limiting current from the photoelectrochemical results for any given modeled photoanode. This is typically  $\sim 25 \text{ mA cm}^{-2}$  for a photoanode with 5 s of Ni electrodeposition. For modeling the *operando* data, a photocurrent of  $125 \text{ mA cm}^{-2}$  is used which accounts for the 5-fold increase in locally generated minority carriers under the 690 nm laser.

For modeling of photoelectrochemical results the modified ideal-diode expression is placed in series with a Butler-Volmer expression which represents the catalytic behavior. The exchange current density ( $J_{\text{cat}}^0$ ) for the Butler-Volmer expression was determined by fitting the electrochemical OER response of a Pt electrode where Ni had been electrodeposited for 5 s (Figure G.S8 - identical deposition parameters as for n-Si electrodeposition). The potential applied to the semiconductor back contact (versus the solution potential) is partitioned between potential drops across the semiconductor/catalyst interface as well as the catalyst/solution interface such that current continuity is upheld, satisfying the relationship

$$\frac{ff}{A} A^* T^2 C_a \left( e^{\frac{-q\phi_b^0}{kT} + C_b} \right) \left( 1 - e^{\frac{q(V_{\text{jxn}})}{nkT}} \right) + J_{\text{photo}} = J_{\text{cat}}^0 \left( e^{\frac{\alpha q}{kT}(V_{\text{cat}})} \right) \quad (\text{S1.5})$$

For depictions of the conduction-band potential-energy surface, the “point-dipole” approximation was employed,<sup>1</sup> simplified here as:

$$E_{\text{CB}}(R, Z, V_{\text{jxn}}) = q \left[ V_{\text{bb}} \left( 1 - \frac{Z}{w} \right)^2 + V_{\text{n}} + V_{\text{jxn}} - \frac{2\gamma^3 Z}{27 (Z^2 + R^2)^{3/2}} \right] \quad (\text{S1.6})$$

where R and Z are the radial and depth coordinates, respectively. We note that this approximation accurately reflects the potential profile except near the center of the patch at the n-Si/Ni interface.<sup>4</sup> This discrepancy is an outcome of the denominator in the final term approaching zero and is suppressed in the model by setting a minimum value for the expression.

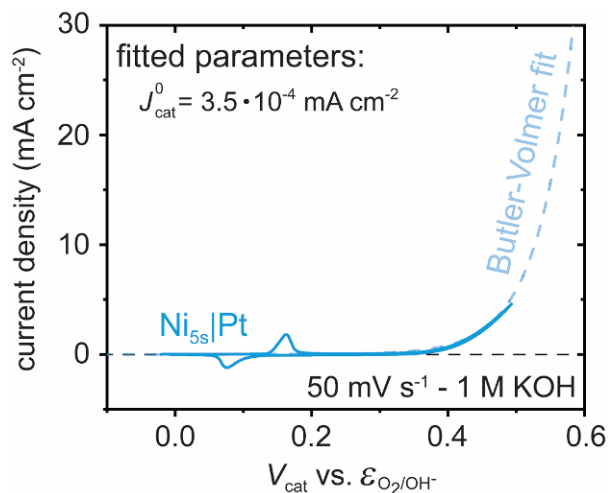


**Figure G.S8. The photoelectrochemical behavior of Ni islands electrodeposited onto a Pt substrate and Butler-Volmer fit.** Electrodeposition was accomplished using the same deposition parameters as for a 5-s electrodeposition of Ni on n-Si ( $-1.5$  V vs.  $E_{\text{Ag}/\text{AgCl}}$  in aq.  $0.01$  M  $\text{NiCl}_2$  +  $0.1$  M  $\text{H}_3\text{BO}_3$ ). The catalyst was then activated via a 50 cyclic voltammogram cycles in  $1$  M KOH at  $50$   $\text{mV s}^{-1}$ . Once activated, a Butler-Volmer relationship was fit to the current onset region using  $J_{\text{cat}}^0 = 0.00035$   $\text{mA cm}^{-2}$ .

### Section 5. Mott-Schottky Analysis for Bare n-Si

During photoelectrochemical activation the surface of the exposed n-Si passivates via formation of an  $\text{SiO}_x$  layer. To evaluate whether this layer affects the pinched-off nanocontacts, the barrier height was extracted periodically during passivation of bare n-Si photoelectrodes. Photoelectrode construction followed the procedure previously described for the nanocontacts except without nanocontact deposition. The analysis was accomplished by alternating between cyclic voltammetry ( $0 - 0.7$  V vs.  $E_{\text{O}_2/\text{OH}^-}$ ) in  $1$  M K-borate buffer (pH 9.5) under  $1$  sun illumination and impedance analysis in aq.  $1$  M KCl +  $0.05$  M  $\text{K}_3\text{Fe}(\text{CN})_6$  +  $0.35$  M  $\text{K}_4\text{Fe}(\text{CN})_6$ . The ferro/ferricyanide redox electrolyte was selected to establish a well-defined solution electrochemical potential against which to measure the flat-band potential (and barrier height) of the n-Si. The Nyquist form of the impedance data was fit with the Randall's circuit to extract the parallel capacitance associated with the semiconductor depletion region as a function of reverse bias and Mott-Schottky analysis was used to extract the flat-band potential and barrier height. The results show that the barrier height drops below the n-Si/Ni Schottky barrier height (extracted from dry conducting-AFM  $J$ - $V$  measurements) after the fourth anodic CV cycle (Figure G.S9a and S9b). Because the solution electrochemical potential remains constant, the changes in barrier height are

due to shifts in the band-edge position as the  $\text{SiO}_x$  layer forms (Figures G.S9c and G.S9d). These results demonstrate that the  $\text{SiO}_x$  layer, in the absence of the Ni-metal nanocontacts, tends to pin the barrier height to  $\sim 0.5$  V. As the n-Si/ $\text{SiO}_x$  barrier is less than the n-Si/Ni barrier, surface passivation to form  $\text{SiO}_x$  cannot be responsible for setting the background large barrier height that surrounds the n-Si/Ni nanocontacts and therefore is not responsible for the experimentally observed pinch-off behavior.

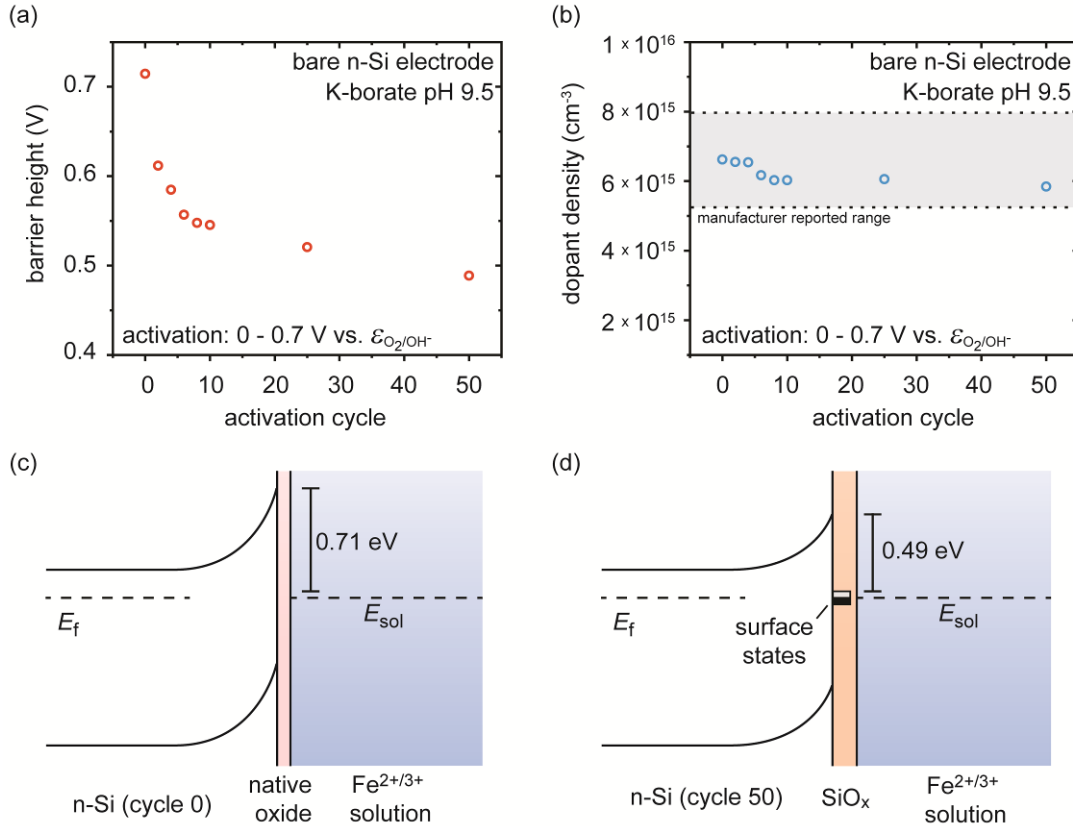


**Figure G.S9. Mott-Schottky analysis results for bare Si as a function of activation cycles (50  $\text{mV s}^{-1}$  in 1 M K-borate buffer from 0 - 0.7 V vs.  $\epsilon_{\text{O}_2/\text{OH}^-}$ ).** (a) Barrier heights decrease below those calculated for the n-Si/Ni nanocontacts ( $\sim 0.61$  V) within four cycles. (b) Dopant densities are extracted to verify that the measured capacitances are from the semiconductor depletion region. The dopant densities are consistent with those reported by the manufacturer (range shown in grey). (c) The equilibrated band diagram is shown, as estimated based on the Mott-Schottky analysis, depicting the n-Si electrode in the ferro/ferricyanide solution. (d) The equilibrated band diagram after the 50 CV cycles shows a decrease in band bending, a decrease in the barrier height, and shifts in the band-edge positions.  $E_f$ ,  $E_{\text{SiO}_2}$ ,  $E_{\text{SiO}_x}$ , and  $E_{\text{sol}}$  are the electrochemical potential for the

semiconductor, native oxide, grown SiO<sub>x</sub> layer, and solution, respectively.  $E_{sol}$  is set by the Nernst potential of the poised solution. Growth of the SiO<sub>x</sub> layer introduces surface states responsible for pinning/moving the semiconductor Fermi level relative to the solution level.

### **Section 6. Dual-Working-Electrode Approach for Measuring n-Si/SiO<sub>x</sub>/NiOOH Barrier Height**

To understand how oxidized, nominally NiOOH, catalyst would affect the barrier height with n-Si, a dual-working-electrode-type device was constructed. Photoelectrode fabrication followed the procedure previously described for the nanocontacts except epoxy (Hysol Loctite 9460) was used to insulate the backside of the electrode, as hot glue would melt during subsequent thermal evaporation of the metal layers. After construction of the photoelectrode, 2 nm of Ni metal was evaporated (0.02 nm s<sup>-1</sup>) onto the n-Si surface via electron-beam deposition (Ni-metal pellets, 99.995%, packed in a Fabmate crucible, both from Kurt Lesker) using an Amod evaporation system. Excess Ni was then photodeposited onto the electrode surface by applying 0.625 V vs.  $E_{O_2/OH^-}$  for 30 s in 1 M K-borate buffer (pH 9.5) saturated with NiCl<sub>2</sub> (sufficient NiCl<sub>2</sub>·6H<sub>2</sub>O was added to yield a 1 M solution but some did not dissolve) under 1 sun illumination. The electrodes were then cycled, at 50 mV s<sup>-1</sup>, in 1 M K-borate buffer (pH 9.5) under 1 sun illumination until the Ni layer fully converted into redox-active Ni(OH)<sub>2</sub>/NiOOH. Full conversion is marked by the passivation of the n-Si surface to SiO<sub>x</sub> which results in a flat photoelectrochemical response (no current flows). A porous Au layer was then evaporated onto the Ni(OH)<sub>2</sub>/NiOOH surface to serve as a second working electrode (WE2) and directly control the oxidation state of the catalyst. Impedance experiments were conducted in 1 M K-borate buffer (pH 9.5) while using WE2 to hold the Ni(OH)<sub>2</sub>/NiOOH either in its oxidized or reduced state. The Nyquist data (Figure G.S10 e & f) was fit to the Randall circuit and Mott-Schottky analysis was performed to extract the barrier height and dopant density (Figure G.S11).

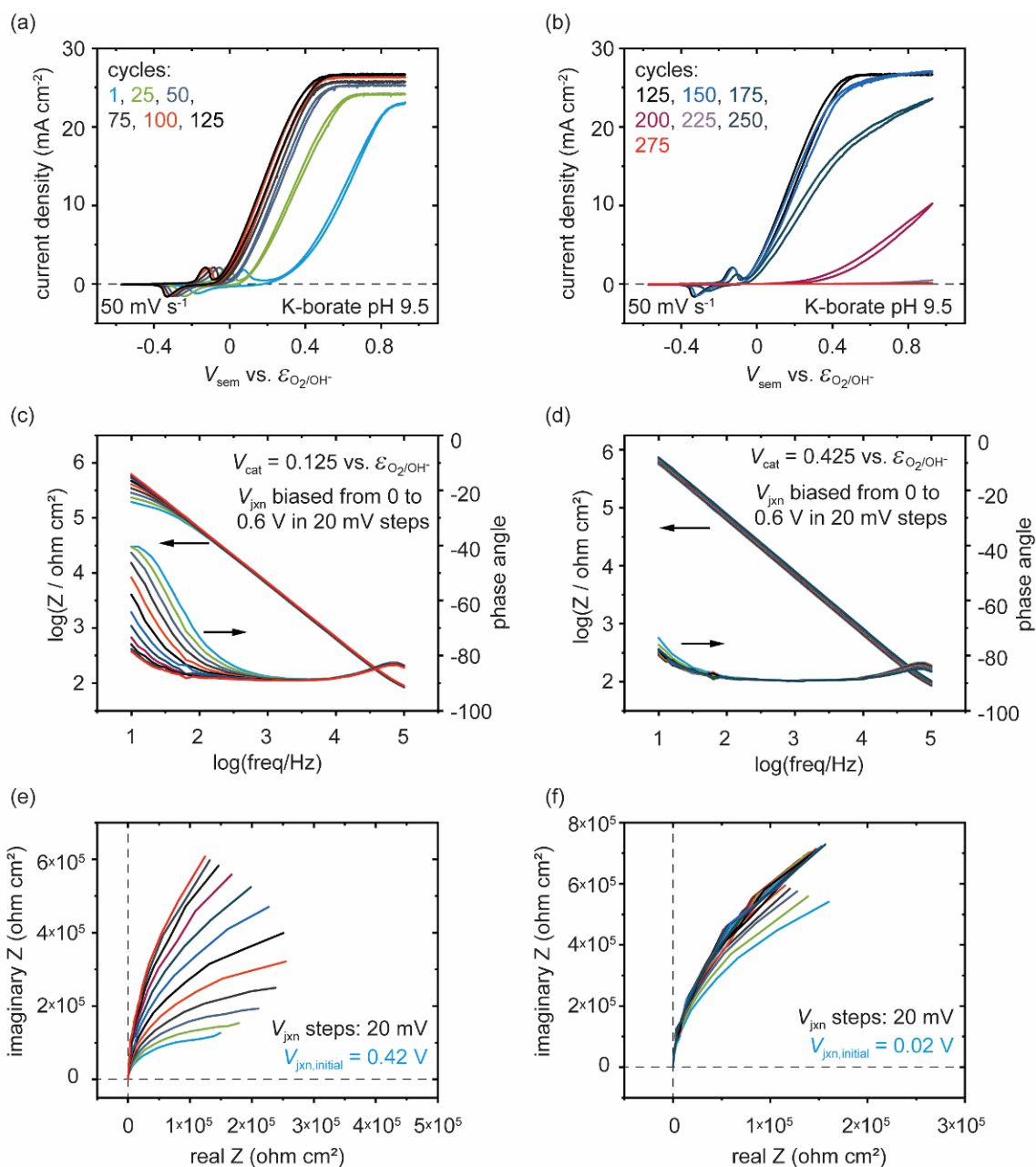


**Figure G.S10. Example impedance behavior of a dual-working-electrode device with the catalyst held in either an oxidized or reduced state.** For impedance measurements, the catalyst is held in either its oxidized or reduced state while the semiconductor is biased from 0 to 0.6 V vs.  $V_{cat}$  in steps of 20 mV. (a) After photodeposition of excess NiOOH the device was cycled in 1 M K-borate buffer under 1 sun illumination. For the initial 125 cycles the photocurrent onset improves. (b) Upon continued cycling the photocurrent onset and limiting photocurrent both decay until no potential-dependence is apparent. This indicates that the Ni metal has fully converted to

electrolyte-permeable Ni (oxy)hydroxide and can no longer protect the Si from passivation. (c) Bode impedance results while the catalyst is held in its reduced state and the (d) analogous data when held in its oxidized state. (e) Nyquist impedance while the catalyst is held in its reduced state and (f) its oxidized state. The Nyquist form was fit with a Randall circuit and the parallel capacitance was extracted.

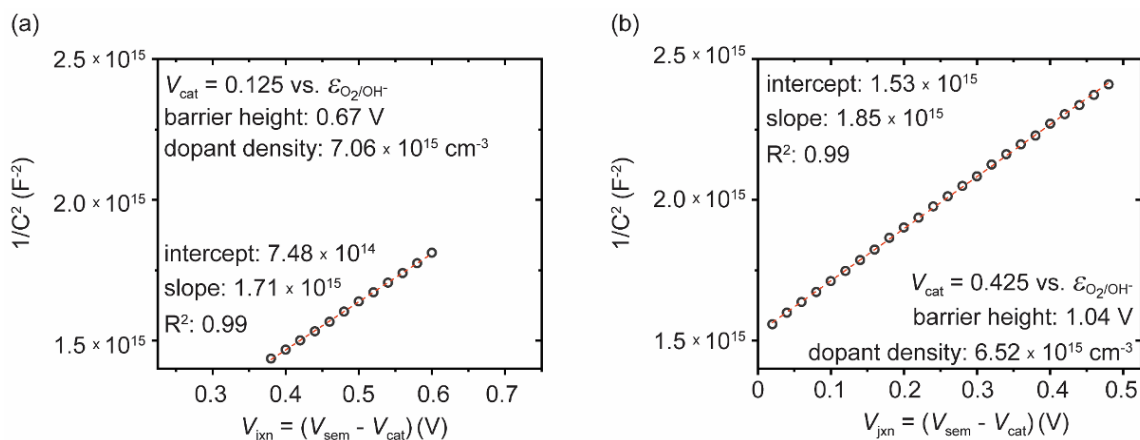


**Figure G.S11. Mott-Schottky data representation and fits for the dual-working-electrode devices.** (a) The fit when the catalyst is reduced exhibits a low barrier height of  $\sim 0.67$  V relative to the larger  $\sim 1.04$  V barrier height (b) for the oxidized catalyst analogue. Dopant densities, extracted the slope fit, are similar in each case and within the manufacturer-reported range.

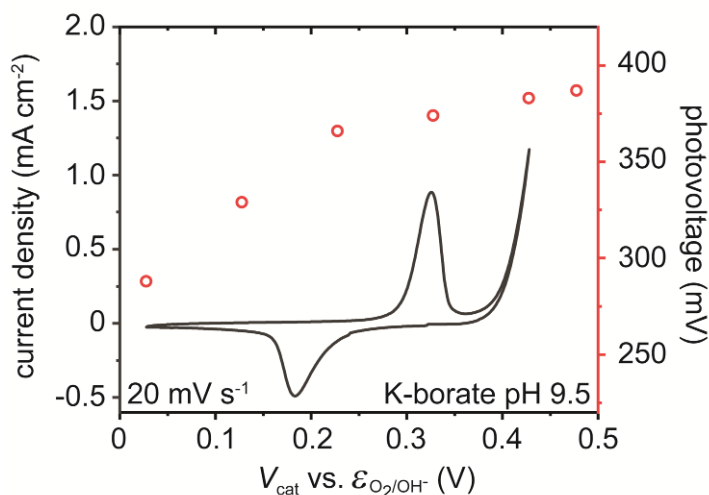


**Figure G.S12. Photovoltage measurements from the dual-working-electrode (DWE) devices.** The voltammogram shows the  $\text{Ni}(\text{OH})_2/\text{NiOOH}$  redox behavior as it is cycled through the Au secondary working electrode at  $20 \text{ mV s}^{-1}$  in 1 M K-borate buffer at pH 9.5. Photovoltages are



collected by applying a constant potential to the Au secondary working electrode (i.e. top contact to the catalyst), under 1 sun illumination, and sensing the potential at the primary working electrode (ohmic back contact to semiconductor). Once a stable potential is achieved the photovoltage is calculated as the difference between the primary and secondary working electrodes:  $V_{\text{cat}} - V_{\text{sem}}$ . The results illustrate a correlation between extent of catalyst oxidation and improved photovoltage. This is consistent the hypothesized physical picture in which the barrier height increases as the catalyst is oxidized. However, we note that these results are qualitative, as illumination of the semiconductor is poorly defined. This dual-working-electrode architecture places a relatively thick  $\text{Ni}(\text{OH})_2/\text{NiOOH}$  layer and a 10 nm thick Au layer between the 1 sun illumination source and the n-Si surface, effectively blocking the majority of the incident light.

### **Section 7. The Effect of Activation on Photocurrent Onset**

A 50-cycle activation procedure was used in this work for all electrodes irrespective of Ni deposition time. This extent of activation was selected because it does not induce nanocontact passivation (as would be noted by a decrease in the limiting current) and because with the 50-cycle the nanocontact radius is only partially reduced compared to the as-deposited radius which facilitates quantitative evaluation of the pinch-off effect. Improvements in photocurrent onset can be realized by additional cycling (Figure G.S13a). This is likely caused by enhanced pinch-off as the Ni islands are increasing converted into  $\text{Ni}(\text{OH})_2/\text{NiOOH}$  and the n-Si/Ni cross-sectional area decreases. However, after  $\sim 400$  cycles the photocurrent onset and limiting current decay (Figure G.S13b). This is likely caused by complete conversion of the Ni nanocontacts to  $\text{Ni}(\text{OH})_2/\text{NiOOH}$  and the related passivation of the underlying n-Si.

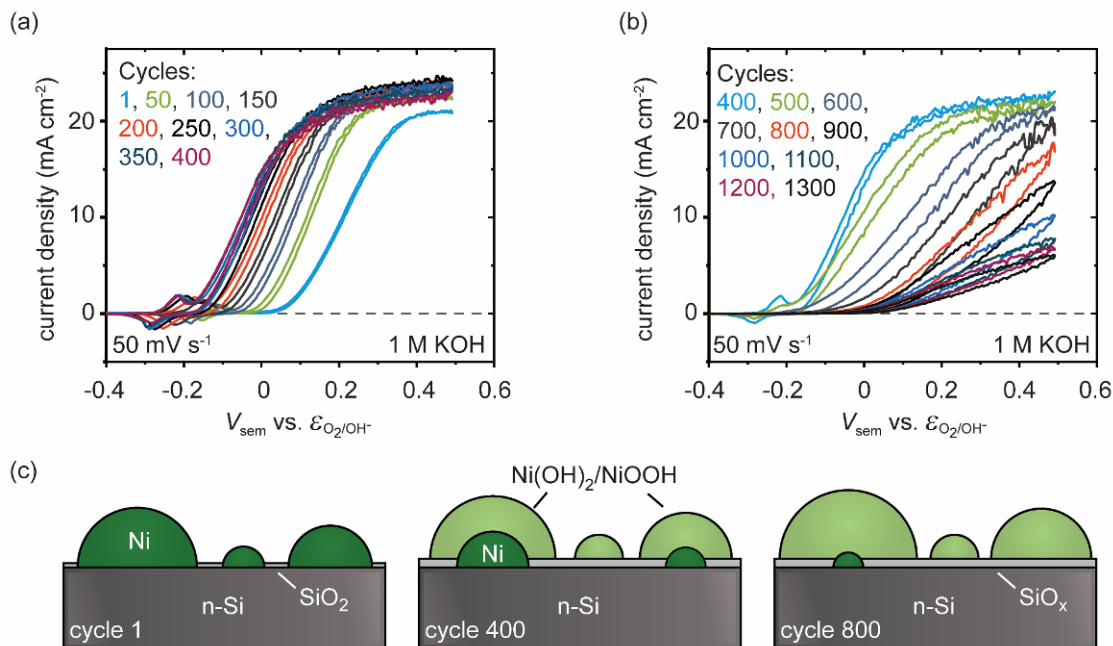


**Figure G.S13. The effect of continued activation on n-Si photoanodes with 5 s Ni electrodeposition.** (a) Initially the photocurrent onset improves. This is likely caused by enhanced pinch-off as the n-Si/Ni cross-sectional area decreases. (b) After 400 cycles the limiting current and photocurrent onset begin to decay. This is consistent with passivation of the n-Si as the Ni becomes electrolyte permeable and SiO<sub>x</sub> forms underneath the Ni(OH)<sub>2</sub>/NiOOH. (c) A qualitative depiction of the activation process at cycles 1, 400, and 800 is shown. Initially, at cycle 1, the islands are comprised of only metallic Ni. The activation cycles increasingly convert the outer shell of the metallic Ni to Ni(OH)<sub>2</sub>/NiOOH. This increases the magnitude of the pinch-off effect and is the hypothesized cause of the significant negative shift in photocurrent onset seen from cycles 1-400. At cycle 400 the light-limited current begins to decrease, indicating that some of the smaller islands have fully converted to Ni(OH)<sub>2</sub>/NiOOH and a passivating SiO<sub>x</sub> layer has isolated them from the semiconductor (preventing them from collecting holes). By cycle 800, the Ni(OH)<sub>2</sub>/NiOOH reduction/oxidation peaks are largely absent which indicates that most of the catalyst is no longer in contact with the underlying semiconductor. The remaining photocurrent is likely driven by a few large Ni features and a few remaining nanocontacts with significant resistive losses across the SiO<sub>x</sub> layer.

Possible effects of optical shading induced by changes in Ni to NiOOH can be inferred by examining the light-limited photocurrent for the extended cycling experiment in Figure G.S13. Although conversion of Ni to Ni(OH)<sub>2</sub>/NiOOH increases between cycles 50 and 400, the light-

limited photocurrent remains largely invariant. For an ideal diode, the relationship between the light-limited photocurrent and photovoltage is such that a one order of magnitude change in the light-limited photocurrent results in a  $\sim 60$  mV change in the photovoltage. Thus, for the minor variability observed experimentally, we expect a negligible impact on the photovoltage. We also note that the hole diffusion length in n-Si is quite long ( $>100$   $\mu\text{m}$ ). Any local suppression of hole generation due to shading will be averaged out by diffusion from adjacent non-shaded regions.

### **Section 8. Spatial Extent of High-Barrier Region Required to Produce Pinch-off**

The analytical model for pinch-off assumes an extended high-barrier region surrounding the pinched-off nanocontact. The model does not account for a spatially limited high-barrier region which may more-accurately reflect the model system where the Ni nanocontact converts to NiOOH at the surface. To evaluate whether this discrepancy causes meaningful differences in the barrier height fits we numerically simulate pinch-off using COMSOL Multiphysics v4.4. An n-Si semiconductor (dopant density  $5.25 \cdot 10^{15} \text{ cm}^{-3}$ ) cylinder with a  $1\text{-}\mu\text{m}$  radius and a  $1\text{-}\mu\text{m}$  height is modeled with a circular  $60\text{-nm}$ -radius Schottky contact ( $\phi_b = 0.61 \text{ V}$ ) in the center of the top face of the cylinder. A second contact is placed, surrounding the Schottky contact, extending either  $25 \text{ nm}$  or  $940 \text{ nm}$  and with a barrier height of either  $0.92 \text{ V}$  or  $1.03 \text{ V}$  (Figure G.S14). The  $25\text{-nm}$  extension represents an initially  $85\text{-nm}$ -radius island where  $25 \text{ nm}$  has converted into NiOOH, whereas the  $940 \text{ nm}$  extension (to the edge of the model) represents the extended contact that the analytical model assumes. The barrier heights were selected to represent the analytically determined fit ( $0.92 \text{ V}$ ) and the DWE Mott-Schottky extracted barrier height ( $1.03 \text{ V}$ ).

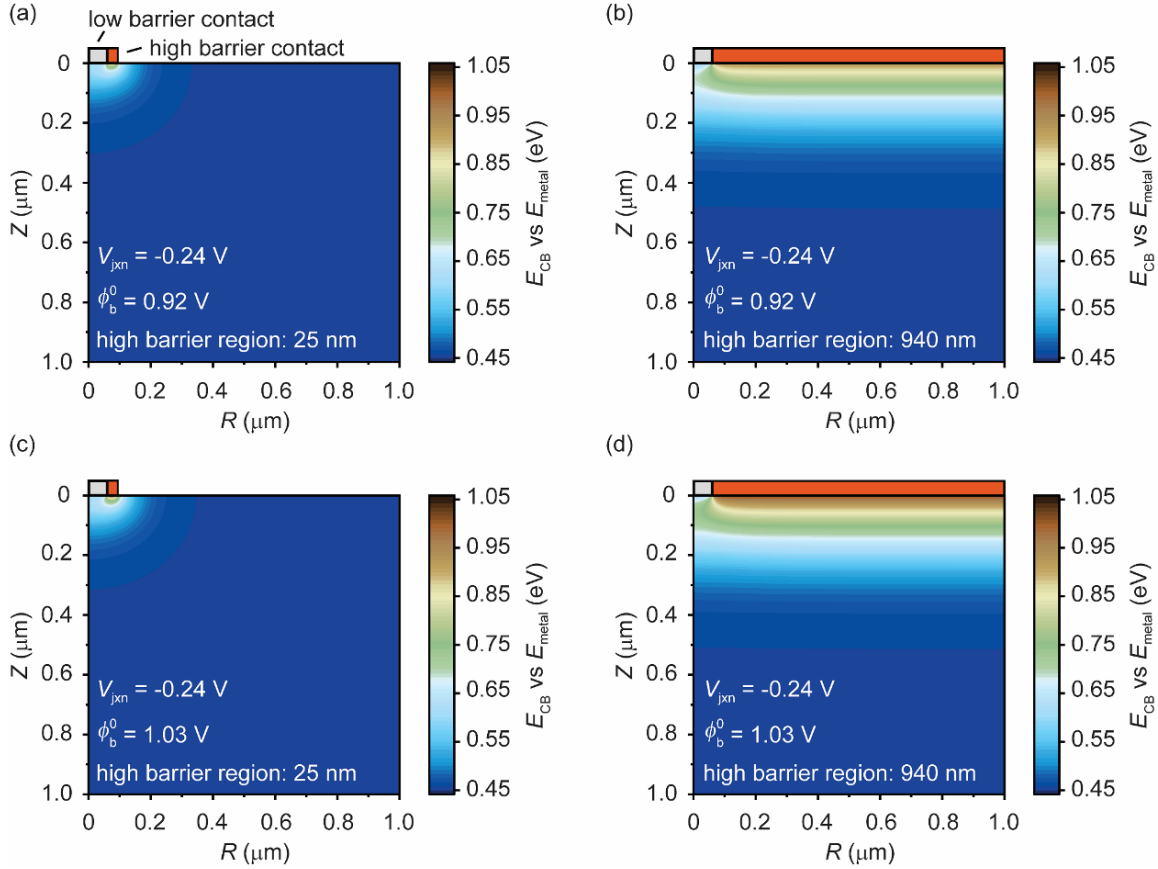


**Figure G.S14. COMSOL Multiphysics numerical model for pinched-off contacts.** A cross-section of the model is depicted running from the center of an n-Si/Ni contact ( $\phi_b = 0.61$  V) to the edge of the n-Si (radial symmetry is present around  $R = 0$   $\mu\text{m}$ ). The conduction band energy ( $E_{CB}$ ) is shown as referenced to the metal Fermi level ( $E_{metal}$ ) at  $V_{jxn} = -0.24$  V (the  $V_{oc}$  for a bulk n-Si/Ni contact). The data depict the **(a)** 25-nm edge contact with  $\phi_b^0 = 0.92$  V, **(b)** 940-nm edge contact with  $\phi_b^0 = 0.92$  V, **(c)** 25-nm edge contact with  $\phi_b^0 = 1.03$  V, and **(d)** 940-nm edge contact with  $\phi_b^0 = 1.03$  V. The depictions indicate that more-extensive pinch-off is present for the extended high-barrier contacts.

The numerical simulation data indicate that a larger pinched-off saddle point ( $\sim 100$  mV increase) is present for the extended barrier region (940 nm) relative to the limited region (25 nm). We extract dark  $J$ - $V$  curves from the numerical model for each case (Figure G.S15a). To facilitate comparison with the experimental data in Figure G.3b of the main text, the  $V_{oc}$  is determined (Figure G.S15a - inset) by adding the 5-sun-equivalent photocurrent ( $125$  mA  $\text{cm}^{-2}$ ) and accounting for the fill factor of the Ni metal nanocontacts on the surface ( $ff = 0.1$ ). The 500-mV  $V_{oc}$  for the 940-nm edge contact with  $\phi_b^0 = 1.03$  V is similar to the experimental data collected in Figure G.3b of the

main manuscript. The  $V_{oc}$  data for the limited (25 nm) high-barrier contact is smaller than those experimentally measured. From a numerical modeling perspective, the discrepancy is partially accounted for by noting we do not explicitly treat the ideality factor in the model described above. The experimentally measured ideality factors ( $n = \sim 1.42$ ) are not input into the model and ideality factors extracted from the model  $J$ - $V$  curves are ideal ( $n = 1$ ). Since an increased ideality factor suppresses the dark current, neglecting non-ideality artificially lowers the  $V_{oc}$ . From the perspective of the model system, we note that the high barrier region may extend well beyond the initial nanocontact island. Photoanodes activated in 1 M K-borate buffer exhibit redeposition of the Ni-based catalyst on the n-Si surface (Figure G.S15b). This effect is consistent with previous in situ morphology studies NiOOH-based catalysts.<sup>5</sup> If the redeposited catalyst electrically contacts the nanoislands then it may be oxidized and serve as a high barrier contact. We note that the redeposition is not observable via ex-situ SEM imaging on the electrodes activated in 1 M KOH. The discrepancy is attributed to n-Si dissolution more readily occurring in 1 M KOH (as seen by cross-sectional TEM) which causes poor surface adhesion for any redepositing Ni catalyst (which is likely ion permeable). Although the redeposited catalyst is likely present during illuminated operation, where the SiO<sub>2</sub> surface is stabilized by the quasi-hole Fermi level<sup>6</sup>, it is easily removed when illumination is ceased during any subsequent rinsing. We therefore expect that, in reality, the interface behaves somewhere intermediate between the ideal homogeneous background barrier and the high-barrier shell models described in Figure G.S14.

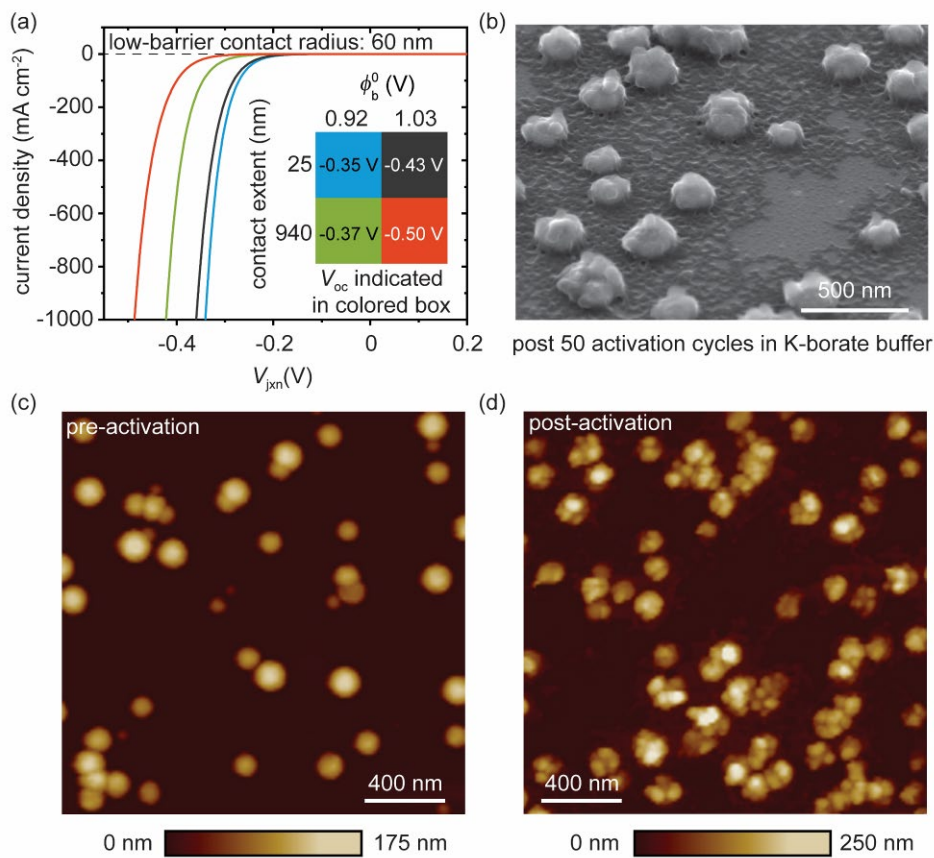


**Figure G.S15. COMSOL Multiphysics numerical  $J$ - $V$  data for pinched-off contacts and SEM/AFM images depicting catalyst redeposition after activation in 1 M K-borate. (a)**  $J$ - $V$  curves extracted from the model in Figure G.S14. The inset illustrates the four different model cases with variable high-barrier spatial extents and heights. A  $V_{oc}$  is calculated for each case by adding the 5-sun-equivalent light-limiting current ( $125 \text{ mA cm}^{-2}$ ) and accounting for the experimental Ni island fill factor from Figure G.3b in the main text ( $ff = 0.1$ ). The case with a 940-nm edge contact and  $\phi_b^0 = 1.03 \text{ V}$  is most similar to the experimental data, however we note that the model neglects ideality factors which would increase all  $V_{oc}$  values. **(b)** A photoanode where Ni was deposited via the 5-s electrodeposition strategy is shown after a 50-cycle activation in 1 M K-borate buffer under 1 sun illumination. The SEM image reveals that some Ni has dissolved and redeposited around the Ni islands. This redeposition should increase the extent of the high-barrier region if it remains in electrical contact with the Ni island. **(c)** An AFM image collected ex situ showing the lack of redeposition prior to photoanodic activation. **(d)** An AFM image collected in situ near the same area shown in **(c)**, after 50 photoanodic activation cycles. The catalyst shell has become rougher and  $\text{Ni(OH)}_2/\text{NiOOH}$  redistribution is apparent surrounding the Ni islands.

## Section 9. Sequential Deposition Interspersed with Activation

To further illustrate the importance of the pinched-off nanocontacts, we show that photoanodes with 60 s of Ni electrodeposition can exhibit decent photocurrent onset potentials if the pinched-off junction is intentionally fabricated. This is demonstrated by pausing the electrodeposition after the 5 and 10 s marks to perform a full photoelectrochemical activation. The final cycle of each activation is shown in Figure G.S16. The electrodes fabricated in this manner exhibit decreased limiting current, consistent with the parasitic light loss due to increased Ni layer thickness, but the photocurrent onset potential remains near the 5-s electrodeposited samples. In fact, the electrode in Figure G.S16 with a sequential 5 + 5 + 50 s electrodeposition exhibits a lower limiting current than the 60-s continuous deposition but a photocurrent onset potential  $\sim 250$  mV more negative. This behavior most likely occurs because the n-Si/Ni nanocontact formed after the first 5 s of electrodeposition is retained/protected during the activation procedure as  $\text{SiO}_x$  grows. The continued electrodeposition is then prevented from disrupting the nanocontacts because  $\text{SiO}_x$  prevents charge transfer everywhere except at the direct n-Si/Ni junctions.

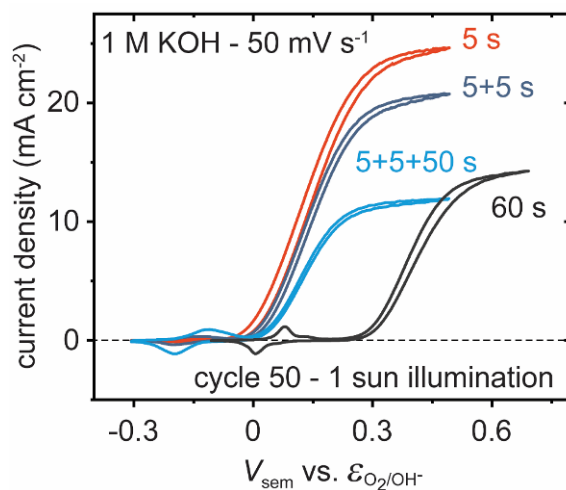


**Figure G.S16. Comparison between photoanodes with continuous 60 s Ni electrodeposition and those with sequential electrodeposition where an activation procedure is performed at 5 and 10 s.** The sequentially deposited photoanode exhibits a photocurrent potential onset  $\sim 250$  mV more negative than the photoanode fabricated by a continued 60 s deposition.

## Section 10. Design of Devices Utilizing Selective Contacts

The understanding of how the pinch-off effect influences photoanode behavior may be useful in designing devices that are simultaneously efficient and durable. Intentional fabrication of pinched-off interfaces may be used to produce photoelectrodes with selective contacts from

material that might not otherwise produce selective contacts. An example is illustrated in Figure G.S17, wherein conductive contacts of sufficiently small dimension become selective contacts when surrounded by a suitable material capable of inducing pinch-off. The material could be deposited in a chemical form such that it induces pinch-off due to the formation of a large depletion region in the semiconductor, but the results of this work also illustrate an alternative path wherein a redox-active layer is converted during operation to a sufficiently large (or small) work function through the collection of minority carriers. For photoelectrochemical applications, either the conductive contacts or the surrounding contact could serve the catalytic role.

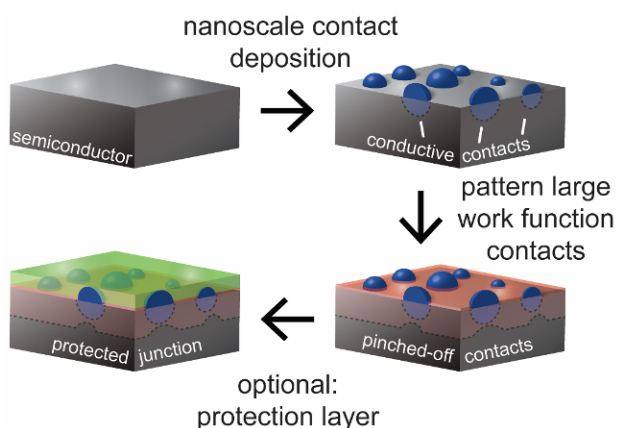


**Figure G.S17. A possible strategy for creating selective contacts using pinch-off.** In the first step conductive nanocontacts are deposited onto a semiconductor. This contact will be used to collect photogenerated minority carriers. In the second step a surrounding material is deposited to induce band bending in the semiconductor. This material could directly induce pinch-off or be electrochemically converted during operation to serve that function (as is the case for the NiOOH material investigated here). In a third, optional step, a protection layer is deposited which prevents solution penetration.

## Section 11. Python Code Compilation

Modeling of pinch-off was coded in Jupyter Notebooks using Python 3. The source code has been exported from python and isolated in the 18 images presented below. The code is annotated with comments throughout.



```

Import Statements and Global Parameters

In [1]: from numba import jit
        from matplotlib import *
        from matplotlib import pyplot as plt
        from matplotlib import animation
        import matplotlib.cm as cm
        from mpl_toolkits.mplot3d import Axes3D
        from numpy import *

        import time
        import numpy as np
        import pandas as pd
        import scipy.optimize
        from scipy.optimize import curve_fit

        from IPython.display import *

        from moviepy.video.io.bindings import mplfig_to_npimage
        import moviepy.editor as mpy

        # plt.style.use('classic')
        # plt.style.use('seaborn-dark-palette')

        %matplotlib nbagg

        #Pretty Plots
        rcParams['font.size'] = 12
        rcParams['axes.linewidth'] = 2
        rcParams['xtick.major.width'] = 2
        rcParams['ytick.major.width'] = 2
        rcParams['xtick.labelsize'] = 12
        rcParams['ytick.labelsize'] = 12
        rcParams['axes.labelsize'] = 16
        rcParams['legend.fontsize'] = 12
        rcParams['figure.autolayout'] = True

Initialize Variables

In [2]: q = 1.6021*10**(-19)          #C
        k = 1.3806*10**(-19)          #cm2 kg s-1 K-1
        T = 298.15                    #K
        eps = float(12)
        eps0 = 8.85419*10**(-14)       #Farads/cm
        mu = float(100)                #cm2 V-1 s-1
        effMass = 9.10938*10**(-31)    #kg
        plank = 6.63*10**(-30)         #cm2 kg s-1

        Nc = 2*(2*np.pi*effMass*k*T/plank**2)**(3/2)          #cm-3
        Nd = 5.25*10**15                                       #cm-3
        Vn = ((K/100**2)*T)/q*np.log(Nc/Nd)                   #V

        debye = ((eps*eps0*k*T)/(q**2*(Nd))**(1/2))           #cm
        ideality = 1.42                                       #average measured ideality
        fillFactor = 0.15                                     #extent of surface coverage for 5s Ni deposition

```

Figure G.S18 Python 3 code for modeling pinch-off: #1. Import statements and initializing variables.

```

Input parameters for model testing: radius of patches (r), applied potential ( $V_{zen}$ ), surrounding barrier height ( $\phi_b^0$ ) and island barrier height ( $\phi_b^{Ni}$ )

In [3]: def input_Params(surroundingBarrier, islandBarrier, radius, appliedPotential):
        global phib_0, phib_Ni, r, Vjxn, Vbb, delta, W
        phib_0 = surroundingBarrier          #surrounding region barrier height (V)
        phib_Ni = islandBarrier              #barrier height for Ni-Si (V)
        r = radius*10**7                    #radius of patches (cm)
        Vjxn = appliedPotential              #applied potential (V)
        Vbb = phib_0 - Vn + Vjxn             #band bending in Volts
        delta = phib_0 - phib_Ni            #difference in barrier height
        W = (2*eps*eps0*Vbb/(q*Nd))**(1/2)  #depletion width in cm

        input_Params(1, 0.61, 85, 0)

Meshing in Z (depth) and R (radial distance)

In [4]: def generate_Mesh():
        global Z, r, V
        Z = np.arange(10**(-7), W*10**(-7), 10**(-7)) #cm mesh into semiconductor (spanning from 1 nm to 1000 nm)
        R = np.arange(-r, r, 10**(-7))                 #cm mesh from middle of island (-0) to edge = (R)
        V = np.zeros((len(Z)), float)                  #list for calculated voltages

        generate_Mesh()

```

Figure G.S19 Python 3 code for modeling pinch-off: #2. Input variables and mesh.

### Section 1 - 1D Pinch-Off Model

Single dimensional analytical solution for a circular patch with low barrier height ( $\phi_b^{Ni}$ ) surrounded by a larger barrier region ( $\phi_b^0$ )

$$V(0, Z) = V_{bb} * \left(1 - \frac{Z}{w}\right)^2 + V_a + V_{jxn} - \Delta \left(1 - \frac{Z}{(Z^2 + r^2)^{1/2}}\right)$$

where  $\Delta$  is the difference between the bulk ( $\phi_b^0$ ) and island barrier heights ( $\phi_b^{Ni}$ ).  $R$  is the island radius, and  $Z$  is the distance into the semiconductor. Solution for the electrostatic potential through the center of the island.

```
In [5]: input_Params(1, 0.61, 85, 0)
generate_Mesh()
V[0:len(V):1] = Vbb*(1-Z[0:len(Z):1]/W)**2+Vn+Vjxn-delta*(1-Z[0:len(Z):1]/(Z[0:len(Z):1]**2+r**2)**(1/2))
```

Single dimensional plot - CB voltage vs. Z

```
In [6]: plt.figure(1)
plt.plot(Z*10**7, V)
plt.xlabel("Z (nm)")
plt.ylabel("$E_{CB}$ vs. $E_{f, bulk}$ (eV)")
plt.text(220, 0.6, "maximum point = %.3f V" % np.max(V))
plt.text(220, 0.55, "island radius = %.2f nm" % (r*10**7))
plt.show()
```

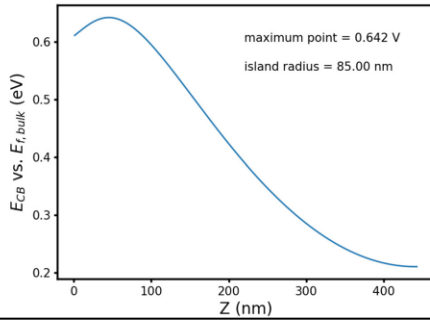


Figure G.S20 Python 3 code for modeling pinch-off: #3. Single dimension pinch-off model.

Single dimensional plot - variable  $\phi_b^0$  (0.7 - 1.3 V)

```
In [7]: fig = plt.figure(2)
ax2 = fig.add_subplot(111)
for phib_0 in np.arange(0.7, 1.4, 0.1):
    input_Params(phib_0, 0.61, 85, 0)
    generate_Mesh()
    V[0:len(V):1] = Vbb*(1-Z[0:len(Z):1]/W)**2+Vn+Vjxn-delta*(1-Z[0:len(Z):1]/(Z[0:len(Z):1]**2+r**2)**(1/2))
    ax2.plot(Z*10**7, V, label=phib_0, linewidth=1.5)
plt.legend(loc='upper right')
leg = plt.legend()
leg.set_title("$\phi_{b_0}$ (V)")
plt.xlabel("Z (nm)")
plt.ylabel("$E_{CB}$ vs. $E_{f, bulk}$ (eV)")
ax2.tick_params(labelsize=14)
plt.text(10, 0.22, "radius = %.2f nm" % (r * 10**7))
plt.show()
```

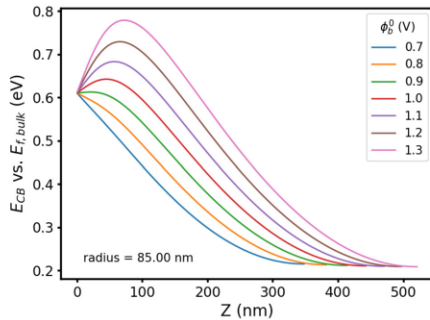
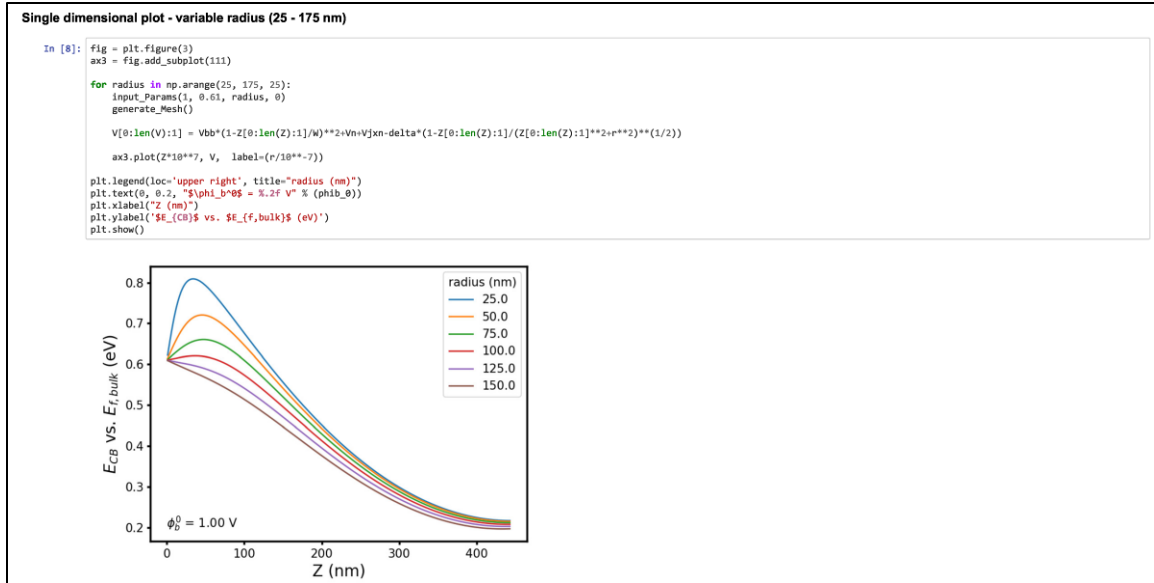
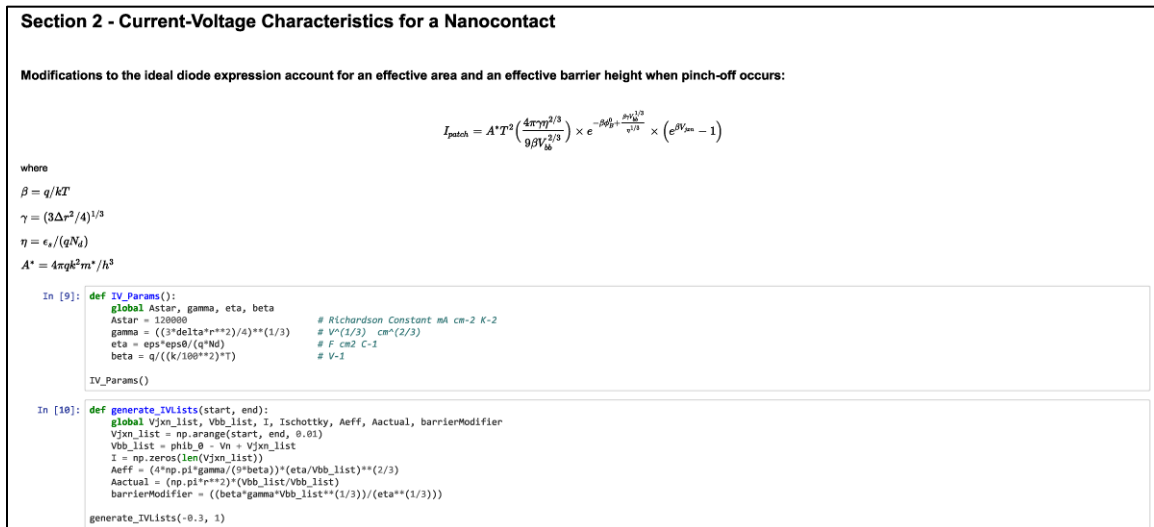


Figure G.S21 Python 3 code for modeling pinch-off: #4. Single dimension pinch-off model with variable barrier heights.



**Figure G.S22 Python 3 code for modeling pinch-off: #5.** Single dimensional pinch-off model with variable radii.



**Figure G.S23 Python 3 code for modeling pinch-off: #6.** Modifications to the ideal diode equation to account for pinch-off.

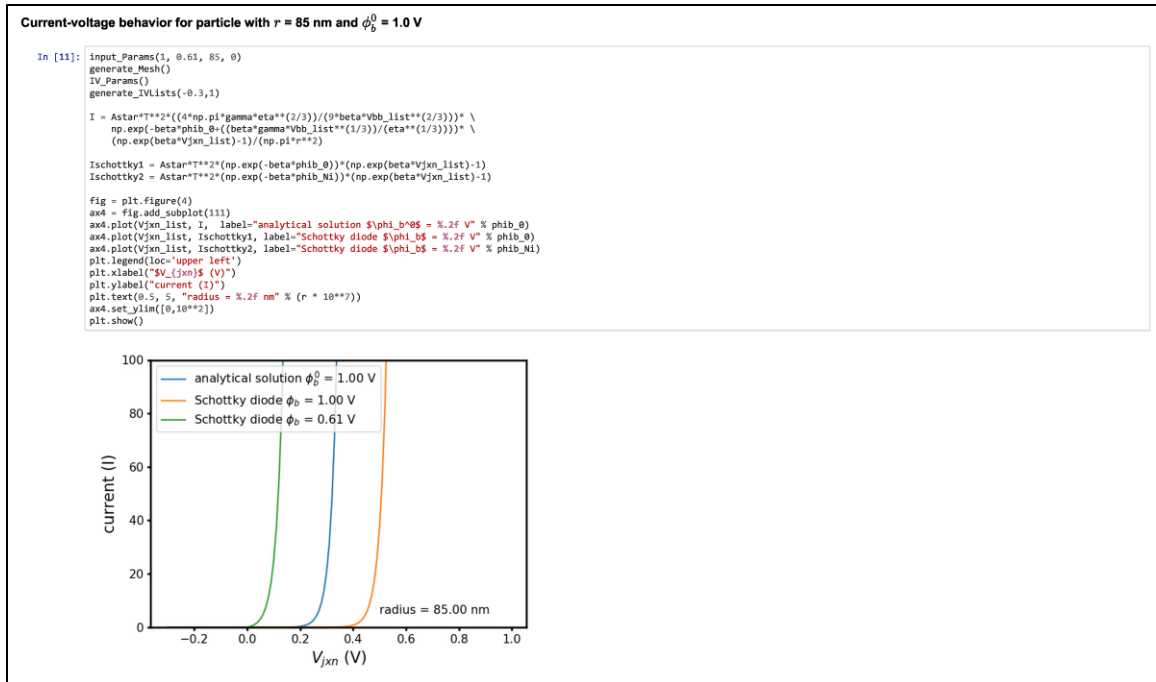


Figure G.S24 Python 3 code for modeling pinch-off: #7. Example current-voltage behavior.

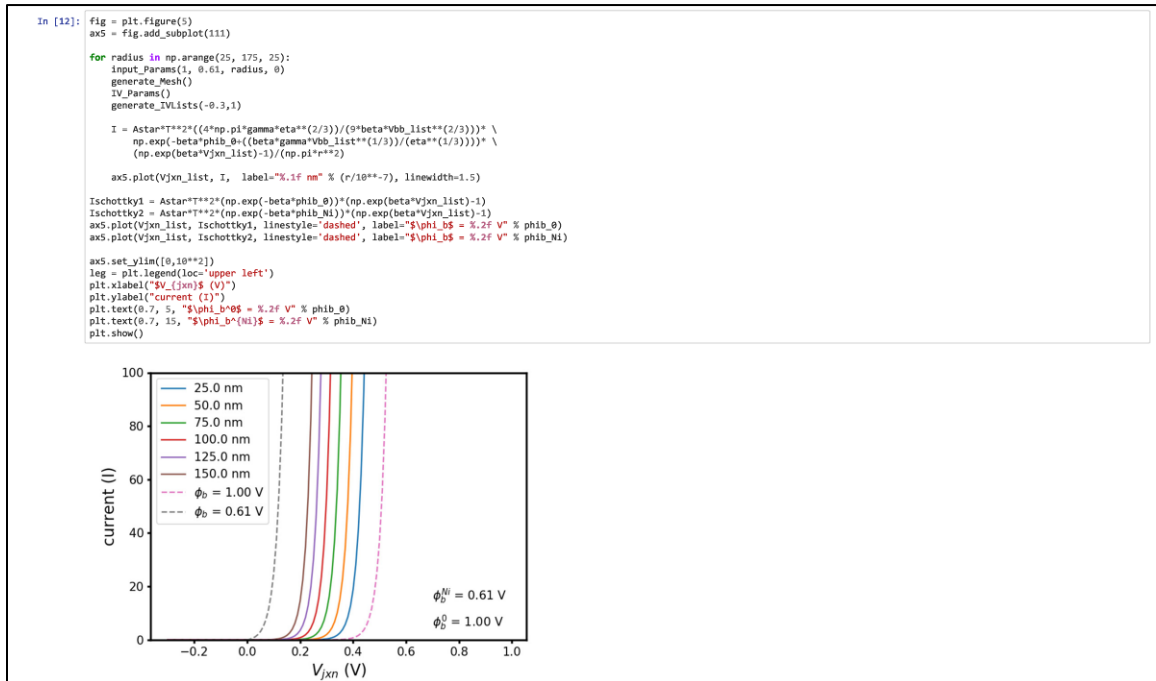
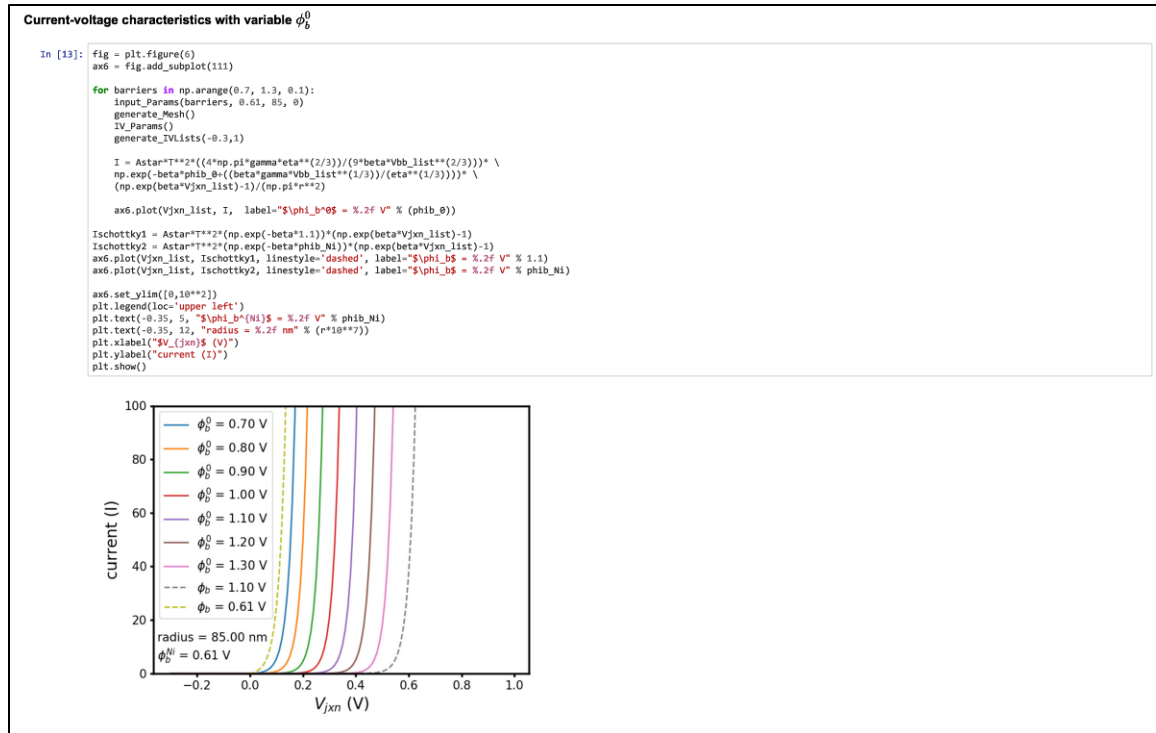
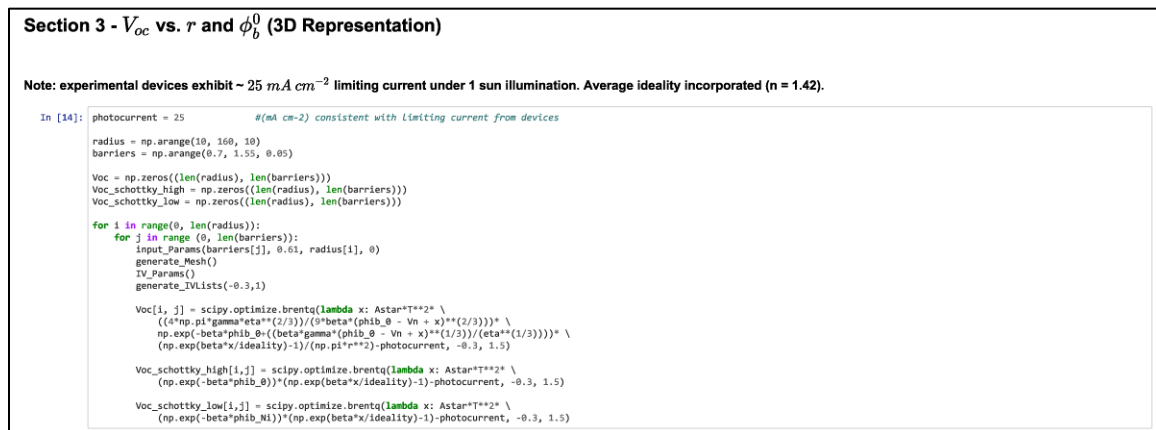


Figure G.S25 Python 3 code for modeling pinch-off: #8. Example current-voltage behavior with variable radii.



**Figure G.S26 Python 3 code for modeling pinch-off: #9.** Example current-voltage behavior with variable barrier heights.



**Figure G.S27 Python 3 code for modeling pinch-off: #10.** Initialization of 3D  $V_{oc}$  surface.

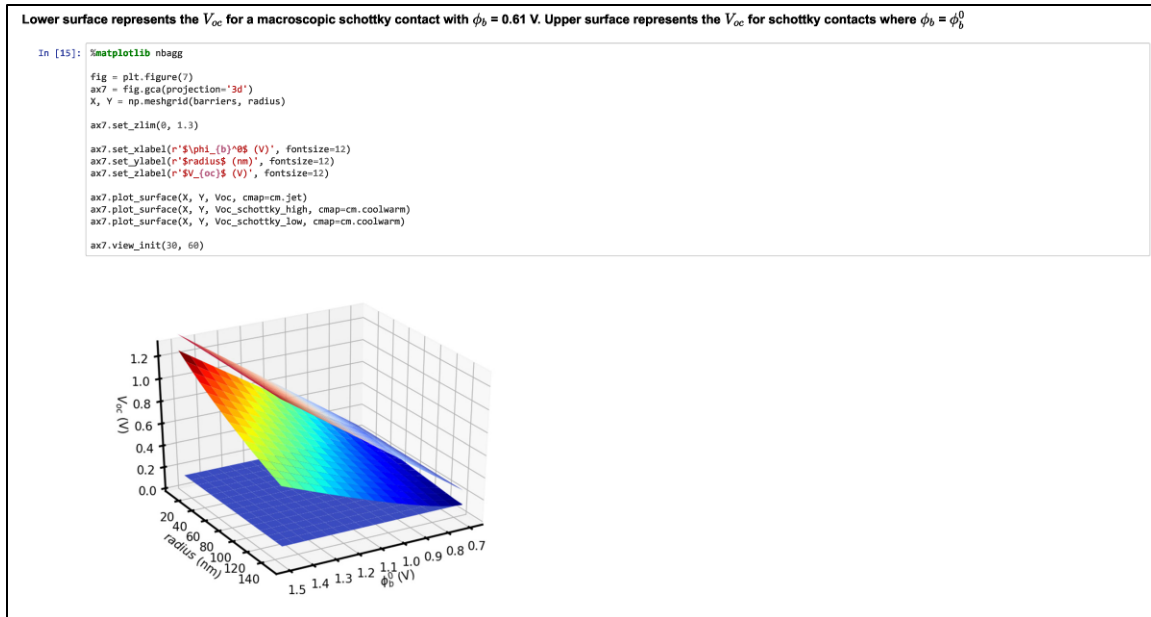


**Figure G.S28 Python 3 code for modeling pinch-off: #11.** 3D surface plot illustrating the  $V_{oc}$  as a function of radii and barrier heights.

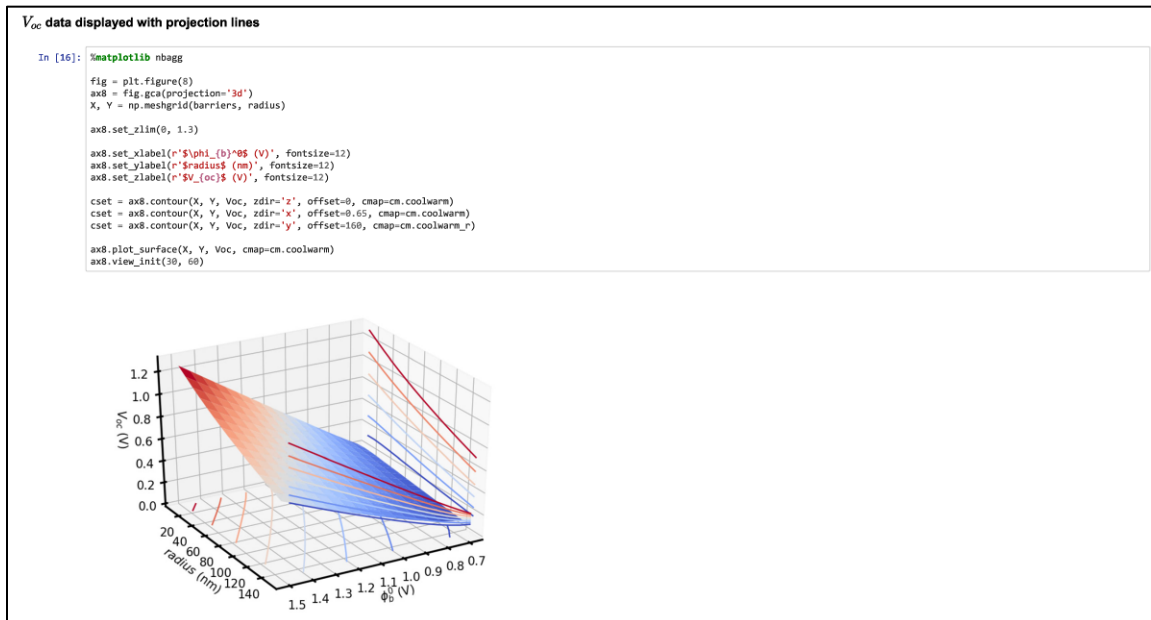


**Figure G.S29 Python 3 code for modeling pinch-off: #12.** 3D surface plot illustrating the  $V_{oc}$  as a function of radii and barrier heights. Select curves projected onto xy, xz, and yz planes.

#### Section 4 - $V_{oc}$ vs. $r$ and $\phi_b^0$ (2D Representation)

```
In [17]: fig = plt.figure(9)
ax9 = fig.add_subplot(111)
ax9.set_ylim(0, 1.0)

for i in range(1, len(barriers)-1):
    ax9.plot(radius, Voc[:,i], label="%.2f V" % barriers[i])

ax9.plot(radius, Voc_schottky_low[:,0], dashes=[2, 2, 2, 2])

plt.text(20, 0.05, "macroscopic schottky diode with  $\phi_b^0 = %.2f$  V" % phib_Ni)
plt.legend(loc='upper right', title="$\phi_b^0$", ncol=2)
plt.xlabel("radius (nm)")
plt.ylabel("$V_{oc}$ (V)")
plt.show()
```

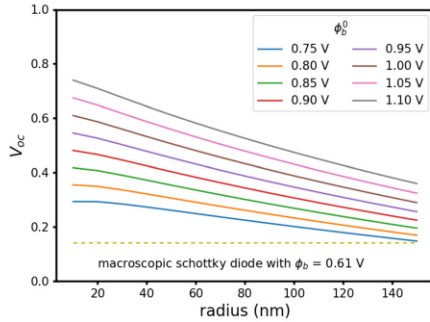


Figure G.S30 Python 3 code for modeling pinch-off: #13. 2D projection of the  $V_{oc}$  as a function of radii and barrier heights.

The in operando photovoltages are collected under illumination via the AFM laser. Calibration with a reference photodiode reveals a current density  $\sim 15\times$  greater than that of the 1 sun solar illuminator. However, the measurement is collected with the AFM probe partially obscuring the incident light. Under this condition the absolute current collected by the reference photodiode is  $1/3rd$  of that collected during the non-observed measurement. Thus for modeling the in operando data we use a local photocurrent just  $5\times$  larger than the limiting current in the 1 sun illumination case ( $= 25 \text{ mA cm}^{-2}$ ). Note that if the photocurrent is further decreased the fits compensate for this by increasing the surrounding barrier height ( $\phi_b^0$ ).

```
In [18]: #In operando photovoltages before activation (V vs. rad(i))
experimental_set1_x = np.array([59.49, 98.39, 116.86, 93.8, 128.465, 73.63, 84.35, \
64.55, 86.22, 53.5, 72.9, 101, 114.11, 68.465, 86.88])

#adjustment to account for AFM broadening (4 nm +/- 3)
experimental_set1_x = experimental_set1_x - 4

experimental_set1_y = np.array([0.4357, 0.3714, 0.3398, 0.3958, 0.3844, 0.4188, 0.4383, \
0.41274, 0.3777, 0.4438, 0.44928, 0.3746, 0.3479, 0.40186, 0.39494])

#In operando photovoltages after activation (V vs. rad(i))
experimental_set2_x = np.array([90.92, 44.81, 84.67, 104.96, 108.97, 68.18, 86.28, 61.42, \
86.53, 85.96, 104.98, 79.65, 95.37, 108.16, 67.69, 93.68, 80.68, 67.42, 109.38, 78.48])

#adjust to account for AFM broadening (4 nm +/-3) and consumption of Ni core (5.7% redox active = 2% rad(i) decrease)
experimental_set2_x = 0.98*(experimental_set2_x - 4)

experimental_set2_y = np.array([0.43445, 0.51339, 0.48819, 0.4299, 0.43025, 0.51687, \
0.48351, 0.50417, 0.46226, 0.489, 0.43119, 0.48844, 0.46476, 0.44181, 0.51315, \
0.42767, 0.46907, 0.49273, 0.42805, 0.47895])

#Reminder: for fig 2b the surface coverage was about 10% - adjust for Voc calculation

fig = plt.figure(10)
ax10 = fig.add_subplot(111)
ax10.set_ylim(0, 1.0)
ax10.set_xlim(40, 140)
ax10.set_ylim(0.3, 0.6)
ax10.scatter(experimental_set1_x, experimental_set1_y, label="non-activated")
ax10.scatter(experimental_set2_x, experimental_set2_y, label = "activated")
plt.legend(loc='upper right', title="experimental data")
plt.xlabel("radius (nm)")
plt.ylabel("$V_{oc}$ (V)")
plt.show()
```

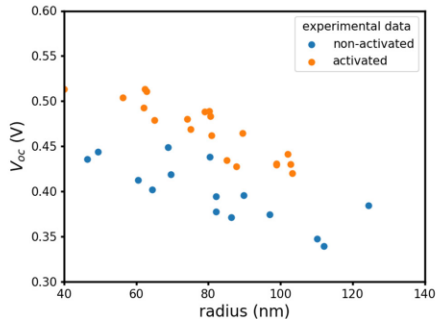


Figure G.S31 Python 3 code for modeling pinch-off: #14. The experimental photovoltages plotted vs. radius.

```

Least squares fit for datasets - solving for  $\phi_b^0$ 

In [19]: photocurrent = 125          #consistent limiting current of 5x the 1 sun illumination
         Input_Params(100, 0.61, 100, 0) # $\phi_b^0$  and R are unimportant here
         generate_Mesh()
         IV_Params()
         fillFactor=0.15
         ideality = 1.415

         def helperFunc(radius, barrier): #the model's Voc solution given a radius and barrier
             delta = barrier - phib_NI
             gamma = (3*(delta*(radius)**2)/4)**(1/3)
             return scipy.optimize.brents(lambda y: fillFactor*Astar**2 * \
             ((4*np.pi*gamma*eta**(2/3))/(9*beta*(barrier - Vn + y))**(2/3))) * \
             np.exp(-beta*barrier*((beta*gamma*(barrier - Vn + y))**(1/3))/(eta**(1/3)))) * \
             (np.exp(beta*y/ideality)-1)/(np.pi*radius**2)-photocurrent, -0.3, 1.5)

         def leastSquares(start, end, step, dataX, dataY): #evaluate the least squares for all surrounding barriers from start to stop
             leastSquaresMinimum = 100 #arbitrarily large number
             bMinimum = 100 #arbitrarily large number

             for b in np.linspace(start, end, step):
                 residualSum = 0
                 for i in range(0, len(dataX)):
                     residualSum = residualSum + (helperFunc(dataX[i]*10**-7, b) - dataY[i])**2

                 if residualSum<leastSquaresMinimum: #if this fit is better than the last then save it
                     leastSquaresMinimum = residualSum
                     bMinimum = b

             return bMinimum, (1-leastSquaresMinimum)

         fitBarrier, fitR = leastSquares(0.7, 1.2, 4001, experimental_set1_x, experimental_set1_y)

         print('Non-activated fit: ')
         display(Math(r"\phi_b^0" + " = %.3f \: V" % fitBarrier + "\: and \:" + r"%2-%.3f" % fitR))

         fitBarrier, fitR = leastSquares(0.7, 1.2, 4001, experimental_set2_x, experimental_set2_y)

         print("\n")
         print("Activated fit: ")
         display(Math(r"\phi_b^0" + " = %.3f \: V" % fitBarrier + "\: and \:" + r"%2-%.3f" % fitR))

         Non-activated fit:
          $\phi_b^0 = 0.825 \text{ V}$  and  $R^2 = 0.992$ 

         Activated fit:
          $\phi_b^0 = 0.905 \text{ V}$  and  $R^2 = 0.995$ 

```

**Figure G.S32 Python 3 code for modeling pinch-off: #15.** Custom least squares regression for fitting the experimental data with the pinch-off model.



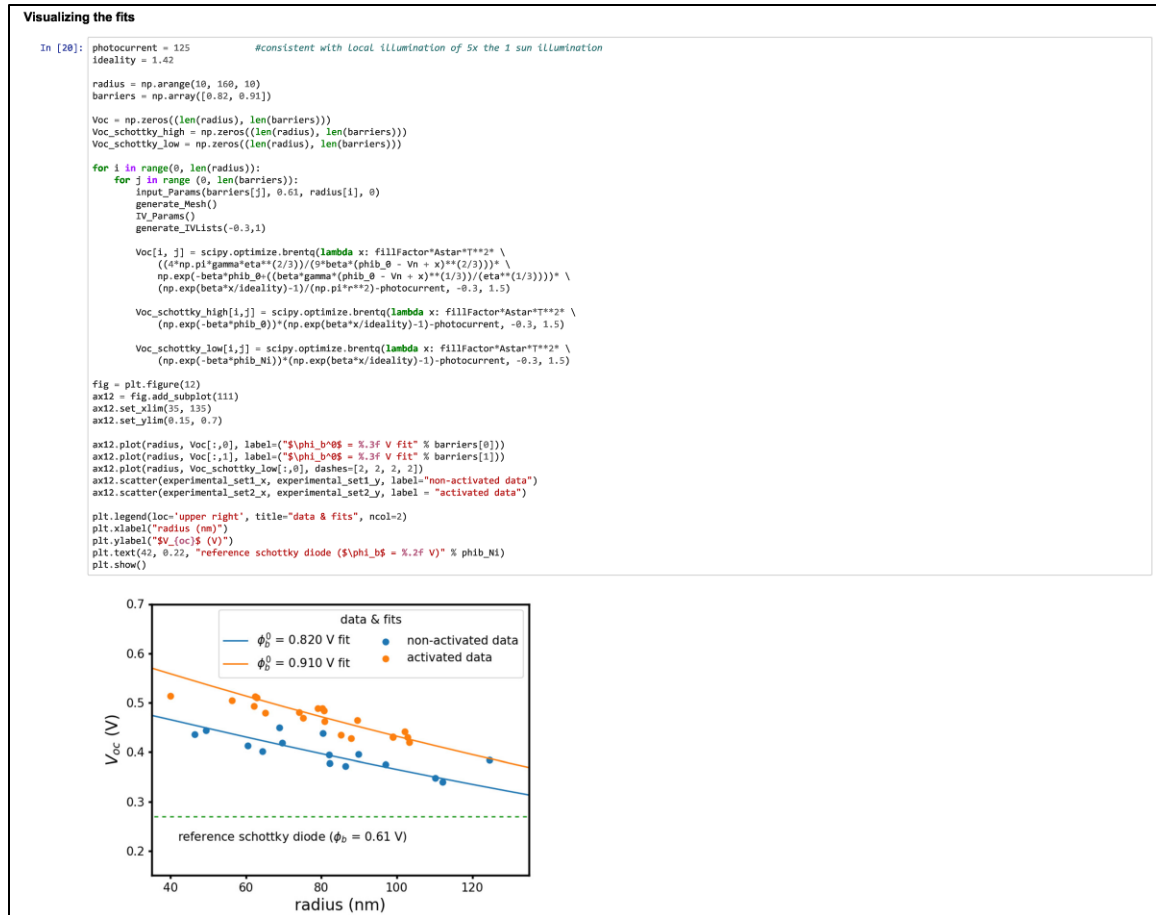


**Figure G.S33 Python 3 code for modeling pinch-off: #16.** Fits visualized with experimental photovoltages.

## Section 6 - Fitting Macroscopic Photoelectrochemical Data Sets

Photoanode comprised of uniform radius nano-contacts (represented by pinched-off nanocontact model) in series with a catalyst (represented by a Butler-Volmer expression)

Catalyst Current Density:

$$J_{cat} = J_{cat}^0 \left( e^{\beta(V_{cat})} - e^{-(1-\alpha)\beta(V_{cat})} \right)$$

Pinched-Off Diode Current Density:

$$J_{PO\_diode} = \left( \frac{ff}{\pi r^2} \right) A^* T^2 \left( \frac{4\pi\eta^{2/3}}{9\beta V_{cat}^{2/3}} \right) \times e^{-\beta\phi_0^* + \frac{\beta\eta V_{cat}}{V_{cat}^{2/3}}} \times \left( -e^{-\beta V_{sem}/n} + 1 \right) + J_0$$

where

$$\beta = q/kT$$

$$\gamma = (3\Delta r^2/4)^{1/3}$$

$$\eta = \epsilon_s / (qN_A)$$

$$A^* = 4\pi q k^2 m^2 / h^3$$

$J_{cat}^0$  is the catalyst exchange current and  $\alpha$  is the charge transfer coefficient (0.5)

$ff$  is the fill factor or percent of surface coated by islands,  $r$  is the uniform island radius,  $n$  is the ideality factor, and  $J_0$  is the photocurrent

```
In [22]: #Catalyst Parameters - Jcat manually tuned to fit experimental catalyst curve
Jcat = 3.5*10**4 #mA cm-2
beta = q/(k/100**2)*T
alpha = 0.5

#Photocurrents tuned to represent limiting currents of experimental data
photocurrent1 = 26 #mA cm-2
photocurrent2 = 14 #mA cm-2

#fill factor (portion of surface covered by Ni particles)
fillfactor=0.15

input_Params(0.91, 0.61, 60, 0)
generate_Mesh()
TV_Params()

Vjxn_list = np.arange(-0.6, 0.7, 0.01)

catalystCurrent = Jcat*(np.exp(alpha*beta*(Vjxn_list))-np.exp(alpha*-beta*(Vjxn_list)))
semiconductorCurrent = fillfactor*Astar**2 * \
    ((4*np.pi*gamma**eta**(2/3))/(9**beta*(phi0 - Vn - Vjxn_list)**(2/3))) * \
    np.exp(-beta*phi0 + (beta*gamma*(phi0 - Vn - Vjxn_list)**(1/3))/(eta**(1/3))) * \
    (-np.exp(-beta*Vjxn_list/ideality)+1)/(np.pi*r**2)+photocurrent1

fig = plt.figure(11)
ax13 = fig.add_subplot(111)
ax13.plot(Vjxn_list, catalystCurrent, label="cat")
ax13.plot(Vjxn_list, semiconductorCurrent, label="Sem")
ax13.set_ylim([-100,100])
ax13.set_title("J-V behavior of catalyst and pinched-off diode")
plt.legend(["catalyst (Butler-Volmer)", "pinched-off diode"], loc='lower left')
plt.xlabel("$V_{sem}$ or $V_{cat}$ (V)")
plt.ylabel("current density $(mA\ cm^{-2})$")
plt.show()
```

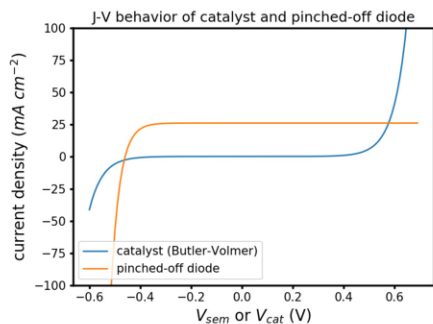


Figure G.S34 Python 3 code for modeling pinch-off: #17. Modified ideal diode equation placed in series with an experimentally fit Butler-Volmer expression to calculate photoelectrochemical  $J$ - $V$  behavior.

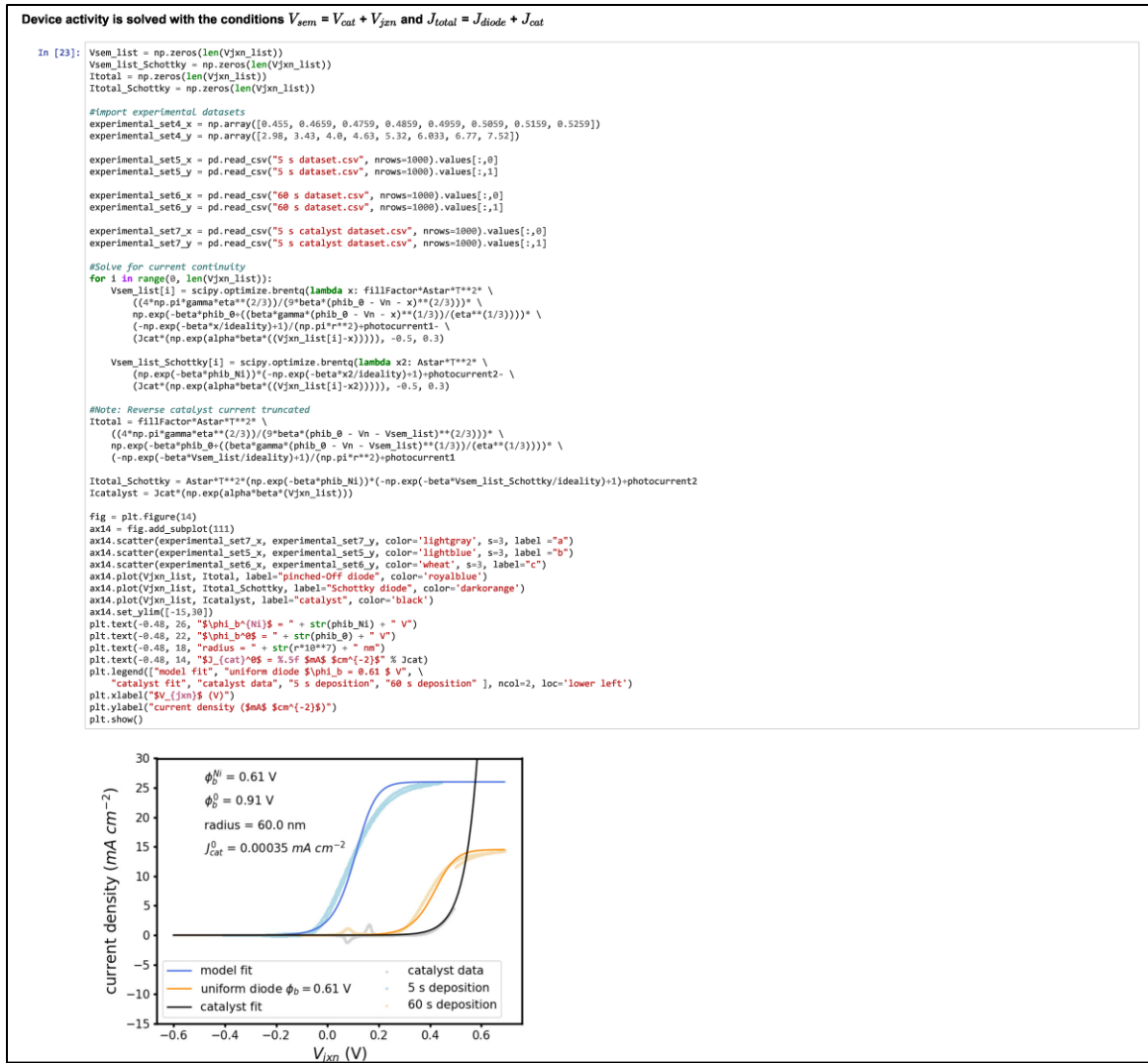


Figure G.S35 Python 3 code for modeling pinch-off: #18. Photoelectrochemical fits superimposed on the experimental  $J$ - $V$  curves for the 5-s Ni deposition, 60-s Ni deposition, Ni deposited on Pt.

## Section 7 - Visualizing Pinch-off

3D representation of pinch-off ( $V_{gzn} = V_{oc} = -0.468$  V and  $r = 60$  nm)

$$E_{CB}(r, z)/q = V_{\phi} * (1 - \frac{z}{w})^2 + V_n + V_{gzn} - \left( \frac{2\gamma^2 z}{27(z^2 + r^2)^{3/2}} \right)$$

```
In [25]: Input_Params(0.91, 0.61, 60, -0.458)
photocurrent = 25
generate_Mesh()
IV_Params()

Voc = scipy.optimize.brentq(lambda x: fillFactor*Astar**T**2 * \
    ((4*np.pi*gamma**eta**(2/3))/(9*beta*(phi_b - Vn + x)**(2/3))) * \
    np.exp(-beta*phi_b/(beta*gamma*(phi_b - Vn + x)**(1/3)))/(eta**(1/3))) * \
    (-np.exp(beta*x/ideality)+1)/(np.pi*r**2)-photocurrent, -0.3, 1.5)

print("A Voc of %.3f mV" % Voc + " for a %.2f nm radii" % (r*10**7))
A Voc of 0.458 mV for a 60.00 nm radii

In [26]: Input_Params(0.91, 0.61, 60, -0.458)
generate_Mesh()
IV_Params()

phi_b_effective = phi_b*(gamma*(Vbb/eta)**(1/3))

Z = np.arange(1*10**+7, W*10**+7+(50*10**+7), 10**+7) #cm mesh into semiconductor (spanning from 10 nm to 1000 nm)
R = np.arange(-2*r, 2*r, 10**+7) #cm mesh from middle of island (=0) to edge =(r)
V3D = np.zeros((len(R), len(Z)), float)

for i in range(0, len(R)):
    for j in range(0, len(Z)):
        V3D[i, j] = Vbb*(1-np.minimum(Z[j],W)/W)**2+Vn+Vjxn- \
            (2*gamma**3*np.minimum(Z[j],W)/(27*(R[i]**2+np.minimum(Z[j],W)**2)**(3/2)))-Vjxn-Vn-Vbb-phi_b_0

#the model breaks down near the center of the patch, this constraint suppresses that output
V3D[V3D<(0.2-Vjxn)]=phi_b_Ni
```

Figure G.S36 Python 3 code for modeling pinch-off: #19. Code to plot the conduction band energy vs. R and Z.

```
In [27]: fig = plt.figure(15)
ax15 = fig.gca(projection='3d')
X, Y = np.meshgrid(Z/10**+7, R/10**+7)

ax15.set_xlabel('Z (nm)', fontsize=12)
ax15.set_ylabel('R (nm)', fontsize=12)
ax15.set_zlabel('$E_{CB}$ (eV)', fontsize=12)

ax15.plot_surface(X, Y, V3D, cmap=cm.coolwarm)

fig = plt.figure(16)
ax16 = fig.add_subplot(111)
ax16.plot(Z/10**+7, V3D[int(len(R)/2),:], label="Middle")
ax16.set_ylim([0,2])
plt.text(5, 1.3, "maximum point = %.4f V" % np.max(V3D[int(len(R)/2),:]))
plt.text(5, 1.5, "$\phi_{b}$ effective = %.4f V" % phi_b_effective)
plt.legend(["cross section through R=0"], loc='upper right')
plt.xlabel("Z (nm)")
plt.ylabel('$E_{CB}$ (eV)')
plt.show()
```

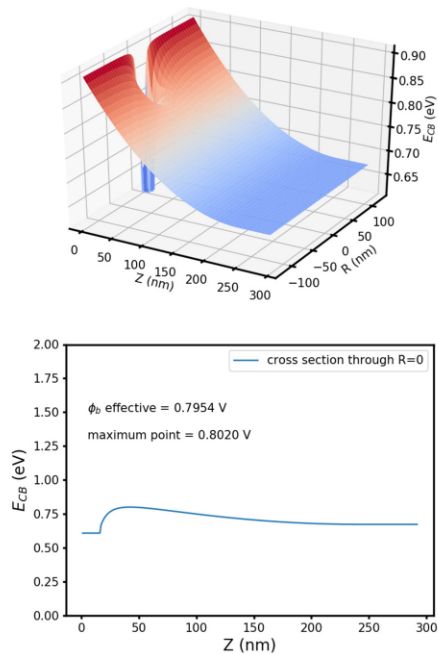


Figure G.S37 Python 3 code for modeling pinch-off: #20.  $E_{CB}$  vs.  $Z$  &  $R$ .

```

3D representation with variable  $V_{jzn}$ 

In [29]: input_params(0.91, 0.61, 60, 0)
generate_Mesh()

Vjxn_list = np.arange(-0.5, 0.001, 0.001) #range of applied voltages
Vbb = phib_0 - Vn + Vjxn_list[-1] #band bending in Volts for max case
W = (2*eps*eps0*Vbb/(q*Nd))**(1/2) #depletion width in cm

Z = np.arange(10*10**7, W, 10**7) #cm mesh into semiconductor (spanning from 10 nm to 1000 nm)
R = np.arange(-2*r, 2*r, 10**6) #cm mesh from center of island (=0) to edge =r)
V3D = np.zeros((len(Vjxn_list), len(R), len(Z)), float) #conduction band potential

for v in range(0, len(Vjxn_list)):
    Vjxn = Vjxn_list[v]
    Vbb = phib_0 - Vn + Vjxn
    W = (2*eps*eps0*Vbb/(q*Nd))**(1/2)

    for i in range(0, len(R)):
        for j in range(0, len(Z)):
            #note: minimum statement used here to stop the calculation once the depletion edge is reached
            #required because the depletion width changes as a function of Vjxn but a static mesh is being used
            V3D[v, i, j] = Vbb*(1-np.minimum(Z[j],W)/W)**2+Vn+Vjxn- \
                (2*gamma**3*np.minimum(Z[j],W)/(27*(R[i]**2+np.minimum(Z[j],W)**2))**(3/2))- \
                Vjxn-Vn-Vbb-phib_0

            #the model breaks down near the center of the patch, this constraint suppresses that output
            if (V3D[v, i, j]<(0.2*Vjxn)):
                V3D[v, i, j]=0.2*Vjxn
    
```

Figure G.S38 Python 3 code for modeling pinch-off: #21. Code to plot  $E_{CB}$  at various applied potentials.

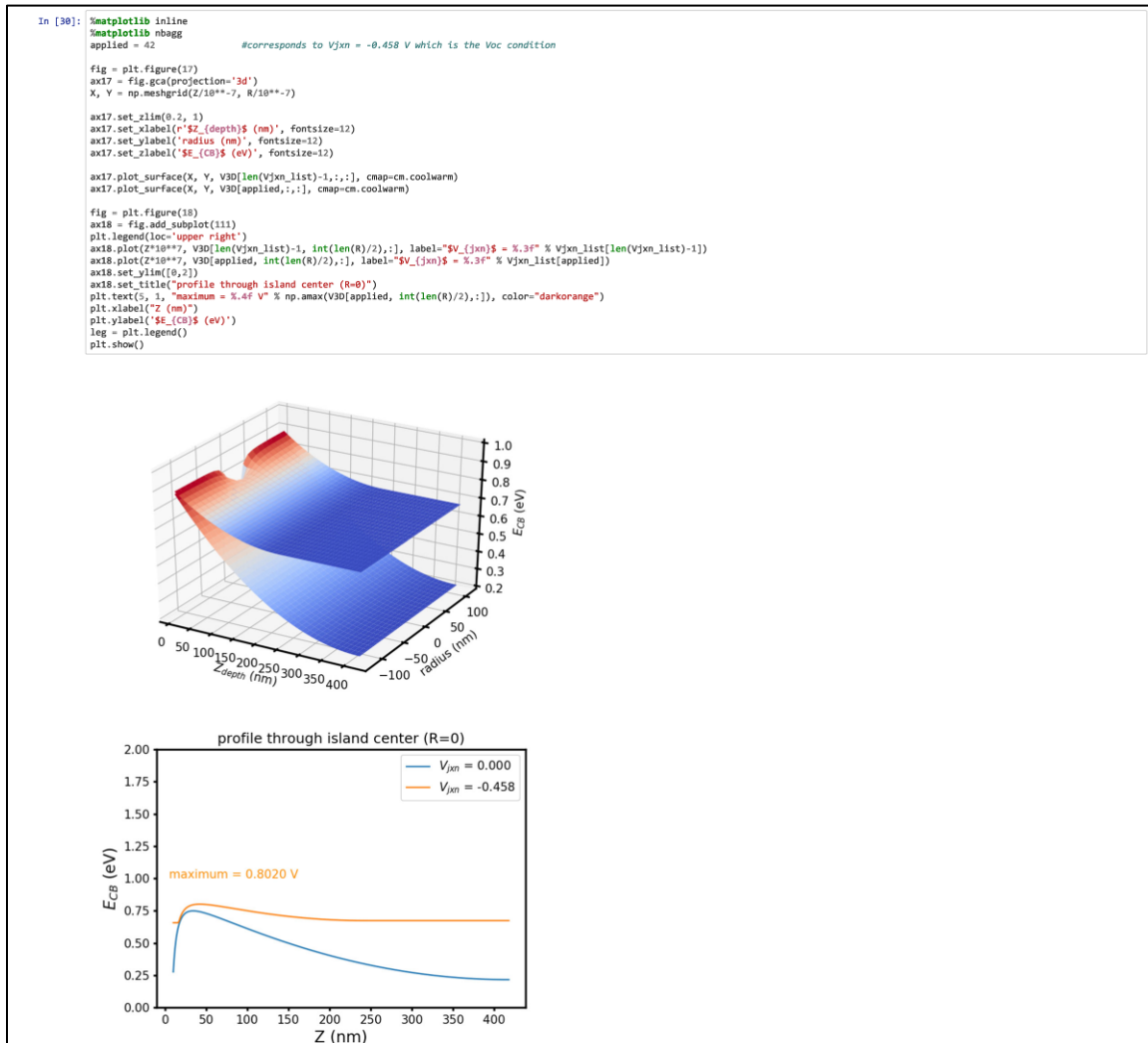


Figure G.S39 Python 3 code for modeling pinch-off: #22.  $E_{CB}$  plotted at various applied potentials.

## REFERENCES CITED

### A. References for Paper A

Style: Journal of the American Chemical Society

- (1) Walter, M. G.; Warren, E. L.; McKone, J. R.; Boettcher, S. W.; Mi, Q. X.; Santori, E. A.; Lewis, N. S. Solar Water Splitting Cells. *Chem. Rev.* **2010**, *110* (11), 6446-6473.
- (2) Cowan, A. J.; Durrant, J. R. Long-Lived Charge Separated States in Nanostructured Semiconductor Photoelectrodes for the Production of Solar Fuels. *Chem. Soc. Rev.* **2013**, *42* (6), 2281-2293.
- (3) Sivula, K. Metal Oxide Photoelectrodes for Solar Fuel Production, Surface Traps, and Catalysis. *J. Phys. Chem. Lett.* **2013**, *4* (10), 1624-1633.
- (4) Zandi, O.; Hamann, T. W. The Potential Versus Current State of Water Splitting with Hematite. *Phys. Chem. Chem. Phys.* **2015**, *17* (35), 22485-22503.
- (5) Sivula, K.; van de Krol, R. Semiconducting Materials for Photoelectrochemical Energy Conversion. *Nat. Rev. Mater.* **2016**, *1* (2), 15010.
- (6) Carroll, G. M.; Zhong, D. K.; Gamelin, D. R. Mechanistic Insights into Solar Water Oxidation by Cobalt-Phosphate-Modified  $\alpha$ -Fe<sub>2</sub>O<sub>3</sub> Photoanodes. *Energy Environ. Sci.* **2015**, *8* (2), 577-584.
- (7) Zhong, D. K.; Choi, S.; Gamelin, D. R. Near-Complete Suppression of Surface Recombination in Solar Photoelectrolysis by "Co-Pi" Catalyst-Modified W:BiVO<sub>4</sub>. *J. Am. Chem. Soc.* **2011**, *133* (45), 18370-18377.
- (8) Zhong, D. K.; Gamelin, D. R. Photoelectrochemical Water Oxidation by Cobalt Catalyst ("Co-Pi")/ $\alpha$ -Fe<sub>2</sub>O<sub>3</sub> Composite Photoanodes: Oxygen Evolution and Resolution of a Kinetic Bottleneck. *J. Am. Chem. Soc.* **2010**, *132* (12), 4202-4207.
- (9) Barroso, M.; Cowan, A. J.; Pendlebury, S. R.; Gratzel, M.; Klug, D. R.; Durrant, J. R. The Role of Cobalt Phosphate in Enhancing the Photocatalytic Activity of  $\alpha$ -Fe<sub>2</sub>O<sub>3</sub> toward Water Oxidation. *J. Am. Chem. Soc.* **2011**, *133* (38), 14868-14871.
- (10) Montoya, J. H.; Seitz, L. C.; Chakthranont, P.; Vojvodic, A.; Jaramillo, T. F.; Norskov, J. K. Materials for Solar Fuels and Chemicals. *Nat. Mater.* **2017**, *16* (1), 70-81.
- (11) Gamelin, D. R. Water Splitting Catalyst or Spectator? *Nat. Chem.* **2012**, *4* (12), 965-967.
- (12) Toma, F. M.; Cooper, J. K.; Kunzelmann, V.; McDowell, M. T.; Yu, J.; Larson, D. M.; Borys, N. J.; Abelyan, C.; Beeman, J. W.; Yu, K. M.; Yang, J. H.; Chen, L.; Shaner, M. R.; Spurgeon, J.; Houle, F. A.; Persson, K. A.; Sharp, I. D. Mechanistic Insights into Chemical and Photochemical Transformations of Bismuth Vanadate Photoanodes. *Nat. Commun.* **2016**, *7*, 12012.

- (13) Li, R. G.; Zhang, F. X.; Wang, D. G.; Yang, J. X.; Li, M. R.; Zhu, J.; Zhou, X.; Han, H. X.; Li, C. Spatial Separation of Photogenerated Electrons and Holes among {010} and {110} Crystal Facets of BiVO<sub>4</sub>. *Nat. Commun.* **2013**, *4*, 1432.
- (14) Liu, R.; Zheng, Z.; Spurgeon, J.; Yang, X. G. Enhanced Photoelectrochemical Water-Splitting Performance of Semiconductors by Surface Passivation Layers. *Energy Environ. Sci.* **2014**, *7* (8), 2504-2517.
- (15) de Respinis, M.; Joya, K. S.; De Groot, H. J. M.; D'Souza, F.; Smith, W. A.; van de Krol, R.; Dam, B. Solar Water Splitting Combining a BiVO<sub>4</sub> Light Absorber with a Ru-Based Molecular Cocatalyst. *J. Phys. Chem. C* **2015**, *119* (13), 7275-7281.
- (16) Burke, M. S.; Kast, M. G.; Trotochaud, L.; Smith, A. M.; Boettcher, S. W. Cobalt-Iron (Oxy)Hydroxide Oxygen Evolution Electrocatalysts: The Role of Structure and Composition on Activity, Stability, and Mechanism. *J. Am. Chem. Soc.* **2015**, *137* (10), 3638-3648.
- (17) Enman, L. J.; Burke, M. S.; Batchellor, A. S.; Boettcher, S. W. Effects of Intentionally Incorporated Metal Cations on the Oxygen Evolution Electrocatalytic Activity of Nickel (Oxy)Hydroxide in Alkaline Media. *ACS Catal.* **2016**, *6* (4), 2416-2423.
- (18) Stevens, M. B.; Trang, C. D. M.; Enman, L. J.; Deng, J.; Boettcher, S. W. Reactive Fe-Sites in Ni/Fe (Oxy)Hydroxide Are Responsible for Exceptional Oxygen Electrocatalysis Activity. *J. Am. Chem. Soc.* **2017**, *139* (33), 11361-11364.
- (19) Burke, M. S.; Zou, S. H.; Enman, L. J.; Kellon, J. E.; Gabor, C. A.; Pledger, E.; Boettcher, S. W. Revised Oxygen Evolution Reaction Activity Trends for First-Row Transition-Metal (Oxy)Hydroxides in Alkaline Media. *J. Phys. Chem. Lett.* **2015**, *6* (18), 3737-3742.
- (20) Roger, I.; Shipman, M. A.; Symes, M. D. Earth-Abundant Catalysts for Electrochemical and Photoelectrochemical Water Splitting. *Nat. Rev. Chem.* **2017**, *1* (1), 0003.
- (21) Yang, J. H.; Wang, D. G.; Han, H. X.; Li, C. Roles of Cocatalysts in Photocatalysis and Photoelectrocatalysis. *Acc. Chem. Res.* **2013**, *46* (8), 1900-1909.
- (22) Carroll, G. M.; Gamelin, D. R. Kinetic Analysis of Photoelectrochemical Water Oxidation by Mesostructured Co-Pi/ $\alpha$ -Fe<sub>2</sub>O<sub>3</sub> Photoanodes. *J. Mater. Chem. A* **2016**, *4* (8), 2986-2994.
- (23) Klahr, B.; Gimenez, S.; Fabregat-Santiago, F.; Bisquert, J.; Hamann, T. W. Photoelectrochemical and Impedance Spectroscopic Investigation of Water Oxidation with "Co-Pi"-Coated Hematite Electrodes. *J. Am. Chem. Soc.* **2012**, *134* (40), 16693-16700.
- (24) Li, W.; He, D.; Sheehan, S. W.; He, Y. M.; Thorne, J. E.; Yao, X. H.; Brudvig, G. W.; Wang, D. W. Comparison of Heterogenized Molecular and Heterogeneous Oxide Catalysts for Photoelectrochemical Water Oxidation. *Energy Environ. Sci.* **2016**, *9* (5), 1794-1802.
- (25) Zachäus, C.; Abdi, F. F.; Peter, L. M.; Van De Krol, R. Photocurrent of BiVO<sub>4</sub> Is Limited by Surface Recombination, Not Surface Catalysis. *Chem. Sci.* **2017**, *8* (5), 3712-3719.



- (26) Thorne, J. E.; Jang, J. W.; Liu, E. Y.; Wang, D. W. Understanding the Origin of Photoelectrode Performance Enhancement by Probing Surface Kinetics. *Chem. Sci.* **2016**, *7* (5), 3347-3354.
- (27) Barroso, M.; Mesa, C. A.; Pendlebury, S. R.; Cowan, A. J.; Hisatomi, T.; Sivula, K.; Gratzel, M.; Klug, D. R.; Durrant, J. R. Dynamics of Photogenerated Holes in Surface Modified  $\alpha$ -Fe<sub>2</sub>O<sub>3</sub> Photoanodes for Solar Water Splitting. *Proc. Natl. Acad. Sci. U. S. A.* **2012**, *109* (39), 15640-15645.
- (28) Godin, R.; Kafizas, A.; Durrant, J. R. Electron Transfer Dynamics in Fuel Producing Photosystems. *Curr. Opin. Electrochem.* **2017**, *2* (1), 136-143.
- (29) Ma, Y. M.; Kafizas, A.; Pendlebury, S. R.; Le Formal, F.; Durrant, J. R. Photoinduced Absorption Spectroscopy of CoPi on BiVO<sub>4</sub>: The Function of CoPi During Water Oxidation. *Adv. Funct. Mater.* **2016**, *26* (27), 4951-4960.
- (30) Cowan, A. J.; Barnett, C. J.; Pendlebury, S. R.; Barroso, M.; Sivula, K.; Gratzel, M.; Durrant, J. R.; Klug, D. R. Activation Energies for the Rate-Limiting Step in Water Photooxidation by Nanostructured  $\alpha$ -Fe<sub>2</sub>O<sub>3</sub> and TiO<sub>2</sub>. *J. Am. Chem. Soc.* **2011**, *133* (26), 10134-10140.
- (31) Barroso, M.; Pendlebury, S. R.; Cowan, A. J.; Durrant, J. R. Charge Carrier Trapping, Recombination and Transfer in Hematite ( $\alpha$ -Fe<sub>2</sub>O<sub>3</sub>) Water Splitting Photoanodes. *Chem. Sci.* **2013**, *4* (7), 2724-2734.
- (32) Pendlebury, S. R.; Cowan, A. J.; Barroso, M.; Sivula, K.; Ye, J. H.; Gratzel, M.; Klug, D. R.; Tang, J. W.; Durrant, J. R. Correlating Long-Lived Photogenerated Hole Populations with Photocurrent Densities in Hematite Water Oxidation Photoanodes. *Energy Environ. Sci.* **2012**, *5* (4), 6304-6312.
- (33) Pendlebury, S. R.; Barroso, M.; Cowan, A. J.; Sivula, K.; Tang, J. W.; Gratzel, M.; Klug, D.; Durrant, J. R. Dynamics of Photogenerated Holes in Nanocrystalline  $\alpha$ -Fe<sub>2</sub>O<sub>3</sub> Electrodes for Water Oxidation Probed by Transient Absorption Spectroscopy. *Chem. Commun.* **2011**, *47* (2), 716-718.
- (34) Pendlebury, S. R.; Wang, X. L.; Le Formal, F.; Cornuz, M.; Kafizas, A.; Tilley, S. D.; Gratzel, M.; Durrant, J. R. Ultrafast Charge Carrier Recombination and Trapping in Hematite Photoanodes under Applied Bias. *J. Am. Chem. Soc.* **2014**, *136* (28), 9854-9857.
- (35) Kafizas, A.; Wang, X. L.; Pendlebury, S. R.; Barnes, P.; Ling, M.; Sotelo-Vazquez, C.; Quesada-Cabrera, R.; Li, C.; Parkin, I. P.; Durrant, J. R. Where Do Photogenerated Holes Go in Anatase:Rutile TiO<sub>2</sub>? A Transient Absorption Spectroscopy Study of Charge Transfer and Lifetime. *J. Phys. Chem. A* **2016**, *120* (5), 715-723.
- (36) Ma, Y. M.; Mesa, C. A.; Pastor, E.; Kafizas, A.; Francas, L.; Le Formal, F.; Pendlebury, S. R.; Durrant, J. R. Rate Law Analysis of Water Oxidation and Hole Scavenging on a BiVO<sub>4</sub> Photoanode. *ACS Energy Lett.* **2016**, *1* (3), 618-623.
- (37) Le Formal, F.; Pastor, E.; Tilley, S. D.; Mesa, C. A.; Pendlebury, S. R.; Gratzel, M.; Durrant, J. R. Rate Law Analysis of Water Oxidation on a Hematite Surface. *J. Am. Chem. Soc.* **2015**, *137* (20), 6629-6637.

- (38) Kafizas, A.; Ma, Y. M.; Pastor, E.; Pendlebury, S. R.; Mesa, C.; Francas, L.; Le Formal, F.; Noor, N.; Ling, M.; Sotelo-Vazquez, C.; Carmalt, C. J.; Parkin, I. P.; Durrant, J. R. Water Oxidation Kinetics of Accumulated Holes on the Surface of a TiO<sub>2</sub> Photoanode: A Rate Law Analysis. *ACS Catal.* **2017**, *7* (7), 4896-4903.
- (39) Bahnemann, D. W.; Hilgendorff, M.; Memming, R. Charge Carrier Dynamics at TiO<sub>2</sub> Particles: Reactivity of Free and Trapped Holes. *J. Phys. Chem. B* **1997**, *101* (21), 4265-4275.
- (40) Bahnemann, D.; Henglein, A.; Lilie, J.; Spanhel, L. Flash Photolysis Observation of the Absorption Spectra of Trapped Positive Holes and Electrons in Colloidal Titanium Dioxide. *The Journal of Physical Chemistry* **1984**, *88* (4), 709-711.
- (41) Yoshihara, T.; Katoh, R.; Furube, A.; Tamaki, Y.; Murai, M.; Hara, K.; Murata, S.; Arakawa, H.; Tachiya, M. Identification of Reactive Species in Photoexcited Nanocrystalline TiO<sub>2</sub> Films by Wide-Wavelength-Range (400-2500 nm) Transient Absorption Spectroscopy. *J. Phys. Chem. B* **2004**, *108* (12), 3817-3823.
- (42) Su, J. Z.; Vayssieres, L. A Place in the Sun for Artificial Photosynthesis? *ACS Energy Lett.* **2016**, *1* (1), 121-135.
- (43) Ravensbergen, J.; Abdi, F. F.; van Santen, J. H.; Frese, R. N.; Dam, B.; van de Krol, R.; Kennis, J. T. M. Unraveling the Carrier Dynamics of BiVO<sub>4</sub>: A Femtosecond to Microsecond Transient Absorption Study. *J. Phys. Chem. C* **2014**, *118* (48), 27793-27800.
- (44) Klotz, D.; Ellis, D. S.; Dotan, H.; Rothschild, A. Empirical in Operando Analysis of the Charge Carrier Dynamics in Hematite Photoanodes by PEIS, IMPS and IMVS. *Phys. Chem. Chem. Phys.* **2016**, *18* (34), 23438-23457.
- (45) Ponomarev, E. A.; Peter, L. M. A Generalized Theory of Intensity-Modulated Photocurrent Spectroscopy (IMPS). *J. Electroanal. Chem.* **1995**, *396* (1-2), 219-226.
- (46) Cummings, C. Y.; Marken, F.; Peter, L. M.; Tahir, A. A.; Wijayantha, K. G. U. Kinetics and Mechanism of Light-Driven Oxygen Evolution at Thin Film  $\alpha$ -Fe<sub>2</sub>O<sub>3</sub> Electrodes. *Chem. Commun.* **2012**, *48* (14), 2027-2029.
- (47) Peter, L. M.; Wijayantha, K. G. U.; Tahir, A. A. Kinetics of Light-Driven Oxygen Evolution at  $\alpha$ -Fe<sub>2</sub>O<sub>3</sub> Electrodes. *Faraday Discuss.* **2012**, *155*, 309-322.
- (48) Cummings, C. Y.; Marken, F.; Peter, L. M.; Wijayantha, K. G. U.; Tahir, A. A. New Insights into Water Splitting at Mesoporous  $\alpha$ -Fe<sub>2</sub>O<sub>3</sub> Films: A Study by Modulated Transmittance and Impedance Spectroscopies. *J. Am. Chem. Soc.* **2012**, *134* (2), 1228-1234.
- (49) Lin, F. D.; Boettcher, S. W. Adaptive Semiconductor/Electrocatalyst Junctions in Water-Splitting Photoanodes. *Nat. Mater.* **2014**, *13* (1), 81-86.
- (50) Lin, F.; Boettcher, S. W., Advanced Photoelectrochemical Characterization: Principles and Applications of Dual-Working-Electrode Photoelectrochemistry. In *Photoelectrochemical Solar Fuel Production*, Springer: 2016; pp 323-351.

- (51) Nellist, M. R.; Chen, Y. K.; Mark, A.; Godrich, S.; Stelling, C.; Jiang, J. J.; Poddar, R.; Li, C. Z.; Kumar, R.; Papastavrou, G.; Retsch, M.; Brunschwig, B. S.; Huang, Z. Q.; Xiang, C. X.; Boettcher, S. W. Atomic Force Microscopy with Nanoelectrode Tips for High Resolution Electrochemical, Nanoadhesion and Nanoelectrical Imaging. *Nanotechnology* **2017**, *28* (9), 095711.
- (52) Qiu, J. J.; Hajibabaei, H.; Nellist, M. R.; Laskowski, F. A. L.; Oener, S. Z.; Hamann, T. W.; Boettcher, S. W. Catalyst Deposition on Photoanodes: The Roles of Intrinsic Catalytic Activity, Catalyst Electrical Conductivity, and Semiconductor Morphology. *ACS Energy Lett.* **2018**, *3* (4), 961-969.
- (53) Qiu, J. J.; Hajibabaei, H.; Nellist, M. R.; Laskowski, F. A. L.; Hamann, T. W.; Boettcher, S. W. Direct in Situ Measurement of Charge Transfer Processes During Photoelectrochemical Water Oxidation on Catalyzed Hematite. *ACS Cent. Sci.* **2017**, *3* (9), 1015-1025.
- (54) Laskowski, F. A. L.; Nellist, M. R.; Venkatkarthick, R.; Boettcher, S. W. Junction Behavior of n-Si Photoanodes Protected by Thin Ni Elucidated from Dual Working Electrode Photoelectrochemistry. *Energy Environ. Sci.* **2017**, *10* (2), 570-579.
- (55) Nellist, M. R.; Laskowski, F. A. L.; Qiu, J. J.; Hajibabaei, H.; Sivula, K.; Hamann, T. W.; Boettcher, S. W. Potential-Sensing Electrochemical Atomic Force Microscopy for in Operando Analysis of Water-Splitting Catalysts and Interfaces. *Nat. Energy* **2018**, *3* (1), 46-52.
- (56) Nellist, M. R.; Laskowski, F. A. L.; Lin, F. D.; Mills, T. J.; Boettcher, S. W. Semiconductor-Electrocatalyst Interfaces: Theory, Experiment, and Applications in Photoelectrochemical Water Splitting. *Acc. Chem. Res.* **2016**, *49* (4), 733-740.
- (57) Laskowski, F. A. L.; Qiu, J.; Nellist, M. R.; Oener, S. Z.; Gordon, A. M.; Boettcher, S. Transient Photocurrents on Catalyst-Modified n-Si Photoelectrodes: Insight from Dual-Working Electrode Photoelectrochemistry. *Sustainable Energy Fuels* **2018**, *2*, 1995-2005.
- (58) Lobato, K.; Peter, L. M.; Wurfel, U. Direct Measurement of the Internal Electron Quasi-Fermi Level in Dye Sensitized Solar Cells Using a Titanium Secondary Electrode. *J. Phys. Chem. B* **2006**, *110* (33), 16201-16204.
- (59) Pinson, W. E. Quasi-Fermi Level Measurement in an Illuminated GaP Photoelectrolysis Cell. *Nature* **1977**, *269* (5626), 316-318.
- (60) Lonergan, M. C. A Tunable Diode Based on an Inorganic-Semiconductor|Conjugated-Polymer Interface. *Science* **1997**, *278* (5346), 2103-2106.
- (61) Boettcher, S. W.; Strandwitz, N. C.; Schierhorn, M.; Lock, N.; Lonergan, M. C.; Stucky, G. D. Tunable Electronic Interfaces between Bulk Semiconductors and Ligand-Stabilized Nanoparticle Assemblies. *Nat. Mater.* **2007**, *6* (8), 592-596.
- (62) Cui, W.; Niu, W. Z.; Wick-Joliat, R.; Moehl, T.; Tilley, S. D. Operando Deconvolution of Photovoltaic and Electrocatalytic Performance in ALD TiO<sub>2</sub> Protected Water Splitting Photocathodes. *Chem. Sci.* **2018**, *9* (28), 6062-6067.

- (63) Guijarro, N.; Liu, Y.; Le Formal, F.; Yao, L.; Sivula, K., Operando Potential-Sensing at the Semiconductor-Liquid Junctions: Tracking the Surface Energetics and Interfacial Kinetics During Photoelectrosynthetic Reactions. In *nanoGe Fall Meeting 2018*, DOI: 10.29363/nanoge.fallmeeting.2018.088
- (64) Xu, P. T.; Huang, T.; Huang, J. B.; Yan, Y.; Mallouk, T. E. Dye-Sensitized Photoelectrochemical Water Oxidation through a Buried Junction. *Proc. Natl. Acad. Sci. U. S. A.* **2018**, *115* (27), 6946-6951.
- (65) Eichhorn, J.; Kastl, C.; Cooper, J. K.; Ziegler, D.; Schwartzberg, A. M.; Sharp, I. D.; Toma, F. M. Nanoscale Imaging of Charge Carrier Transport in Water Splitting Photoanodes. *Nat. Commun.* **2018**, *9*.
- (66) Lin, F. D.; Bachman, B. F.; Boettcher, S. W. Impact of Electrocatalyst Activity and Ion Permeability on Water-Splitting Photoanodes. *J. Phys. Chem. Lett.* **2015**, *6* (13), 2427-2433.
- (67) Bard, A. J.; Faulkner, L. R.; Leddy, J.; Zoski, C. G. *Electrochemical Methods: Fundamentals and Applications*. Wiley New York: 1980; Vol. 2.
- (68) Kenney, M. J.; Gong, M.; Li, Y. G.; Wu, J. Z.; Feng, J.; Lanza, M.; Dai, H. J. High-Performance Silicon Photoanodes Passivated with Ultrathin Nickel Films for Water Oxidation. *Science* **2013**, *342* (6160), 836-840.
- (69) Han, T. T.; Shi, Y. Y.; Song, X. X.; Mio, A.; Valenti, L.; Hui, F.; Privitera, S.; Lombardo, S.; Lanza, M. Ageing Mechanisms of Highly Active and Stable Nickel-Coated Silicon Photoanodes for Water Splitting. *J. Mater. Chem. A* **2016**, *4* (21), 8053-8060.
- (70) Klahr, B. M.; Martinson, A. B. F.; Hamann, T. W. Photoelectrochemical Investigation of Ultrathin Film Iron Oxide Solar Cells Prepared by Atomic Layer Deposition. *Langmuir* **2011**, *27* (1), 461-468.
- (71) Martinson, A. B. F.; DeVries, M. J.; Libera, J. A.; Christensen, S. T.; Hupp, J. T.; Pellin, M. J.; Elam, J. W. Atomic Layer Deposition of Fe<sub>2</sub>O<sub>3</sub> Using Ferrocene and Ozone. *J. Phys. Chem. C* **2011**, *115* (10), 4333-4339.
- (72) Kim, T. W.; Choi, K. S. Nanoporous BiVO<sub>4</sub> Photoanodes with Dual-Layer Oxygen Evolution Catalysts for Solar Water Splitting. *Science* **2014**, *343* (6174), 990-994.
- (73) Shi, X. J.; Choi, Y.; Zhang, K.; Kwon, J.; Kim, D. Y.; Lee, J. K.; Oh, S. H.; Kim, J. K.; Park, J. H. Efficient Photoelectrochemical Hydrogen Production from Bismuth Vanadate-Decorated Tungsten Trioxide Helix Nanostructures. *Nat. Commun.* **2014**, *5*, 4775.
- (74) Zachaus, C.; Abdi, F. F.; Peter, L. M.; van de Krol, R. Photocurrent of BiVO<sub>4</sub> Is Limited by Surface Recombination, Not Surface Catalysis. *Chem. Sci.* **2017**, *8* (5), 3712-3719.
- (75) Warren, S. C.; Voitchovsky, K.; Dotan, H.; Leroy, C. M.; Cornuz, M.; Stellacci, F.; Hebert, C.; Rothschild, A.; Gratzel, M. Identifying Champion Nanostructures for Solar Water-Splitting. *Nat. Mater.* **2013**, *12* (9), 842-849.

- (76) Nellist, M. R.; Qiu, J.; Laskowski, F. A. L.; Toma, F. M.; Boettcher, S. W. Potential-Sensing Electrochemical Afm Shows CoPi Is a Hole Collector and Oxygen Evolution Catalyst on BiVO<sub>4</sub> Water-Splitting Photoanodes. *ACS Energy Lett.* **2018**.
- (77) Lee, D.; Kvit, A.; Choi, K.-S. Enabling Solar Water Oxidation by BiVO<sub>4</sub> Photoanodes in Basic Media. *Chem. Mater.* **2018**, *30* (14), 4704-4712.
- (78) Klahr, B.; Gimenez, S.; Fabregat-Santiago, F.; Bisquert, J.; Hamann, T. W. Electrochemical and Photoelectrochemical Investigation of Water Oxidation with Hematite Electrodes. *Energy Environ. Sci.* **2012**, *5* (6), 7626-7636.
- (79) Gerling, L. G.; Mahato, S.; Morales-Vilches, A.; Masmitja, G.; Ortega, P.; Voz, C.; Alcubilla, R.; Puigdollers, J. Transition Metal Oxides as Hole-Selective Contacts in Silicon Heterojunctions Solar Cells. *Sol. Energy Mater. Sol. Cells* **2016**, *145*, 109-115.
- (80) Battaglia, C.; de Nicolas, S. M.; De Wolf, S.; Yin, X. T.; Zheng, M.; Ballif, C.; Javey, A. Silicon Heterojunction Solar Cell with Passivated Hole Selective MoO<sub>x</sub> Contact. *Appl. Phys. Lett.* **2014**, *104* (11), 113902.
- (81) Boix, P. P.; Ajuria, J.; Etxebarria, I.; Pacios, R.; Garcia-Belmonte, G.; Bisquert, J. Role of ZnO Electron-Selective Layers in Regular and Inverted Bulk Heterojunction Solar Cells. *J. Phys. Chem. Lett.* **2011**, *2* (5), 407-411.
- (82) Geissbuhler, J.; Werner, J.; de Nicolas, S. M.; Barraud, L.; Hessler-Wyser, A.; Despeisse, M.; Nicolay, S.; Tomasi, A.; Niesen, B.; De Wolf, S.; Ballif, C. 22.5% Efficient Silicon Heterojunction Solar Cell with Molybdenum Oxide Hole Collector. *Appl. Phys. Lett.* **2015**, *107* (8), 081601.
- (83) Roe, E. T.; Egelhofer, K. E.; Lonergan, M. C. Limits of Contact Selectivity/Recombination on the Open-Circuit Voltage of a Photovoltaic. *ACS Appl. Energy Mater.* **2018**, *1* (3), 1037-1046.
- (84) Peter, L. M.; Li, J.; Peat, R. Surface Recombination at Semiconductor Electrodes: 1. Transient and Steady-State Photocurrents. *J. Electroanal. Chem.* **1984**, *165* (1-2), 29-40.
- (85) Shewchun, J.; Singh, R.; Green, M. A. Theory of Metal-Insulator-Semiconductor Solar-Cells. *J. Appl. Phys.* **1977**, *48* (2), 765-770.

## B. References for Paper B

Style: Accounts of Chemical Research

- (1) Peter, L. M.; Wijayantha, K. G. U. Photoelectrochemical Water Splitting at Semiconductor Electrodes: Fundamental Problems and New Perspectives. *ChemPhysChem* **2014**, *15*, 1983-1995.
- (2) Gamelin, D. R. Water Splitting: Catalyst or Spectator? *Nat. Chem.* **2012**, *4*, 965-967.
- (3) Liu, R.; Zheng, Z.; Spurgeon, J.; Yang, X. G. Enhanced Photoelectrochemical Water-Splitting Performance of Semiconductors by Surface Passivation Layers. *Energy Environ. Sci.* **2014**, *7*, 2504-2517.
- (4) Zhong, D. K.; Choi, S.; Gamelin, D. R. Near-Complete Suppression of Surface Recombination in Solar Photoelectrolysis by “Co-Pi” Catalyst-Modified W:BiVO<sub>4</sub>. *J. Am. Chem. Soc.* **2011**, *133*, 18370-18377.
- (5) Barroso, M.; Mesa, C. A.; Pendlebury, S. R.; Cowan, A. J.; Hisatomi, T.; Sivula, K.; Gratzel, M.; Klug, D. R.; Durrant, J. R. Dynamics of Photogenerated Holes in Surface Modified  $\alpha$ -Fe<sub>2</sub>O<sub>3</sub> Photoanodes for Solar Water Splitting. *Proc. Natl. Acad. Sci. U. S. A.* **2012**, *109*, 15640-15645.
- (6) Le Formal, F.; Pendlebury, S. R.; Cornuz, M.; Tilley, S. D.; Gratzel, M.; Durrant, J. R. Back Electron-Hole Recombination in Hematite Photoanodes for Water Splitting. *J. Am. Chem. Soc.* **2014**, *136*, 2564-2574.
- (7) Trotochaud, L.; Mills, T. J.; Boettcher, S. W. An Optocatalytic Model for Semiconductor-Catalyst Water-Splitting Photoelectrodes Based on In Situ Optical Measurements on Operational Catalysts. *J. Phys. Chem. Lett.* **2013**, *4*, 931-935.
- (8) Du, C.; Yang, X.; Mayer, M. T.; Hoyt, H.; Xie, J.; McMahon, G.; Bischofing, G.; Wang, D. Hematite-Based Water Splitting with Low Turn-On Voltages. *Angew. Chem., Int. Ed.* **2013**, *52*, 12692-12695.
- (9) Young, K. M. H.; Hamann, T. W. Enhanced Photocatalytic Water Oxidation Efficiency with Ni(OH)<sub>2</sub> Catalysts Deposited on  $\alpha$ -Fe<sub>2</sub>O<sub>3</sub> via ALD. *Chem. Commun.* **2014**, *50*, 8727-8730.
- (10) Carroll, G. M.; Zhong, D. K.; Gamelin, D. R. Mechanistic Insights into Solar Water Oxidation by Cobalt-Phosphate-Modified  $\alpha$ -Fe<sub>2</sub>O<sub>3</sub> Photoanodes. *Energy Environ. Sci.* **2015**, *8*, 577-584.
- (11) Kim, T. W.; Choi, K. S. Nanoporous BiVO<sub>4</sub> Photoanodes with Dual-Layer Oxygen Evolution Catalysts for Solar Water Splitting. *Science* **2014**, *343*, 990-994.
- (12) Huang, Z.; Lin, Y.; Xiang, X.; Rodriguez-Cordoba, W.; McDonald, K. J.; Hagen, K. S.; Choi, K.-S.; Brunschwig, B. S.; Musaev, D. G.; Hill, C. L.; Wang, D.; Lian, T. In Situ Probe

of Photocurrent Dynamics in Water-Splitting Hematite ( $\alpha$ -Fe<sub>2</sub>O<sub>3</sub>) Electrodes. *Energy Environ. Sci.* **2012**, *5*, 8923-8926.

(13) Klahr, B.; Gimenez, S.; Fabregat-Santiago, F.; Bisquert, J.; Hamann, T. W. Photoelectrochemical and Impedance Spectroscopic Investigation of Water Oxidation with "Co-Pi"-Coated Hematite Electrodes. *J. Am. Chem. Soc.* **2012**, *134*, 16693-16700.

(14) Walter, M. G.; Warren, E. L.; McKone, J. R.; Boettcher, S. W.; Mi, Q.; Santori, E. A.; Lewis, N. S. Solar Water Splitting Cells. *Chem. Rev.* **2010**, *110*, 6446-6473.

(15) Sivula, K. Metal Oxide Photoelectrodes for Solar Fuel Production, Surface Traps, and Catalysis. *J. Phys. Chem. Lett.* **2013**, *4*, 1624-1633.

(16) Hu, S.; Lewis, N. S.; Ager, J. W.; Yang, J.; McKone, J. R.; Strandwitz, N. C. Thin-Film Materials for the Protection of Semiconducting Photoelectrodes in Solar-Fuel Generators. *J. Phys. Chem. C* **2015**, *119*, 24201-24228.

(17) Lin, F.; Bachman, B. F.; Boettcher, S. W. Impact of Electrocatalyst Activity and Ion Permeability on Water-Splitting Photoanodes. *J. Phys. Chem. Lett.* **2015**, *6*, 2427-2433.

(18) Burke, M. S.; Enman, L. J.; Batchellor, A. S.; Zou, S.; Boettcher, S. W. Oxygen Evolution Reaction Electrocatalysis on Transition Metal Oxides and (Oxy)hydroxides: Activity Trends and Design Principles. *Chem. Mater.* **2015**, *27*, 7549-7558.

(19) Trotochaud, L.; Ranney, J. K.; Williams, K. N.; Boettcher, S. W. Solution-Cast Metal Oxide Thin Film Electrocatalysts for Oxygen Evolution. *J. Am. Chem. Soc.* **2012**, *134*, 17253-17261.

(20) Louie, M. W.; Bell, A. T. An Investigation of Thin-Film Ni-Fe Oxide Catalysts for the Electrochemical Evolution of Oxygen. *J. Am. Chem. Soc.* **2013**, *135*, 12329-12337.

(21) Friebel, D.; Louie, M. W.; Bajdich, M.; Sanwald, K. E.; Cai, Y.; Wise, A. M.; Cheng, M.-J.; Sokaras, D.; Weng, T.-C.; Alonso-Mori, R.; Davis, R. C.; Bargar, J. R.; Nørskov, J. K.; Nilsson, A.; Bell, A. T. Identification of Highly Active Fe Sites in (Ni,Fe)OOH for Electrocatalytic Water Splitting. *J. Am. Chem. Soc.* **2015**, *137*, 1305-1313.

(22) Trotochaud, L.; Young, S. L.; Ranney, J. K.; Boettcher, S. W. Nickel-Iron Oxyhydroxide Oxygen-Evolution Electrocatalysts: The Role of Intentional and Incidental Iron Incorporation. *J. Am. Chem. Soc.* **2014**, *136*, 6744-6753.

(23) Batchellor, A. S.; Boettcher, S. W. Pulse-Electrodeposited Ni-Fe (Oxy)hydroxide Oxygen Evolution Electrocatalysts with High Geometric and Intrinsic Activities at Large Mass Loadings. *ACS Catal.* **2015**, *5*, 6680-6689.

(24) Burke, M. S.; Kast, M. G.; Trotochaud, L.; Smith, A. M.; Boettcher, S. W. Cobalt-Iron (Oxy)hydroxide Oxygen Evolution Electrocatalysts: The Role of Structure and Composition on Activity, Stability, and Mechanism. *J. Am. Chem. Soc.* **2015**, *137*, 3638-3648.

(25) Klingan, K.; Ringleb, F.; Zaharieva, I.; Heidkamp, J.; Chernev, P.; Gonzalez-Flores, D.; Risch, M.; Fischer, A.; Dau, H. Water Oxidation by Amorphous Cobalt-Based Oxides: Volume Activity and Proton Transfer to Electrolyte Bases. *ChemSusChem* **2014**, *7*, 1301-1310.

- (26) Bediako, D. K.; Lassalle-Kaiser, B.; Surendranath, Y.; Yano, J.; Yachandra, V. K.; Nocera, D. G. Structure–Activity Correlations in a Nickel–Borate Oxygen Evolution Catalyst. *J. Am. Chem. Soc.* **2012**, *134*, 6801-6809.
- (27) Farrow, C. L.; Bediako, D. K.; Surendranath, Y.; Nocera, D. G.; Billinge, S. J. L. Intermediate-Range Structure of Self-Assembled Cobalt-Based Oxygen-Evolving Catalyst. *J. Am. Chem. Soc.* **2013**, *135*, 6403-3406.
- (28) Simon, P.; Gogotsi, Y. Materials for Electrochemical Capacitors. *Nat. Mater.* **2008**, *7*, 845-854.
- (29) McKeown, D. A.; Hagans, P. L.; Carette, L. P. L.; Russell, A. E.; Swider, K. E.; Rolison, D. R. Structure of Hydrous Ruthenium Oxides: Implications for Charge Storage. *J. Phys. Chem. B* **1999**, *103*, 4825-4832.
- (30) Nielander, A. C.; Shaner, M. R.; Papadantonakis, K. M.; Francis, S. A.; Lewis, N. S. A taxonomy for solar fuels generators. *Energy Environ. Sci.* **2015**, *8*, 16-25.
- (31) Bansal, A.; Tan, M. X.; Tufts, B. J.; Lewis, N. S. Distinguishing Between Buried Semiconductor/Metal Contacts and Hybrid Semiconductor/Metal/Liquid Contacts at n-Gallium Arsenide/Potassium Hydroxide-Selenium ( $\text{Se}^{-2}$ )(aq) Junctions. *J. Phys. Chem.* **1993**, *97*, 7309-7315.
- (32) Tilley, S. D.; Cornuz, M.; Sivula, K.; Graetzel, M. Light-Induced Water Splitting with Hematite: Improved Nanostructure and Iridium Oxide Catalysis. *Angew. Chem. Int. Ed.* **2010**, *49*, 6405-6408.
- (33) Lin, F.; Walker, E. M.; Lonergan, M. C. Photochemical Doping of an Adaptive Mix-Conducting p-n Junction. *J. Phys. Chem. Lett.* **2010**, *1*, 720-723.
- (34) Reiss, H. Photocharacteristics for Electrolyte-Semiconductor Junctions. *J. Electrochem. Soc.* **1978**, *125*, 937-949.
- (35) Miller, E. L.; Rocheleau, R. E.; Deng, X. M. Design Considerations for a Hybrid Amorphous Silicon/Photoelectrochemical Multijunction Cell for Hydrogen Production. *Int. J. Hydrogen Energy* **2003**, *28*, 615-623.
- (36) Surendranath, Y.; Bediako, D. K.; Nocera, D. G. Interplay of Oxygen-Evolution Kinetics and Photovoltaic Power Curves on the Construction of Artificial Leaves. *Proc. Natl. Acad. Sci. U. S. A.* **2012**, *109*, 15617-15621.
- (37) Winkler, M. T.; Cox, C. R.; Nocera, D. G.; Buonassisi, T. Modeling Integrated Photovoltaic-Electrochemical Devices Using Steady-state Equivalent Circuits. *Proc. Natl. Acad. Sci. U. S. A.* **2013**, *110*, E1076-E1082.
- (38) Reece, S. Y.; Hamel, J. A.; Sung, K.; Jarvi, T. D.; Esswein, A. J.; Pijpers, J. J. H.; Nocera, D. G. Wireless Solar Water Splitting Using Silicon-Based Semiconductors and Earth-Abundant Catalysts. *Science* **2011**, *334*, 645-648.
- (39) Mills, T. J.; Lin, F.; Boettcher, S. W. Theory and Simulations of Electrocatalyst-Coated Semiconductor Electrodes for Solar Water Splitting. *Phys. Rev. Lett.* **2014**, *112*, 148304.



- (40) Bard, A. J.; Fan, F.-R. F.; Gioda, A. S.; Nagasubramanian, G.; White, H. S. On the Role of Surface States in Semiconductor Electrode Photoelectrochemical Cells. *Faraday Discuss. Chem. Soc.* **1980**, *70*, 19-31.
- (41) Lin, F.; Boettcher, S. W. Adaptive Semiconductor/Electrocatalyst Junctions in Water-Splitting Photoanodes. *Nat. Mater.* **2014**, *13*, 81-86.
- (42) Barroso, M.; Cowan, A. J.; Pendlebury, S. R.; Gratzel, M.; Klug, D. R.; Durrant, J. R. The Role of Cobalt Phosphate in Enhancing the Photocatalytic Activity of  $\alpha$ -Fe<sub>2</sub>O<sub>3</sub> Toward Water Oxidation. *J. Am. Chem. Soc.* **2011**, *133*, 14868-14871.
- (43) Klahr, B.; Gimenez, S.; Fabregat-Santiago, F.; Hamann, T.; Bisquert, J. Water Oxidation at Hematite Photoelectrodes: The Role of Surface States. *J. Am. Chem. Soc.* **2012**, *134*, 4294-4302.
- (44) Bard, A. J.; Bocarsly, A. B.; Fan, F. R. F.; Walton, E. G.; Wrighton, M. S. The Concept of Fermi Level Pinning at Semiconductor/Liquid Junctions. Consequences for Energy Conversion Efficiency and Selection of Useful Solution Redox Couples in Solar Devices. *J. Am. Chem. Soc.* **1980**, *102*, 3671-3677.
- (45) Gerischer, H. Electron-Transfer Kinetics of Redox Reactions at the Semiconductor Electrolyte Contact - A New Approach. *J. Phys. Chem.* **1991**, *95*, 1356-1359.
- (46) Vanmaekelbergh, D. Direct and Surface-state Mediated Electron Transfer at Semiconductor/Electrolyte Junctions. 1. A Comparison of Steady-state Results. *Electrochim. Acta* **1997**, *42*, 1121-1134.
- (47) Peter, L. M. Dynamic Aspects of Semiconductor Photoelectrochemistry. *Chem. Rev.* **1990**, *90*, 753-769.
- (48) Peter, L. M.; Li, J.; Peat, R. Surface Recombination at Semiconductor Electrodes. 1. Transient and Steady-state Photocurrents. *J. Electroanal. Chem.* **1984**, *165*, 29-40.
- (49) Nishida, M. A Theoretical Treatment of Charge-Transfer via Surface States at a Semiconductor-Electrolyte Interface - Analysis of the Water Photoelectrolysis Process. *J. Appl. Phys.* **1980**, *51*, 1669-1675.
- (50) Carroll, G. M.; Gamelin, D. R. Kinetic Analysis of Photoelectrochemical Water Oxidation by Mesoporous Co-Pi/ $\alpha$ -Fe<sub>2</sub>O<sub>3</sub> Photoanodes. *J. Mat. Chem. A* **2016**, *4*, 2986-2994.
- (51) Hu, S.; Shaner, M. R.; Beardslee, J. A.; Lichterman, M.; Brunschwig, B. S.; Lewis, N. S. Amorphous TiO<sub>2</sub> Coatings Stabilize Si, GaAs, and GaP Photoanodes for Efficient Water Oxidation. *Science* **2014**, *344*, 1005-1009.
- (52) Smith, W. A.; Sharp, I. D.; Strandwitz, N. C.; Bisquert, J. Interfacial Band-Edge Energetics for Solar Fuels Production. *Energy Environ. Sci.* **2015**, *8*, 2851-2862.
- (53) Würfel, P.: *Physics of Solar Cells*; Wiley: Weinheim, 2009.



### C. References for Paper C

Style: Sustainable Energy & Fuels

- (1) Walter, M. G.; Warren, E. L.; McKone, J. R.; Boettcher, S. W.; Mi, Q. X.; Santori, E. A.; Lewis, N. S. Solar Water Splitting Cells. *Chem Rev* **2010**, *110*, 6446-6473.
- (2) Ahmed, S. M.; Leduc, J.; Haller, S. F. Photoelectrochemical and Impedance Characteristics of Specular Hematite. 1. Photoelectrochemical, Parallel Conductance, and Trap Rate Studies. *J Phys Chem-Us* **1988**, *92*, 6655-6660.
- (3) Barroso, M.; Mesa, C. A.; Pendlebury, S. R.; Cowan, A. J.; Hisatomi, T.; Sivula, K.; Gratzel, M.; Klug, D. R.; Durrant, J. R. Dynamics of photogenerated holes in surface modified alpha-Fe<sub>2</sub>O<sub>3</sub> photoanodes for solar water splitting. *P Natl Acad Sci USA* **2012**, *109*, 15640-15645.
- (4) Dareedwards, M. P.; Goodenough, J. B.; Hamnett, A.; Trelvellick, P. R. Electrochemistry and Photoelectrochemistry of Iron(III) Oxide. *J Chem Soc Farad T 1* **1983**, *79*, 2027-2041.
- (5) Glasscock, J. A.; Barnes, P. R. F.; Plumb, I. C.; Savvides, N. Enhancement of photoelectrochemical hydrogen production from hematite thin films by the introduction of Ti and Si. *J Phys Chem C* **2007**, *111*, 16477-16488.
- (6) Hisatomi, T.; Le Formal, F.; Cornuz, M.; Brillet, J.; Tetreault, N.; Sivula, K.; Gratzel, M. Cathodic shift in onset potential of solar oxygen evolution on hematite by 13-group oxide overlayers. *Energ Environ Sci* **2011**, *4*, 2512-2515.
- (7) Horowitz, G. Capacitance Voltage Measurements and Flat-Band Potential Determination on Zr-Doped Alpha-Fe<sub>2</sub>O<sub>3</sub> Single-Crystal Electrodes. *J Electroanal Chem* **1983**, *159*, 421-436.
- (8) Iwanski, P.; Curran, J. S.; Gissler, W.; Memming, R. The Photoelectrochemical Behavior of Ferric-Oxide in the Presence of Redox Reagents. *J Electrochem Soc* **1981**, *128*, 2128-2133.
- (9) Le Formal, F.; Sivula, K.; Gratzel, M. The Transient Photocurrent and Photovoltage Behavior of a Hematite Photoanode under Working Conditions and the Influence of Surface Treatments. *J Phys Chem C* **2012**, *116*, 26707-26720.
- (10) Leduc, J.; Ahmed, S. M. Photoelectrochemical and Impedance Characteristics of Specular Hematite. 2. Deep Bulk Traps in Specular Hematite at Small Alternating-Current Frequencies. *J Phys Chem-Us* **1988**, *92*, 6661-6665.
- (11) Leng, W. H.; Zhang, Z.; Zhang, J. Q.; Cao, C. N. Investigation of the kinetics of a TiO<sub>2</sub> photoelectrocatalytic reaction involving charge transfer and recombination through surface states by electrochemical impedance spectroscopy. *J Phys Chem B* **2005**, *109*, 15008-15023.
- (12) Sanchez, C.; Sieber, K. D.; Somorjai, G. A. The Photoelectrochemistry of Niobium Doped Alpha-Fe<sub>2</sub>O<sub>3</sub>. *J Electroanal Chem* **1988**, *252*, 269-290.
- (13) Zandi, O.; Hamann, T. W. Enhanced Water Splitting Efficiency Through Selective Surface State Removal. *J Phys Chem Lett* **2014**, *5*, 1522-1526.

- (14) Thorne, J. E.; Jang, J. W.; Liu, E. Y.; Wang, D. W. Understanding the origin of photoelectrode performance enhancement by probing surface kinetics. *Chem Sci* **2016**, *7*, 3347-3354.
- (15) Zhong, D. K.; Choi, S.; Gamelin, D. R. Near-Complete Suppression of Surface Recombination in Solar Photoelectrolysis by "Co-Pi" Catalyst-Modified W:BiVO<sub>4</sub>. *J Am Chem Soc* **2011**, *133*, 18370-18377.
- (16) Zachäus, C.; Abdi, F. F.; Peter, L. M.; Van De Krol, R. Photocurrent of BiVO<sub>4</sub> is limited by surface recombination, not surface catalysis. *Chem Sci* **2017**, *8*, 3712-3719.
- (17) Carroll, G. M.; Zhong, D. K.; Gamelin, D. R. Mechanistic insights into solar water oxidation by cobalt-phosphate-modified alpha-Fe<sub>2</sub>O<sub>3</sub> photoanodes. *Energ Environ Sci* **2015**, *8*, 577-584.
- (18) Zhong, D. K.; Gamelin, D. R. Photoelectrochemical Water Oxidation by Cobalt Catalyst ("Co-Pi")/alpha-Fe<sub>2</sub>O<sub>3</sub> Composite Photoanodes: Oxygen Evolution and Resolution of a Kinetic Bottleneck. *J Am Chem Soc* **2010**, *132*, 4202-4207.
- (19) Barroso, M.; Cowan, A. J.; Pendlebury, S. R.; Gratzel, M.; Klug, D. R.; Durrant, J. R. The Role of Cobalt Phosphate in Enhancing the Photocatalytic Activity of alpha-Fe<sub>2</sub>O<sub>3</sub> toward Water Oxidation. *J Am Chem Soc* **2011**, *133*, 14868-14871.
- (20) Gamelin, D. R. WATER SPLITTING Catalyst or spectator? *Nat Chem* **2012**, *4*, 965-967.
- (21) de Respinis, M.; Joya, K. S.; De Groot, H. J. M.; D'Souza, F.; Smith, W. A.; van de Krol, R.; Dam, B. Solar Water Splitting Combining a BiVO<sub>4</sub> Light Absorber with a Ru-Based Molecular Cocatalyst. *J Phys Chem C* **2015**, *119*, 7275-7281.
- (22) Liu, R.; Zheng, Z.; Spurgeon, J.; Yang, X. G. Enhanced photoelectrochemical water-splitting performance of semiconductors by surface passivation layers. *Energ Environ Sci* **2014**, *7*, 2504-2517.
- (23) Klahr, B.; Gimenez, S.; Fabregat-Santiago, F.; Bisquert, J.; Hamann, T. W. Photoelectrochemical and Impedance Spectroscopic Investigation of Water Oxidation with "Co-Pi"-Coated Hematite Electrodes. *J Am Chem Soc* **2012**, *134*, 16693-16700.
- (24) Peter, L. M. Dynamic Aspects of Semiconductor Photoelectrochemistry. *Chem Rev* **1990**, *90*, 753-769.
- (25) Steier, L.; Herraiz-Cardona, I.; Gimenez, S.; Fabregat-Santiago, F.; Bisquert, J.; Tilley, S. D.; Gratzel, M. Understanding the Role of Underlayers and Overlayers in Thin Film Hematite Photoanodes. *Adv Funct Mater* **2014**, *24*, 7681-7688.
- (26) Tamirat, A. G.; Rick, J.; Dubale, A. A.; Su, W. N.; Hwang, B. J. Using hematite for photoelectrochemical water splitting: a review of current progress and challenges. *Nanoscale Horiz* **2016**, *1*, 243-267.
- (27) Gurudayal; Chee, P. M.; Boix, P. P.; Ge, H.; Fang, Y. N.; Barber, J.; Wong, L. H. Core-Shell Hematite Nanorods: A Simple Method To Improve the Charge Transfer in the Photoanode for Photoelectrochemical Water Splitting. *Acs Appl Mater Inter* **2015**, *7*, 6852-6859.

- (28) Gurudayal; Chiam, S. Y.; Kumar, M. H.; Bassi, P. S.; Seng, H. L.; Barber, J.; Wong, L. H. Improving the Efficiency of Hematite Nanorods for Photoelectrochemical Water Splitting by Doping with Manganese. *Acs Appl Mater Inter* **2014**, *6*, 5852-5859.
- (29) Kim, D. W.; Riha, S. C.; DeMarco, E. J.; Martinson, A. B.; Farha, O. K.; Hupp, J. T. Greenlighting photoelectrochemical oxidation of water by iron oxide. *ACS nano* **2014**, *8*, 12199-12207.
- (30) Klahr, B.; Gimenez, S.; Fabregat-Santiago, F.; Bisquert, J.; Hamann, T. W. Electrochemical and photoelectrochemical investigation of water oxidation with hematite electrodes. *Energ Environ Sci* **2012**, *5*, 7626-7636.
- (31) Subramanian, A.; Annamalai, A.; Lee, H. H.; Choi, S. H.; Ryu, J.; Park, J. H.; Jang, J. S. Trade-off between Zr Passivation and Sn Doping on Hematite Nanorod Photoanodes for Efficient Solar Water Oxidation: Effects of a ZrO<sub>2</sub> Underlayer and FTO Deformation. *Acs Appl Mater Inter* **2016**, *8*, 19428-19437.
- (32) Wang, Z. L.; Liu, G. J.; Ding, C. M.; Chen, Z.; Zhang, F. X.; Shi, J. Y.; Li, C. Synergetic Effect of Conjugated Ni(OH)<sub>2</sub>/IrO<sub>2</sub> Cocatalyst on Titanium-Doped Hematite Photoanode for Solar Water Splitting. *J Phys Chem C* **2015**, *119*, 19607-19612.
- (33) Cibrev, D.; Tallarida, M.; Das, C.; Lana-Villarreal, T.; Schmeisser, D.; Gomez, R. New insights into water photooxidation on reductively pretreated hematite photoanodes. *Phys Chem Chem Phys* **2017**, *19*, 21807-21817.
- (34) Cordova, I. A.; Peng, Q.; Ferrall, I. L.; Rieth, A. J.; Hoertz, P. G.; Glass, J. T. Enhanced photoelectrochemical water oxidation via atomic layer deposition of TiO<sub>2</sub> on fluorine-doped tin oxide nanoparticle films. *Nanoscale* **2015**, *7*, 12226-12226.
- (35) Courtin, E.; Baldinozzi, G.; Sougrati, M. T.; Stievano, L.; Sanchez, C.; Laberty-Robert, C. New Fe<sub>2</sub>TiO<sub>5</sub>-based nanoheterostructured mesoporous photoanodes with improved visible light photoresponses. *J Mater Chem A* **2014**, *2*, 6567-6577.
- (36) Dharmadasa, R.; Lavery, B.; Dharmadasa, I. M.; Druffel, T. Intense Pulsed Light Treatment of Cadmium Telluride Nanoparticle-Based Thin Films. *Acs Appl Mater Inter* **2014**, *6*, 5034-5040.
- (37) Kment, S.; Hubicka, Z.; Krysa, J.; Sekora, D.; Zlamal, M.; Olejnicek, J.; Cada, M.; Ksirova, P.; Remes, Z.; Schmuki, P.; Schubert, E.; Zboril, R. On the improvement of PEC activity of hematite thin films deposited by high-power pulsed magnetron sputtering method. *Appl Catal B-Environ* **2015**, *165*, 344-350.
- (38) Le Formal, F.; Pendlebury, S. R.; Cornuz, M.; Tilley, S. D.; Gratzel, M.; Durrant, J. R. Back Electron-Hole Recombination in Hematite Photoanodes for Water Splitting. *J Am Chem Soc* **2014**, *136*, 2564-2574.
- (39) Li, S. P.; Zhang, P.; Song, X. F.; Gao, L. Ultrathin Ti-doped hematite photoanode by pyrolysis of ferrocene. *Int J Hydrogen Energ* **2014**, *39*, 14596-14603.
- (40) Li, T. F.; He, J. F.; Pena, B.; Berlinguette, C. P. Curing BiVO<sub>4</sub> Photoanodes with Ultraviolet Light Enhances Photoelectrocatalysis. *Angew Chem Int Edit* **2016**, *55*, 1769-1772.

- (41) Li, Z. S.; Feng, J. Y.; Yan, S. C.; Zou, Z. G. Solar fuel production: Strategies and new opportunities with nanostructures. *Nano Today* **2015**, *10*, 468-486.
- (42) Liu, Y.; Li, J.; Li, W. Z.; Liu, Q.; Yang, Y. H.; Li, Y. M.; Chen, Q. Y. Enhanced photoelectrochemical performance of WO<sub>3</sub> film with HfO<sub>2</sub> passivation layer. *Int J Hydrogen Energ* **2015**, *40*, 8856-8863.
- (43) Rovelli, L.; Tilley, S. D.; Sivula, K. Optimization and Stabilization of Electrodeposited Cu<sub>2</sub>ZnSnS<sub>4</sub> Photocathodes for Solar Water Reduction. *Acs Appl Mater Inter* **2013**, *5*, 8018-8024.
- (44) Yang, J. S.; Lin, W. H.; Lin, C. Y.; Wang, B. S.; Wu, J. J. n-Fe<sub>2</sub>O<sub>3</sub> to N<sup>+</sup>-TiO<sub>2</sub> Heterojunction Photoanode for Photoelectrochemical Water Oxidation. *Acs Appl Mater Inter* **2015**, *7*, 13314-13321.
- (45) Ahmed, M. G.; Kretschmer, I. E.; Kandiel, T. A.; Ahmed, A. Y.; Rashwan, F. A.; Bahnemann, D. W. A Facile Surface Passivation of Hematite Photoanodes with TiO<sub>2</sub> Overlayers for Efficient Solar Water Splitting. *Acs Appl Mater Inter* **2015**, *7*, 24053-24062.
- (46) Fu, Z. W.; Jiang, T. F.; Zhang, L. J.; Liu, B. K.; Wang, D. J.; Wang, L. L.; Xie, T. F. Surface treatment with Al<sup>3+</sup> on a Ti-doped alpha-Fe<sub>2</sub>O<sub>3</sub> nanorod array photoanode for efficient photoelectrochemical water splitting. *J Mater Chem A* **2014**, *2*, 13705-13712.
- (47) Ma, Y. M.; Pendlebury, S. R.; Reynal, A.; Le Formal, F.; Durrant, J. R. Dynamics of photogenerated holes in undoped BiVO<sub>4</sub> photoanodes for solar water oxidation. *Chem Sci* **2014**, *5*, 2964-2973.
- (48) Yang, T. Y.; Kang, H. Y.; Jin, K.; Park, S.; Lee, J. H.; Sim, U.; Jeong, H. Y.; Joo, Y. C.; Nam, K. T. An iron oxide photoanode with hierarchical nanostructure for efficient water oxidation. *J Mater Chem A* **2014**, *2*, 2297-2305.
- (49) Ding, Q.; Meng, F.; English, C. R.; Caban-Acevedo, M.; Shearer, M. J.; Liang, D.; Daniel, A. S.; Hamers, R. J.; Jin, S. Efficient Photoelectrochemical Hydrogen Generation Using Heterostructures of Si and Chemically Exfoliated Metallic MoS<sub>2</sub>. *J Am Chem Soc* **2014**, *136*, 8504-8507.
- (50) Moir, J. W.; Sackville, E. V.; Hintermair, U.; Ozin, G. A. Kinetics versus Charge Separation: Improving the Activity of Stoichiometric and Non-Stoichiometric Hematite Photoanodes Using a Molecular Iridium Water Oxidation Catalyst. *J Phys Chem C* **2016**, *120*, 12999-13012.
- (51) Wang, J. J.; Hu, Y. L.; Toth, R.; Fortunato, G.; Braun, A. A facile nonpolar organic solution process of a nanostructured hematite photoanode with high efficiency and stability for water splitting. *J Mater Chem A* **2016**, *4*, 2821-2825.
- (52) Ding, C. M.; Shi, J. Y.; Wang, Z. L.; Li, C. Photoelectrocatalytic Water Splitting: Significance of Cocatalysts, Electrolyte, and Interfaces. *Acs Catal* **2017**, *7*, 675-688.
- (53) Du, C.; Wang, J.; Liu, X.; Yang, J.; Cao, K.; Wen, Y. W.; Chen, R.; Shan, B. Ultrathin CoO<sub>x</sub>-modified hematite with low onset potential for solar water oxidation. *Phys Chem Chem Phys* **2017**, *19*, 14178-14184.

- (54) Wang, T. H.; Hung, H. T.; Cheng, Y. R.; Huang, M. C.; Hsieh, Y. K.; Wang, C. F. Understanding the role of phosphate in the photoelectrochemical performance of cobaltphosphate/hematite electrode systems. *Rsc Adv* **2016**, *6*, 28236-28247.
- (55) Young, K. M. H.; Hamann, T. W. Enhanced photocatalytic water oxidation efficiency with Ni(OH)<sub>2</sub> catalysts deposited on alpha-Fe<sub>2</sub>O<sub>3</sub> via ALD. *Chem Commun* **2014**, *50*, 8727-8730.
- (56) Shi, X. J.; Zhang, K.; Park, J. H. Understanding the positive effects of (Co-Pi) co-catalyst modification in inverse-opal structured alpha-Fe<sub>2</sub>O<sub>3</sub>-based photoelectrochemical cells. *Int J Hydrogen Energ* **2013**, *38*, 12725-12732.
- (57) Eftekharinia, B.; Moshaii, A.; Dabirian, A.; Vayghan, N. S. Optimization of charge transport in a Co-Pi modified hematite thin film produced by scalable electron beam evaporation for photoelectrochemical water oxidation. *J Mater Chem A* **2017**, *5*, 3412-3424.
- (58) Bu, Q. J.; Li, S.; Cao, S.; Zhao, Q. D.; Chen, Y.; Wang, D. J.; Xie, T. F. A Ni<sub>2</sub>P modified Ti<sup>4+</sup> doped Fe<sub>2</sub>O<sub>3</sub> photoanode for efficient solar water oxidation by promoting hole injection. *Dalton T* **2017**, *46*, 10549-10552.
- (59) Carbonare, N. D.; Cristino, V.; Berardi, S.; Carli, S.; Argazzi, R.; Caramori, S.; Meda, L.; Tacca, A.; Bignozzi, C. A. Hematite Photoanodes Modified with an FeIII Water Oxidation Catalyst. *Chemphyschem* **2014**, *15*, 1164-1174.
- (60) Schafer, H.; Sadaf, S.; Walder, L.; Kuepper, K.; Dinklage, S.; Wollschlager, J.; Schneider, L.; Steinhart, M.; Hardege, J.; Daum, D. Stainless steel made to rust: a robust water-splitting catalyst with benchmark characteristics. *Energ Environ Sci* **2015**, *8*, 2685-2697.
- (61) Huang, X. N.; Yang, L. B.; Hao, S.; Zheng, B. Z.; Yan, L.; Qu, F. L.; Asiri, A. M.; Sun, X. P. N-Doped carbon dots: a metal-free co-catalyst on hematite nanorod arrays toward efficient photoelectrochemical water oxidation. *Inorg Chem Front* **2017**, *4*, 537-540.
- (62) Riha, S. C.; Klahr, B. M.; Tyo, E. C.; Seifert, S.; Vajda, S.; Pellin, M. J.; Hamann, T. W.; Martinson, A. B. F. Atomic Layer Deposition of a Submonolayer Catalyst for the Enhanced Photoelectrochemical Performance of Water Oxidation with Hematite. *Acs Nano* **2013**, *7*, 2396-2405.
- (63) Bornoz, P.; Abdi, F. F.; Tilley, S. D.; Dam, B.; van de Krol, R.; Graetzel, M.; Sivula, K. A Bismuth Vanadate-Cuprous Oxide Tandem Cell for Overall Solar Water Splitting. *J Phys Chem C* **2014**, *118*, 16959-16966.
- (64) Abdi, F. F.; van de Krol, R. Nature and Light Dependence of Bulk Recombination in Co-Pi-Catalyzed BiVO<sub>4</sub> Photoanodes. *J Phys Chem C* **2012**, *116*, 9398-9404.
- (65) Ma, Y.; Le Formal, F.; Kafizas, A.; Pendlebury, S. R.; Durrant, J. R. Efficient suppression of back electron/hole recombination in cobalt phosphate surface-modified undoped bismuth vanadate photoanodes. *J Mater Chem A* **2015**, *3*, 20649-20657.
- (66) Ma, Y. M.; Kafizas, A.; Pendlebury, S. R.; Le Formal, F.; Durrant, J. R. Photoinduced Absorption Spectroscopy of CoPi on BiVO<sub>4</sub>: The Function of CoPi during Water Oxidation. *Adv Funct Mater* **2016**, *26*, 4951-4960.

- (67) Pilli, S. K.; Furtak, T. E.; Brown, L. D.; Deutsch, T. G.; Turner, J. A.; Herring, A. M. Cobalt-phosphate (Co-Pi) catalyst modified Mo-doped BiVO<sub>4</sub> photoelectrodes for solar water oxidation. *Energ Environ Sci* **2011**, *4*, 5028-5034.
- (68) Qiu, W. T.; Huang, Y. C.; Tang, S. T.; Ji, H. B.; Tong, Y. X. Thin-Layer Indium Oxide and Cobalt Oxyhydroxide Cobalt-Modified BiVO<sub>4</sub> Photoanode for Solar-Assisted Water Electrolysis. *J Phys Chem C* **2017**, *121*, 17150-17159.
- (69) Dabirian, A.; van de Krol, R. High-Temperature Ammonolysis of Thin Film Ta<sub>2</sub>O<sub>5</sub> Photoanodes: Evolution of Structural, Optical, and Photoelectrochemical Properties. *Chem Mater* **2015**, *27*, 708-715.
- (70) Liu, G. J.; Shi, J. Y.; Zhang, F. X.; Chen, Z.; Han, J. F.; Ding, C. M.; Chen, S. S.; Wang, Z. L.; Han, H. X.; Li, C. A Tantalum Nitride Photoanode Modified with a Hole-Storage Layer for Highly Stable Solar Water Splitting. *Angew Chem Int Edit* **2014**, *53*, 7295-7299.
- (71) Liu, G. J.; Ye, S.; Yan, P. L.; Xiong, F. Q.; Fu, P.; Wang, Z. L.; Chen, Z.; Shi, J. Y.; Li, C. Enabling an integrated tantalum nitride photoanode to approach the theoretical photocurrent limit for solar water splitting. *Energ Environ Sci* **2016**, *9*, 1327-1334.
- (72) Xu, G. Z.; Xu, Z.; Shi, Z.; Pei, L.; Yan, S. C.; Gu, Z. B.; Zou, Z. G. Silicon Photoanodes Partially Covered by Ni@Ni(OH)<sub>2</sub> Core-Shell Particles for Photoelectrochemical Water Oxidation. *Chemsuschem* **2017**, *10*, 2897-2903.
- (73) Pastor, E.; Le Formal, F.; Mayer, M. T.; Tilley, S. D.; Francas, L.; Mesa, C. A.; Gratzel, M.; Durrant, J. R. Spectroelectrochemical analysis of the mechanism of (photo)electrochemical hydrogen evolution at a catalytic interface. *Nat Commun* **2017**, *8*.
- (74) Sarkar, A.; Karmakar, K.; Khan, G. G. Designing Co-Pi Modified One-Dimensional n-p TiO<sub>2</sub>/ZnCo<sub>2</sub>O<sub>4</sub> Nanoheterostructure Photoanode with Reduced Electron-Hole Pair Recombination and Excellent Photoconversion Efficiency (> 3%). *J Phys Chem C* **2017**, *121*, 25705-25717.
- (75) Laskowski, F. A. L.; Nellist, M. R.; Venkatkarthick, R.; Boettcher, S. W. Junction behavior of n-Si photoanodes protected by thin Ni elucidated from dual working electrode photoelectrochemistry. *Energ Environ Sci* **2017**, *10*, 570-579.
- (76) Cowley, A. M.; Sze, S. M. Surface States and Barrier Height of Metal-Semiconductor Systems. *J Appl Phys* **1965**, *36*, 3212-&.
- (77) Konofaos, N.; McClean, I. P.; Thomas, C. B. Characterisation of the interface states between amorphous diamond-like carbon films and (100) silicon. *Phys Status Solidi A* **1997**, *161*, 111-123.
- (78) Monllor-Satoca, D.; Bartsch, M.; Fabrega, C.; Genc, A.; Reinhard, S.; Andreu, T.; Arbiol, J.; Niederberger, M.; Morante, J. R. What do you do, titanium? Insight into the role of titanium oxide as a water oxidation promoter in hematite-based photoanodes. *Energ Environ Sci* **2015**, *8*, 3242-3254.
- (79) Sahay, P.; Shamsuddin, M.; Srivastava, R. Electrical characterization of interface states in Ni/n-Si (111) Schottky diodes from (CV) characteristics. *Microelectronics journal* **1992**, *23*, 625-632.



- (80) Saxena, A. N. Forward Current-Voltage Characteristics of Schottky Barriers on N-Type Silicon. *Surf Sci* **1969**, *13*, 151-171.
- (81) Shi, Q.; Murcia-López, S.; Tang, P.; Flox, C.; Morante, J. R.; Bian, Z.; Wang, H.; Andreu, T. Role of tungsten doping on the surface states in BiVO<sub>4</sub> photoanodes for water oxidation: tuning the electron trapping process. *Acs Catal* **2018**.
- (82) Lin, F. D.; Boettcher, S. W. Adaptive semiconductor/electrocatalyst junctions in water-splitting photoanodes. *Nat Mater* **2014**, *13*, 81-86.
- (83) Qiu, J.; Hajibabaei, H.; Nellist, M. R.; Laskowski, F. A.; Hamann, T. W.; Boettcher, S. W. Direct in situ measurement of charge transfer processes during photoelectrochemical water oxidation on catalyzed hematite. *ACS central science* **2017**, *3*, 1015-1025.
- (84) Burke, M. S.; Enman, L. J.; Batchellor, A. S.; Zou, S. H.; Boettcher, S. W. Oxygen Evolution Reaction Electrocatalysis on Transition Metal Oxides and (Oxy)hydroxides: Activity Trends and Design Principles. *Chem Mater* **2015**, *27*, 7549-7558.
- (85) Smith, A. M.; Trotochaud, L.; Burke, M. S.; Boettcher, S. W. Contributions to activity enhancement via Fe incorporation in Ni-(oxy) hydroxide/borate catalysts for near-neutral pH oxygen evolution. *Chem Commun* **2015**, *51*, 5261-5263.
- (86) Trotochaud, L.; Young, S. L.; Ranney, J. K.; Boettcher, S. W. Nickel-Iron Oxyhydroxide Oxygen-Evolution Electrocatalysts: The Role of Intentional and Incidental Iron Incorporation. *J Am Chem Soc* **2014**, *136*, 6744-6753.
- (87) Ma, Y. M.; Mesa, C. A.; Pastor, E.; Kafizas, A.; Francas, L.; Le Formal, F.; Pendlebury, S. R.; Durrant, J. R. Rate Law Analysis of Water Oxidation and Hole Scavenging on a BiVO<sub>4</sub> Photoanode. *Acs Energy Lett* **2016**, *1*, 618-623.
- (88) Sivula, K. Metal Oxide Photoelectrodes for Solar Fuel Production, Surface Traps, and Catalysis. *J Phys Chem Lett* **2013**, *4*, 1624-1633.
- (89) Ai, G. J.; Mo, R.; Li, H. X.; Zhong, J. X. Cobalt phosphate modified TiO<sub>2</sub> nanowire arrays as co-catalysts for solar water splitting. *Nanoscale* **2015**, *7*, 6722-6728.
- (90) Wang, L. D.; Mitoraj, D.; Turner, S.; Khavryuchenko, O. V.; Jacob, T.; Hocking, R. K.; Beranek, R. Ultrasmall CoO(OH)<sub>x</sub> Nanoparticles As a Highly Efficient "True" Cocatalyst in Porous Photoanodes for Water Splitting. *Acs Catal* **2017**, *7*, 4759-4767.
- (91) Xu, D. D.; Fu, Z. W.; Wang, D. J.; Lin, Y. H.; Sun, Y. J.; Meng, D. D.; Xie, T. F. A Ni(OH)<sub>2</sub>-modified Ti-doped alpha-Fe<sub>2</sub>O<sub>3</sub> photoanode for improved photoelectrochemical oxidation of urea: the role of Ni(OH)<sub>2</sub> as a cocatalyst. *Phys Chem Chem Phys* **2015**, *17*, 23924-23930.

## D. References for Paper D

Style: ACS Energy Letters

- (1) Walter, M. G.; Warren, E. L.; McKone, J. R.; Boettcher, S. W.; Mi, Q. X.; Santori, E. A.; Lewis, N. S. Solar water splitting cells. *Chem. Rev.* **2010**, *110*, 6446-6473.
- (2) Dareedwards, M. P.; Goodenough, J. B.; Hamnett, A.; Trelvelick, P. R. Electrochemistry and photoelectrochemistry of iron(III) oxide. *J. Chem. Soc., Faraday Trans.* **1983**, *79*, 2027-2041.
- (3) Le Formal, F.; Tetreault, N.; Cornuz, M.; Moehl, T.; Gratzel, M.; Sivula, K. Passivating surface states on water splitting hematite photoanodes with alumina overlayers. *Chem. Sci.* **2011**, *2*, 737-743.
- (4) Sanchez, C.; Sieber, K. D.; Somorjai, G. A. The photoelectrochemistry of niobium doped  $\alpha$ -Fe<sub>2</sub>O<sub>3</sub>. *J. Electroanal. Chem.* **1988**, *252*, 269-290.
- (5) Wijayantha, K. G. U.; Saremi-Yarahmadi, S.; Peter, L. M. Kinetics of oxygen evolution at  $\alpha$ -Fe<sub>2</sub>O<sub>3</sub> photoanodes: a study by photoelectrochemical impedance spectroscopy. *Phys. Chem. Chem. Phys.* **2011**, *13*, 5264-5270.
- (6) Liu, G. J.; Shi, J. Y.; Zhang, F. X.; Chen, Z.; Han, J. F.; Ding, C. M.; Chen, S. S.; Wang, Z. L.; Han, H. X.; Li, C. A tantalum nitride photoanode modified with a hole-storage layer for highly stable solar water splitting. *Angew. Chem. Int. Ed.* **2014**, *53*, 7295-7299.
- (7) Tamirat, A. G.; Su, W. N.; Dubale, A. A.; Chen, H. M.; Hwang, B. J. Photoelectrochemical water splitting at low applied potential using a NiOOH coated codoped (Sn, Zr)  $\alpha$ -Fe<sub>2</sub>O<sub>3</sub> photoanode. *J. Mat. Chem. A* **2015**, *3*, 5949-5961.
- (8) Liu, G. J.; Ye, S.; Yan, P. L.; Xiong, F. Q.; Fu, P.; Wang, Z. L.; Chen, Z.; Shi, J. Y.; Li, C. Enabling an integrated tantalum nitride photoanode to approach the theoretical photocurrent limit for solar water splitting. *Energy Environ. Sci.* **2016**, *9*, 1327-1334.
- (9) Ning, F. Y.; Shao, M. F.; Xu, S. M.; Fu, Y.; Zhang, R. K.; Wei, M.; Evans, D. G.; Duan, X. TiO<sub>2</sub>/graphene/NiFe-layered double hydroxide nanorod array photoanodes for efficient photoelectrochemical water splitting. *Energy Environ. Sci.* **2016**, *9*, 2633-2643.
- (10) Dotan, H.; Sivula, K.; Gratzel, M.; Rothschild, A.; Warren, S. C. Probing the photoelectrochemical properties of hematite ( $\alpha$ -Fe<sub>2</sub>O<sub>3</sub>) electrodes using hydrogen peroxide as a hole scavenger. *Energy Environ. Sci.* **2011**, *4*, 958-964.
- (11) Iwanski, P.; Curran, J. S.; Gissler, W.; Memming, R. The photoelectrochemical behavior of ferric-oxide in the presence of redox reagents. *J. Electrochem. Soc.* **1981**, *128*, 2128-2133.
- (12) Young, K. M. H.; Klahr, B. M.; Zandi, O.; Hamann, T. W. Photocatalytic water oxidation with hematite electrodes. *Catalysis Science & Technology* **2013**, *3*, 1660-1671.

- (13) Abel, A. J.; Garcia-Torregrosa, I.; Patel, A. M.; Opananont, B.; Baxter, J. B. SILAR-deposited hematite films for photoelectrochemical water splitting: effects of Sn, Ti, thickness, and nanostructuring. *J. Phys. Chem. C* **2015**, *119*, 4454-4465.
- (14) Aleksic, O. S.; Vasiljevic, Z. Z.; Vujkovic, M.; Nikolic, M.; Labus, N.; Lukovic, M. D.; Nikolic, M. V. Structural and electronic properties of screen-printed Fe<sub>2</sub>O<sub>3</sub>/TiO<sub>2</sub> thick films and their photoelectrochemical behavior. *J. Mater. Sci.* **2017**, *52*, 5938-5953.
- (15) Bassi, P. S.; Li, X. L.; Fang, Y. A.; Loo, J. S. C.; Barber, J.; Wong, L. H. Understanding charge transport in non-doped pristine and surface passivated hematite (Fe<sub>2</sub>O<sub>3</sub>) nanorods under front and backside illumination in the context of light induced water splitting. *Phys. Chem. Chem. Phys.* **2016**, *18*, 30370-30378.
- (16) Bu, X. B.; Wang, G.; Tian, Y. Foreign In<sup>3+</sup> treatment improving the photoelectrochemical performance of a hematite nanosheet array for water splitting. *Nanoscale* **2017**, *9*, 17513-17523.
- (17) Cheng, W. R.; He, J. F.; Sun, Z. H.; Peng, Y. H.; Yao, T.; Liu, Q. H.; Jiang, Y.; Hu, F. C.; Xie, Z.; He, B.; Wei, S. Q. Ni-doped overlayer hematite nanotube: a highly photoactive architecture for utilization of visible light. *J. Phys. Chem. C* **2012**, *116*, 24060-24067.
- (18) Cho, I. S.; Han, H. S.; Logar, M.; Park, J.; Zheng, X. L. Enhancing low-bias performance of hematite photoanodes for solar water splitting by simultaneous reduction of bulk, interface, and surface recombination pathways. *Adv. Energy Mater.* **2016**, *6*, 1501840.
- (19) Cots, A.; Gomez, R. Ytterbium modification of pristine and molybdenum-modified hematite electrodes as a strategy for efficient water splitting photoanodes. *Appl. Catal. B-Environ.* **2017**, *219*, 492-500.
- (20) de Carvalho, W. M.; Souza, F. L. Recent advances on solar water splitting using hematite nanorod film produced by purpose-built material methods. *J. Mater. Res.* **2014**, *29*, 16-28.
- (21) Eftekharinia, B.; Moshaii, A.; Dabirian, A.; Vayghan, N. S. Optimization of charge transport in a Co-Pi modified hematite thin film produced by scalable electron beam evaporation for photoelectrochemical water oxidation. *J. Mat. Chem. A* **2017**, *5*, 3412-3424.
- (22) Emery, J. D.; Schleputz, C. M.; Guo, P. J.; Riha, S. C.; Chang, R. P. H.; Martinson, A. B. F. Atomic layer deposition of metastable beta-Fe<sub>2</sub>O<sub>3</sub> via isomorphic epitaxy for photoassisted water oxidation. *ACS Appl. Mater. Interfaces* **2014**, *6*, 21894-21900.
- (23) Fang, T.; Guo, Y. S.; Cai, S. H.; Zhang, N. S.; Hu, Y. F.; Zhang, S. Y.; Li, Z. S.; Zou, Z. G. Improved charge separation efficiency of hematite photoanodes by coating an ultrathin p-type LaFeO<sub>3</sub> overlayer. *Nanotechnology* **2017**, *28*, 394003.
- (24) Forster, M.; Potter, R. J.; Ling, Y. C.; Yang, Y.; Klug, D. R.; Li, Y.; Cowan, A. J. Oxygen deficient alpha-Fe<sub>2</sub>O<sub>3</sub> photoelectrodes: a balance between enhanced electrical properties and trap-mediated losses. *Chem. Sci.* **2015**, *6*, 4009-4016.

- (25) Freitas, A. L. M.; Souza, F. L. Synergetic effect of Sn addition and oxygen-deficient atmosphere to fabricate active hematite photoelectrodes for light-induced water splitting. *Nanotechnology* **2017**, *28*, 454002.
- (26) Grave, D. A.; Dotan, H.; Levy, Y.; Piekner, Y.; Scherrer, B.; Malviya, K. D.; Rothschild, A. Heteroepitaxial hematite photoanodes as a model system for solar water splitting. *J. Mat. Chem. A* **2016**, *4*, 3052-3060.
- (27) Gurudayal; John, R. A.; Boix, P. P.; Yi, C. Y. Y.; Shi, C.; Scott, M. C.; Veldhuis, S. A.; Minor, A. M.; Zakeeruddin, S. M.; Wong, L. H.; Gratzel, M.; Mathews, N. Atomically altered hematite for highly efficient perovskite tandem water-splitting devices. *ChemSuschem* **2017**, *10*, 2449-2456.
- (28) Hisatomi, T.; Dotan, H.; Stefiik, M.; Sivula, K.; Rothschild, A.; Gratzel, M.; Mathews, N. Enhancement in the performance of ultrathin hematite photoanode for water splitting by an oxide underlayer. *Adv. Mater.* **2012**, *24*, 2699-2702.
- (29) Huang, J. W.; Hu, G. W.; Ding, Y.; Pang, M. C.; Ma, B. C. Mn-doping and NiFe layered double hydroxide coating: Effective approaches to enhancing the performance of  $\alpha$ - $\text{Fe}_2\text{O}_3$  in photoelectrochemical water oxidation. *J. Catal.* **2016**, *340*, 261-269.
- (30) Iandolo, B.; Wickman, B.; Svensson, E.; Paulsson, D.; Hellman, A. Tailoring charge recombination in photoelectrodes using oxide nanostructures. *Nano Lett.* **2016**, *16*, 2381-2386.
- (31) Ishaq, S.; Sikora, A.; Scheidler, N.; Hambleton, C.; Katz, J. E. Enhancement of water oxidation photocurrent for hematite thin films electrodeposited with polyvinylpyrrolidone. *J. Electrochem. Soc.* **2016**, *163*, F1330-F1336.
- (32) Jeon, T. H.; Moon, G. H.; Park, H.; Choi, W. Ultra-efficient and durable photoelectrochemical water oxidation using elaborately designed hematite nanorod arrays. *Nano Energy* **2017**, *39*, 211-218.
- (33) Kay, A.; Grave, D. A.; Ellis, D. S.; Dotan, H.; Rothschild, A. Heterogeneous doping to improve the performance of thin-film hematite photoanodes for solar water splitting. *ACS Energy Lett.* **2016**, *1*, 827-833.
- (34) Kay, A.; Grave, D. A.; Malviya, K. D.; Ellis, D. S.; Dotan, H.; Rothschild, A. Wavelength dependent photocurrent of hematite photoanodes: reassessing the hole collection length. *J. Phys. Chem. C* **2017**, *121*, 28287-28292.
- (35) Kim, D. W.; Riha, S. C.; DeMarco, E. J.; Martinson, A. B.; Farha, O. K.; Hupp, J. T. Greenlighting photoelectrochemical oxidation of water by iron oxide. *ACS Nano* **2014**, *8*, 12199-12207.
- (36) Kim, J. Y.; Youn, D. H.; Kim, J. H.; Kim, H. G.; Lee, J. S. Nanostructure-preserved hematite thin film for efficient solar water splitting. *ACS Appl. Mater. Interfaces* **2015**, *7*, 14123-14129.

- (37) Klahr, B.; Gimenez, S.; Fabregat-Santiago, F.; Bisquert, J.; Hamann, T. W. Electrochemical and photoelectrochemical investigation of water oxidation with hematite electrodes. *Energy Environ. Sci.* **2012**, *5*, 7626-7636.
- (38) Klotz, D.; Ellis, D. S.; Dotan, H.; Rothschild, A. Empirical in operando analysis of the charge carrier dynamics in hematite photoanodes by PEIS, IMPS and IMVS. *Phys. Chem. Chem. Phys.* **2016**, *18*, 23438-23457.
- (39) Klotz, D.; Grave, D. A.; Dotan, H.; Rothschild, A. Empirical analysis of the photoelectrochemical impedance response of hematite photoanodes for water photo-oxidation. *J. Phys. Chem. Lett.* **2018**, *9*, 1466-1472.
- (40) Klotz, D.; Grave, D. A.; Rothschild, A. Accurate determination of the charge transfer efficiency of photoanodes for solar water splitting. *Phys. Chem. Chem. Phys.* **2017**, *19*, 20383-20392.
- (41) Kment, S.; Schmuki, P.; Hubicka, Z.; Machala, L.; Kirchgeorg, R.; Liu, N.; Wang, L.; Lee, K.; Olejnicek, J.; Cada, M.; Gregora, I.; Zboril, R. Photoanodes with fully controllable texture: the enhanced water splitting efficiency of thin hematite films exhibiting solely (110) crystal orientation. *ACS Nano* **2015**, *9*, 7113-7123.
- (42) Li, S.; Cai, J. J.; Liu, Y. L.; Gao, M. Q.; Cao, F.; Qin, G. W. Tuning orientation of doped hematite photoanodes for enhanced photoelectrochemical water oxidation. *Sol. Energy Mater. Sol. Cells* **2018**, *179*, 328-333.
- (43) Liu, K.; Wang, H. Y.; Wu, Q. P.; Zhao, J.; Sun, Z.; Xue, S. Nanocube-based hematite photoanode produced in the presence of Na<sub>2</sub>HPO<sub>4</sub> for efficient solar water splitting. *J. Power Sources* **2015**, *283*, 381-388.
- (44) Qin, D. D.; Li, Y.; Ning, X. M.; Wang, Q. H.; He, C. H.; Quan, J. J.; Chen, J.; Li, Y. T.; Lu, X. Q.; Tao, C. L. A nanostructured hematite film prepared by a facile "top down" method for application in photoelectrochemistry. *Dalton Trans.* **2016**, *45*, 16221-16230.
- (45) Qiu, W. T.; Huang, Y. C.; Long, B.; Li, H. B.; Tong, Y. X.; Ji, H. B. Enhanced photoelectrochemical oxygen evolution reaction ability of iron-derived hematite photoanode with titanium modification. *Chem.-Eur. J.* **2015**, *21*, 19250-19256.
- (46) Santangelo, S.; Frontera, P.; Panto, F.; Stelitano, S.; Marelli, M.; Patane, S.; Malaya, F.; Dal Santo, V.; Antonucci, P. Effect of Ti- or Si-doping on nanostructure and photo-electro-chemical activity of electro-spun iron oxide fibres. *Int. J. Hydrogen Energy* **2017**, *42*, 28070-28081.
- (47) Sivula, K. Metal oxide photoelectrodes for solar fuel production, surface traps, and catalysis. *J. Phys. Chem. Lett.* **2013**, *4*, 1624-1633.
- (48) Subramanian, A.; Gracia-Espino, E.; Annamalai, A.; Lee, H. H.; Lee, S. Y.; Choi, S. H.; Jang, J. S. Effect of tetravalent dopants on hematite nanostructure for enhanced photoelectrochemical water splitting. *Appl. Surf. Sci.* **2018**, *427*, 1203-1212.
- (49) Sun, Y. Q.; Chemelewski, W. D.; Berglund, S. P.; Li, C.; He, H. C.; Shi, G. Q.; Mullins, C. B. Antimony-doped tin oxide nanorods as a transparent conducting electrode for

enhancing photoelectrochemical oxidation of water by hematite. *ACS Appl. Mater. Interfaces* **2014**, *6*, 5494-5499.

(50) Taffa, D. H.; Hamm, I.; Dunkel, C.; Sinev, I.; Bahnemann, D.; Wark, M. Electrochemical deposition of Fe<sub>2</sub>O<sub>3</sub> in the presence of organic additives: a route to enhanced photoactivity. *RSC Adv.* **2015**, *5*, 103512-103522.

(51) Tamirat, A. G.; Su, W. N.; Dubale, A. A.; Pan, C. J.; Chen, H. M.; Ayele, D. W.; Lee, J. F.; Hwang, B. J. Efficient photoelectrochemical water splitting using three dimensional urchin-like hematite nanostructure modified with reduced graphene oxide. *J. Power Sources* **2015**, *287*, 119-128.

(52) Wang, D.; Chen, Y.; Zhang, Y.; Zhang, X. T.; Suzuki, N.; Terashima, C. Boosting photoelectrochemical performance of hematite photoanode with TiO<sub>2</sub> underlayer by extremely rapid high temperature annealing. *Appl. Surf. Sci.* **2017**, *422*, 913-920.

(53) Wang, L.; Nguyen, N. T.; Huang, X. J.; Schmuki, P.; Bi, Y. P. Hematite photoanodes: synergetic enhancement of light harvesting and charge management by sandwiched with Fe<sub>2</sub>TiO<sub>5</sub>/Fe<sub>2</sub>O<sub>3</sub>/Pt structures. *Adv. Funct. Mater.* **2017**, *27*, 1703527.

(54) Wang, M.; Wang, H. Y.; Wu, Q. P.; Zhang, C. L.; Xue, S. Morphology regulation and surface modification of hematite nanorods by aging in phosphate solutions for efficient PEC water splitting. *Int. J. Hydrogen Energy* **2016**, *41*, 6211-6219.

(55) Xu, Z.; Fan, Z. W.; Shi, Z.; Li, M. Y.; Feng, J. Y.; Pei, L.; Zhou, C. G.; Zhou, J. K.; Yang, L. X.; Li, W. C.; Xu, G. Z.; Yan, S. C.; Zou, Z. G. Interface manipulation to improve plasmon-coupled photoelectrochemical water splitting on alpha-Fe<sub>2</sub>O<sub>3</sub> photoanodes. *Chemsuschem* **2018**, *11*, 237-244.

(56) Yang, J. S.; Lin, W. H.; Lin, C. Y.; Wang, B. S.; Wu, J. J. n-Fe<sub>2</sub>O<sub>3</sub> to N<sup>+</sup>-TiO<sub>2</sub> heterojunction photoanode for photoelectrochemical water oxidation. *ACS Appl. Mater. Interfaces* **2015**, *7*, 13314-13321.

(57) Yang, Y.; Forster, M.; Ling, Y. C.; Wang, G. M.; Zhai, T.; Tong, Y. X.; Cowan, A. J.; Li, Y. Acid treatment enables suppression of electron-hole recombination in hematite for photoelectrochemical water splitting. *Angew. Chem. Int. Ed.* **2016**, *55*, 3403-3407.

(58) Zandi, O.; Hamann, T. W. Enhanced water splitting efficiency through selective surface state removal. *J. Phys. Chem. Lett.* **2014**, *5*, 1522-1526.

(59) Zandi, O.; Schon, A. R.; Hajibabaei, H.; Hamann, T. W. Enhanced charge separation and collection in high-performance electrodeposited hematite films. *Chem. Mater.* **2016**, *28*, 765-771.

(60) Zhang, K.; Dong, T. J.; Xie, G. C.; Guan, L. M.; Guo, B. D.; Xiang, Q.; Dai, Y. W.; Tian, L. Q.; Batool, A.; Jan, S. U.; Boddula, R.; Thebo, A. A.; Gong, J. R. Sacrificial interlayer for promoting charge transport in hematite photoanode. *ACS Appl. Mater. Interfaces* **2017**, *9*, 42723-42733.

- (61) Zhang, Q.; Wang, H. Y.; Dong, Y. X.; Wu, Q. P.; Xue, S. Highly efficient hematite films via mid-/ex-situ Sn-doping for photoelectrochemical water oxidation. *Int. J. Hydrogen Energy* **2017**, *42*, 16012-16022.
- (62) Zhang, R.; Fang, Y. Y.; Chen, T.; Qu, F. L.; Liu, Z.; Du, G.; Asiri, A. M.; Gao, T.; Sun, X. P. Enhanced photoelectrochemical water oxidation performance of Fe<sub>2</sub>O<sub>3</sub> nanorods array by S doping. *ACS Sustainable Chem. Eng.* **2017**, *5*, 7502-7506.
- (63) Zhao, X.; Feng, J. Y.; Chen, S.; Huang, Y. Z.; Sum, T. C.; Chen, Z. New insight into the roles of oxygen vacancies in hematite for solar water splitting. *Phys. Chem. Chem. Phys.* **2017**, *19*, 1074-1082.
- (64) Abdi, F. F.; Han, L. H.; Smets, A. H. M.; Zeman, M.; Dam, B.; van de Krol, R. Efficient solar water splitting by enhanced charge separation in a bismuth vanadate-silicon tandem photoelectrode. *Nat. Commun.* **2013**, *4*, 2195.
- (65) Antony, R. P.; Zhang, M. Y.; Zhou, K. Q.; Loo, S. C. J.; Barber, J.; Wong, L. H. Synergistic effect of porosity and gradient doping in efficient solar water oxidation of catalyst-free gradient Mo:BiVO<sub>4</sub>. *ACS Omega* **2018**, *3*, 2724-2734.
- (66) Baek, J. H.; Kim, B. J.; Han, G. S.; Hwang, S. W.; Kim, D. R.; Cho, I. S.; Jung, H. S. BiVO<sub>4</sub>/WO<sub>3</sub>/SnO<sub>2</sub> double-heterojunction photoanode with enhanced charge separation and visible-transparency for bias-free solar water-splitting with a perovskite solar cell. *ACS Appl. Mater. Interfaces* **2017**, *9*, 1479-1487.
- (67) Biset-Peiro, M.; Murcia-Lopez, S.; Fabrega, C.; Morante, J. R.; Andreu, T. Multilayer Ni/Fe thin films as oxygen evolution catalysts for solar fuel production. *J. Phys. D: Appl. Phys.* **2017**, *50*, 104003.
- (68) Cai, L. L.; Zhao, J. H.; Li, H.; Park, J.; Cho, I. S.; Han, H. S.; Zheng, X. L. One-step hydrothermal deposition of Ni:FeOOH onto photoanodes for enhanced water oxidation. *ACS Energy Lett.* **2016**, *1*, 624-632.
- (69) Chemseddine, A.; Ullrich, K.; Mete, T.; Abdi, F. F.; van de Krol, R. Solution-processed multilayered BiVO<sub>4</sub> photoanodes: influence of intermediate heat treatments on the photoactivity. *J. Mat. Chem. A* **2016**, *4*, 1723-1728.
- (70) Gong, H.; Freudenberg, N.; Nie, M.; van de Krol, R.; Ellmer, K. BiVO<sub>4</sub> photoanodes for water splitting with high injection efficiency, deposited by reactive magnetron co-sputtering. *AIP Adv.* **2016**, *6*, 045108.
- (71) He, W. H.; Wang, R. R.; Zhou, C.; Yang, J. J.; Li, F.; Xiang, X. Controlling the structure and photoelectrochemical performance of BiVO<sub>4</sub> photoanodes prepared from electrodeposited bismuth precursors: effect of zinc ions as directing agent. *Ind. Eng. Chem. Res.* **2015**, *54*, 10723-10730.
- (72) Hilliard, S.; Friedrich, D.; Kressman, S.; Strub, H.; Artero, V.; Laberty-Robert, C. Solar-water-splitting BiVO<sub>4</sub> thin-film photoanodes prepared by using a sol-gel dip-coating technique. *Chemphotochem* **2017**, *1*, 273-280.

- (73) Jang, J. W.; Friedrich, D.; Muller, S.; Lamers, M.; Hempel, H.; Lardhi, S.; Cao, Z.; Harb, M.; Cavallo, L.; Heller, R.; Eichberger, R.; van de Krol, R.; Abdi, F. F. Enhancing charge carrier lifetime in metal oxide photoelectrodes through mild hydrogen treatment. *Adv. Energy Mater.* **2017**, *7*, 1701536.
- (74) Jeong, H. W.; Jeon, T. H.; Jang, J. S.; Choi, W.; Park, H. Strategic modification of BiVO<sub>4</sub> for improving photoelectrochemical water oxidation performance. *J. Phys. Chem. C* **2013**, *117*, 9104-9112.
- (75) Kim, E. S.; Kang, H. J.; Magesh, G.; Kim, J. Y.; Jang, J. W.; Lee, J. S. Improved photoelectrochemical activity of CaFe<sub>2</sub>O<sub>4</sub>/BiVO<sub>4</sub> heterojunction photoanode by reduced surface recombination in solar water oxidation. *ACS Appl. Mater. Interfaces* **2014**, *6*, 17762-17769.
- (76) Kim, T. W.; Ping, Y.; Galli, G. A.; Choi, K. S. Simultaneous enhancements in photon absorption and charge transport of bismuth vanadate photoanodes for solar water splitting. *Nat. Commun.* **2015**, *6*, 8769.
- (77) Lamm, B.; Sarkar, A.; Stefik, M. Surface functionalized atomic layer deposition of bismuth vanadate for single-phase scheelite. *J. Mat. Chem. A* **2017**, *5*, 6060-6069.
- (78) Lamm, B.; Trzesniewski, B. J.; Doscher, H.; Smith, W. A.; Stefik, M. Emerging postsynthetic improvements of BiVO<sub>4</sub> photoanodes for solar water splitting. *ACS Energy Lett.* **2018**, *3*, 112-124.
- (79) Murcia-Lopez, S.; Fabrega, C.; Monllor-Satoca, D.; Hernandez-Alonso, M. D.; Penelas-Perez, G.; Morata, A.; Morante, J. R.; Andreu, T. Tailoring multilayered BiVO<sub>4</sub> photoanodes by pulsed laser deposition for water splitting. *ACS Appl. Mater. Interfaces* **2016**, *8*, 4076-4085.
- (80) Seabold, J. A.; Zhu, K.; Neale, N. R. Efficient solar photoelectrolysis by nanoporous Mo: BiVO<sub>4</sub> through controlled electron transport. *Phys. Chem. Chem. Phys.* **2014**, *16*, 1121-1131.
- (81) Stefik, M. Atomic layer deposition of bismuth vanadates for solar energy materials. *Chemsuschem* **2016**, *9*, 1727-1735.
- (82) Trzesniewski, B. J.; Smith, W. A. Photocharged BiVO<sub>4</sub> photoanodes for improved solar water splitting. *J. Mat. Chem. A* **2016**, *4*, 2919-2926.
- (83) Yang, J. S.; Wu, J. J. Low-potential driven fully-depleted BiVO<sub>4</sub>/ZnO heterojunction nanodendrite array photoanodes for photoelectrochemical water splitting. *Nano Energy* **2017**, *32*, 232-240.
- (84) Zhao, X.; Chen, Z. Enhanced photoelectrochemical water splitting performance using morphology-controlled BiVO<sub>4</sub> with W doping. *Beilstein J. Nanotechnol.* **2017**, *8*, 2640-2647.
- (85) Zhong, D. K.; Choi, S.; Gamelin, D. R. Near-complete suppression of surface recombination in solar photoelectrolysis by "Co-Pi" catalyst-modified W:BiVO<sub>4</sub>. *J. Am. Chem. Soc.* **2011**, *133*, 18370-18377.



- (86) Bohra, D.; Smith, W. A. Improved charge separation via Fe-doping of copper tungstate photoanodes. *Phys. Chem. Chem. Phys.* **2015**, *17*, 9857-9866.
- (87) Gao, Y.; Hamann, T. W. Quantitative hole collection for photoelectrochemical water oxidation with CuWO<sub>4</sub>. *Chem. Commun.* **2017**, *53*, 1285-1288.
- (88) Gao, Y.; Hamann, T. W. Elucidation of CuWO<sub>4</sub> surface states during photoelectrochemical water oxidation. *J. Phys. Chem. Lett.* **2017**, *8*, 2700-2704.
- (89) Hill, J. C.; Choi, K. S. Synthesis and characterization of high surface area CuWO<sub>4</sub> and Bi<sub>2</sub>WO<sub>6</sub> electrodes for use as photoanodes for solar water oxidation. *J. Mat. Chem. A* **2013**, *1*, 5006-5014.
- (90) Valenti, M.; Dolat, D.; Biskos, G.; Schmidt-Ott, A.; Smith, W. A. Enhancement of the photoelectrochemical performance of CuWO<sub>4</sub> thin films for solar water splitting by plasmonic nanoparticle functionalization. *J. Phys. Chem. C* **2015**, *119*, 2096-2104.
- (91) Ye, W.; Chen, F. J.; Zhao, F. P.; Han, N.; Li, Y. G. CuWO<sub>4</sub> nanoflake array-based single-junction and heterojunction photoanodes for photoelectrochemical water oxidation. *ACS Appl. Mater. Interfaces* **2016**, *8*, 9211-9217.
- (92) Kim, J. H.; Lee, B. J.; Wang, P.; Son, M. H.; Lee, J. S. Facile surfactant driven fabrication of transparent WO<sub>3</sub> photoanodes for improved photoelectrochemical properties. *Appl. Catal., A* **2016**, *521*, 233-239.
- (93) Li, L. F.; Zhao, X. L.; Pan, D. L.; Li, G. S. Nanotube array-like WO<sub>3</sub>/W photoanode fabricated by electrochemical anodization for photoelectrocatalytic overall water splitting. *Chin. J. Catal.* **2017**, *38*, 2132-2140.
- (94) Liu, C.; Su, J. Z.; Guo, L. J. Comparison of sandwich and fingers-crossing type WO<sub>3</sub>/BiVO<sub>4</sub> multilayer heterojunctions for photoelectrochemical water oxidation. *RSC Adv.* **2016**, *6*, 27557-27565.
- (95) Rao, P. M.; Cai, L. L.; Liu, C.; Cho, I. S.; Lee, C. H.; Weisse, J. M.; Yang, P. D.; Zheng, X. L. Simultaneously efficient light absorption and charge separation in WO<sub>3</sub>/BiVO<sub>4</sub> core/shell nanowire photoanode for photoelectrochemical water oxidation. *Nano Lett.* **2014**, *14*, 1099-1105.
- (96) Shi, X. J.; Herraiz-Cardona, I.; Bertoluzzi, L.; Lopez-Varo, P.; Bisquert, J.; Park, J. H.; Gimenez, S. Understanding the synergistic effect of WO<sub>3</sub>-BiVO<sub>4</sub> heterostructures by impedance spectroscopy. *Phys. Chem. Chem. Phys.* **2016**, *18*, 9255-9261.
- (97) Shin, S.; Han, H. S.; Kim, J. S.; Park, I. J.; Lee, M. H.; Hong, K. S.; Cho, I. S. A tree-like nanoporous WO<sub>3</sub> photoanode with enhanced charge transport efficiency for photoelectrochemical water oxidation. *J. Mat. Chem. A* **2015**, *3*, 12920-12926.
- (98) Wang, D. P.; Bassi, P. S.; Qi, H.; Zhao, X.; Gurudayal; Wong, L. H.; Xu, R.; Sritharan, T.; Chen, Z. Improved charge separation in WO<sub>3</sub>/CuWO<sub>4</sub> composite photoanodes for photoelectrochemical water oxidation. *Materials* **2016**, *9*, 348.

- (99) Wang, G. M.; Yang, Y.; Ling, Y. C.; Wang, H. Y.; Lu, X. H.; Pu, Y. C.; Zhang, J. Z.; Tong, Y. X.; Li, Y. An electrochemical method to enhance the performance of metal oxides for photoelectrochemical water oxidation. *J. Mat. Chem. A* **2016**, *4*, 2849-2855.
- (100) Zhao, Z. F.; Zhou, H.; Zheng, L. X.; Niu, P.; Yang, G.; Hu, W. W.; Ran, J. R.; Qiao, S. Z.; Wang, J. G.; Zheng, H. J. Molecules interface engineering derived external electric field for effective charge separation in photoelectrocatalysis. *Nano Energy* **2017**, *42*, 90-97.
- (101) Cho, I. S.; Lee, C. H.; Feng, Y. Z.; Logar, M.; Rao, P. M.; Cai, L. L.; Kim, D. R.; Sinclair, R.; Zheng, X. L. Codoping titanium dioxide nanowires with tungsten and carbon for enhanced photoelectrochemical performance. *Nat. Commun.* **2013**, *4*, 1723.
- (102) Rambabu, Y.; Jaiswal, M.; Roy, S. C. Photo-electrochemical properties of graphene wrapped hierarchically branched nanostructures obtained through hydrothermally transformed TiO<sub>2</sub> nanotubes. *Nanotechnology* **2017**, *28*, 405706.
- (103) Yang, W. G.; Yu, Y. H.; Starr, M. B.; Yin, X.; Li, Z. D.; Kvit, A.; Wang, S. F.; Zhao, P.; Wang, X. D. Ferroelectric polarization-enhanced photoelectrochemical water splitting in TiO<sub>2</sub>-BaTiO<sub>3</sub> core-shell nanowire photoanodes. *Nano Lett.* **2015**, *15*, 7574-7580.
- (104) Zhu, H.; Yan, S. C.; Li, Z. S.; Zou, Z. G. Back electron transfer at TiO<sub>2</sub> nanotube photoanodes in the presence of a H<sub>2</sub>O<sub>2</sub> hole scavenger. *ACS Appl. Mater. Interfaces* **2017**, *9*, 33887-33895.
- (105) Abdi, F. F.; Chemseddine, A.; Berglund, S. P.; van de Krol, R. Assessing the suitability of iron tungstate (Fe<sub>2</sub>WO<sub>6</sub>) as a photoelectrode material for water oxidation. *J. Phys. Chem. C* **2017**, *121*, 153-160.
- (106) Arunachalam, P.; Al-Mayouf, A.; Ghanem, M. A.; Shaddad, M. N.; Weller, M. T. Photoelectrochemical oxidation of water using La(Ta,Nb)O<sub>2</sub>N modified electrodes. *Int. J. Hydrogen Energy* **2016**, *41*, 11644-11652.
- (107) Baek, M.; Kim, D.; Yong, K. Simple but effective way to enhance photoelectrochemical solar-water-splitting performance of zno nanorod arrays: charge-trapping Zn(OH)<sub>2</sub> annihilation and oxygen vacancy generation by vacuum annealing. *ACS Appl. Mater. Interfaces* **2017**, *9*, 2317-2325.
- (108) Cardenas-Morcoso, D.; Peiro-Franch, A.; Herraiz-Cardona, I.; Gimenez, S. Chromium doped copper vanadate photoanodes for water splitting. *Catal. Today* **2017**, *290*, 65-72.
- (109) Chitrada, K. C.; Gakhar, R.; Chidambaram, D.; Aston, E.; Raja, K. S. Enhanced performance of beta-Bi<sub>2</sub>O<sub>3</sub> by in-situ photo-conversion to Bi<sub>2</sub>O<sub>3</sub>-BiO<sub>2-x</sub> composite photoanode for solar water splitting. *J. Electrochem. Soc.* **2016**, *163*, H546-H558.
- (110) Courtin, E.; Baldinozzi, G.; Sougrati, M. T.; Stievano, L.; Sanchez, C.; Laberty-Robert, C. New Fe<sub>2</sub>TiO<sub>5</sub>-based nanoheterostructured mesoporous photoanodes with improved visible light photoresponses. *J. Mat. Chem. A* **2014**, *2*, 6567-6577.
- (111) Feng, J. Y.; Cao, D. P.; Wang, Z. Q.; Luo, W. J.; Wang, J. J.; Li, Z. S.; Zou, Z. G. Ge-mediated modification in Ta<sub>3</sub>N<sub>5</sub> photoelectrodes with enhanced charge transport for solar water splitting. *Chem.-Eur. J.* **2014**, *20*, 16384-16390.

- (112) Feng, J. Y.; Luo, W. J.; Fang, T.; Lv, H.; Wang, Z. Q.; Gao, J.; Liu, W. M.; Yu, T.; Li, Z. S.; Zou, Z. G. Highly photo-responsive LaTiO<sub>2</sub>N photoanodes by improvement of charge carrier transport among film particles. *Adv. Funct. Mater.* **2014**, *24*, 3535-3542.
- (113) Guijarro, N.; Borno, P.; Prevot, M.; Yu, X.; Zhu, X.; Johnson, M.; Jeanbourquin, X.; Le Formal, F.; Sivula, K. Evaluating spinel ferrites MFe<sub>2</sub>O<sub>4</sub> (M = Cu, Mg, Zn) as photoanodes for solar water oxidation: prospects and limitations. *Sustainable Energy Fuels* **2018**, *2*, 103-117.
- (114) Kamimura, J.; Bogdanoff, P.; Abdi, F. F.; Lahnemann, J.; van de Krol, R.; Riechert, H.; Geelhaar, L. Photoelectrochemical properties of GaN photoanodes with cobalt phosphate catalyst for solar water splitting in neutral electrolyte. *J. Phys. Chem. C* **2017**, *121*, 12540-12545.
- (115) Kamimura, J.; Bogdanoff, P.; Corfdir, P.; Brandt, O.; Riechert, H.; Geelhaar, L. Broad band light absorption and high photocurrent of (In,Ga)N nanowire photoanodes resulting from a radial stark effect. *ACS Appl. Mater. Interfaces* **2016**, *8*, 34490-34496.
- (116) Kim, J. H.; Jang, Y. J.; Kim, J. H.; Jang, J. W.; Choi, S. H.; Lee, J. S. Defective ZnFe<sub>2</sub>O<sub>4</sub> nanorods with oxygen vacancy for photoelectrochemical water splitting. *Nanoscale* **2015**, *7*, 19144-19151.
- (117) Liu, X. B.; Wang, Z. Y.; Chen, P.; Zhou, H. F.; Kong, L. B.; Niu, C. M.; Que, W. X. New insights into the electronic structure and photoelectrochemical properties of nitrogen-doped HNb<sub>3</sub>O<sub>8</sub> via a combined in situ experimental and DFT investigation. *ACS Appl. Mater. Interfaces* **2017**, *9*, 42751-42760.
- (118) Pinheiro, A. N.; Firmiano, E. G. S.; Rabelo, A. C.; Dalmaschio, C. J.; Leite, E. R. Revisiting SrTiO<sub>3</sub> as a photoanode for water splitting: development of thin films with enhanced charge separation under standard solar irradiation. *RSC Adv.* **2014**, *4*, 2029-2036.
- (119) Wang, Z. L.; Zong, X.; Gao, Y. Y.; Han, J. F.; Xu, Z. Q.; Li, Z.; Ding, C. M.; Wang, S. Y.; Li, C. Promoting charge separation and injection by optimizing the interfaces of GaN:ZnO photoanode for efficient solar water oxidation. *ACS Appl. Mater. Interfaces* **2017**, *9*, 30696-30702.
- (120) Wu, M. H.; Wang, Y. X.; Xu, Y.; Ming, J.; Zhou, M.; Xu, R.; Fu, Q.; Lei, Y. Self-supported Bi<sub>2</sub>MoO<sub>6</sub> nanowall for photoelectrochemical water splitting. *ACS Appl. Mater. Interfaces* **2017**, *9*, 23647-23653.
- (121) Zhong, Y. J.; Li, Z. S.; Zhao, X.; Fang, T.; Huang, H. T.; Qian, Q. F.; Chang, X. F.; Wang, P.; Yan, S. C.; Yu, Z. T.; Zou, Z. G. Enhanced water-splitting performance of perovskite SrTaO<sub>2</sub>N photoanode film through ameliorating interparticle charge transport. *Adv. Funct. Mater.* **2016**, *26*, 7156-7163.
- (122) Abdi, F. F.; Dabirian, A.; Dam, B.; van de Krol, R. Plasmonic enhancement of the optical absorption and catalytic efficiency of BiVO<sub>4</sub> photoanodes decorated with Ag@SiO<sub>2</sub> core-shell nanoparticles. *Phys. Chem. Chem. Phys.* **2014**, *16*, 15272-15277.
- (123) Abel, A. J.; Patel, A. M.; Smolin, S. Y.; Opananont, B.; Baxter, J. B. Enhanced photoelectrochemical water splitting via SILAR-deposited Ti-doped hematite thin films with an FeOOH overlayer. *J. Mat. Chem. A* **2016**, *4*, 6495-6504.

- (124) Bu, Q. J.; Li, S.; Cao, S.; Zhao, Q. D.; Chen, Y.; Wanga, D. J.; Xie, T. F. A Ni<sub>2</sub>P modified Ti<sup>4+</sup> doped Fe<sub>2</sub>O<sub>3</sub> photoanode for efficient solar water oxidation by promoting hole injection. *Dalton Trans.* **2017**, *46*, 10549-10552.
- (125) Chu, S.; Vanka, S.; Wang, Y. C.; Gim, J.; Wang, Y. J.; Ra, Y. H.; Hovden, R.; Guo, H.; Shih, I.; Mi, Z. T. Solar water oxidation by an InGaN nanowire photoanode with a bandgap of 1.7 eV. *ACS Energy Lett.* **2018**, *3*, 307-314.
- (126) Fan, W. Q.; Li, C. F.; Bai, H. Y.; Zhao, Y. Y.; Luo, B. F.; Li, Y. J.; Ge, Y. L.; Shi, W. D.; Li, H. P. An in situ photoelectroreduction approach to fabricate Bi/BiOCl heterostructure photocathodes: understanding the role of Bi metal for solar water splitting. *J. Mat. Chem. A* **2017**, *5*, 4894-4903.
- (127) Hegner, F. S.; Cardenas-Morcoso, D.; Gimenez, S.; Lopez, N.; Galan-Mascaros, J. R. Level alignment as descriptor for semiconductor/catalyst systems in water splitting: the case of hematite/cobalt hexacyanoferrate photoanodes. *Chemsuschem* **2017**, *10*, 4552-4560.
- (128) Hegner, F. S.; Herraiz-Cardona, I.; Cardenas-Morcoso, D.; Lopez, N.; Galan-Mascaros, J. R.; Gimenez, S. Cobalt hexacyanoferrate on BiVO<sub>4</sub> photoanodes for robust water splitting. *ACS Appl. Mater. Interfaces* **2017**, *9*, 37671-37681.
- (129) Kamimura, J.; Bogdanoff, P.; Ramsteiner, M.; Geelhaar, L.; Riechert, H. Photoelectrochemical properties of InN nanowire photoelectrodes for solar water splitting. *Semicond. Sci. Technol.* **2016**, *31*, 074001.
- (130) Kang, B. K.; Han, G. S.; Baek, J. H.; Lee, D. G.; Song, Y. H.; Kwon, S. B.; Cho, I. S.; Jung, H. S.; Yoon, D. H. Nanodome structured BiVO<sub>4</sub>/GaO<sub>x</sub>N<sub>1-x</sub> photoanode for solar water oxidation. *Adv. Mater. Interfaces* **2017**, *4*, 1700323.
- (131) Kim, J. Y.; Youn, D. H.; Kang, K.; Lee, J. S. Highly conformal deposition of an ultrathin FeOOH layer on a hematite nanostructure for efficient solar water splitting. *Angew. Chem. Int. Ed.* **2016**, *55*, 10854-10858.
- (132) Kim, T. W.; Choi, K. S. Nanoporous BiVO<sub>4</sub> photoanodes with dual-layer oxygen evolution catalysts for solar water splitting. *Science* **2014**, *343*, 990-994.
- (133) Liu, B.; Li, J.; Wu, H. L.; Liu, W. Q.; Jiang, X.; Li, Z. J.; Chen, B.; Tung, C. H.; Wu, L. Z. Improved photoelectrocatalytic performance for water oxidation by earth-abundant cobalt molecular porphyrin complex-integrated BiVO<sub>4</sub> photoanode. *ACS Appl. Mater. Interfaces* **2016**, *8*, 18577-18583.
- (134) Park, Y.; Kang, D.; Choi, K. S. Marked enhancement in electron-hole separation achieved in the low bias region using electrochemically prepared Mo-doped BiVO<sub>4</sub> photoanodes. *Phys. Chem. Chem. Phys.* **2014**, *16*, 1238-1246.
- (135) Pihosh, Y.; Turkevych, I.; Mawatari, K.; Uemura, J.; Kazoe, Y.; Kosar, S.; Makita, K.; Sugaya, T.; Matsui, T.; Fujita, D.; Tosa, M.; Kondo, M.; Kitamori, T. Photocatalytic generation of hydrogen by core-shell WO<sub>3</sub>/BiVO<sub>4</sub> nanorods with ultimate water splitting efficiency. *Sci. Rep.* **2015**, *5*, 11141.

(136) Qiu, W. T.; Huang, Y. C.; Wang, Z. L.; Xiao, S.; Ji, H. B.; Tong, Y. X. Effective strategies towards high-performance photoanodes for photoelectrochemical water splitting. *Acta Phys.—Chim. Sin.* **2017**, *33*, 80-102.

(137) Shaddad, M. N.; Ghanem, M. A.; Al-Mayouf, A. M.; Gimenez, S.; Bisquert, J.; Herraiz-Cardona, I. Cooperative catalytic effect of ZrO<sub>2</sub> and alpha-Fe<sub>2</sub>O<sub>3</sub> nanoparticles on BiVO<sub>4</sub> photoanodes for enhanced photoelectrochemical water splitting. *Chemsuschem* **2016**, *9*, 2779-2783.

(138) Si, W. P.; Pergolesi, D.; Haydous, F.; Fluri, A.; Wokaun, A.; Lippert, T. Investigating the behavior of various cocatalysts on LaTaON<sub>2</sub> photoanode for visible light water splitting. *Phys. Chem. Chem. Phys.* **2017**, *19*, 656-662.

(139) Tong, H.; Jiang, Y.; Zhang, Q.; Li, J.; Jiang, W.; Zhang, D.; Li, N.; Xia, L. Enhanced interfacial charge transfer on WO<sub>3</sub> photoanode by molecular iridium catalyst. *ChemSusChem* **2017**, *10*, 3268-3275.

(140) Wang, G. M.; Xiao, X. H.; Li, W. Q.; Lin, Z. Y.; Zhao, Z. P.; Chen, C.; Wang, C.; Li, Y. J.; Huang, X. Q.; Miao, L.; Jiang, C. Z.; Huang, Y.; Duan, X. F. Significantly enhanced visible light photoelectrochemical activity in TiO<sub>2</sub> nanowire arrays by nitrogen implantation. *Nano Lett.* **2015**, *15*, 4692-4698.

(141) Wang, J.; Yang, J. Y.; Zheng, Z. Y.; Lu, T. B.; Gao, W. H. The role of thin NiPi film for enhancing solar water splitting performance of Ti doped hematite. *Appl. Catal. B-Environ.* **2017**, *218*, 277-286.

(142) Wang, M.; Wang, M.; Fu, Y. M.; Shen, S. H. Cobalt oxide and carbon modified hematite nanorod arrays for improved photoelectrochemical water splitting. *Chin. Chem. Lett.* **2017**, *28*, 2207-2211.

(143) Xu, Y. F.; Wang, X. D.; Chen, H. Y.; Kuang, D. B.; Su, C. Y. Toward high performance photoelectrochemical water oxidation: combined effects of ultrafine cobalt iron oxide nanoparticle. *Adv. Funct. Mater.* **2016**, *26*, 4414-4421.

(144) Yang, L.; Xiong, Y. L.; Dong, H. M.; Peng, H. R.; Zhang, Y. H.; Xiao, P. Enhanced charge separation and oxidation kinetics of BiVO<sub>4</sub> photoanode by double layer structure. *J. Power Sources* **2017**, *343*, 67-75.

(145) Ye, K. H.; Wang, Z. L.; Gu, J. W.; Xiao, S.; Yuan, Y. F.; Zhu, Y.; Zhang, Y. M.; Mai, W. J.; Yang, S. H. Carbon quantum dots as a visible light sensitizer to significantly increase the solar water splitting performance of bismuth vanadate photoanodes. *Energy Environ. Sci.* **2017**, *10*, 772-779.

(146) Yu, X. W.; Yang, P.; Chen, S.; Zhang, M.; Shi, G. Q. NiFe alloy protected silicon photoanode for efficient water splitting. *Adv. Energy Mater.* **2017**, *7*, 1601805.

(147) Yuan, Y. F.; Gu, J. W.; Ye, K. H.; Chai, Z. S.; Yu, X.; Chen, X. B.; Zhao, C. X.; Zhang, Y. M.; Mai, W. J. Combining bulk/surface engineering of hematite to synergistically improve its photoelectrochemical water splitting performance. *ACS Appl. Mater. Interfaces* **2016**, *8*, 16071-16077.

(148) Lin, F. D.; Boettcher, S. W. Adaptive semiconductor/electrocatalyst junctions in water-splitting photoanodes. *Nat. Mater.* **2014**, *13*, 81-86.

(149) Laskowski, F. A. L.; Nellist, M. R.; Venkatkarthick, R.; Boettcher, S. W. Junction behavior of n-Si photoanodes protected by thin Ni elucidated from dual working electrode photoelectrochemistry. *Energy Environ. Sci.* **2017**, *10*, 570-579.

(150) Qiu, J. J.; Hajibabaei, H.; Nellist, M. R.; Laskowski, F. A. L.; Hamann, T. W.; Boettcher, S. W. Direct in situ measurement of charge transfer processes during photoelectrochemical water oxidation on catalyzed hematite. *ACS Cent. Sci.* **2017**, *3*, 1015-1025.

(151) Sun, K.; Ritzert, N. L.; John, J.; Tan, H.; Hale, W. G.; Jiang, J.; Moreno-Hernandez, I.; Papadantonakis, K. M.; Moffat, T. P.; Brunschwig, B. S. Performance and failure modes of Si anodes patterned with thin-film Ni catalyst islands for water oxidation. *Sustainable Energy Fuels* **2018**, *2*, 983-998.

(152) Xu, G. Z.; Xu, Z.; Shi, Z.; Pei, L.; Yan, S. C.; Gu, Z. B.; Zou, Z. G. Silicon photoanodes partially covered by Ni@Ni(OH)<sub>2</sub> core-shell particles for photoelectrochemical water oxidation. *ChemSuschem* **2017**, *10*, 2897-2903.

(153) Trotochaud, L.; Young, S. L.; Ranney, J. K.; Boettcher, S. W. Nickel-iron oxyhydroxide oxygen-evolution electrocatalysts: the role of intentional and incidental iron incorporation. *J. Am. Chem. Soc.* **2014**, *136*, 6744-6753.

(154) Burke, M. S.; Enman, L. J.; Batchellor, A. S.; Zou, S. H.; Boettcher, S. W. Oxygen evolution reaction electrocatalysis on transition metal oxides and (oxy)hydroxides: activity trends and design principles. *Chem. Mater.* **2015**, *27*, 7549-7558.

(155) Smith, A. M.; Trotochaud, L.; Burke, M. S.; Boettcher, S. W. Contributions to activity enhancement via Fe incorporation in Ni-(oxy) hydroxide/borate catalysts for near-neutral pH oxygen evolution. *Chem. Commun.* **2015**, *51*, 5261-5263.

(156) Hu, C. W.; Yamada, Y.; Yoshimura, K. Fabrication of nickel oxyhydroxide/palladium (NiOOH/Pd) thin films for gasochromic application. *J. Mater. Chem. C* **2016**, *4*, 5390-5397.

(157) Goldsmith, Z. K.; Harshan, A. K.; Gerken, J. B.; Voros, M.; Galli, G.; Stahl, S. S.; Hammes-Schiffer, S. Characterization of NiFe oxyhydroxide electrocatalysts by integrated electronic structure calculations and spectroelectrochemistry. *Proc. Natl. Acad. Sci. U. S. A.* **2017**, *114*, 3050-3055.

(158) Costentin, C.; Porter, T. R.; Saveant, J. M. Conduction and reactivity in heterogeneous-molecular catalysis: new insights in water oxidation catalysis by phosphate cobalt oxide films. *J. Am. Chem. Soc.* **2016**, *138*, 5615-5622.

(159) Li, H. X.; Yu, Y. H.; Starr, M. B.; Li, Z. D.; Wang, X. D. Piezotronic-enhanced photoelectrochemical reactions in Ni(OH)<sub>2</sub>-decorated ZnO photoanodes. *J. Phys. Chem. Lett.* **2015**, *6*, 3410-3416.

(160) Wang, L.; Lin, C.; Zhang, F. X.; Jin, J. Phase transformation guided single-layer beta-Co(OH)<sub>2</sub> nanosheets for pseudocapacitive electrodes. *ACS Nano* **2014**, *8*, 3724-3734.

(161) El Gabaly, F.; McCarty, K. F.; Bluhm, H.; McDaniel, A. H. Oxidation stages of Ni electrodes in solid oxide fuel cell environments. *Phys. Chem. Chem. Phys.* **2013**, *15*, 8334-8341.

(162) Tuomi, D. The forming process in nickel positive electrodes. *J. Electrochem. Soc.* **1965**, *112*, 1-12.

(163) Sun, K.; Moreno-Hernandez, I. A.; Schmidt, W. C.; Zhou, X. H.; Crompton, J. C.; Liu, R.; Saadi, F. H.; Chen, Y. K.; Papadantonakis, K. M.; Lewis, N. S. A comparison of the chemical, optical and electrocatalytic properties of water-oxidation catalysts for use in integrated solar-fuel generators. *Energy Environ. Sci.* **2017**, *10*, 987-1002.

## E. References for Paper E

Style: Physical Review Letters

- [1] L. M. Peter, *J. Solid State Electrochem.* **17**, 315 (2013).
- [2] L. M. Peter, K. G. U. Wijayantha, and A. A. Tahir, *Faraday Discuss.* **155**, 309 (2012).
- [3] K. G. U. Wijayantha, S. Saremi-Yarahmadi, and L. M. Peter, *Phys. Chem. Chem. Phys.* **13**, 5264 (2011).
- [4] J. A. Seabold and K. S. Choi, *Chem. Mater.* **23**, 1105 (2011).
- [5] B. Klahr, S. Gimenez, F. Fabregat-Santiago, J. Bisquert, and T. W. Hamann, *J. Am. Chem. Soc.* **134**, 16693 (2012).
- [6] C. M. Ding, J. Y. Shi, D. G. Wang, Z. J. Wang, N. Wang, G. J. Liu, F. Q. Xiong, and C. Li, *Phys. Chem. Chem. Phys.* **15**, 4589 (2013).
- [7] T. W. Kim and K. S. Choi, *Science* **343**, 990 (2014).
- [8] F. Le Formal, N. Tetreault, M. Cornuz, T. Moehl, M. Gratzel, and K. Sivula, *Chem. Sci.* **2**, 737 (2011).
- [9] Y. Q. Liang and J. Messinger, *Phys. Chem. Chem. Phys.* **16**, 12014 (2014).
- [10] M. F. Lichterman, M. R. Shaner, S. G. Handler, B. S. Brunshwig, H. B. Gray, N. S. Lewis, and J. M. Spurgeon, *J. Phys. Chem. Lett.* **4**, 4188 (2013).
- [11] K. J. McDonald and K. S. Choi, *Chem. Mater.* **23**, 1686 (2011).
- [12] D. K. Zhong, S. Choi, and D. R. Gamelin, *J. Am. Chem. Soc.* **133**, 18370 (2011).
- [13] D. K. Zhong, J. W. Sun, H. Inumaru, and D. R. Gamelin, *J. Am. Chem. Soc.* **131**, 6086 (2009).
- [14] T. Hisatomi, F. Le Formal, M. Cornuz, J. Brillet, N. Tetreault, K. Sivula, and M. Gratzel, *Energy Environ. Sci.* **4**, 2512 (2011).
- [15] S. R. Pendlebury, M. Barroso, A. J. Cowan, K. Sivula, J. W. Tang, M. Gratzel, D. Klug, and J. R. Durrant, *Chem. Commun.* **47**, 716 (2011).
- [16] M. Barroso, C. A. Mesa, S. R. Pendlebury, A. J. Cowan, T. Hisatomi, K. Sivula, M. Gratzel, D. R. Klug, and J. R. Durrant, *Proc. Natl. Acad. Sci. U. S. A.* **109**, 15640 (2012).
- [17] A. J. Cowan, C. J. Barnett, S. R. Pendlebury, M. Barroso, K. Sivula, M. Gratzel, J. R. Durrant, and D. R. Klug, *J. Am. Chem. Soc.* **133**, 10134 (2011).



- [18] A. J. Cowan, J. W. Tang, W. H. Leng, J. R. Durrant, and D. R. Klug, *J. Phys. Chem. C* **114**, 4208 (2010).
- [19] F. M. Pesci, A. J. Cowan, B. D. Alexander, J. R. Durrant, and D. R. Klug, *J. Phys. Chem. Lett.* **2**, 1900 (2011).
- [20] M. Barroso, A. J. Cowan, S. R. Pendlebury, M. Gratzel, D. R. Klug, and J. R. Durrant, *J. Am. Chem. Soc.* **133**, 14868 (2011).
- [21] D. R. Gamelin, *Nat. Chem.* **4**, 965 (2012).
- [22] F. D. Lin and S. W. Boettcher, *Nat. Mater.* **13**, 81 (2014).
- [23] T. J. Mills, F. D. Lin, and S. W. Boettcher, *Phys. Rev. Lett.* **112** (2014).
- [24] W. H. Leng, Z. Zhang, J. Q. Zhang, and C. N. Cao, *J. Phys. Chem. B* **109**, 15008 (2005).
- [25] A. J. Bard, A. B. Bocarsly, F. R. F. Fan, E. G. Walton, and M. S. Wrighton, *J. Am. Chem. Soc.* **102**, 3671 (1980).
- [26] L. M. Peter, J. Li, and R. Peat, *J. Electroanal. Chem.* **165**, 29 (1984).
- [27] W. Shockley and W. Read Jr, *Phys. Rev.* **87**, 835 (1952).
- [28] R. N. Hall, *Phys. Rev.* **87**, 387 (1952).
- [29] A. G. Tamirat, W. N. Su, A. A. Dubale, H. M. Chen, and B. J. Hwang, *J. Mat. Chem. A* **3**, 5949 (2015).
- [30] L. M. Peter, E. A. Ponomarev, and D. J. Fermin, *J. Electroanal. Chem.* **427**, 79 (1997).
- [31] W. W. Gärtner, *Phys. Rev. Lett.* **116**, 84 (1959).
- [32] F. Elguibaly and K. Colbow, *J. Appl. Phys.* **53**, 1737 (1982).
- [33] W. J. Albery and P. N. Bartlett, *J. Electrochem. Soc.* **130**, 1699 (1983).
- [34] L. M. Peter and K. G. U. Wijayantha, *ChemPhysChem* **15**, 1983 (2014).
- [35] W. J. Albery, P. N. Bartlett, A. Hamnett, and M. P. Dareedwards, *J. Electrochem. Soc.* **128**, 1492 (1981).
- [36] J. Reichman, *Appl. Phys. Lett.* **36**, 574 (1980).
- [37] H. Gerischer, *Adv. Electrochem. Eng.* **1**, 139 (1961).
- [38] D. Vanmaekelbergh, *Electrochim. Acta* **42**, 1121 (1997).

## F. References for Paper F

Style: Energy & Environmental Science

1. M. G. Walter, E. L. Warren, and J. R. McKone, *Chem. Rev.*, 2010, **110**, 6446–6473.
2. K. Sun, S. Shen, Y. Liang, P. E. Burrows, S. S. Mao, and D. Wang, *Chem. Rev.*, 2014, **114**, 8662–8719.
3. T. Han, Y. Shi, X. Song, A. Mio, L. Valenti, F. Hui, S. Privitera, S. Lombardo, and M. Lanza, *J. Mater. Chem. A*, 2016, **4**, 8053–8060.
4. R. O'Connor, J. Bogan, N. Fleck, A. McCoy, L. A. Walsh, C. Byrne, P. Casey, and G. Hughes, *Sol. Energy Mater. Sol. Cells*, 2015, **136**, 64–69.
5. R. C. Kainthla, *J. Electrochem Soc.*, 1986, **133**, 248–253.
6. S. Hu, N. S. Lewis, J. W. Ager, J. Yang, J. R. McKone, and N. C. Strandwitz, *J. Phys. Chem. C*, 2015, **119**, 24201–24228.
7. I. Katsounaros, S. Cherevko, A. R. Zeradjanin, and K. J. J. Mayrhofer, *Angew. Chem. Int. Ed.*, 2013, **53**, 102–121.
8. W. A. Smith, I. D. Sharp, N. C. Strandwitz, and J. Bisquert, *Energy Environ. Sci.*, 2015, **8**, 2851–2862.
9. X. Zhou, R. Liu, K. Sun, K. M. Papadantonakis, B. S. Brunshwig, and N. S. Lewis, *Energy Environ. Sci.*, 2016, **9**, 892–897.
10. M. Hannula, K. Lahtonen, H. Ali-Löyty, A. A. Zakharov, T. Isotalo, J. Saari, and M. Valden, *Scr. Mater.*, 2016, **119**, 76–81.
11. A. G. Scheuermann, J. P. Lawrence, K. W. Kemp, and T. Ito, *Nat. Mater.*, 2015, **15**, 99–105.
12. J. C. Hill, A. T. Landers, and J. A. Switzer, *Nat. Mater.*, 2015, **14**, 1150–1155.
13. B. Mei, T. Pedersen, P. Malacrida, and D. Bae, *J. Phys. Chem. C*, 2015, **119**, 15019–15027.
14. S. Hu, M. R. Shaner, J. A. Beardslee, M. Lichterman, B. S. Brunshwig, and N. S. Lewis, *Science*, 2014, **344**, 1005.
15. H. J. Kim, K. L. Kearney, L. H. Le, R. T. Pekarek, and M. J. Rose, *ACS Appl. Mater. Interfaces*, 2015, **7**, 8572–8584.
16. Y. W. Chen, J. D. Prange, S. Dühnen, Y. Park, M. Gunji, C. E. D. Chidsey, and P. C. McIntyre, *Nat. Mater.*, 2011, **10**, 539–544.
17. K. Sun, S. Shen, J. S. Cheung, X. Pang, N. Park, J. Zhou, Y. Hu, Z. Sun, S. Y. Noh, C. T. Riley, P. K. L. Yu, S. Jin, and D. Wang, *Phys. Chem. Chem. Phys.*, 2014, **16**, 4612–4625.

18. K. Sun, N. Park, Z. Sun, J. Zhou, J. Wang, X. Pang, S. Shen, S. Y. Noh, Y. Jing, S. Jin, P. K. L. Yu, and D. Wang, *Energy Environ. Sci.*, 2012, **5**, 7872–7877.
19. J. Yang, J. K. Cooper, F. M. Toma, K. A. Walczak, M. Favaro, J. W. Beeman, L. H. Hess, C. Wang, C. Zhu, S. Gul, J. Yano, C. Kisielowski, A. Schwartzberg, and I. D. Sharp, *Nat. Mater.*, 2016.
20. J. Yang, S. Klaus, L. J. Lee, R. Woods-Robinson, J. Ma, Y. Lum, J. K. Cooper, F. M. Toma, L.-W. Wang, I. D. Sharp, A. T. Bell, and J. W. Ager, *J. Am. Chem. Soc.*, 2015, **137**, 9595–9603.
21. X. Zhou, R. Liu, K. Sun, D. Friedrich, M. T. McDowell, F. Yang, S. T. Omelchenko, F. H. Saadi, A. C. Nielander, S. Yalamançhili, K. M. Papadantonakis, B. S. Brunshwig, and N. S. Lewis, *Energy Environ. Sci.*, 2015, **8**, 2644–2649.
22. K. Sun, M. T. McDowell, A. C. Nielander, S. Hu, M. R. Shaner, F. Yang, B. S. Brunshwig, and N. S. Lewis, *J. Phys. Chem. Lett.*, 2015, **6**, 592–598.
23. B. Mei, A. A. Permyakova, R. Frydendal, D. Bae, T. Pedersen, P. Malacrida, O. Hansen, I. E. L. Stephens, P. C. K. Vesborg, B. Seger, and I. Chorkendorff, *J. Phys. Chem. Lett.*, 2014, **5**, 3456–3461.
24. J. Yang, K. Walczak, E. Anzenberg, F. M. Toma, G. Yuan, J. Beeman, A. Schwartzberg, Y. Lin, M. Hettick, A. Javey, J. W. Ager, J. Yano, H. Frei, and I. D. Sharp, *J. Am. Chem. Soc.*, 2014, **136**, 6191–6194.
25. N. C. Strandwitz, D. J. Comstock, R. L. Grimm, A. C. Nichols-Nielander, J. Elam, and N. S. Lewis, *J. Phys. Chem. C*, 2013, **117**, 4931–4936.
26. Y. Shi, C. Gimbert-Suriñach, T. Han, S. Berardi, M. Lanza, and A. Llobet, *ACS Appl. Mater. Interfaces*, 2016, **8**, 696–702.
27. E. R. Young, R. Costi, S. Paydavosi, D. G. Nocera, and V. Bulović, *Energy Environ. Sci.*, 2011, **4**, 2058–2061.
28. M. J. Kenney, M. Gong, Y. Li, J. Z. Wu, J. Feng, M. Lanza, and H. Dai, *Science*, 2013, **342**, 836–840.
29. P. F. Satterthwaite, A. G. Scheuermann, P. K. Hurley, C. E. D. Chidsey, and P. C. McIntyre, *ACS Appl. Mater. Interfaces*, 2016, **8**, 13140–13149.
30. A. G. Scheuermann and P. C. McIntyre, *J. Phys. Chem. Lett.*, 2016, **7**, 2867–2878.
31. M. T. McDowell, M. F. Lichterman, A. I. Carim, R. Liu, S. Hu, B. S. Brunshwig, and N. S. Lewis, *ACS Appl. Mater. Interfaces*, 2015, **7**, 15189–15199.
32. A. G. Scheuermann, J. P. Lawrence, A. C. Meng, K. Tang, O. L. Hendricks, C. E. D. Chidsey, and P. C. McIntyre, *ACS Appl. Mater. Interfaces*, 2016, **8**, 14596–14603.
33. M.-J. Park, J.-Y. Jung, S.-M. Shin, J.-W. Song, Y.-H. Nam, D.-H. Kim, and J.-H. Lee, *Thin Solid Films*, 2016, **599**, 54–58.

34. H.-P. Wang, K. Sun, S. Y. Noh, A. Kargar, M.-L. Tsai, M.-Y. Huang, D. Wang, and J.-H. He, *Nano Lett.*, 2015, **15**, 2817–2824.
35. M. F. Lichterman, K. Sun, S. Hu, X. Zhou, M. T. McDowell, M. R. Shaner, M. H. Richter, E. J. Crumlin, A. I. Carim, F. H. Saadi, B. S. Brunschwig, and N. S. Lewis, *Catal. Today*, 2016, **262**, 11–23.
36. T. Zhu and M. N. Chong, *Nano Energy*, 2015, **12**, 347–373.
37. J. A. Turner, *Science*, 2013, **342**, 811–812.
38. F. Lin, B. F. Bachman, and S. W. Boettcher, *J. Phys. Chem. Lett.*, 2015, **6**, 2427–2433.
39. F. Lin and S. W. Boettcher, *Nat. Mater.*, 2013, **13**, 81–86.
40. M. R. Nellist, F. A. L. Laskowski, F. Lin, T. J. Mills, and S. W. Boettcher, *Acc. of Chem. Res.*, 2016, **49**, 733–740.
41. T. W. Hamann, *Nat. Mater.*, 2013, **13**, 3–4.
42. B. S. Yeo and A. T. Bell, *J. Phys. Chem. C*, 2012, **116**, 8394.
43. L. Trotochaud, S. L. Young, J. K. Ranney, and S. W. Boettcher, *J. Am. Chem. Soc.*, 2014, **136**, 6744–6753.
44. M. B. Stevens, L. J. Enman, A. S. Batchellor, M. R. Cosby, A. E. Vise, and S. W. Boettcher, *Chem. Mater.*, 2016.
45. M. S. Burke, L. J. Enman, A. S. Batchellor, S. Zou, and S. W. Boettcher, *Chem. Mater.*, 2015, **27**, 7549–7558.
46. A. M. Smith, L. Trotochaud, M. S. Burke, and S. W. Boettcher, *Chem. Comm.*, 2015, **51**, 5261–5263.
47. S. M. Sze and K. K. Ng, *Physics of Semiconductor Devices*, 2006.
48. S. M. Sze, *Semiconductor Devices: Physics and Technology*, 2008.
49. T. J. Mills, F. Lin, and S. W. Boettcher, *Phys. Rev. Lett.*, 2014, **112**, 148304.
50. R. C. Rossi, M. X. Tan, and N. S. Lewis, *Appl. Phys. Lett.*, 2000, **77**, 2698–2700.
51. H. Doğan, N. Yildirim, A. Turut, M. Biber, E. Ayyildiz, and Ç. Nuhoglu, *Semicond. Sci. Technol.*, 2006, **21**, 822–828.
52. R. T. Tung, *Appl. Phys. Rev.*, 2014, **1**, 011304.
53. R. T. Tung, *Mater. Sci. Eng. R Rep.*, 2001, **35**, 1–138.

54. M. R. Nellist, Y. Chen, A. Mark, S. Goedrich, C. Stelling, J. Jiang, R. Poddar, C. Li, R. Kumar, G. Papastavrou, M. Retsch, B. Brunschwig, Z. Huang, C. Xiang, and S. W. Boettcher, *Nanotechnology*, 2017, Accepted.
54. Z. Huang, P. De Wolf, R. Poddar, C. Li, A. Mark, M. R. Nellist, Y. Chen, J. Jiang, G. Papastavrou, S. W. Boettcher, C. Xiang, and B. S. Brunschwig, *Microsc. Today*, 2016, **24**, 18.
55. R. M. Swanson, *Sol. Cells*, 1986, **17**, 85–118.
56. S. De Vecchi, T. Desrues, F. Souche, D. Muñoz, P. J. Ribeyron, and M. Lemitte, *Energy Proc.*, 2012, **27**, 549–554.

## G. References for Paper G

Style: Nature Materials

1. Sivula, K. & van de Krol, R. Semiconducting materials for photoelectrochemical energy conversion. *Nat. Rev. Mater.* **1**, 15010, (2016).
2. Walter, M. G., Warren, E. L., McKone, J. R., Boettcher, S. W., Mi, Q. X., Santori, E. A. & Lewis, N. S. Solar water splitting cells. *Chem. Rev.* **110**, 6446-6473, (2010).
3. Lewerenz, H. J., Heine, C., Skorupska, K., Szabo, N., Hannappel, T., Vo-Dinh, T., Campbell, S. A., Klemm, H. W. & Muñoz, A. G. Photoelectrocatalysis: principles, nanoemitter applications and routes to bio-inspired systems. *Energy Environ. Sci.* **3**, 748-760, (2010).
4. Chen, R. T., Fan, F. T., Dittrich, T. & Li, C. Imaging photogenerated charge carriers on surfaces and interfaces of photocatalysts with surface photovoltage microscopy. *Chem. Soc. Rev.* **47**, 8238-8262, (2018).
5. Mei, B., Han, K. & Mul, G. D. Driving surface redox reactions in heterogeneous photocatalysis: the active state of illuminated semiconductor-supported nanoparticles during overall water-splitting. *ACS Catal.* **8**, 9154-9164, (2018).
6. Laskowski, F. A. L., Nellist, M. R., Qu, J. J. & Boettcher, S. W. Metal oxide/(oxy)hydroxide overlayers as hole collectors and oxygen-evolution catalysts on water-splitting photoanodes. *J. Am. Chem. Soc.* **141**, 1394-1405, (2019).
7. Laskowski, F. A. L., Nellist, M. R., Venkatkarthick, R. & Boettcher, S. W. Junction behavior of n-Si photoanodes protected by thin Ni elucidated from dual working electrode photoelectrochemistry. *Energy Environ. Sci.* **10**, 570-579, (2017).
8. Tung, R. T. The physics and chemistry of the Schottky barrier height. *Appl. Phys. Rev.* **1**, 011304, (2014).
9. Tung, R. T. Electron-transport of inhomogeneous schottky barriers. *Appl. Phys. Lett.* **58**, 2821-2823, (1991).
10. Tennyson, E. M., Gong, C. & Leite, M. S. Imaging energy harvesting and storage systems at the nanoscale. *ACS Energy Lett.* **2**, 2761-2777, (2017).
11. Collins, L. *et al.* Probing charge screening dynamics and electrochemical processes at the solid-liquid interface with electrochemical force microscopy. *Nat. Commun.* **5**, 3871, (2014).
12. Collins, L., Kilpatrick, J. I., Kalinin, S. V. & Rodriguez, B. J. Towards nanoscale electrical measurements in liquid by advanced KPFM techniques: a review. *Rep. Prog. Phys.* **81**, 086101, (2018).

13. Eichhorn, J., Kastl, C., Cooper, J. K., Ziegler, D., Schwartzberg, A. M., Sharp, I. D. & Toma, F. M. Nanoscale imaging of charge carrier transport in water splitting photoanodes. *Nat. Commun.* **9**, 2597, (2018).
14. Handoko, A. D., Wei, F. X., Jenndy, Yeo, B. S. & Seh, Z. W. Understanding heterogeneous electrocatalytic carbon dioxide reduction through operando techniques. *Nat. Catal.* **1**, 922-934, (2018).
15. Esposito, D. V., Levin, I., Moffat, T. P. & Talin, A. A. H<sub>2</sub> evolution at Si-based metal-insulator-semiconductor photoelectrodes enhanced by inversion channel charge collection and H spillover. *Nat. Mater.* **12**, 562-568, (2013).
16. Mariano, R. G., McKelvey, K., White, H. S. & Kanan, M. W. Selective increase in CO<sub>2</sub> electroreduction activity at grain-boundary surface terminations. *Science* **358**, 1187-1191, (2017).
17. Hurth, C., Li, C. Z. & Bard, A. J. Direct probing of electrical double layers by scanning electrochemical potential microscopy. *J. Phys. Chem. C* **111**, 4620-4627, (2007).
18. Yoon, Y. H., Woo, D. H., Shin, T., Chung, T. D. & Kang, H. Real-space investigation of electrical double layers. Potential gradient measurement with a nanometer potential probe. *J. Phys. Chem. C* **115**, 17384-17391, (2011).
19. Nellist, M. R., Laskowski, F. A. L., Qiu, J. J., Hajibabaei, H., Sivula, K., Hamann, T. W. & Boettcher, S. W. Potential-sensing electrochemical atomic force microscopy for in operando analysis of water-splitting catalysts and interfaces. *Nat. Energy* **3**, 46-52, (2018).
20. Loget, G., Fabre, B., Fryars, S., Meriadec, C. & Ababou-Girard, S. Dispersed Ni nanoparticles stabilize silicon photoanodes for efficient and inexpensive sunlight-assisted water oxidation. *ACS Energy Lett.* **2**, 569-573, (2017).
21. Kenney, M. J., Gong, M., Li, Y. G., Wu, J. Z., Feng, J., Lanza, M. & Dai, H. J. High-performance silicon photoanodes passivated with ultrathin nickel films for water oxidation. *Science* **342**, 836-840, (2013).
22. Oh, K., Meriadec, C., Lassalle-Kaiser, B., Dorcet, V., Fabre, B., Ababou-Girard, S., Joanny, L., Gouttefangeas, F. & Loget, G. Elucidating the performance and unexpected stability of partially coated water-splitting silicon photoanodes. *Energy Environ. Sci.* **11**, 2590-2599, (2018).
23. Loget, G. Water oxidation with inhomogeneous metal-silicon interfaces. *Curr. Opin. Colloid Interface Sci.* **39**, 40-50, (2019).
24. Sullivan, J. P., Tung, R. T., Pinto, M. R. & Graham, W. R. Electron-transport of inhomogeneous Schottky barriers - a numerical study. *J. Appl. Phys.* **70**, 7403-7424, (1991).
25. Tung, R. T. Electron-transport at metal-semiconductor interfaces - general theory. *Phys. Rev. B* **45**, 13509-13523, (1992).

26. Hill, J. C., Landers, A. T. & Switzer, J. A. An electrodeposited inhomogeneous metal-insulator-semiconductor junction for efficient photoelectrochemical water oxidation. *Nat. Mater.* **14**, 1150, (2015).
27. Rossi, R. C., Tan, M. X. & Lewis, N. S. Size-dependent electrical behavior of spatially inhomogeneous barrier height regions on silicon. *Appl. Phys. Lett.* **77**, 2698-2700, (2000).
28. Roe, E. T., Egelhofer, K. E. & Lonergan, M. C. Limits of contact selectivity/recombination on the open-circuit voltage of a photovoltaic. *ACS Appl. Energy Mater.* **1**, 1037-1046, (2018).
29. Oener, S. Z., Cavalli, A., Sun, H. Y., Haverkort, J. E. M., Bakkers, E. P. A. M. & Garnett, E. C. Charge carrier-selective contacts for nanowire solar cells. *Nat. Commun.* **9**, 3248, (2018).
30. Burke, M. S., Enman, L. J., Batchellor, A. S., Zou, S. H. & Boettcher, S. W. Oxygen evolution reaction electrocatalysis on transition metal oxides and (oxy)hydroxides: activity trends and design principles. *Chem. Mater.* **27**, 7549-7558, (2015).
31. Li, S. Y., She, G. W., Chen, C., Zhang, S. Y., Mu, L. X., Guo, X. X. & Shi, W. S. Enhancing the photovoltage of Ni/n-Si photoanode for water oxidation through a rapid thermal process. *ACS Appl. Mater. Interfaces* **10**, 8594-8598, (2018).
32. Nellist, M. R. *et al.* Atomic force microscopy with nanoelectrode tips for high resolution electrochemical, nanoadhesion and nanoelectrical imaging. *Nanotechnology* **28**, 095711, (2017).
33. Tung, R. T. Recent advances in Schottky barrier concepts. *Mater. Sci. Eng., R* **35**, 1-138, (2001).
34. Lin, F. D. & Boettcher, S. W. Adaptive semiconductor/electrocatalyst junctions in water-splitting photoanodes. *Nat. Mater.* **13**, 81-86, (2014).
35. Nellist, M. R., Laskowski, F. A. L., Lin, F. D., Mills, T. J. & Boettcher, S. W. Semiconductor-electrocatalyst interfaces: theory, experiment, and applications in photoelectrochemical water splitting. *Acc. Chem. Res.* **49**, 733-740, (2016).
36. Digdaya, I. A., Adhyaksa, G. W. P., Trzesniewski, B. J., Garnett, E. C. & Smith, W. A. Interfacial engineering of metal-insulator-semiconductor junctions for efficient and stable photoelectrochemical water oxidation. *Nat. Commun.* **8**, 15968, (2017).
37. Ratcliff, E. L., Meyer, J., Steirer, K. X., Garcia, A., Berry, J. J., Ginley, D. S., Olson, D. C., Kahn, A. & Armstrong, N. R. Evidence for near-surface NiOOH species in solution-processed NiO<sub>x</sub> selective interlayer materials: Impact on energetics and the performance of polymer bulk heterojunction photovoltaics. *Chem. Mater.* **23**, 4988-5000, (2011).
38. Röppischer, H., Bumai, Y. A. & Feldmann, B. Flatband potential studies at the n-Si/electrolyte interface by electroreflectance and C-V measurements. *J. Electrochem. Soc.* **142**, 650-655, (1995).



39. Xu, G. Z., Xu, Z., Shi, Z., Pei, L., Yan, S. C., Gu, Z. B. & Zou, Z. G. Silicon photoanodes partially covered by Ni@Ni(OH)<sub>2</sub> core-shell particles for photoelectrochemical water oxidation. *Chemsuschem* **10**, 2897-2903, (2017).
40. Lee, S. A., Lee, T. H., Kim, C., Lee, M. G., Choi, M. J., Park, H., Choi, S., Oh, J. & Jang, H. W. Tailored NiO<sub>x</sub>/Ni cocatalysts on silicon for highly efficient water splitting photoanodes via pulsed electrodeposition. *ACS Catal.* **8**, 7261-7269, (2018).
41. Choi, K., Kim, K., Moon, I. K., Oh, I. & Oh, J. Evaluation of electroless Pt deposition and electron beam Pt evaporation on p-GaAs as a photocathode for hydrogen evolution. *ACS Appl. Energy Mater.* **2**, 770-776, (2019).
42. Zhang, H. X. *et al.* A p-Si/NiCoSe<sub>x</sub> core/shell nanopillar array photocathode for enhanced photoelectrochemical hydrogen production. *Energy Environ. Sci.* **9**, 3113-3119, (2016).
43. Wang, N., Tachikawa, T. & Majima, T. Single-molecule, single-particle observation of size-dependent photocatalytic activity in Au/TiO<sub>2</sub> nanocomposites. *Chem. Sci.* **2**, 891-900, (2011).
44. Yoshikawa, K. *et al.* Silicon heterojunction solar cell with interdigitated back contacts for a photoconversion efficiency over 26%. *Nat. Energy* **2**, 17032, (2017).
45. Hu, S., Lewis, N. S., Ager, J. W., Yang, J. H., McKone, J. R. & Strandwitz, N. C. Thin-film materials for the protection of semiconducting photoelectrodes in solar-fuel generators. *J. Phys. Chem. C* **119**, 24201-24228, (2015).
46. Takata, T. & Domen, K. Particulate photocatalysts for water splitting: recent advances and future prospects. *ACS Energy Lett.* **4**, 542-549, (2019).
47. Wang, Q. *et al.* Scalable water splitting on particulate photocatalyst sheets with a solar-to-hydrogen energy conversion efficiency exceeding 1%. *Nat. Mater.* **15**, 611, (2016).
48. Su, Y. D., Liu, C., Britzman, S., Tang, J. Y., Fu, A., Kornienko, N., Kong, Q. & Yang, P. D. Single-nanowire photoelectrochemistry. *Nat. Nanotechnol.* **11**, 609, (2016).
49. Wang, J., Zhao, J. & Osterloh, F. E. Photochemical charge transfer observed in nanoscale hydrogen evolving photocatalysts using surface photovoltage spectroscopy. *Energy Environ. Sci.* **8**, 2970-2976, (2015).
50. Litster, S. & McLean, G. PEM fuel cell electrodes. *J. Power Sources* **130**, 61-76, (2004).
51. Inomata, H., Takahashi, Y., Takamatsu, D., Kumatani, A., Ida, H., Shiku, H. & Matsue, T. Visualization of inhomogeneous current distribution on ZrO<sub>2</sub>-coated LiCoO<sub>2</sub> thin-film electrodes using scanning electrochemical cell microscopy. *Chem. Commun.* **55**, 545-548, (2019).
52. Takahashi, Y. *et al.* Nanoscale visualization of redox activity at lithium-ion battery cathodes. *Nat. Commun.* **5**, 5420, (2014).

53. Marliere, C. & Dhahri, S. An in vivo study of electrical charge distribution on the bacterial cell wall by atomic force microscopy in vibrating force mode. *Nanoscale* **7**, 8843-8857, (2015).
54. Pfreundschuh, M., Hensen, U. & Muller, D. J. Quantitative imaging of the electrostatic field and potential generated by a transmembrane protein pore at subnanometer resolution. *Nano Lett.* **13**, 5585-5593, (2013).

## H. References for Paper E Supporting Information

Style: Physical Review Letters

- [1] J. Bisquert, P. Cendula, L. Bertoluzzi, and S. Gimenez, *J. Phys. Chem. Lett.* **5**, 205 (2014).
- [2] S. M. Sze, *Semiconductor devices: physics and technology* (John Wiley & Sons, 2008).
- [3] H. Gerischer, *Adv. Electrochem. Eng.* **1**, 139 (1961).
- [4] W. W. Gärtner, *Phys. Rev. Lett.* **116**, 84 (1959).
- [5] W. J. Albery and P. N. Bartlett, *J. Electrochem. Soc.* **130**, 1699 (1983).
- [6] W. J. Albery, P. N. Bartlett, A. Hamnett, and M. P. Dareedwards, *J. Electrochem. Soc.* **128**, 1492 (1981).
- [7] F. Elguibaly and K. Colbow, *J. Appl. Phys.* **53**, 1737 (1982).
- [8] L. M. Peter, E. A. Ponomarev, and D. J. Fermin, *J. Electroanal. Chem.* **427**, 79 (1997).
- [9] L. M. Peter, K. G. U. Wijayantha, and A. A. Tahir, *Faraday Discuss.* **155**, 309 (2012).
- [10] F. Berz, *J. Appl. Phys.* **50**, 4479 (1979).
- [11] D. Vanmaekelbergh, *Electrochim. Acta* **42**, 1121 (1997).
- [12] T. J. Mills, F. D. Lin, and S. W. Boettcher, *Phys. Rev. Lett.* **112** (2014).

## I. References for Paper F Supporting Information

Style: Energy & Environmental Science

1. A. M. Smith, L. Trotochaud, M. S. Burke, and S. W. Boettcher, *Chem. Commun.*, 2015, **51**, 5261–5263.
2. M. S. Burke, L. J. Enman, A. S. Batchellor, S. Zou, and S. W. Boettcher, *Chem. Mater.*, 2015, **27**, 7549–7558.
3. L. Trotochaud, S. L. Young, J. K. Ranney, and S. W. Boettcher, *J. Am. Chem. Soc.*, 2014, **136**, 6744–6753.
4. S. M. Sze, *Semiconductor Devices: Physics and Technology*, 2008.
5. A. Kraut, *NIST X-ray Photoelectron Spectroscopy Database 20. Version 4.1*, 2012.
6. J. F. Moulder, W. F. Stickle, P. E. Sobol, and K. D. Bomben, *Standard Spectra for Identification and Interpretation of XPS Data*, 1992.
7. K. S. Kim and N. Winograd, *Surface Science*, 1974, **43**, 625–643.

## J. References for Paper G Supporting Information

Style: Nature Materials

- (1) Tung, R. T. Recent advances in Schottky barrier concepts. *Mater. Sci. Eng., R* **35**, 1-138 (2001).
- (2) Loget, G.; Fabre, B.; Fryars, S.; Meriadec, C.; Ababou-Girard, S. Dispersed Ni nanoparticles stabilize silicon photoanodes for efficient and inexpensive sunlight-assisted water oxidation. *ACS Energy Lett.* **2**, 569-573 (2017).
- (3) Tung, R. T. The physics and chemistry of the Schottky barrier height. *Appl. Phys. Rev.* **1**, 011304 (2014).
- (4) Tung, R. T. Electron-transport at metal-semiconductor interfaces - general-theory. *Phys. Rev. B* **45**, 13509-13523 (1992).
- (5) Deng, J.; Nellist, M. R.; Stevens, M. B.; Dette, C.; Wang, Y.; Boettcher, S. W. Morphology dynamics of single-layered Ni(OH)<sub>2</sub>/NiOOH nanosheets and subsequent Fe incorporation studied by *in situ* electrochemical atomic force microscopy. *Nano Lett.* **17**, 6922-6926 (2017).
- (6) Oh, K.; Meriadec, C.; Lassalle-Kaiser, B.; Dorcet, V.; Fabre, B.; Ababou-Girard, S.; Joanny, L.; Gouttefangeas, F.; Loget, G. Elucidating the performance and unexpected stability of partially coated water-splitting silicon photoanodes. *Energy Environ. Sci.* **11**, 2590-2599 (2018).